

Bangor University

DOCTOR OF PHILOSOPHY

Growth and characterisation of functional molecular wires

Barnes, Susan Andrea

Award date:
2012

Awarding institution:
Bangor University

[Link to publication](#)

General rights

Copyright and moral rights for the publications made accessible in the public portal are retained by the authors and/or other copyright owners and it is a condition of accessing publications that users recognise and abide by the legal requirements associated with these rights.

- Users may download and print one copy of any publication from the public portal for the purpose of private study or research.
- You may not further distribute the material or use it for any profit-making activity or commercial gain
- You may freely distribute the URL identifying the publication in the public portal ?

Take down policy

If you believe that this document breaches copyright please contact us providing details, and we will remove access to the work immediately and investigate your claim.

Download date: 09. Apr. 2024

Growth and Characterisation of Functional Molecular Wires

A thesis submitted to the
University of Wales
in candidature for the

Degree of
Philosophiæ Doctor

by

Susan Andrea Barnes

Supervisor: Professor Geoffrey J. Ashwell

PRIFYSGOL
BANGOR
UNIVERSITY



School of Chemistry
Prifysgol Bangor – Bangor University

2012



ACKNOWLEDGEMENTS

Firstly, I would like to extend my sincerest thanks to my supervisor, Professor Geoffrey J. Ashwell, whose frequent advice and enthusiasm have made this thesis possible. I am extremely grateful for funding provided by the Bangor University Price Davies Studentship and the Engineering and Physical Sciences Research Council (EPSRC). I would also like to acknowledge the continued encouragement, guidance and support of Dr Mike Beckett, Dr Ben Robinson, Dr Barbara Urasinska-Wojcik, Dr Laurie Phillips and Aled Williams. Further thanks to the EPSRC for access to the Cardiff X-ray photoelectron spectroscopy Analysis Centre and Dr David Morgan for his aid and advice. For their unshakeable support and friendship over the past eight years of University life, I thank my fellow chemists Helen and Claire. Finally I dedicate this thesis to my wonderful parents, Jenny and Malcolm, and to my fiancé Mike.

ABSTRACT

With the miniaturisation of silicon based technology approaching its fundamental physical limit, molecular electronic components are considered an alternative route to prolong the lifetime of integrated circuit technology. In order to realise this technology, the fundamental physical and electronic properties of such nanoscopic materials and devices must be fully understood.

This thesis reports the successful formation and characterisation of a series of novel molecular wires on both planar and nanoparticulate surfaces, from which two papers have been published. Formation of these wires was achieved using the reproducible chemical self-assembly method often utilised in bottom-up molecular electronics. After the initial chemisorption of a functional headgroup to a suitable substrate, subsequent layers were chemically reacted by means of an imine bond formation. This allowed multilayer donor- π -bridge-acceptor systems of up to *ca.* 10.4 nm in length to be constructed. Not only does this method allow the formation of reasonably complex systems, it also enables functionality to be incorporated into the wire. The assembly characteristics of various wires have been characterised using Quartz Crystal Microbalance and X-ray Photoelectron Spectroscopy, and in the case of those on TiO₂ nanoparticles, with Infrared Spectroscopy. Furthermore, an investigation into the factors affecting the formation of upright, homogeneous monolayers was carried out on a set of related compounds, revealing the importance of molecule-molecule and molecule-substrate interactions.

Multiple molecular wires were also characterised with respect to their electrical properties which show symmetrical or asymmetrical current-voltage curves. This was done using Scanning Tunnelling Spectroscopy to obtain current-voltage characteristics, as well as the so called current jump method to measure single molecule current or that of small clusters of molecules. The effect of increasing molecular length and steric hindrance on molecular current rectification was examined, as well as the effect of increasing length on single molecule conductance.

CONTENTS

Acknowledgements	i
Abstract.....	ii
Abbreviations	vi
Compounds.....	viii
 1.0 Introduction	 1
1.1 Silicon Technology	1
1.2 Molecular Electronics	2
1.3 Practical Devices.....	3
1.3.1 Molecular Wires	3
1.3.2 Molecular Diodes	5
 2.0 Monolayer Construction	 13
2.1 Molecular self-assembly	13
2.1.1 The Gold-Sulfur bond.....	14
2.1.2 The Gold-Amine bond.....	17
2.1.3 The Titania-Acid bond.....	18
2.2 Molecular Wire Extension	20
2.3 Electrostatic Self-assembly.....	20
2.4 Langmuir-Blodgett.....	22
 3.0 Characterisation techniques	 26
3.1 Physical Characterisation.....	26
3.1.1 Quartz Crystal Microbalance.....	26
3.1.2 X-ray Photoelectron Spectroscopy	29
3.1.3 Infrared Spectroscopy.....	31
3.2 Electronic Characterisation.....	33
3.2.1 Scanning Tunnelling Microscope.....	33
3.2.1.1 STM for Single Molecule Conductance	37
3.2.1.2 STM for I(s)	40
3.2.1.3 STM for I(t)	41
 4.0 Experimental.....	 44
4.1 Substrate preparation	44
4.1.1 Quartz Crystals	44
4.1.2 Highly Ordered Pyrolytic Graphite	45
4.2 Monolayer Preparation	46
4.3 Physical characterisation.....	47
4.3.1 Quartz Crystal Microbalance.....	47
4.3.2 X-ray Photoelectron Spectroscopy	48
4.3.3 Infrared Spectroscopy.....	49

4.4	Electronic characterisation.....	49
4.4.1	STM for I - V	49
4.4.2	STM for $I(t)$	50
4.5	Studied Compounds.....	50
4.5.1	Synthesis of C1	53
4.5.2	Synthesis of Titania Nanoparticles	53
4.6	Errors	54
5.0	Results.....	55
5.1	Formation of S1	55
5.1.1	C1 synthesis: Analysis.....	55
5.1.2	Physical characterisation: QCM.....	56
5.1.3	Physical characterisation: XPS.....	57
5.1.4	Electrical characterisation: I - V	60
5.1.5	Summary.....	61
5.2	Formation of S2	61
5.2.1	Physical characterisation: QCM.....	61
5.2.2	Physical characterisation: XPS.....	62
5.2.3	Summary.....	64
5.3	Formation of S3 _a	65
5.3.1	Physical Characterisation: QCM	65
5.3.2	Physical Characterisation: XPS	66
5.3.3	Electrical characterisation: I - V	67
5.3.4	Summary.....	68
5.4	Formation of a 10-step system: S3 _a -S7 _a	69
5.4.1	Physical characterisation: QCM.....	69
5.4.2	Electrical characterisation: I - V	70
5.4.3	Summary.....	73
5.5	Rectification investigation of S4 _b and S4 _c	73
5.5.1	Physical Characterisation: QCM	74
5.5.2	Electrical characterisation: I - V	74
5.5.3	Summary.....	75
5.6	Formation of 11-step system S3 _b -S7 _b	76
5.6.1	Physical characterisation: QCM.....	76
5.6.2	Electrical characterisation: I - V	77
5.6.3	Summary.....	80
5.7	Current Jumps.....	80
5.7.1	Summary.....	85
5.8	Formation of S8 _a -S10 _a	88
5.8.1	Physical characterisation: QCM.....	89
5.8.2	Physical characterisation: XPS.....	91
5.8.3	Electrical characterisation: I - V	94
5.8.4	Summary.....	95
5.9	Formation of S11	95
5.9.1	Physical characterisation: QCM	96
5.10	Formation of S12 _a -S13 _a	96
5.10.1	Physical characterisation: QCM.....	97
5.11	Formation of S14	99
5.11.1	Physical characterisation: QCM.....	99

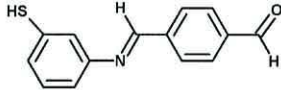
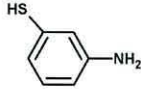
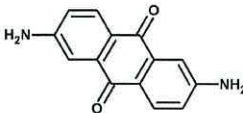
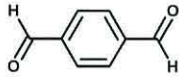
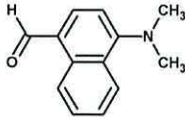
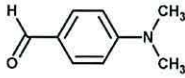
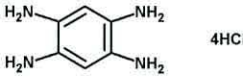
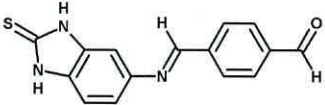
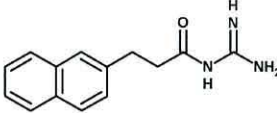
5.11.2	Physical characterisation: XPS.....	100
5.11.3	Summary.....	104
5.12	Assembly Characteristics of C9-C15.....	105
5.12.1	Physical characterisation: QCM.....	105
5.12.2	Physical characterisation: XPS.....	110
5.13	Formation of S15-S17.....	110
5.13.1	Formation of S15.....	111
5.13.2	Physical characterisation: QCM.....	111
5.13.3	Physical characterisation: XPS.....	112
5.13.4	Formation of S16 and S17.....	117
5.13.5	Physical characterisation: QCM.....	117
5.13.6	Infrared Spectroscopy analysis of Titania Nanoparticles.....	118
5.13.7	Summary.....	120
6.0	Conclusions	122
7.0	Further Work.....	125
8.0	References.....	127
9.0	Publications and Conferences	143

ABBREVIATIONS

ARXPS	Angle-resolved x-ray photoelectron spectroscopy
A _s	Strong acceptor
CNT	Carbon nanotube
DFT	Density functional theory
DNA	Deoxyribonucleic acid
D _s	Strong donor
D _w	Weak donor
ESA	Electrostatic self-assembly
EQCM	Electrochemical quartz crystal microbalance
FT-IR	Fourier transform infrared
HOMO	Highest occupied molecular orbital
HOPG	Highly ordered pyrolytic gold
IR	Infrared
I(s)	Current-distance
I(t)	Current-time
I-V	Current-voltage
LB	Langmuir Blodgett
LUMO	Lowest unoccupied molecular orbital
MMI	Monolayer matrix isolation
MOSFET	Metal-oxide semiconductor field-effect transistor
MW	Molecular wire
OLED	Organic light emitting diode
QCM	Quartz crystal microbalance
RR	Rectification ratio
<RR>	Average rectification ratio
RSF	Relative sensitivity factor
SA	Self-assembly

SAM	Self-assembled monolayer
STM	Scanning tunnelling microscope
STS	Scanning tunnelling spectroscopy
TCNQ	Tetracyanoquinodimethane
THF	Tetrahydrofuran
TTF	Tetrathiafulvalene
XPS	X-ray photoelectron spectroscopy

COMPOUNDS

Pseudonym	Name	Structure
C1	4-[(3-mercaptophenylimino)-methyl]-benzaldehyde	
C2	3-Aminothiophenol	
C3	2,6-diaminoanthra-9,10-quinone	
C4	Terephthalaldehyde	
C5	4-Dimethylamino-1-naphthaldehyde	
C6	4-(Dimethylamino)benzaldehyde	
C7	1,2,4,5-Benzenetetramine tetrahydrochloride	
C8	4-{(E)-1,3-dihydro-2H-benzimidazol-2-thione-5-yl}imino]methyl} benzaldehyde	
C9	<i>N</i> -carbamimidoyl-3-(naphthalen-2-yl)propanamide	

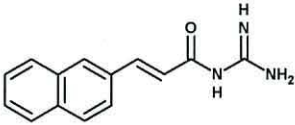
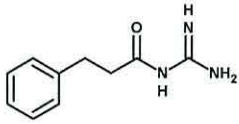
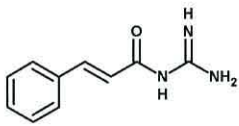
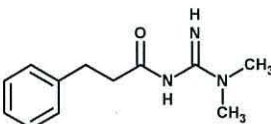
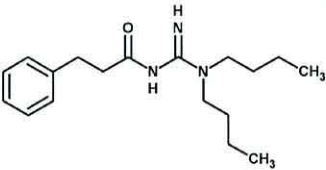
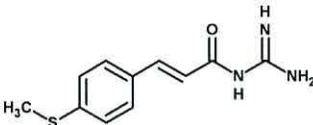
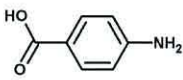
C10	(E)-N-carbamimidoyl-3-(naphthalen-2-yl)acrylamide	
C11	N-carbamimidoyl-3-phenylpropanamide	
C12	N-carbamimidoylcinnamamide	
C13	N-(N,N-dimethylcarbamimidoyl)-3-phenylpropanamide	
C14	N-(N,N-dibutylcarbamimidoyl)-3-phenylpropanamide	
C15	(E)-N-carbamimidoyl-3-(4-(methylthio)phenyl)acrylamide	
C16	4-Aminobenzoic acid	

Table (i): Summary of compounds used in preparation of S1-S17.

1.0 INTRODUCTION

1.1 SILICON TECHNOLOGY

The current electronics market is dominated by the silicon-based complementary metal-oxide semiconductor (CMOS) transistor, which consists of a source, drain, channel and gate region. The first transistor was produced in 1947 by Shockley, Bardeen and Brattain of Bell Labs, although the initial model was soon replaced by the modern junction transistor. The first commercially available transistor radio was released in the 1950's and consisted of just four germanium transistors. From this point onwards, the miniaturisation process evolved at a substantial pace, so much so that we can compare the first microprocessor launched by Intel in 1971, consisting of 2250 transistors and measuring 1/8 by 1/6 of an inch with that of microprocessors built in the mid 1980's which contained some 275,000 transistors. Transistor sizes have continued to decrease, and more recently (May 2011) the first 22 nm 3-D tri-gate transistor was successfully designed and entered mass production.¹ In keeping with the pattern of introducing a new technology generation every 2 years, the Intel technology roadmap suggests a continued size decrease down to 10 nm by 2015. Microelectronics technology has continued scaling down by introducing thinner gate oxides and shorter channel lengths. By scaling these devices down, improvements in speed, power efficiency and transistor density have thus far been achieved.

This trend in miniaturisation was first vocalised in 1965 by Gordon Moore, formulator of 'Moore's Law'.² Moore famously predicted that the number of transistors in an integrated circuit would increase exponentially, doubling every two years, such was the demand for faster processors to perform complex electronic functions. When Gordon Moore made his prediction there were just 30 transistors on a single chip – at present they number a few hundred million which can be accommodated on just a few square centimetres of silicon, resulting in greater computing power and improved performance in devices such as PCs, mobile phones and satellites. Although the semiconductor industry continues to adhere to Moore's Law, the demand for ever-smaller and more powerful electronic devices has grown. Many limitations and obstacles are expected to arise within the next few technological generations. The continued development and improvement of lithographic tools has overcome

a number of issues with regards to concerns arising over scaling problems, although there are fundamental physical limitations that cannot be overcome. At such minute scales, the insulating gate oxide layer measures only a couple of nm thick, resulting in a substantial amount of current leakage from quantum mechanical tunnelling of electrons, which can lead to circuit failures.³ The solid solubility limit for silicon has already reached its saturation point for dopant atoms currently in use, having steadily increased for the past few decades. Eventually, it will no longer be feasible to continue reducing these silicon-based electronic devices, thus generating an essential drive in the diversification of current technology and exploration of alternative fabrication methods.

1.2 MOLECULAR ELECTRONICS

One approach to overcoming the miniaturisation threshold is the study of nanoscale molecular electronics,⁴⁻⁸ which can potentially be utilised in hybrid silicon-molecular electronic devices. Such multidisciplinary endeavours have attracted great interest over the last 10 years, and are of interest to both the academic and industrial sectors.

Defined as a system ranging from 1 to 100 nm, nanoscale organic compounds were first proposed by Aviram and Ratner in 1974 as a pathway through which electrons could travel for use as functional electronic components.⁹ Organic compounds, some 30,000 times smaller than typical transistors, offer many potential advantages over their silicon counterparts, from their scalability, inherent ability to assemble and organise, to the ability to modify constituent parts in order to control their electrical characteristics. However, little is known about their reliability and long term stability under differing conditions.^{10,11} At present, organic molecules have proved unstable at high temperatures, making them incompatible and therefore unsuitable for use in current device architectures.

The simplest practical systems consist of one or more molecules sandwiched between two electrodes, using the bottom-up approach, and can be utilised as molecular counterparts to wires,^{12,13} diodes¹⁴ and rectifying junctions,¹⁵ providing they are able to offer a pathway for electron transport. These important electronic devices will be discussed in greater detail further on. The bottom-up approach consists of designing and manufacturing systems from the smallest possible component upwards, whereas the top-down approach involves *reducing*

bulk systems. The principle advantage, from a chemistry perspective, of the bottom-up approach is in the ability to form self-assembled monolayers (SAMs), allowing accurate control of dimensions and electrical properties of the organic components on a molecular length scale.

1.3 PRACTICAL DEVICES

1.3.1 MOLECULAR WIRES

Molecular wires (MWs) are conceptually the simplest electronic devices, facilitating electron transport under the influence of electrical stimulus by providing an efficient pathway through which electrons can travel. As key components in circuits, MWs must be able to transport charge over distances of tens of angstroms, as well as being able to bond to a wide range of materials, from metal surfaces to biomolecules. As interconnects between a wide range of devices, including molecular switches, transistors and logic chips, several classes of molecular structures have been proposed, the most promising examples of which include π -conjugated organic molecules, DNA and carbon nanotubes (CNTs).^{16,17}

The most thoroughly investigated molecular wires at this time are planar conjugated hydrocarbons, with long-distance conduction occurring through the conjugated π -system. Already, polymerised wires such as poly(*p*-phenylene vinylene) have found applications in optoelectronics as organic light emitting diodes (OLEDs) for devices such as mobile phones.¹⁸ An example of this particular class is that of the rigid oligo(2,5-thiophene ethynylene)s, with the longest archetype measuring 12.8 nm in length (Figure 1.1).¹⁹

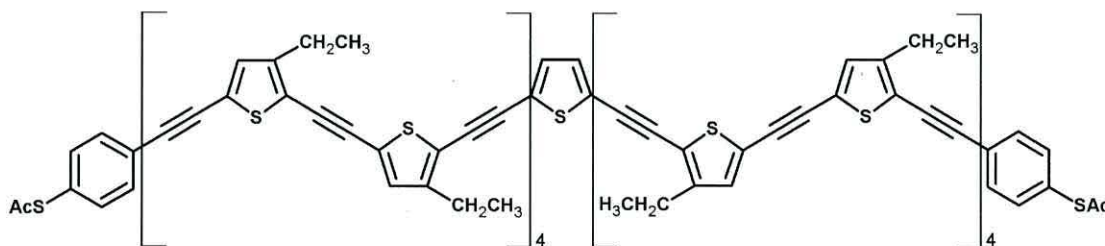


Figure 1.1: A 12.8 nm long oligo(2,5-thiophene ethynylene) wire synthesised by Pearson and Tour.¹⁹

The presence of a dithiol element allows the wire to bond to a gold (Au) surface, thus enabling electrons to flow from the metal Fermi levels through the thiol molecular orbitals to the conjugated section of the system. Another example of a long functional molecular wire (7 nm) synthesised by a method other than self-assembly has been reported by Bryce *et al.*²⁰ The hexyloxy side chains ensure the system is soluble in organic solvents whereas the terminating thiol groups allow deposition of the system onto a gold electrode for electrical characterisation. Such studies, both experimental and theoretical, show an average rectification ratio $\langle RR \rangle$ of 1.0 at ± 1 V, where the rectification ratio is defined as the ratio of forward to reverse current, providing an indication of the ability of the system to allow current to flow more readily in one direction than another. An $\langle RR \rangle$ of 1.0 at ± 1 V corresponds to the symmetrical nature of the wire, whereby current flows relatively freely in both directions. More recently, a π -bridged donor-acceptor molecular wire measuring *ca.* 5 nm has been synthesised via a six-step assembly process and verified using Sauerbrey analysis and X-ray Photoelectron Spectroscopy (XPS).²¹

MWs constructed from biologically important materials such as deoxyribonucleic acid (DNA) strands have shown promising results in terms of their conductivity. Barton and colleagues have reported a 34 nm-long strand of DNA composed of 100 base pairs that are able to conduct low levels of current without being damaged.²² As with the previously discussed wires, DNA strands were bound in an upright, ordered monolayer to a gold surface using thiol linkers. It is interesting to note that a break in the sugar-phosphate backbone does not result in retarded current flow. Instead, it was a break in the base pairs that caused the current to be significantly reduced. This suggests that the helical π -orbitals of the stacked pairs provide a delocalised pathway for electrons or holes to travel.

Although advantageous in sensor applications due to its sensitivity to environmental conditions, the relative ease at which DNA can be damaged has been found to have a detrimental effect on conductance through the wire.²³ Controversy also surrounds the issue of electron transport in DNA, with reports indicating behaviour analogous to insulating,²⁴ semiconducting²⁵ and conducting devices²⁶ respectively. This is thought to be due to the diversity of experimental approaches and conditions used.

CNTs, first discovered in 1991 by Iijima and co-workers,²⁷ are cylindrical constructs made up exclusively of covalently bound carbon atoms. These can be arranged in an armchair, zig-zag

or chiral pattern, depending on the orientation of the 6-membered ring. The seamless graphene tubes have many attractive physical and electronic properties, although difficulty remains in accurately controlling the chirality of the hexagonal lattice as well as diameter size, which can measure less than 1 nm. As the conductance is greatly dependent on these properties,²⁸ many theoretical and experimental studies have been carried out on a variety of CNTs. Of these, the majority were found to be semiconducting, with the remaining structures exhibiting metallic conduction characteristics.²⁹ CNTs have undergone extensive testing and have proved extremely resilient with regards to environmental stresses. For example, rather than fracturing when bent, the tube buckles reversibly. This stress-induced tolerance, as well as their light weight, means CNTs are of great interest to the aerospace industry. Their performance in simulated space settings has been investigated with respect to their performance in vacuum, under exposure to large thermal loads and rapid temperature changes. Furthermore, CNTs exhibit an impressive resistance to corrosion, as shown in a comparison between the ability of CNT and stranded Cu wire to withstand acidic conditions.³⁰ After 8 days in 1M HCl, the Cu wire began to show an increase in resistivity, whereas the CNT wire withstood a further 72 days before declining. This extensive list of desirous properties has resulted in many potential applications being proposed for CNTs, including energy storage,³¹ sensors,³² and molecular electronics devices.³³

1.3.2 MOLECULAR DIODES

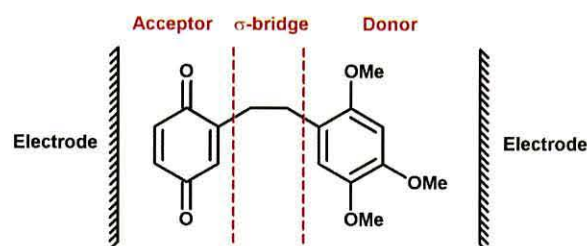


Figure 1.2: A rectifying hemiquinone as suggested by Aviram and Ratner.⁹

To be of use in practical electronic devices such as rectifying junctions and diodes, the organic structure in question must allow current to pass more readily in one direction than the other, as in a semiconductor p-n junction. The first theoretical organic molecular rectifier was proposed in 1974 by Aviram and Ratner⁹ and consists of an asymmetric hemiquinone

molecule that can be considered in three parts (Figure 1.2). Part 1 is a benzoquinone comprising an aromatic ring di-substituted with electron withdrawing C=O groups to produce an electron poor (accepting) unit. Part 2 again consists of an aromatic ring, this time tri-substituted with electron donating methoxy groups to generate an electron rich (donating) unit. By substituting an aromatic ring with electron-donating functional groups such as -NH₂, -OH, -CH₃, and -CH₂CH₃, that particular section of the system will become electron rich. This increase in the ring's electron density lowers the ionisation potential of that region, creating an electron donating moiety. In contrast, substitution via electron withdrawing groups such as -NO₂, -CN, and -CHO decreases the electron density of the aromatic ring, thereby increasing the electron affinity and resulting in an electron accepting moiety. These donor and acceptor units are separated by an insulating σ -bridge to ensure that they do not interact electronically. If overlap were to occur between the donor and acceptor orbitals, the electron density of the whole system would be in equilibrium, with little resulting rectification. Hence the proposed molecules should consist of adjacent donor and acceptor moieties sandwiched between two electrodes, and separated by a linking group that impedes the movement of electrons between them. Thus, electrons will find it easier to move towards the electron-deficient area than to the electron-rich. Although theoretically ideal, the synthesis and subsequent electrical analysis of this initial molecule has not been undertaken, and to this day the hemiquinone remains a theoretical model for organic rectifying systems.

The original model was soon adapted by replacing the single σ -bridge (Figure 1.2) with a triple σ -bridge (Figure 1.3 (a)). This maintains the electrical separation of donor and acceptor molecular orbitals as well as ensuring greater molecular rigidity. The acceptor and donor moieties were also replaced by tetracyanoquinodimethane (TCNQ) and tetrathiafulvalene (TTF), respectively. Again, this system has never been experimentally realised, although computational studies regarding their current-voltage (*I-V*) properties have been carried out (Figure 1.3 (b)). The proposed rectification of this system can be considered with the aid of an energy level diagram (Figures 1.4-1.6). Here we can observe the energy levels inherent in a system whereby the molecule is sandwiched between two electrodes, the cathode and anode. As the acceptor possesses a high electron affinity (1-2.5 V) due to its electron-withdrawing nature and the donor a low ionisation potential (6-9 V) because of its electron donating nature, we would expect the LUMO level of the acceptor to be correspondingly lower than that of the donor LUMO level. At this point, when no voltage has been applied to the system, the energy

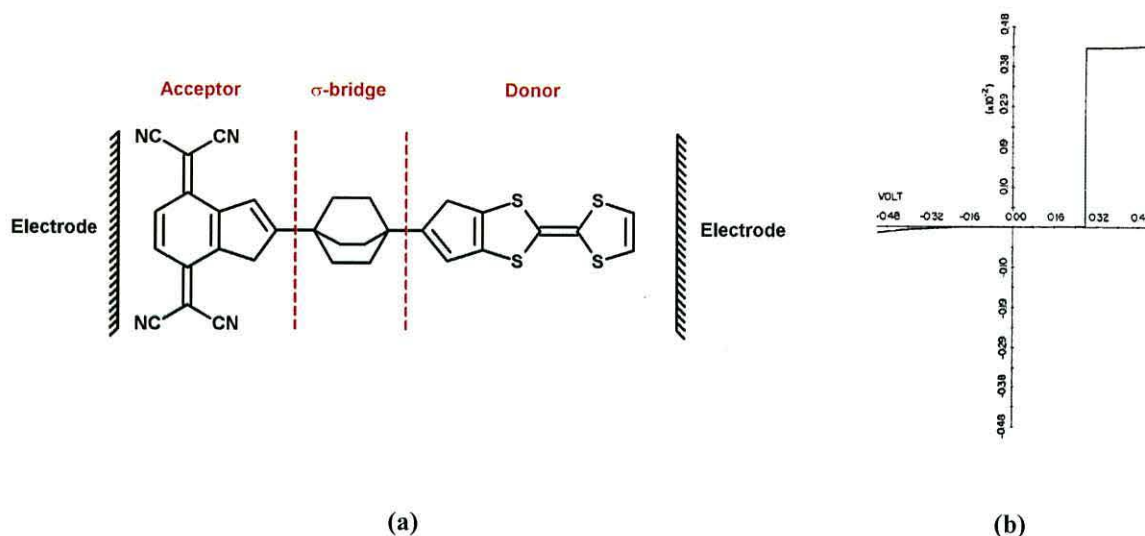
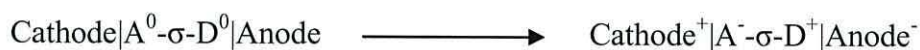


Figure 1.3: Aviram and Ratner proposed (a) a rectifying molecule consisting of an acceptor tetracyanoquinodimethane (TCNQ), donor tetrathiafulvalene (TTF) and σ -bridge sandwiched between two electrodes and (b) the resultant theoretical I - V characteristics.⁹

levels can be seen displayed in Figure 1.4. Also shown are the intrinsic energy levels essential in the construction of an effective rectifier, with the acceptor and donor LUMO (green) and HOMO (red) levels separated by the internal tunnelling barrier (σ -bridge). Also shown is the work function, Φ . For rectifying behaviour to occur under an applied voltage in the forward direction, the acceptor LUMO must lie at or slightly above the Fermi level of the cathode, and the donor LUMO as far as possible above the Fermi level of the anode (Figure 1.5). Similarly, to allow electron transfer from the donor HOMO to the Fermi level of the anode, these two should also be in close proximity, energy-wise. Upon application of a forward bias to the system, a two-stage process occurs, which can be summarised as:

- Electrons tunnel from the cathode to the Acceptor LUMO and from the Donor HOMO to the anode.



- Intramolecular electron transfer from left to right across the tunnelling barrier returns the system from the excited state to the ground state.



When a reverse voltage is applied, the mechanism is energetically unfavourable due to the energy mismatch between the donor LUMO and Fermi level of the right hand electrode (Figure 1.6). This results in little to no current flow in the reverse direction under the equivalent bias voltage, and it is this crucial ability of the system to favour current flow in one direction and not the other that makes these molecules so beneficial to organic diode construction.

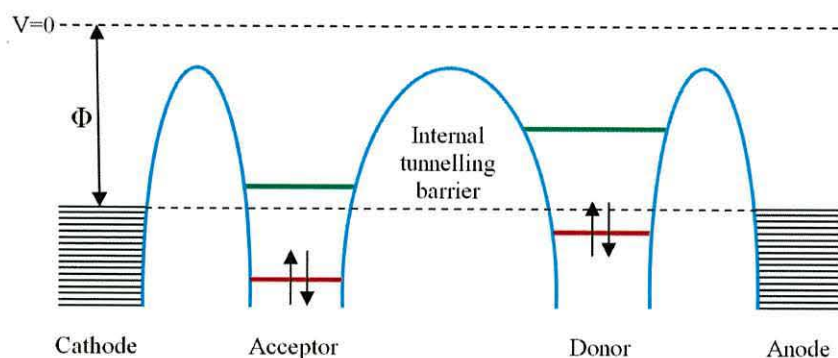


Figure 1.4: The Aviram and Ratner energy model for a rectifier with no applied voltage.

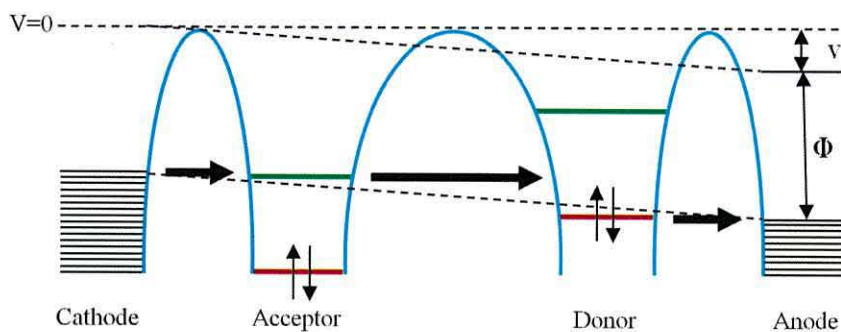


Figure 1.5: The Aviram and Ratner energy model for a rectifier under forward voltage.

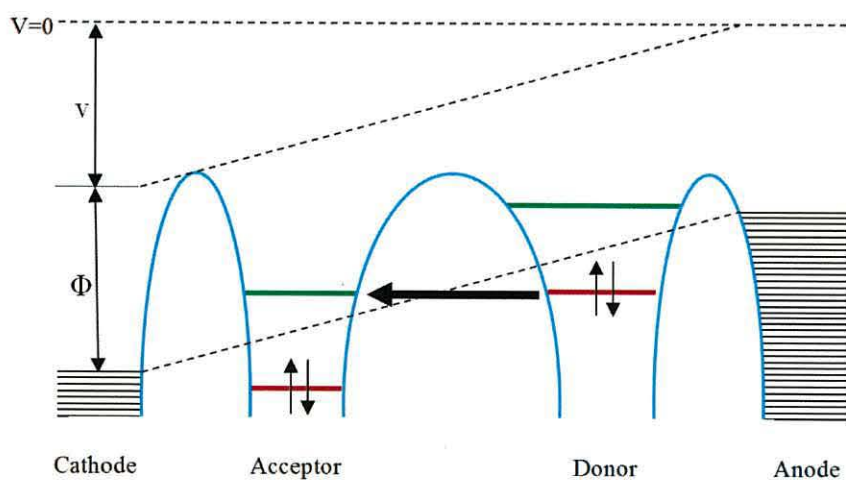


Figure 1.6: The Aviram and Ratner energy model for a rectifier under reverse voltage.

A measure of flow bias is the rectification ratio (RR), whereby the greater the RR the larger the forward bias and smaller the reverse bias.

Assuming the forward voltage (V_α) is equal and opposite to the reverse voltage (V_β).

$$V_\alpha = -V_\beta \quad \text{Equation 1.1}$$

And that the value for V_α is greater than the value for V_β .

$$|V_\alpha| > |V_\beta| \quad \text{Equation 1.2}$$

$$RR = \left| \frac{I(V_\alpha)}{I(V_\beta)} \right| \quad \text{Equation 1.3}$$

Where RR = Rectification Ratio

$I(V_\alpha)$ = Voltage resulting in highest current

$I(V_\beta)$ = Voltage resulting in lowest current

Although Aviram and Ratner proposed using an insulating σ -bridge to induce rectification, very few examples to date have been satisfactorily investigated; including an acceptor- σ -donor system in which (TCNQ) derivatives are aligned by LB deposition onto a platinum substrate to form a metal | LB film | metal construct,³⁴ and a TTF- σ -acceptor derivative (Figure 1.7) contacted by alkanethiolate coated mercury drop electrodes.³⁵

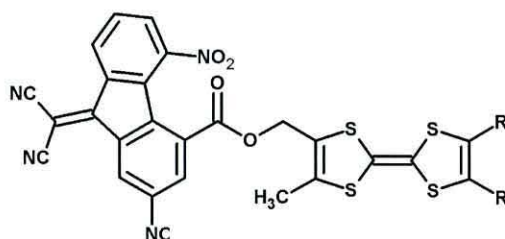


Figure 1.7: Acceptor- σ -TTF, where $R = n\text{-C}_5\text{H}_{11}$.³⁵

The first experimentally achieved rectifier was a modification of the traditional Aviram and Ratner donor- σ -bridge-acceptor model, proposed by Ashwell, Sambles and co-workers in

1990.³⁶ Rather than placing the electro-active portions, in this case a quinolinium acceptor and tricyanodimethanide donor moiety, on either side of a σ -bridge, a π -bridge was introduced to create a π -bridged metal | LB monolayer | metal junction (Figure 1.8). This novel approach to rectification was achieved by constructing hexadecylquinolinium tricyanodimethanide monolayers via Langmuir Blodgetty onto magnesium pads coated with silver. The circuit was completed by engaging a platinum electrode. The subsequent asymmetric I - V properties displayed a RR of 2-8 at ± 1.7 V (Figure 1.9).

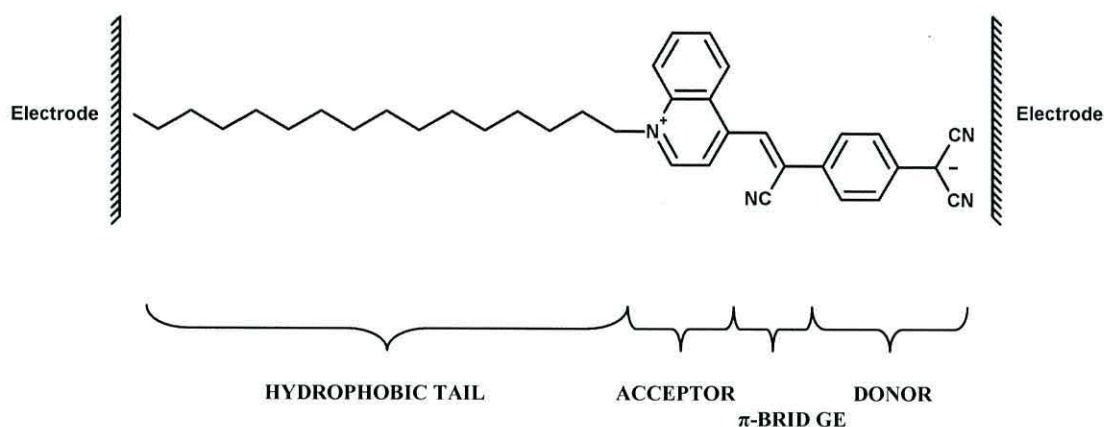


Figure 1.8: Molecular structure of a non-planar A- π -bridge-D system.³⁶

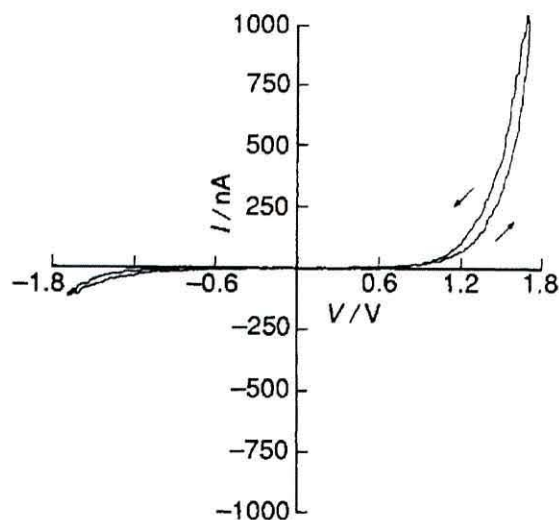


Figure 1.9: I - V plot for Mg|C₁₆H₃₃-Q3CNQ|Pt consisting of four LB layers.³⁶

Previously, the substitution of a σ -bridge with a π -bridge had been discarded as it was believed the donor and acceptor orbitals would overlap, retarding rectification. However, the

addition of sterically hindered groups around the central π -bridge results in a twisted dihedral. This in turn rotates the donor and acceptor orbitals out of plane and breaks the conjugation between them. By confining the electrons to either side of the π -bridge an effective tunnelling barrier can be generated. As well as being easier to synthesise than a σ -bridge, π -bridges create a more stable, rigid system resulting in more ordered packing.

This model was initially met with a great deal of scepticism, with questions arising over the validity of the results. With respect to the electrodes, the initial investigation used two differing metals, magnesium and platinum. The difference in work function (3.66 eV and 5.64 eV respectively) between these two electrodes can cause asymmetry in itself. Magnesium is also highly reactive and easily oxidised, meaning it is less than ideal for electrical characterisation. Another point of contention was the placement of the insulating hexadecyl chain. Whilst this is required for successful LB deposition, the resulting asymmetrical placement of the donor- π -bridge-acceptor unit between the electrodes could once again cause non-molecular rectification.

To eliminate these concerns, further work was carried out by replacing the magnesium and platinum electrodes with two made of aluminium.³⁷ This resulted in a RR of 2.4-26.4 at ± 1.5 V, thus disproving the notion that the difference in work function had caused the rectification. Metzger *et al.*³⁸ continued this work by replacing the electrodes with those of an oxide-free metal, gold, which led to further investigations by a number of groups and ultimately concluded that the observed rectification was indeed molecular in origin.

Further research carried out by Ashwell *et al.*³⁹ confirmed the dependence of rectification on steric hindrance. A series of related quinolinium dyes were self-assembled onto an Au-coated substrate and contacted with a scanning tunnelling microscope (STM) tip to address their I - V properties. The steric hindrance was gradually increased around the central π -bridge by the addition of aromatic benzene rings to first one side and then the other (Figure 1.10). Theoretical modelling of three of these molecules suggested the degree of twist between the donor and acceptor moieties increased from 10° , to 31° , to 61° . Once bulky groups such as benzene rings are introduced into the system the p -orbitals on either side are no longer aligned in such a way that they can interact to such a great extent. This effectively breaks the conjugation and increases the degree of rectification. The I - V properties changed correspondingly, from symmetrical with a RR of 1, to asymmetrical with a RR of 11-18 and

then 50-150 at ± 1 V. With the higher current in the positive quadrant we can infer that electron flow occurred from the cathode (Au-coated substrate) to the acceptor and from the donor to the anode (STM tip). This improved rectification is therefore attributed to the increased steric hindrance around the π -bridge further isolating the donor and acceptor molecular orbitals, as well as having further implications with regards to the question of rectification induced by the insulating alkyl chain (Figure 1.10). As rectification was not witnessed in the single-ringed system (Figure 1.10 (a)), which included a $C_{10}H_{20}$ chain, as well as in a corresponding system with a shorter C_3H_6 chain,⁴⁰ it can be deduced that the presence of this moiety does not affect the I - V properties of the system.

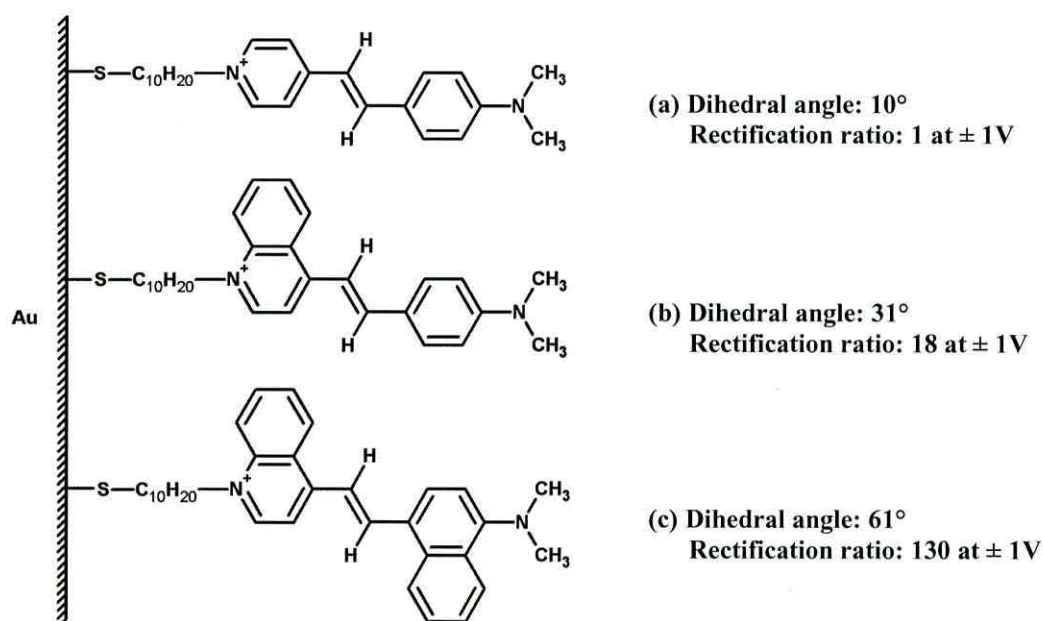


Figure 1.10: An example of the effect steric hindrance has on rectification. Note counterions are not included for clarity.³⁹

2.0 MONOLAYER CONSTRUCTION

This Section outlines three well-established monolayer construction techniques: Molecular self-assembly, Electrostatic self-assembly and Langmuir Blodgettry. Each of these fabrication methods is capable of assembling ordered and reproducible structures from different organic building blocks for physical and electronic investigation. As the metal-molecule bonding architecture is an important aspect of monolayer formation and hence has a great effect on current transport through that system, special attention is paid to the Au-S, Au-NH₂ and TiO₂-COOH bonding mechanisms.

2.1 MOLECULAR SELF-ASSEMBLY

Self-assembly (SA) can be found to occur throughout nature, varying in scale from the nanoscopic to the cosmological. In nature, this self-assembly process is governed by inter- and intra-molecular forces, such as hydrogen bonding and electrostatic interactions, which can lead to the spontaneous formation of organised and stable systems,^{41, 42} of which there are a multitude of examples. Indeed, biological processes such as the formation of cell membranes⁴³ and DNA transcription⁴⁴ all utilise the self-assembly technique to construct important functional constructs. Of particular interest in this thesis is the highly interesting and topical field of molecular self-assembly,⁴⁵ in which the organisation of previously disorganised organic molecules in solution or vapour into a stable system with long-range internal order has proved invaluable, with applications ranging from the biological to the electronic.

Self-assembled monolayer (SAM) formation⁴⁶⁻⁴⁹ is a reproducible method of assembly involving the chemisorption or physisorption of a reactive headgroup to a solid substrate (Figure 2.1), with accounts describing the formation of SAMs found as far back as 1946, with the formation of C₂₀H₄₁OH films on glass.⁵⁰ Control of the self-assembly process allows the surface modification of a variety of materials through the adjustment of terminating functional units. For example, a methyl or hydroxyl group would result in a hydrophobic or hydrophilic surface, respectively, which explains the popularity of organic materials in self-assembly.

This can be extended to include protein resistant groups for bio-applications as well as those that allow for further chemical bonding, such as amine and aldehyde moieties. The ability to custom design surfaces in this way has resulted in the identification and application of SAMs for numerous practical uses, including the formation of films to provide corrosion protection on copper surfaces,⁵¹ as well as chemical sensing⁵² and protein binding.⁵³

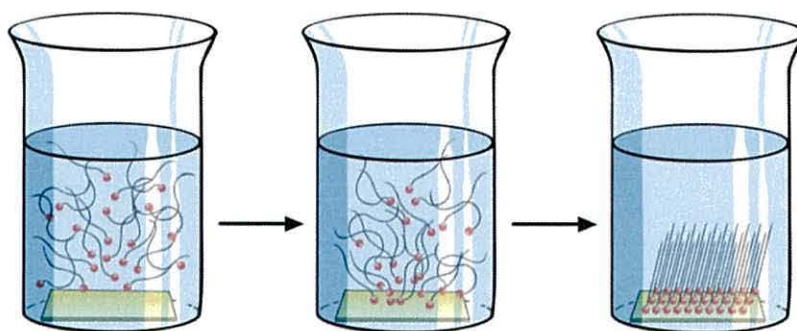


Figure 2.1: Self-assembly of thiols onto gold from solution.⁵⁴

The foremost advantage of SAMs is the ease at which a highly ordered monolayer can be deposited upon an appropriate substrate, although the number of suitable substrates is limited. When compared to physisorbed films produced by Langmuir-Blodgett deposition, self-assembly produces a much sturdier, stable system due to the formation of stronger, chemisorbed connections between substrate and monolayer.⁵⁵ Although recognised as forming highly ordered monolayers, self-assembly cannot produce monolayers with long range order on par with LB films, and are more likely to contain defects. Important in the self-assembly process is the degree of contamination present, as even a small amount of undesirable material can have a considerable impact on the long-range order of the assembled system. Reports of this include the impeded assembly of single stranded thiolated DNA oligomers on gold due to the presence of a dithiothreitol contaminant.⁵⁶

2.1.1 THE GOLD-SULFUR BOND

A well-characterised example of self-assembly is the chemisorption of sulfur to gold, first reported in 1983 by Nuzzo and Allara,⁵⁷ which results in a strong covalent bond (40-45 kcal mol⁻¹) of a slightly polar nature.⁵⁸ This is favourably comparable to anchoring groups such as

amines ($-\text{NH}_2$), which bond through the nitrogen lone pair to form a weak bond with gold ($9\text{--}18\text{ kcal mol}^{-1}$),⁵⁹⁻⁶¹ and carboxylic acids ($-\text{COOH}$), of which the bonding is not completely understood (2 kcal mol^{-1}).⁶² Although amines exhibit a far lower binding energy to gold than thiols, SAMs of diisocyanide and ethynylbenzene anchored to gold have been constructed and used in molecular conductance experiments. Commonly used in self-assembly, gold is a favourable choice of substrate as it is readily available and less prone to oxidation than some other transition metals, such as silver. However, the choice of substrate depends on that which you wish it to chemisorb to. For example, as well as gold, thiol groups readily chemisorb to a wide range of metals, including mercury,⁶³ iron, platinum⁶⁴ and palladium.⁶⁵

In the case of simple alkanethiols, the loss of hydrogen from the thiol headgroup (R-SH) results in a negative charge, which then leads to a high affinity bond between the negatively charged molecule (R-S^-) and positively charged gold surface (Au^{3+}). *Ab initio* studies have reported a net charge on the sulfur of between -0.4 and -0.7 of an electronic charge (e) for thiolates on Au (111), depending on the adsorbed configuration.⁶⁶ Experimental data on alkane thiols of varying hydrocarbon chain lengths has shown a lower net charge on the sulfur of $\sim -0.2e$.⁶⁷ Hence surface active sulfur containing SAMs, such as thiols, (R-SH), disulfides (R-S-S-R), thioacetates ($\text{CH}_3\text{C(O)SR}$) *etc.*,⁶⁸⁻⁷⁰ can be utilised in contacting gold surfaces. An example of this can be seen in Figure 2.2, which details the chemisorption of a thiol-containing system to a gold substrate and the addition of subsequent layers via a condensation reaction.

In order to control and predict the behaviour of such systems, it is essential to understand the underlying processes involved in the self-assembly of organo-sulfurs to gold. However, despite the considerable theoretical and experimental reports into this process, understanding the specific interactions between the sulfur headgroup and gold surface is still proving controversial. For many years, theoretical investigations of the system relied upon the assumption that alkanethiols are static and confined to a threefold hollow site on the Au(111) surface.⁷¹ More recent theoretical and empirical data, however, has revealed that for a system consisting of a low surface coverage of alkane thiols, the sulfur headgroup has a certain degree of surface mobility, rather than being bound to one distinct site.⁷² This degree of surface mobility is expected to be restricted for the formation of a complete monolayer with total surface coverage, as the transition from a lying down to upright conformation results in

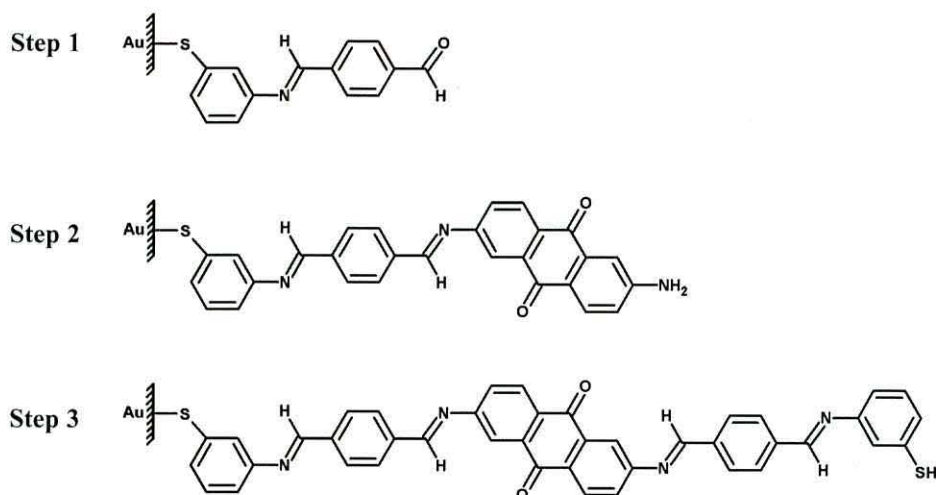


Figure 2.2: A three-step assembly process carried out by Ashwell *et al.*, whereby aldehyde and amino functional groups chemically couple to form a three-component molecular wire.²¹

Van der Waals interactions between adjacent alkyl chains, and an Au-S-C bond angle of 120° .⁷³ Generally, theoretical calculations based on first principles Density Functional Theory (DFT) of simple alkanethiols adsorbed to gold have, in the past, consistently indicated a highly coordinated, symmetrical, threefold hollow configuration to be energetically favourable, and is often referred to as the standard model.^{74,75} Although still prevalent in recent literature, reports have also been made of systems whereby binding of the sulfur headgroup can occur on the bridge site between two gold atoms,⁷⁶ believed to be due to steric repulsion between the sulfur atom and third gold atom in the hollow site, or singly coordinated on an atop site (Figure 2.3).^{77,78} The latter configuration has thus far proved to be energetically less favourable than the two alternatives, with a difference in binding energy of up to 9 kcal mol^{-1} . Investigations in this field have also shown that the strong chemical bond between sulfur and gold reduces the strength of the bonds between the attached gold atom and its neighbours, allowing gold atoms themselves to become more mobile.⁷⁹ This mobility is reduced as the amount of adsorbed material increases due to the attractive interactions between alkyl chains. Grain migration can lead to the formation of atomic gold islands and pitting of the Au electrode to a depth of 0.2-0.3 nm.

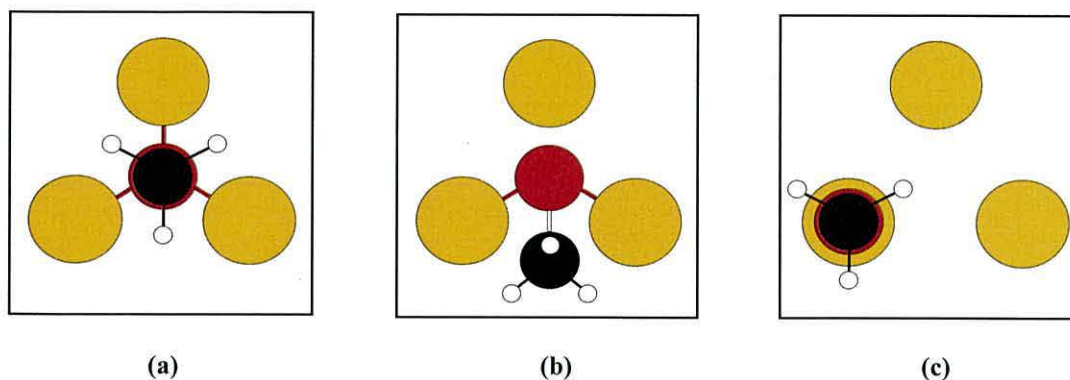


Figure 2.3: Possible bonding configuration of a sulfur headgroup to gold include (a) a threefold hollow site, (b) twofold bridging site or (c) an atop site over a single gold atom.

2.1.2 THE GOLD-AMINE BOND

In-depth studies of the gold-amine bond are numbered far fewer than those of the gold-sulfur bond, although they are being increasingly reported in the field of molecular electronics. Theoretical DFT calculations carried out by Venkataraman *et al.*^{80,81} to determine the preferential binding site of amines to gold atoms indicate that bonding does not occur in bridging or hollow sites. Instead, nitrogen is expected to couple with a coordinatively unsaturated Au adatom. With respect to their bonding abilities, theoretical studies exploring the binding mechanism of amines to gold have thus far revealed a number of potential possibilities. Fagas and Greer⁸² compared the bonding of NH_2CH_3 with its dehydrogenated NHCH_3 form to metallic gold clusters (Figure 2.4), the energies of which were calculated using DFT and Hartree-Fock methods. In line with previous studies carried out by Venkataraman *et al.*, it was assumed the nitrogen atom would bind to gold in an under-coordinated atop site. The calculated Au-N bond distances were given as 2.38 Å for AuNH_2CH_3 and 2.03 Å for the dehydrogenated form. The apparent shortening of the Au-N bond was also observed in an x-ray crystal study on the bonding of 2-(diphenylthiophosphine)aniline and its dehydrogenated form to Au, wherein Au-N bond lengths of 2.157 Å and 2.055 Å were recorded respectively.⁸³ C-N bond lengths were also seen to decrease from 1.448 Å to 1.358 Å, whilst the Au-N-C angle widened from 121.4° to 129.9°. This is consistent with a change in hybridization of the nitrogen atom from sp^3 to sp^2 . This provides unequivocal evidence that both forms can exist, with those structures exhibiting shorter bond lengths occurring due to the formation of a strong covalent bond. This is

reflected in the bond energies calculated by Fagas and Greer, of -1.59 eV for AuNHCH_3 , compared to -0.59 eV for AuNH_2CH_3 .⁸² However, the relative energies of the two systems reveals the AuNH_2CH_3 form to be the most stable and energetically favourable, with bonding occurring through the nitrogen lone pair. A separate DFT-based study also indicates the preferential electronic coupling of amines to gold via the available lone pair by delocalisation, with a lower binding energy than that of thiols to gold.⁶¹ Because of this, amines are thought to form chemically unstable monolayers with little long-range order on Au (111) surfaces when deposited from solution. However, Xu *et al.*⁸⁴ have reported that vapour-phase deposition of amine terminated alkyl chains may result in an ordered and stable monolayer, albeit under specific conditions. However, although nitrogen-based anchoring groups are becoming ever more popular in single molecule conductance studies, direct experimental evidence to identify the nature of the binding structure is still lacking.

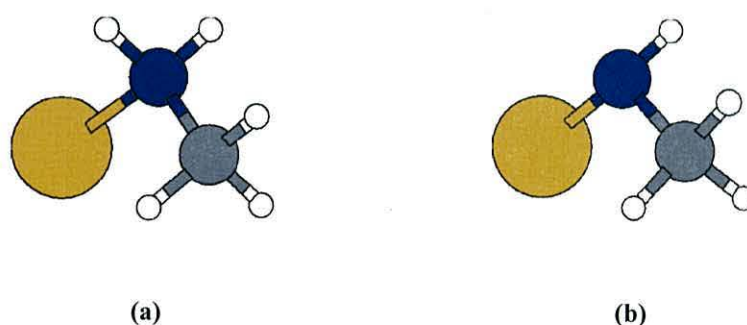


Figure 2.4: Molecular model used to investigate the bonding of (a) an amine to gold and (b) the corresponding dehydrogenated amine to gold.⁸²

2.1.3 THE TITANIA-ACID BOND

Interest in SAM construction on titania (TiO_2) surfaces has arisen in part due to the desirable photocatalytic properties of TiO_2 , and in part because of the ease in which the properties of SAMs can be tailored. This allows properties such as surface hydrophobicity and charge conduction to be altered depending on the desired effect. Interest in this area is very much multi-disciplinary, with potential applications arising in the fields of photocatalysis,⁸⁵ microelectronics,⁸⁶ and corrosion protection⁸⁷ and biomedicine.⁸⁸ An example of the latter category is that of the improved compatibility between blood and titanium-based biomaterials as reported by Yang *et al.*⁸⁸ By self-assembling a hydrophobic 1H,1H,2H,2H-perfluorooctyl-

triethoxysilane monolayer on a layer of TiO_2 nanotubes, which are in turn assembled on an underlying titanium substrate, blood compatibility and anti-coagulation performance was found to have greatly improved.

The chemical modification of TiO_2 surfaces by the addition of SAMs can be achieved via the well-characterised addition of organic anchoring groups such as organosilanes (C-Si),⁸⁹ isocyanates (N=C=O), phosphonic acids (C-PO(OR)_2)⁹⁰ and carboxylic acids (COOH).⁹¹ In particular, carboxylic acid-modified TiO_2 surfaces can be utilised in the construction of dye sensitized solar cells by providing an efficient conduit for electrical current between the dye and substrate. The assembled layer therefore acts as an intermediary between the TiO_2 surface and dye molecule. With regards to the application of SAM-modified TiO_2 in the field of microelectronics, there are many encouraging reports, including the construction of MOSFET transistors and capacitors.⁹² However, one disadvantage of using TiO_2 in such devices is the existence of a relatively high leakage current, thought to be caused by impurities.⁹³

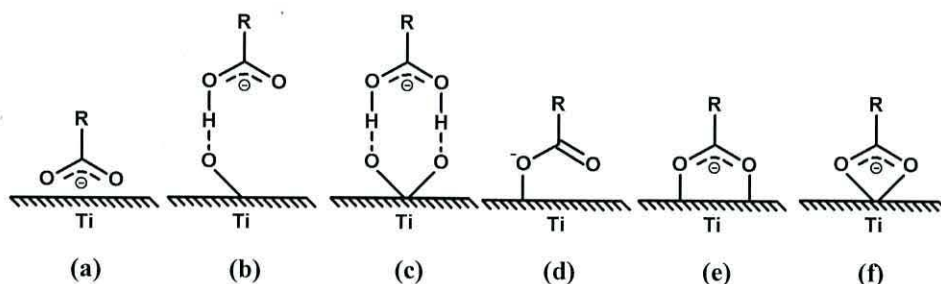


Figure 2.5: Possible binding forms of a carboxylic group on TiO_2 : (a) electrostatic attraction, (b), (c) hydrogen-bonding, (d) monodentate, (e) bridging and (f) chelating.

Despite the interest in surface-modified TiO_2 , the exact nature of the carboxylic acid- TiO_2 bond is still under much debate. Typically, adsorption occurs at the metal oxide surface through either an electrostatic, hydrogen-bonding, monodentate, bidentate, bridging or chelating coordination mode with the deprotonated carboxylic acid as illustrated in Figure 2.5.⁹⁴

2.2 MOLECULAR WIRE EXTENSION

After the initial self-assembly step involving metal-molecule bonding, subsequent layers may be attached providing the functional groups on the contacting ends interact well with one another. One such example of this involves the ability of amine and carbonyl groups to react with one another to form imine bonds, and has proved a useful method by which to extend conjugated systems.^{95,96} Of particular interest is the potential for carbonyl-terminating monolayers to anchor a diverse range of biologically important amine-containing molecules, such as enzymes, to a metal surface.⁹⁷ Consisting of carbon-nitrogen double bonds, imines are reversibly formed when a primary amine reacts with either an aldehyde or ketone. This results in the elimination of water in the presence of an acid catalyst. Figure 2.6 details the initial nucleophilic addition between an aldehyde and amine, resulting in a tetrahedral hemiaminal intermediate, before the elimination of water reveals the final imine product.

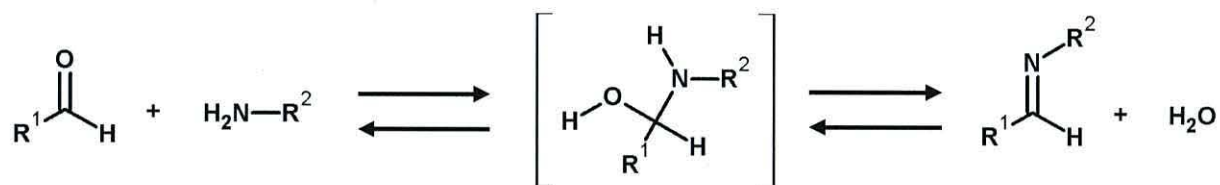


Figure 2.6: Reversible imine formation between an aldehyde and amine via an intermediate.

The reversibility of the reaction can be influenced by a myriad of factors, including but not limited to, solvent, pH and temperature, as well as steric and electronic aspects. It is this ability to control the direction in which the reaction occurs (towards either the formation or cleavage of a covalent imine bond) that has resulted in their utilisation in numerous synthetic chemical applications.⁹⁸ These range from the formation and extension of self-assembling systems,^{99,100} synthetic rotary switches¹⁰¹ and molecular cages¹⁰² to the more recent synthesis of covalent-organic frameworks.¹⁰³

2.3 ELECTROSTATIC SELF-ASSEMBLY

Electrostatic self-assembly (ESA) is based on the electrostatic attraction between oppositely charged particles. Multilayer films can be formed by alternately depositing these anions and

cations onto a suitable substrate (Figure 2.7), which can range from planar surfaces to colloids and biological cells. This results in a uniform film that can encompass a range of length scales. The initial monolayer usually consists of an anion or cation-containing polyelectrolyte, which is able to form organised constructs from solution. This covers a wide range of materials, including electro-active polymers,¹⁰⁴ inorganic compounds,¹⁰⁵ proteins¹⁰⁶ and dyes,¹⁰⁷ to name but a few.

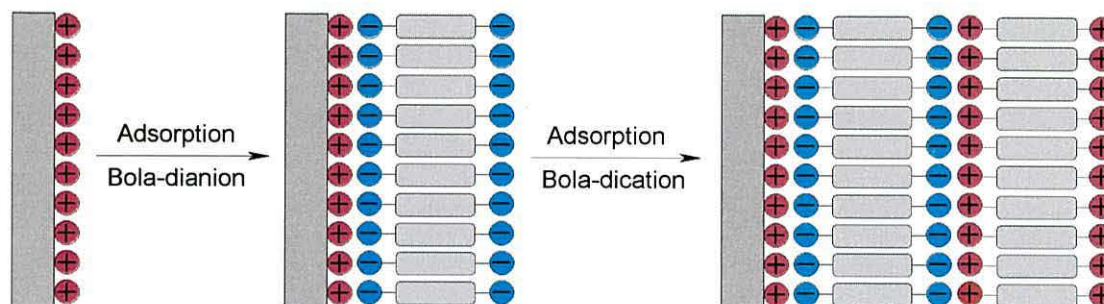


Figure 2.7: The successive deposition of oppositely charged polyelectrolytes.

ESA, also known as layer-by-layer sequential adsorption or ionic self-assembly, was first introduced in 1966 by Iler,¹⁰⁸ who reported the formation of multilayer films consisting of alternating positive and negatively charged colloidal particles. Research in this area remained relatively elusive until a paper detailing the construction of polymeric thin films of oppositely charged polyelectrolytes was published in 1991.¹⁰⁹ Since then, many systems formed in this manner have been investigated, in particular due to the advantage of being able to adapt and modify a surface depending on the desired surface-object interaction. Applications, of which there are numerous, include but are certainly not limited to biocatalysis,¹¹⁰ anti-static coatings,¹¹¹ sensing,¹¹² drug delivery,^{113,114} and surfaces that exhibit certain adhesion¹¹⁵ or wetting properties.¹¹⁶

The largest described and confirmed RR reported to date for such systems is 3000 at $\pm 1V$, a competitive value for the current metal-insulator-metal devices used in circuitry, as reported by Ashwell *et al.*¹⁴ The organic rectifying junction was formed by the initial deposition via chemical self-assembly of a cationic moiety, followed by the subsequent ionic coupling of a counterion (Figure 2.8 (a)). The $I-V$ properties were then measured by contacting the system with non-oxidisable electrodes (Figure 2.8 (b)).

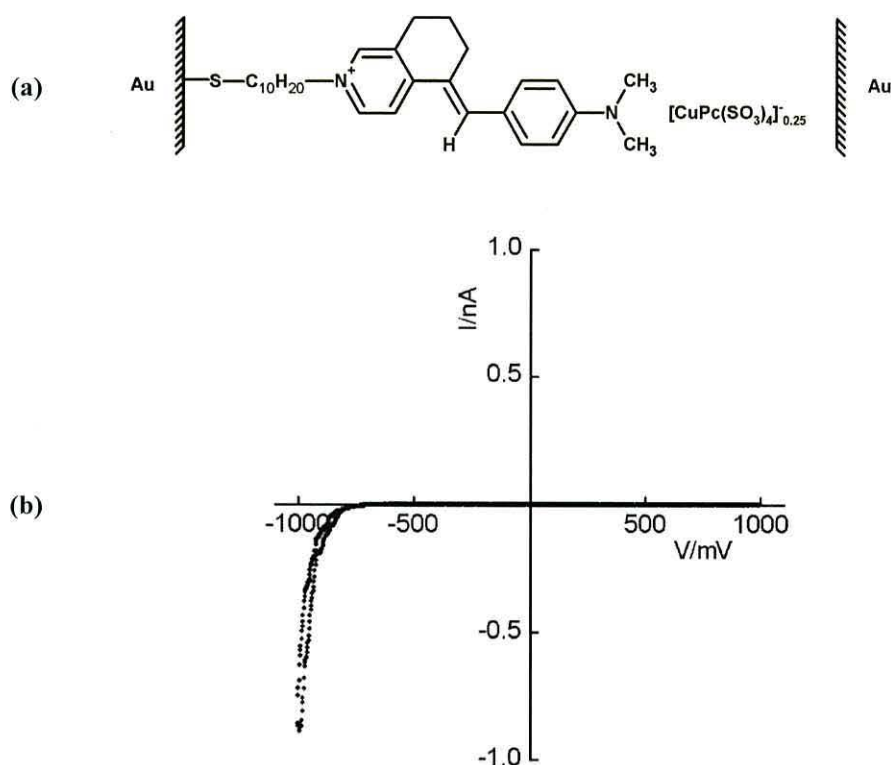


Figure 2.8: (a) The copper phthalocyanine-3,4',4'',4'''-tetrasulfonate salt $\text{Au-S-C}_{10}\text{H}_{20}\text{-A}^+\text{-}\pi\text{-D[D]Au}$ structure exhibiting (b) a RR in excess of 3000 at $\pm 1\text{V}$.¹⁴

2.4 LANGMUIR-BLODGETT

The Langmuir Blodgett (LB) technique was developed jointly by Langmuir and Blodgett in the early twentieth century, inspired by work carried out by Pockels¹¹⁷ and Rayleigh¹¹⁸ on the influence of oil films on water surfaces. In 1917, Langmuir developed specialist equipment with which to study floating monolayers on water surfaces¹¹⁹. Further work published by Blodgett in 1935 reported the first deposition of a fatty acid floating monolayer onto a solid glass substrate.¹²⁰ This, in combination with Langmuir's work, has led to a technique that allows the formation and deposition of ordered monolayers, or LB films.

Langmuir-Blodgettry usually requires that the material of interest, the surfactant be amphiphilic. Thus, it will consist of both a hydrophobic (*e.g.* hydrocarbon chain), as well as hydrophilic component (*e.g.* carboxylic acids, amides, amines). One such example, stearic acid, can be seen in Figure 2.9. This particular arrangement causes the surfactant film to

become ‘trapped’ at the interface between two phases *e.g.* liquid-liquid or gas-liquid, typically air-water. This results in the hydrophilic region pointing down into the aqueous layer, and the hydrophobic section pointing up into the air. This, however, is only the case if the hydrophobic section is sufficiently large, otherwise the entire molecule will be pulled down into the water.

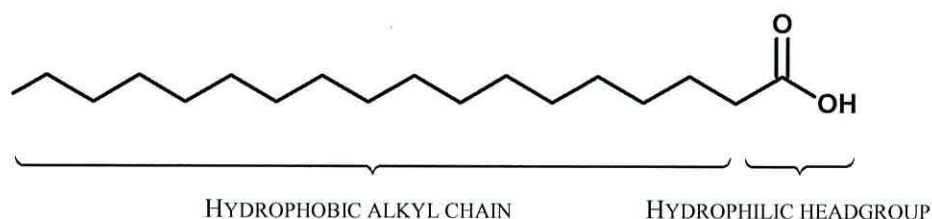


Figure 2.9: Stearic acid, an amphiphilic molecule consisting of a hydrophobic alkyl chain and hydrophilic headgroup.

To create an organic thin film, the material of interest must be dissolved in a solvent which is chemically inert towards the material being used, volatile and insoluble in water, such as chloroform or methanol rather than acetone or isopropanol. This is essential otherwise the solvent, and any material dissolved in it will be carried into the water, instead of forming a floating monolayer at the air-liquid interface. Once dissolved in a suitable solvent, the material is then deposited drop-wise using a microsyringe, whereby the solvent will evaporate to leave a film at the air-liquid interface. Initially, the film possesses little to no long-range order, and is in what is known as a gas phase (Figure 2.10 (a)). At this point the intermolecular distance between molecules is great and thus the molecular interactions small. As pressure is applied, the film is further compressed, passing through both liquid and solid phase (Figure 2.10 (b) and (c)), indicating changes in molecular orientation and packing to produce a monolayer with long-range order. If the film is compressed beyond the solid phase, a point of collapse will be reached, at a collapse pressure, whereby areas of the film will either slide over one another to form multilayers or be ejected from the monolayer (Figures 2.10 (d) – (e)). This is indicated by a sharp decrease in surface pressure and is not necessarily uniform across the film, leading to areas of uncollapsed material and ridges of ejected material. This transition can be seen as gradient changes in a system’s pressure-area isotherm (Figure 2.11). However, in practice, these transitions may not be well-defined and hence difficult to observe. With a known concentration of surfactant, the area per molecule can be calculated.

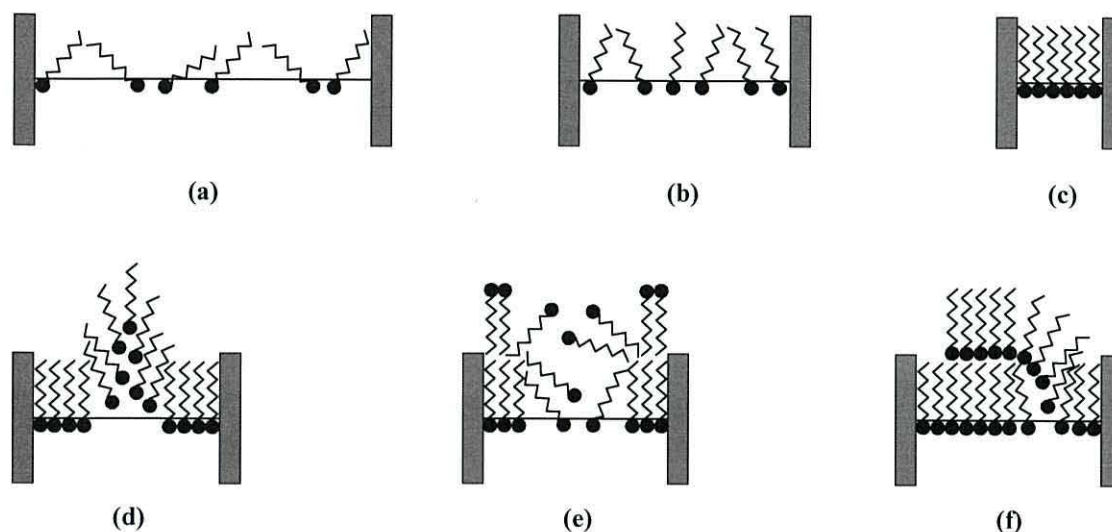


Figure 2.10: As the film is compressed, the surfactant will typically go through the (a) Gas phase (b) Liquid phase (c) Solid phase. If further compression occurs the floating monolayer may collapse, resulting in the ejection of material to form ridges (d) or result in the formation of multilayers (e)-(f).

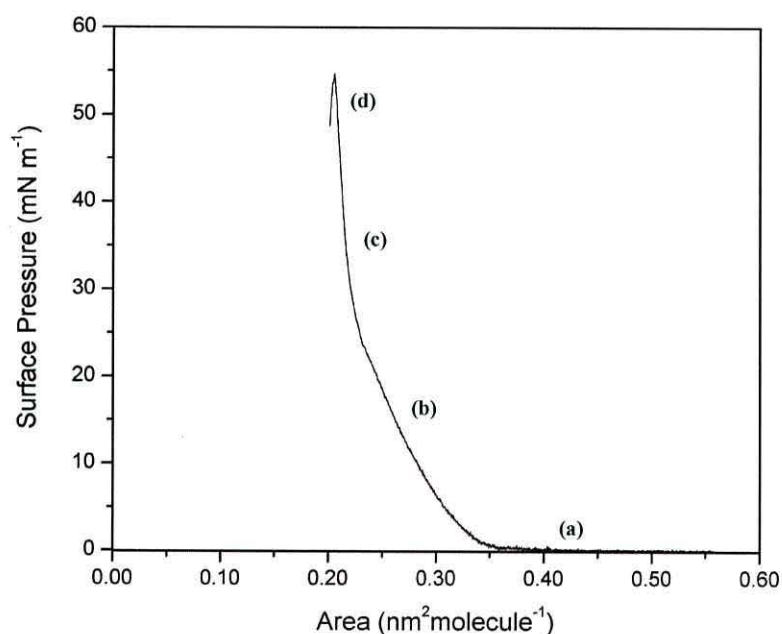


Figure 2.11: A typical isotherm of stearic acid showing transition through the (a) Gas phase (b) Liquid phase (c) Solid Phase and (d) Collapse.

A pressure-area isotherm should be obtained to determine the appropriate pressure at which to deposit the film onto a solid substrate, whilst also providing details such as surface pressure, molecular area and, hence, the packing characteristics of the film *e.g.* orientation and degree

of order. Once this has been achieved, an appropriate substrate can be chosen, and the amphiphilic film can be deposited onto either a hydrophilic or hydrophobic substrate in one of three types; X, Y or Z. Y-type deposition, involves transfer of the floating monolayer onto a solid substrate on the upstroke. The next layer is deposited on the downstroke so that the hydrophobic tails are aligned in parallel to one another. Subsequently, multilayers comprised of this head to head and tail to tail arrangement are formed (Figure 2.12). X-type multilayers are deposited repeatedly on the downstroke (Figure 2.13) and Z-type multilayers on the upstroke (Figure 2.14).

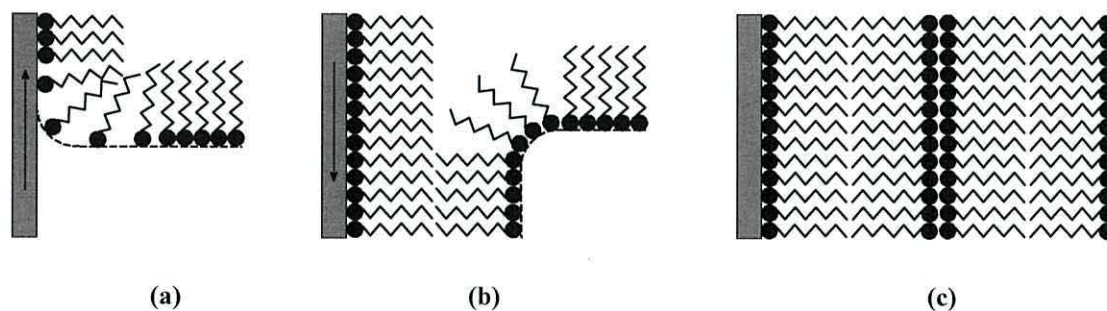


Figure 2.12: (a) Y-type deposition is carried out by alternating the upstroke and (b) downstroke to form (c) a head-tail-tail-head arrangement.

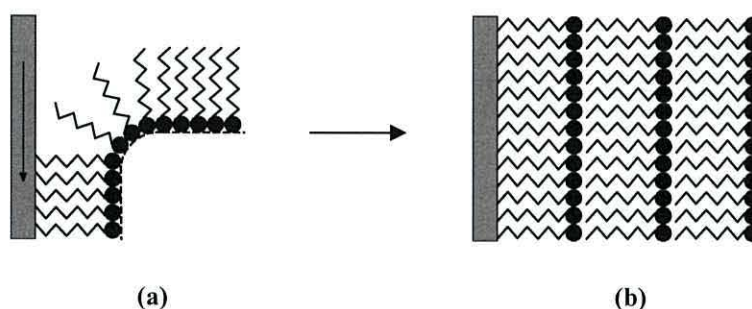


Figure 2.13: (a) X-type deposition is carried out on the downstroke to form (b) a tail-head-tail-head arrangement.

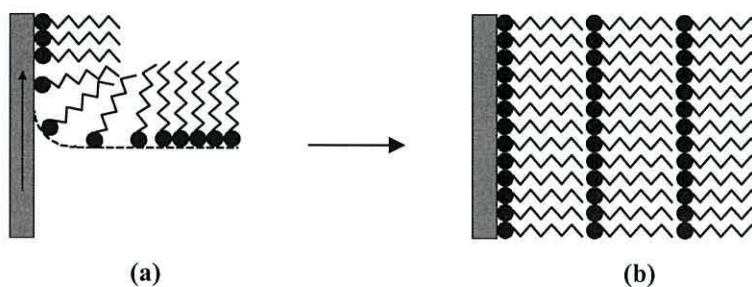


Figure 2.14: (a) Z-type deposition is carried out on the upstroke to form (b) a head-tail-head-tail arrangement.

3.0 CHARACTERISATION TECHNIQUES

Whenever a new material or device is created, a thorough analysis of its physical properties must be undertaken. In the case of SAMs, the ability to monitor the self-assembly process is available in the form of a Quartz Crystal Microbalance (QCM). This method of characterising the adsorption profile of individual monolayers allows a high level of confidence in the subsequent electrical characterisation. A complementary technique to QCM analysis is X-ray Photoelectron Spectroscopy (XPS), which allows the further exploration of surface properties. In particular it can verify the elemental composition and orientation of adsorbed molecules on metallic surfaces.

Of particular interest in the field of molecular electronics is the electrical characterisation of organic devices. Once the system has been formed and analysed using the afore-mentioned physical characterisation techniques, its electrical properties can be probed using a Scanning Tunnelling Spectroscopy (STS).

3.1 PHYSICAL CHARACTERISATION

3.1.1 QUARTZ CRYSTAL MICROBALANCE

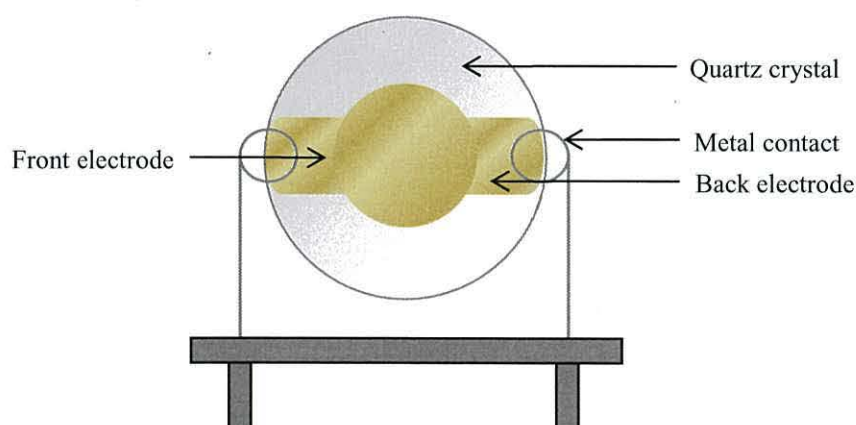


Figure 3.1: Schematic of a quartz crystal used in the self-assembly process.

First observed in 1880 by Pierre and Jacques Curie,¹²¹ the piezoelectric effect is the reversible ability of certain crystalline solids to mechanically deform under the influence of an electric potential. QCM allows the rate of deposition of a mass onto a piezoelectric quartz crystal surface (Figure 3.1) to be obtained and thus the total surface coverage and area occupied by a single molecule may be calculated. This is done by measuring the frequency before and after mass has been deposited onto the crystal and hence, the change in frequency. The change in thickness due to deposited material affects the resonance of the crystal, causing the frequency to decrease from its original, clean value. The total surface coverage can be measured in time increments until the values reach a plateau, implying that maximum surface coverage has been reached (Figure 3.2). To ensure that no physisorbed material remains on the surface to hamper further depositions, the substrate must be thoroughly washed with appropriate solvent.

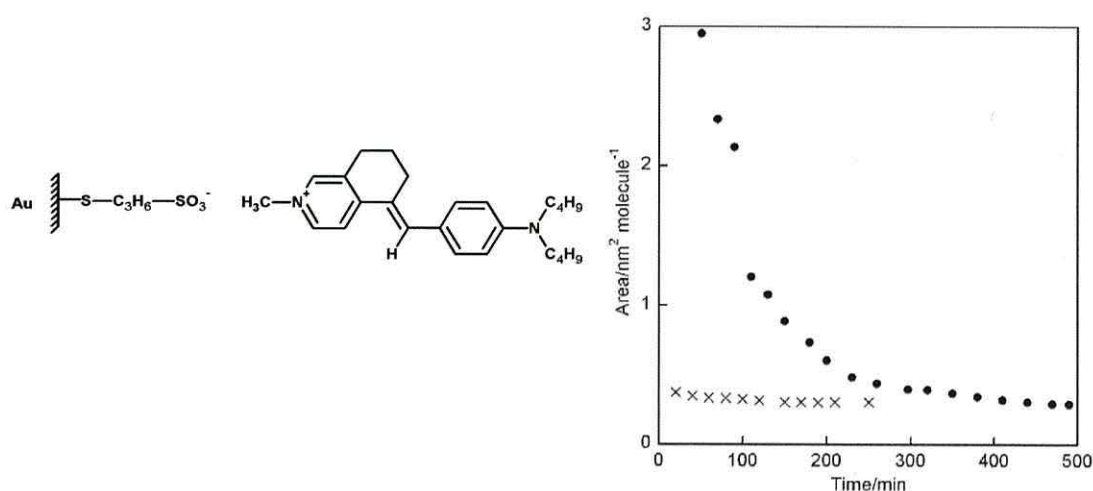


Figure 3.2: An example of QCM readings carried out for the deposition of (x) Au-S-(CH₂)₃SO₃-Na⁺ and (•) cationic N-methyl-5-(4-dibutylaminobenzylidene)-5,6,7,8-tetrahydroisoquinolinium iodide. A plateau can clearly be seen for both fragments.¹²²

The relationship between oscillation frequency and mass was first quantified by G. Sauerbrey in 1959¹²³ and is shown in Equation 3.1. However, this formula, developed for oscillation in air, only applies to rigid and homogeneous thin films. It was King,¹²⁴ in 1964 who first demonstrated the use of quartz crystals in such a way as to detect the presence of mass on a surface. Initially, the QCM was regarded, and utilised, as an exclusively gas-phase nanogram-scale mass detector until the 1980's with reports of QCM measurements made with the crystal either partially or completely submerged in a liquid.¹²⁵ Kanazawa¹²⁶ provided the first

quantitative description of the influence of liquids on oscillation frequency. Since then, this simple, highly-sensitive technique has been refined to the point whereby a single layer of atoms can be detected, for practical applications such as drug delivery,¹²⁷ biochemical sensors,¹²⁸ polymer coatings¹²⁹ and gas sensors,¹³⁰ to name but a few.

$$A_{mol} = \frac{-2f_0^2}{\Delta f (\sqrt{\rho_q \mu_q})} MM \quad \text{Equation 3.1}$$

A_{mol} = Area per molecule (nm²)

f_0 = resonance frequency of crystal prior to deposition (Hz)

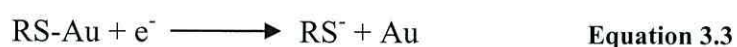
Δf = frequency change upon deposition (Hz)

ρ_q = density of quartz (gm⁻³)

μ_q = shear modulus of quartz (gm⁻¹s⁻²)

MM = molecular mass of deposited molecule

Furthermore, the QCM technique can be combined with complementary analytical methods such as interfacial electrochemistry, allowing for simultaneous gravimetric and electrochemical studies. Electrochemical QCM (EQCM) measurements enable the electrochemical processes involved in the step-by-step formation of thin films to be examined, specifically the oxidative adsorption (Equation 3.2) involved in the construction of SAMs onto a metal electrode, as well as the reductive desorption process (Equation 3.3) in removing them. The resulting anodic and cathodic peaks provide information on monolayer stability¹³¹ and orientation,¹³² adsorption energy¹³³ and formation kinetics.¹³⁴ An early example of this technique involved monitoring mass changes accompanying the oxidation of poly(vinylferrocene).¹³⁵ This combination of simultaneous gravimetric and electrochemical studies carried out in parallel allow the electrochemical adsorption and desorption of a monolayer to be directly related to the change in frequency upon application and removal of material.



3.1.2 X-RAY PHOTOELECTRON SPECTROSCOPY

XPS is a surface sensitive analytical method which allows the quantitative and qualitative analysis of a multi-element system to be analysed, providing detailed information on the chemical and electronic state of each element present. It does this by utilising the photoelectric effect, which was first discovered in 1887 by German physicist H. Hertz, and published in a paper entitled "On an effect of UV light upon the electrical discharge".¹³⁶ Shortly afterwards, Stoletov established the laws of the photoelectric effect, although the theoretical foundations of the photoelectric effect weren't laid down until 1905 by A. Einstein. He suggested that core electrons present in atomic orbitals within a material were able to absorb photons, resulting in either the light being re-emitted, in the case of a photon possessing energy less than that of the electron, or an electron being ejected, if the photon has energy equal to that of the electron. By 1907 the first XPS spectrum had been recorded by P. Innes, using a photographic plate to measure the deflection of photoelectrons in a magnetic field. However, it wasn't until many years later in 1954 that Professor K. Siegbahn and co-workers¹³⁷ created the first high resolution electron spectrometer using K_{α} radiation to observe the chemical shifts of a metal and its oxides. Systematic examination later revealed separate characteristic peaks for the two sulfur atoms present in $\text{Na}_2\text{S}_2\text{O}_3$, allowing the two sulfurs to be separated and identified by their differing chemical environments. By 1969 the first commercial monochromatic XPS instrument was produced.

The XPS technique requires a radiation source, typically monochromatic Al K_{α} , Mg K_{α} x-rays or synchrotron radiation with which to irradiate a sample. Once irradiated and ionised by a beam of photons, core electrons are emitted from *ca.* 10 nm of the sample, allowing the energy distribution to be measured. Electrons released from the surface, or near-surface will experience little to no energy loss, whereas those released from the bulk of the material at a greater depth will undergo an amount of energy loss due to inelastic scattering. This results in a certain amount of noise in the resultant spectrum, which can be reduced by carrying out analyses under ultra-high vacuum conditions, thus eliminating the interference produced from collisions inside the instrument. Each element produces a characteristic set of XPS peaks at a characteristic binding energy, thus allowing any and all elements with an atomic number greater than 2 (and therefore excluding hydrogen and helium) to be identified, as well as being sensitive enough to distinguish between the same element in different chemical environments. The number of electrons ejected from each element can be directly correlated

to the amount of that element present within the sample area by the implementation of a simple formula. This formula requires the signal intensity, and therefore the number of electrons detected, to be divided by a relative sensitivity factor to reveal the concentration, or atomic percentage value of the element in question, thus providing a quantitative analysis of the sample.

Furthermore, the simple XPS technique can be extended with the use of non-destructive angle-resolved XPS (ARXPS).¹³⁸ This can be used to create a depth-distribution profile and thus determine the orientation of a molecule on a surface. Typically, non-angle resolved studies are obtained at a photoelectron take-off angle θ , of 90° . At an angle perpendicular to the sample surface, the electron escape depth is expected to be at its greatest, allowing the photon beam to penetrate deep within the monolayer to yield maximum results (Figure 3.3 (a)). By revolving the sample, the photoelectron take-off angle is decreased, and the exit angle of the emitted electrons is shallower (Figure 3.3 (b)). This means the majority of the signal retrieved is from the surface or near-surface area, with any remaining signal from deeper within the system. Angle-resolved XPS usually requires studies to be carried out at a range of angles. This allows us to examine the signal intensity ratio of peaks of interest, which can be shown to increase or decrease depending on whether the element of interest is closer to the surface or at a greater distance into the bulk of the sample.¹³⁹

Experimentally, an XPS machine consists of a monochromatic x-ray source, sample holder, and analyser to record the electron distribution in terms of their kinetic energies. The technique itself has a wide range of applications, from quality control¹⁴⁰ and catalysis¹⁴¹ to the characterisation of a wide range of materials such as organic electronics,¹⁴² paints¹⁴³ and polymers.¹⁴⁴

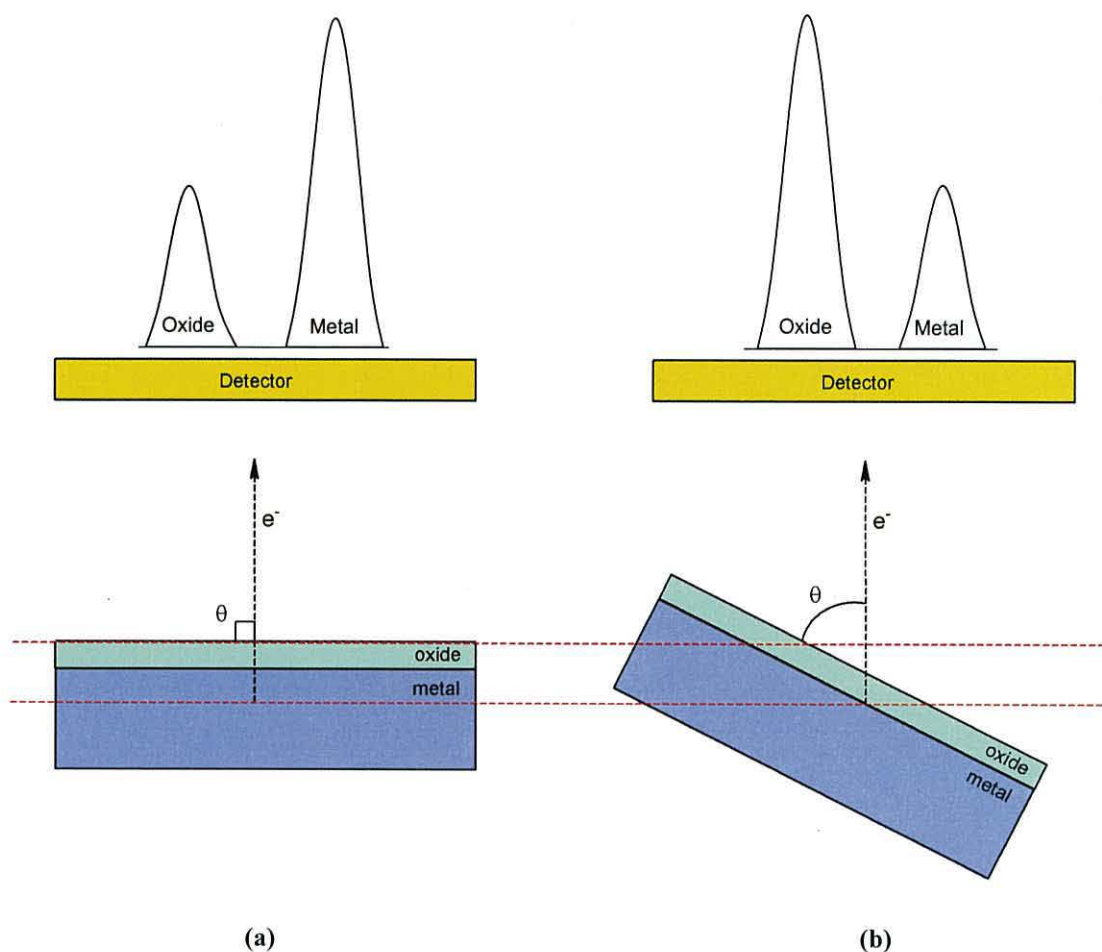


Figure 3.3: An example of ARXPS shows that at (a) high electron emission angles, the maximum depth profile can be analysed and at (b) grazing electron emission angles less information is received from the bulk of the sample, making the technique more surface sensitive.

3.1.3 INFRARED SPECTROSCOPY

The existence of infrared radiation was first discovered by Herschel at the start of the 19th century¹⁴⁵ and within eighty years, hundreds of compounds had been characterised by infrared spectroscopy. In this way, each compound could be associated with its own unique infrared spectra, with particular absorption peaks relating to specific groups within the molecules.

The infrared region of the electromagnetic spectrum consists of radiation which can be converted into vibrational and rotational energy within a molecule. Of most interest is the range of radiation lying between 400 and 4000 cm^{-1} .¹⁴⁶ It should be noted that in order for a molecule to absorb infrared radiation, the vibrational motion must be associated with a net

change in dipole moment of that molecule, and it is for this reason that diatomic molecules such as O₂ and N₂ cannot be examined within the infrared region.

Samples can be prepared as gases, liquid samples or solutions¹⁴⁷ between NaCl plates, or as a solid integrated into a KBr disc. These salt preparations are convenient for use in infrared studies as neither of them exhibit peaks in the region of interest. The spectrometer works by directing infrared radiation of varying wavelengths into the as-prepared sample. The radiation can either be absorbed to a certain degree by the molecule, or transmitted with almost no energy loss. Absorption occurs when the frequency of radiation is equal to the vibrational frequency of a particular bond, the energy of which is transferred to the molecule. Possible vibrational modes include symmetric and asymmetric stretching, as well as bending via scissoring, wagging, rocking and twisting. Thus the presence of different structural environments will lead to the absorption of varying frequencies at varying intensities, demonstrating that a molecule's ability to absorb infrared radiation is characteristic of its structure.

Infrared spectroscopy is a simple and reliable method of analysis which has proven indispensable in structure determination and verification across a range of disciplines. From quality control to microelectronics, IR spectroscopy provides both quantitative and qualitative data on a plethora of chemical systems. Of particular interest is the successful application of infrared spectroscopy in the field of molecular electronics,¹⁴⁸ with examples including structural analysis of *n*-alkylthiol monolayers on gold,¹⁴⁹ and that of organic nanotubes based on a cyclic peptide architecture.¹⁵⁰

Infrared spectroscopy is often used in conjunction with other analytical techniques, such as optical microscopy,¹⁵¹ thermal analysis¹⁵² and dielectric spectroscopy.¹⁵³ Dielectric, or Impedance spectroscopy is a non-destructive, non-invasive method of measuring the permittivity of a solid sample as a function of frequency. The energy absorbed during impedance measurements causes an increase in a polar molecules' rotational energy, providing information on individual molecules as well as systems of molecules and the forces between them.¹⁵³

3.2 ELECTRONIC CHARACTERISATION

3.2.1 SCANNING TUNNELLING MICROSCOPE

The development of the Scanning Tunnelling Microscope (STM) allows us to measure and characterise the electrical properties of individual molecules as well as translating surface irregularities into topographical images of a conducting surface at the atomic level.

The STM was developed in 1981 by G. Binnig and H. Rohrer,¹⁵⁴ who later shared the 1986 Nobel Prize in Physics for their work. Commercially available in the 1990's, the STM has since been adapted to develop a variety of other probing techniques, such as the Atomic Force Microscope (AFM) and Scanning Near-field Microscope (SNOM). STM has proved ideal for the electrical characterisation of conducting organic materials in a variety of conditions – including operation in vacuum, air and liquid environments. Although the injection of charge across organic moieties is non-destructive,¹⁵⁵ reversible changes to the systems, such as the temporary storage of charge by the monolayer can occur. However, this charge will then dissipate, but may result in some hysteresis effects.



Figure 3.4: A close-up view of the STM.

The experimental setup consists of two electrodes, as seen in Figure 3.4; one is an atomically sharp, well-defined, tip, usually a Pt-Ir (80/20) alloy, W or Au and the second is the electrically conductive surface upon which the substrate has been deposited. The tip, in this

case Au, is less prone to oxidation than tungsten, forming only a thin oxide layer, as well as being highly conductive and exhibiting an affinity for many elements. For this reason, Au is a popular choice of substrate in monolayer characterisation. This is brought into near contact with the substrate, with the tip-surface distance connected to, and regulated by a bias voltage and current set-point. The bias voltage is defined as the potential applied between the tip and surface, and the current set-point is the target current and therefore height at which the tip will remain above the surface. Therefore, increasing or decreasing the current set-point results in the tip advancing or retracting respectively. The direction of current flow can be controlled by applying a positive or negative bias voltage, allowing electrons to tunnel from either the tip to the sample or the sample to the tip. The tip's position can also be strictly controlled in the x and y-axis parallel to the surface using three orthogonally placed piezoelectric crystals, allowing sub-nm precision (Figure 3.5).

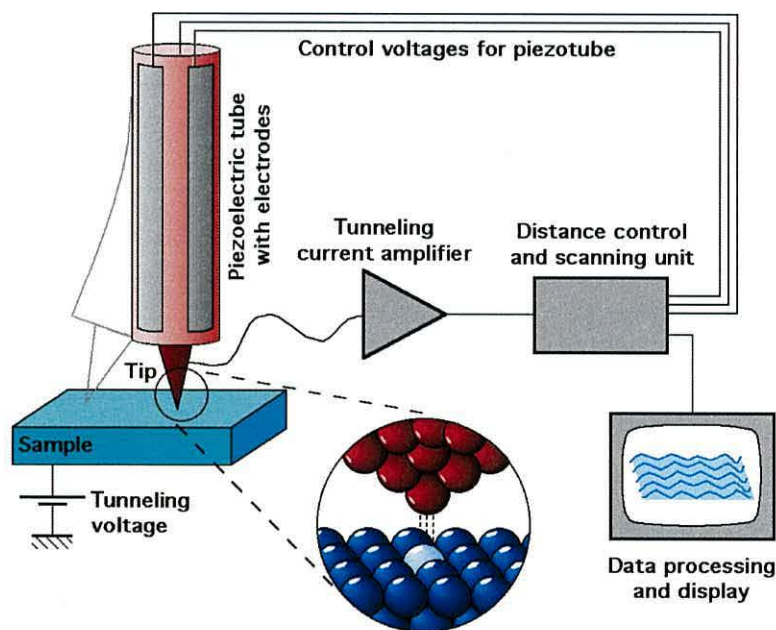


Figure 3.5: Schematic view of an STM.¹⁵⁶

At this point it should be noted that the tip itself does not make physical contact with the surface. Instead, once the tip is close enough to the surface, electrons are able to quantum mechanically tunnel through the potential barrier (the insulating air gap between the two electrodes) to the substrate. This results in a tunnelling current between the probe and film. As the electron passes through the potential barrier, its wavefunction decreases exponentially, *i.e.* there is a limiting gap between the electrode tip and surface. Thus even a minute change in

the tip to sample distance can have a large impact on the tunnelling current. If the gap is adequately small, the wavefunction will not have a chance to decay completely and there is a probability that the electron will be on the opposite side of the barrier from which it started, with the same energy but lower amplitude. This results in a rectification ratio, rather than absolute conductance due to the electron's wavefunction decaying as it passes through the potential barrier. The rectification can be quantified using the ratio of current in the positive and negative quadrants at a particular voltage, usually $\pm 1\text{ V}$, as illustrated in Equation 1.3. From this we can see that the greater the ratio between the two values, the more effective the rectifying ability of the system in question. An ideal rectifier would be expected to have an infinite rectification ratio. Important to note is the potential drawback to the STM technique in the presence of the afore-mentioned tunnelling barrier. As the two contacts are asymmetrical, one being chemically bound to the electrode and the other not, the current-voltage characteristics may also demonstrate a slight asymmetry. This is thought to be limited to a RR of less than 10 where it would not otherwise be expected.

The STM can be run in either a constant current or constant height mode of operation. In constant current mode (Figure 3.6 (a)) the atomically resolved surface topography can be imaged in real-time by using a feedback loop in the applied potential to ensure the tunnelling current between tip and sample remains relatively constant, allowing any height adjustments during a scan to be translated into an atomic-scale topographical image of the surface. The constant height mode (Figure 3.6 (b)), whereby the tip remains at a constant height above the surface, allows any changes in tunnelling current to be monitored and a sample's current-voltage (I - V) characteristics measured. This technique can be most successfully applied when studying atomically flat surfaces, thus reducing any chances the tip will collide with any protruding surface architectures. In order to prevent this and allow the STM method to produce accurate and reliable results, any potential interference from external sources must be minimised. With regards to environmental vibrations and acoustic effects, filters can be utilised to prevent or reduce such interference. Without these measures in place it is possible for the tip to collide with the sample, causing damage to both tip and sample. To reduce the amount of background 'noise' multiple scans of each reading can be averaged.

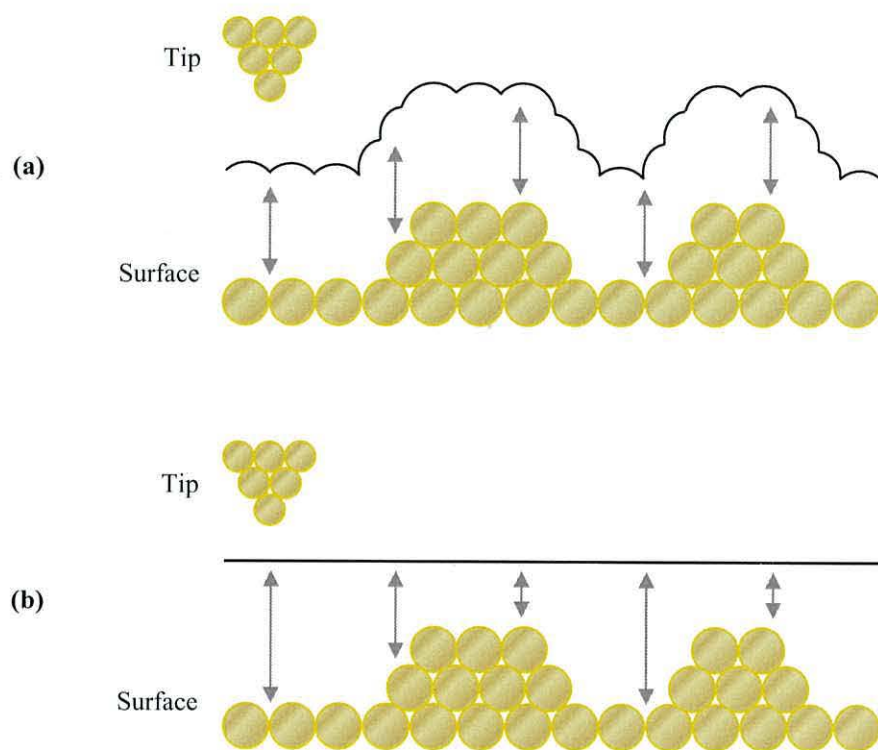


Figure 3.6: (a) STM running in constant current mode and (b) STM running in constant height mode.

Although the STS technique requires the use of an atomically sharp gold tip to characterise single molecule conductance, uncertainty can arise over the exact number of molecules being contacted, and the position of that contact along the length of the moiety. This problem is expected to arise in particular for molecules that are long and do not assemble perpendicular to the surface, whereby charge transfer can occur via chain-to-chain coupling rather than solely through an individual molecule.¹⁵⁷ The uncertainty in both cases can be reduced with the inclusion of a matrix isolation system and the assembly of a closely packed monolayer. The matrix isolation technique, first reported by Pimentel *et al.*,¹⁵⁸ relies on the presence of a relatively insulating organic moiety, such as an *n*-alkanethiolate interspersed with the molecule of interest. This allows the tip to isolate the object of interest. An example of this has been demonstrated by Chidsey *et al.*¹⁵⁹ in the isolation of mercaptoalkyl-ferrocenes in a matrix comprised of an insulating alkanethiol (Figure 3.7). In this case, the alkanethiol separates the ferrocenes and constrains them in an upright position parallel to the surface. Using the alkanethiols as a reference, the electrical characterisation of the ferrocenes can be identified.

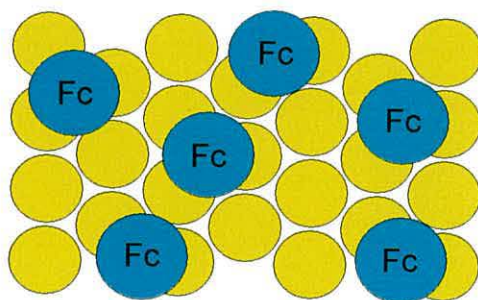


Figure 3.7: An on-top view of a mixed monolayer containing ferrocene-terminated (Fc) and unsubstituted alkanethiols co-adsorbed on an Au surface.

3.2.1.1 STM FOR SINGLE MOLECULE CONDUCTANCE

Interest in the experimental and theoretical characteristics of single molecule conductance has intensified in recent years,¹⁶⁰⁻¹⁶⁵ assisted by the continuing advancement and reliability of nanoscopic probe techniques, such as the extension of the STM technique for Scanning Tunnelling Spectroscopy (STS). Such techniques allow us to increase our fundamental understanding of molecular systems, and are essential for further development in the field of molecular electronics. An insight into electron flow properties through organic systems plays an important, even crucial, role in many key areas, such as the development of organic and biological structures, some of which can be utilised in molecular electronic devices such as organic light emitting diodes (OLEDs).

Coherent electron transport via tunnelling or superexchange is thought to be the dominant process in short molecular wires, characterised by a decrease in conductance with an increase in molecular length, as well as being predominantly independent of temperature. Based on the probability that an electron will traverse the potential barrier, the relationship between tunnelling conductance and length can be expressed in a quantitative form as in Equation 3.4. In this case, the electron crosses the molecular wire, or 'bridge', in a single step, spending appreciably little time on the bridge itself, as seen in a study of *n*-alkanethiols. In longer molecular wires, the favoured method of charge transport is believed to be via an incoherent thermally activated hopping mechanism, whereby the electron is located on the molecular wire, or 'bridge' for a period of time. This can be expressed as an Arrhenious-type

relationship, as shown in Equation 3.5. However, it should be noted that the two conduction methods are not mutually exclusive.

$$G = G_c e^{-\beta L} \quad \text{Equation 3.4}$$

G = conductance

G_c = contact conductance

β = tunnelling decay constant

L = length of molecule

$$G \propto \exp\left(\frac{-E_A}{k_B T}\right) \quad \text{Equation 3.5}$$

E_A = hopping activation energy

k_B = Boltzmann's constant

T = temperature

The relationship between molecular wire length and conductance has been well established, with conjugated wires between 7 and 40 nm undergoing systematic, statistical examination. However, it wasn't until 1971 that Mann and Kuhn¹⁶⁶ released quantitative data of current measurements through monolayers of fatty acid salts deposited between two metal electrodes. Unfortunately, their results could not provide conclusive evidence of the exponential dependence of tunnelling conductance on length, thought to be due to the experimental sensitivity to imperfections in the system. It was Frisbie *et al.*¹⁶⁷ who first used conductive probe atomic force microscopy (CP-AFM) on thin films to show the conversion from tunnelling to hopping in relation to both length and temperature (Figure 3.8). Studies of ten oligophenyleneimine (OPI) wires ranging from 1.5 to 7.3 nm in length showed a clear transition in the conductance transport mechanism from tunnelling to thermally activated hopping at approximately 4 nm.¹⁶⁷ Complementary results were also obtained more recently in a related study on oligophenylenetriazole (OPT)¹⁶⁸ and oligonaphthalene-fluoroeneimine (ONI) wires of varying lengths.¹⁶⁹

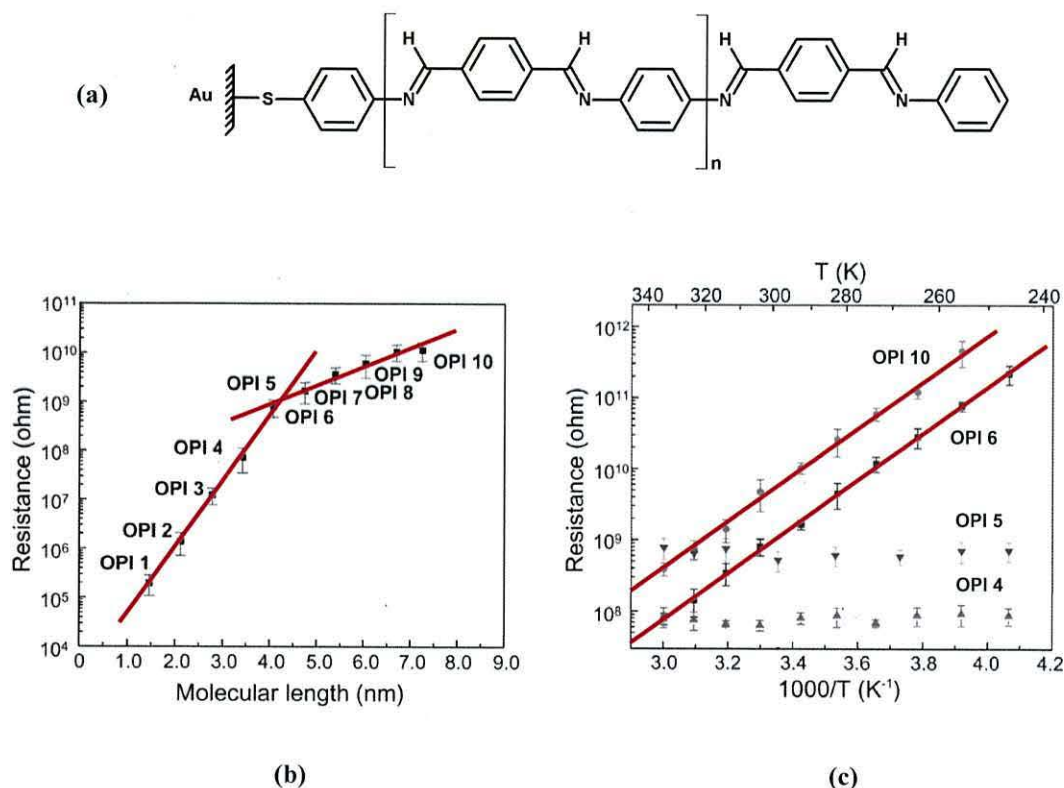


Figure 3.8: (a) Molecular structure of OPI monolayers on Au substrates, (b) a semilog plot of 10 OPI monolayers with respect to their resistance versus molecular length characteristics and (c) an Arrhenius plot of resistance in relation to temperature for selected monolayers.¹⁶⁹

Additionally, Hines *et al.*¹⁷⁰ have carried out both length and temperature dependant conductance measurements on a series of four molecular wires, ranging in length from 3.1 to 9.4 nm. The report suggests that conduction in the two shorter wires exhibit greater length dependence than either of the two longer wires. Subsequent conductance measurements were carried out at differing temperatures, with the shorter wires appearing independent of temperature effects and the longer wires showing some dependence. Such results further support the suggestion of a transition from tunnelling to thermally activated hopping as molecular length increases. Similarly, reports of a change in conduction mechanism have been noted in related conjugated systems, with said transitions occurring at 2.5 nm¹⁷¹ and from 5.6 to 6.8 nm.¹⁷² The systematic examination of these molecular wires has been achieved using a variety of techniques, including mechanically controlled break junctions, in-situ break junctions, I(s), I(t) or nanofabricated gaps. Two of these, the closely related I(s) and I(t) methods shall be looked at in greater detail.

3.2.1.2 STM FOR I(s)

Many decades of solution-based electron transfer studies by groups such as Xu and Tao have led the way forward into the solid state. It was Xu and Tao who first developed the I(s) technique whereby an STM tip could be brought into contact with, and then retracted from, a gold substrate in a 4,4'-bipyridine containing solution, forming and subsequently breaking the Au-Au and Au-N bonds.¹⁷³

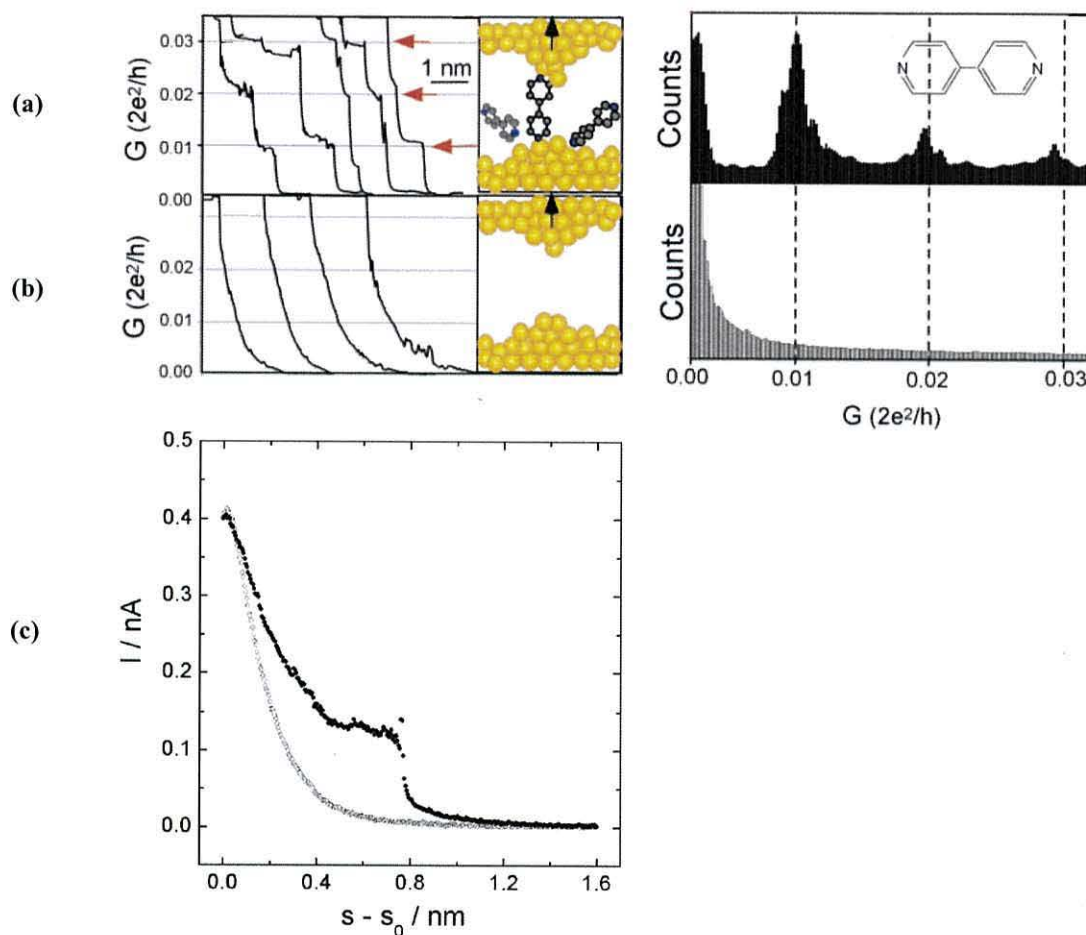


Figure 3.9 (a) Xu and Tao showed that a series of conductance steps could be observed when a bipyridine molecule was present between the gold tip and substrate in solution.¹⁷³ (b) A lack of such steps is seen in the absence of these molecules and (c) Similar steps have been identified by Haiss *et al* in the presence of 1,9-nonanedithiol (solid circles). As in (b), a smooth curve (open circles) is seen in the absence of these molecules between tip and substrate.¹⁷⁴

The initial contact and retraction of tip to substrate resulted in a stepwise decrease in conductance values, thought to be due to the cleavage of Au-Au bonds as the tip shifted away

from the surface. Once this contact was completely broken, a diminished set of conductance steps were observed at values two orders of magnitude smaller than those observed for the Au-Au atomic chain (Figure 3.9 (a)). These steps were attributed to the spontaneous formation of 4,4'-bipyridine junctions between the tip and substrate and occurred at integer values, suggesting the presence of one, two, or more molecules in the junction. In the absence of bipyridine in solution, a corresponding lack of steps can be seen in the conductance trace (Figure 3.9 (b)). This method was modified by Haiss *et al.*,¹⁷⁴ who utilised the same technique in the solid state, rather than in the presence of a solvent. The initial tip-substrate contact was also disregarded, with contact instead being made directly between the tip and molecule of interest (Figure 3.9 (c)).

2.2.1.3 STM FOR I(t)

The simple and reproducible I(t), or 'current jump' method of determining single molecule conductivity was first developed by Haiss *et al.*,¹⁷⁴ and involved the spontaneous formation of bi-substituted molecular wires between a tip and substrate. Experimentally, this could be achieved by setting the gold tip at a fixed distance above the surface under a constant voltage, and then monitoring the current as a function of time.

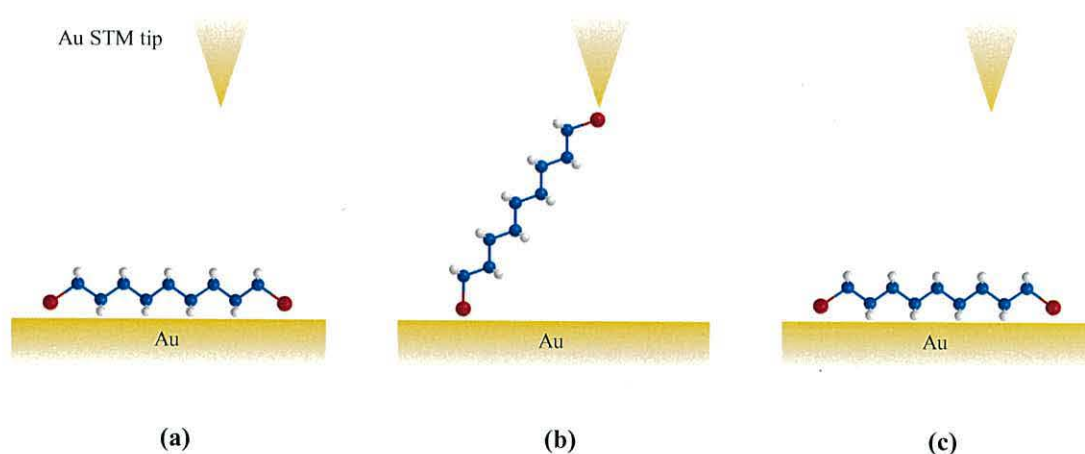


Figure 3.10: The spontaneous formation of an α,ω -alkanedithiol junction between the STM tip and substrate. (a) and (c) represent the molecules before and after chemisorption to the tip, with (b) showing the junction formation which results in a current jump.

On a low surface coverage of viologen-containing α,ω -alkanedithiols chemisorbed onto a gold substrate, Haiss *et al.* monitored the current-time response and observed frequent jumps in the transmitted current. These observed jumps in the tunnelling current are thought to be due to conductance through a single molecule. This was justified by a change in orientation as the flexible molecular wire spontaneously chemisorbed to the tip, creating a bridge between tip and substrate and resulting in an improved current (Figure 3.10). The magnitude of these single molecule current jumps (ΔI) can be measured by comparing the current from both before (I_0) and during (I) the current jump (*i.e.* before and during single molecule contact), and tend to last for a number of microseconds before returning to the pre-jump magnitude. These can be analysed statistically through conductance histograms, with lower values corresponding to conductance through a single molecule, and greater values corresponding to two, three or more molecules contacting the tip at integer multiples (Figure 3.11).

Haiss *et al.* have also reported a lack of observable current jumps during an investigation of monothiol wires. However, it has since been reported that similar jumps can also occur on dicarboxylic acid terminated alkyl chains, demonstrating that chemisorption does not necessarily have to occur between the molecule and tip for a current jump to be observed.

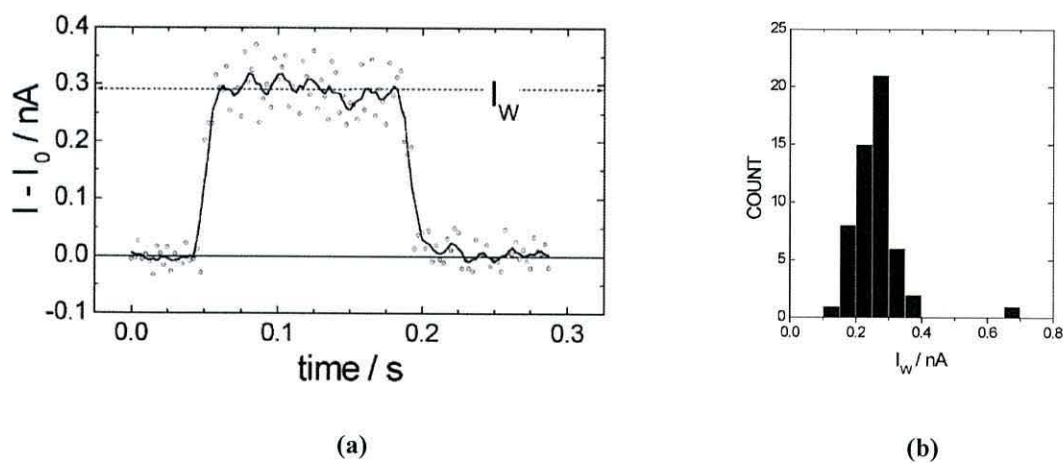


Figure 3.11: (a) A typical current jump exhibited by single molecule conductivity studies on 1,8-octanedithiol and (b) the corresponding histogram of 54 current jumps.¹⁷⁴

A comparison study¹⁷⁵ of a simple Au-octanedithiol-Au system formed by mechanically controlled break junctions, in-situ break junctions, $I(s)$, $I(t)$ and monolayer matrix isolation (MMI) methods have shown a high degree of reproducibility between the different approaches, although discrepancies have been noted between theoretical and experimental

results, as well as widely differing single molecule current values using different experimental techniques. For example, Haiss *et al.* have reported a single molecule current of 0.2 nA for octanethiol, whereas more recent reports suggest a value of 10 nA.¹⁷⁶ Literature also suggests that close-packed monolayers may also exhibit current jumps, despite them being closely packed and therefore unable to 'flip' up to gain contact with the tip, as Haiss *et al.* proposed.¹⁷⁷

4.0 EXPERIMENTAL

4.1 SUBSTRATE PREPARATION

Depending on the physical characterisation technique, QCM or XPS, differing forms of gold substrate were used; a gold-coated quartz crystal for monitoring the self-assembly process, or highly ordered pyrolytic graphite (HOPG) for analysis via XPS. TiO₂-coated quartz crystals were utilised for both QCM and XPS.

4.1.1 QUARTZ CRYSTALS

The 10 MHz quartz crystals (International Crystal Manufacturing, OK, USA) consist of a thin, transparent, crystalline SiO₂ wafer sandwiched between two vapour-deposited Au or TiO₂ electrodes. The quartz crystals employed in this work are AT-cut, forming a highly stable surface with nearly zero frequency drift at room temperature on which to assemble monolayers. The crystal is cleaved from a quartz rod at an angle of $\sim 35^\circ$ with respect to the optical axis (Figure 4.1) to form a disc just a few tenths of a nanometre thick. In the case of TiO₂ quartz crystals, a 10 nm thick layer of titanium is laid on both sides of the exposed quartz. For the Au crystals, a 100 nm-thick layer of Au is simply vapour deposited on top of the initial TiO₂ layer. The Au is then annealed to form the (111) crystal structure.

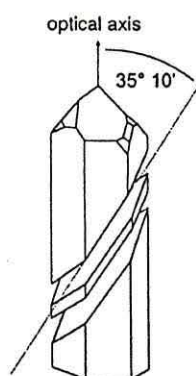


Figure 4.1: AT-cut quartz crystal rod.¹⁷⁸

Before depositing a monolayer, the substrate must be checked for any damage and thoroughly cleaned to remove any unwanted material from the surface and thus avoid contamination. This is done using a nitrogen plasma cleaner (GaLa Instrumente, PlasmaPrep2) to prepare the surface for subsequent deposition. This process removes any unwanted surface oxide and organic material. Experimentally, the quartz crystal is placed in the plasma cleaner (Figure 4.2), the chamber of which is evacuated for 3 minutes, before being flooded with nitrogen for a further 3 minutes. A generator then applies an electric current, ionizing the nitrogen gas and forming a plasma. After 3 minutes, the crystal is removed, allowed to cool and its frequency measured. This 'clean' reading can be compared with the frequency before the plasma cleaning process, to ensure the expected change in frequency has taken place *i.e.* by removing any surface material present, the clean frequency should be greater than the initial unclean one. However, an excessive number of exposures may result in nitrogen doping in the crystal, culminating in erratic QCM readings. As TiO₂ crystals cannot be plasma cleaned, they were instead washed with an appropriate solvent until a stable frequency reading was given.



Figure 4.2: Nitrogen plasma cleaner.

4.1.2 HIGHLY ORDERED PYROLYTIC GRAPHITE

For XPS studies, samples were prepared on gold-coated, highly ordered pyrolytic graphite (HOPG). Although this means that any material being deposited cannot be directly monitored, a satisfactory monolayer can be achieved if the prior deposition of the material has been well-characterised, which can then be used as a guide. HOPG, formed by stress annealing pyrolytic graphite at temperatures above 3300K, has many practical applications, particularly in the

field of microscopy due to its chemical inertness and flat, featureless surface architecture. Due to the lamellar nature of the material it can be easily cleaved to reveal a clean plane and is therefore regarded as being renewable.

The topmost graphite layers were cleaved using adhesive tape to reveal a clean, unbroken surface on which to evaporate the gold. The sample was placed inside the SEM Coating Unit E5000 (Polaron Equipment Ltd), the vacuum chamber of which was evacuated and flooded with nitrogen gas to a pressure of 0.07 Torr. The leak valve was opened and closed twice to ensure that any residual gas in the chamber remained essentially oxygen-free. The gold coating was then thermally evaporated and applied to the HOPG surface for 20 minutes at 1.2 kV and 10 mA to give a layer approximately 50 nm in depth. An approximate measure of the thickness of the deposited gold film can be derived from Equation 4.1.

$$d = I \times V \times t \times K \quad \text{Equation 4.1}$$

I = current (mA)

V = voltage (kV)

t = time (mins)

K = constant, approximately 2 for nitrogen

Unless being used immediately for self-assembly, once gold deposition was complete, the samples were transferred to the nitrogen plasma cleaner and sterilised to ensure the surface remained free of contaminants.

4.2 MONOLAYER PREPARATION

Monolayers were formed throughout using the self-assembly technique. Each compound was dissolved in a suitable solvent at a concentration of 0.1 mg ml⁻¹. C1, C2 and C8 were all dissolved in HPLC acetone, C3 and C4 in either THF or ethanol, C5 and C6 in THF and C7, C9-C15 and C16 in ethanol. Depositions were carried out for between 10 to 120 minutes depending on the molecule in question. After each deposition, the system was removed from solution and rinsed thoroughly with solvent to remove any unwanted physisorbed material, before being left to dry, and in the case of quartz crystal substrates, being measured for

frequency changes. To aid the condensation reaction between subsequent aldehyde and amine functional groups, a trace catalytic amount of acetic acid was added to solutions.

4.3 PHYSICAL CHARACTERISATION

4.3.1 QUARTZ CRYSTAL MICROBALANCE

All QCM frequency measurements were taken using an Agilent 53131A Universal Frequency counter and Thandar TS3021S power unit. The generator delivered a constant voltage of 9 V and current of 0.01 A to the dried and mounted quartz crystal between depositions. The frequency change can be measured in time increments until the values reach a plateau, implying that maximum surface coverage has been reached.

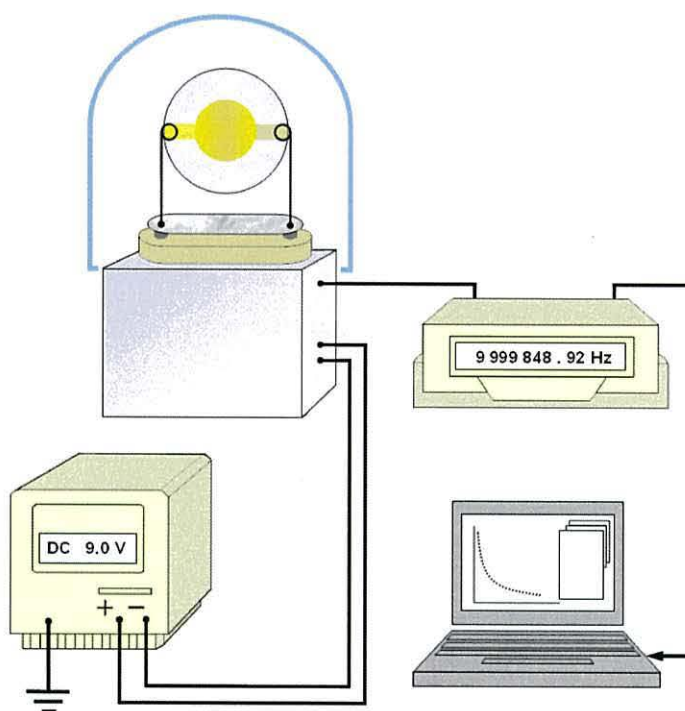


Figure 4.3: Experimental setup for QCM measurements.¹⁷⁹

4.3.2 X-RAY PHOTOELECTRON SPECTROSCOPY

XPS results have been analysed in two locations; by myself and Dr David Morgan at the Cardiff Catalysis Institute, Cardiff University and Kym Ford, Dr Benjamin Robinson (Lancaster University) and Dr Barry Wood at the University of Queensland. All samples were analysed by an Axis Ultra-DLD photoelectron spectrometer (Kratos Analytical Co.) using monochromatic $Al_{K\alpha}$ radiation. Those samples analysed at the Cardiff Catalysis Institute were subject to the following conditions; a sample size of approximately 300 x 220 microns was scrutinised at a base operating pressure of ca. 1×10^{-9} Torr. The initial, low-resolution scan had a dwell time of 0.1 second, a pass energy of 160 eV and a step size of 1 eV. The subsequent high resolution scans were carried out at differing dwell times, with a pass energy of 20 eV and a step size of 0.1 eV. Further samples analysed at the University of Queensland were carried out under similar conditions, at a pressure of $<9 \times 10^{-7}$ Torr and a sample size of 5000 microns square. The initial, low-resolution scan had a dwell time of 0.1 second, a pass energy of 160 eV and a step size of 1 eV. The ensuing high resolution scans were carried out at dwell times of 500 ms, involving two or more averaged sweeps depending on the signal to noise ratio, with a pass energy of 40 eV and a step size of 0.05 eV. Angle resolved studies on systems of interest were taken at 0° , 15° , 30° , 45° , 60° and 75° (where 0° is perpendicular to the surface).

Element	Relative Sensitivity Factor
S 2p	0.668
N 1s	0.477
C 1s	0.278
O 1s	0.780

Table 4.1: Normalisation factors used in able to directly compare elements.

Results were then analysed using the Casa XPS processing software. For a precise determination of binding energies, the spectra of systems assembled on Au were calibrated using the Au $4f_{7/2}$ peak at 84.0 eV, and for those assembled on TiO_2 , using the C 1s peak at 284.8 eV. Peaks were routinely curve-fitted using a convolution of Gaussian and Lorentzian

functions, and the background subtracted using a Shirley type correction method. By dividing the elemental peak areas by their respective Relative Sensitivity Factors (RSF), a direct quantitative comparison can be made between elements (Table 4.1). This normalisation is required to ensure the peak areas are representative of the material present.

4.3.3 INFRARED SPECTROSCOPY

All infrared analysis was undertaken using a Bruker Tensor 27 FT-IR spectrometer with Opus imaging software. Individual samples were prepared by integration with potassium bromide (KBr) crystals. The solid mixture was ground into a fine powder to remove the likelihood of scattering effects, before being placed in a mechanical press under a maximum pressure of 10 tons. This produced a transparent disc through which the radiation beam could pass without difficulty. Before placing the sample within the spectrometer, a background scan was carried out on the empty chamber in order to eliminate any outside influences on the resultant spectra. Radiation was scanned between 450 and 4000 cm^{-1} (wavenumbers).

4.4 ELECTRONIC CHARACTERISATION

4.4.1 STM FOR I - V

A Veeco Instruments Nanoscope IV Nanoscope E was used throughout this study in a vibration-free environment. This was achieved using a vibration filter to protect against external sound and motion, as the tunnelling current is extremely sensitive to changes in tip height. The gold electrode tips were cut from gold wire with a diameter of 0.25 mm and cleaved to form an atomically sharp point. Once the sample had been prepared and mounted, an initial surface scan was undertaken in a 400 nm by 400 nm region. Once a flat, featureless domain, lacking in surface architectures such as grain boundaries had been identified in the initial scan, the scan area was then reduced to approximately 25 nm by 25 nm and the mode changed to I - V from I -s. An average of ~ 100 sites were analysed, and readings were taken for an average of 5 or more scans in a voltage sweep ranging from -1024 mV to 1024 mV. A

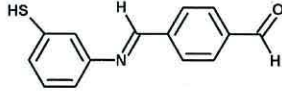
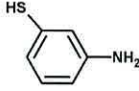
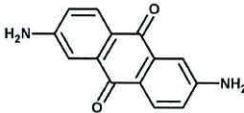
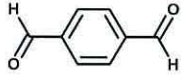
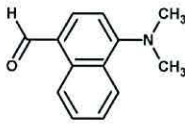
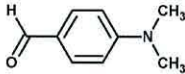
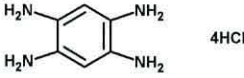
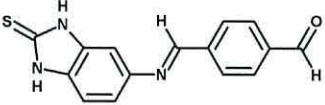
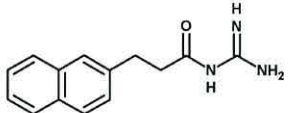
current setpoint of 750 pA and bias of 60 mV were used throughout. All I - V plots displayed in this thesis are representative of the layer from which they were taken.

4.4.2 STM FOR $I(t)$

Initially, the process of studying the single molecule current in specific wires is the same as that applied in studying their rectification properties, in that the sample is mounted on the STM, an initial, large-scale scan taken and an appropriate region chosen for analysis. The $I(t)$ response was monitored with a bias of 50 mV and current setpoint of 600 pA. The feedback was set to -300 mV based on literature values, and readings taken from single scans, 500 of which were recorded for each system under scrutiny. This investigation was accomplished in conjunction with Mr Aled Williams (Bangor University).

4.5 STUDIED COMPOUNDS

Each molecule has been assigned a pseudonym which shall be used in reference to that particular molecule throughout the following Sections. Compounds range from C1 to C16, and each system synthesised is designated S1 to S17. A summary of the compounds used can be found in Table 4.2. The molecules required for each monolayer were obtained from a variety of sources. C1 was synthesised by Mr Eduard Deibel and myself, C2-C7 and C16 were obtained from Sigma-Aldrich and used without further purification. C8 was synthesised by Dr Piotr Wierzchowiec, and C9-C15 by Mr Stephen Vale (Bangor University). The compounds used for direct assembly onto gold include C1, C2, and C7-C15, with C16 acting as the initial anchoring layer on TiO_2 . C4, often used in wire extension reactions involving aldehyde and amine functional groups,^{180, 181} was used to act as a π -bridge between C3 and C7 in various systems, and C5 and C6 used as capping agents. The synthesis of C1 and the TiO_2 nanoparticles required for Section 5.13.6 are also detailed below.

Pseudonym	Name	Structure
C1	4-[(3-mercaptophenylimino)-methyl]-benzaldehyde	
C2	3-Aminothiophenol	
C3	2,6-diaminoanthra-9,10-quinone	
C4	Terephthalaldehyde	
C5	4-Dimethylamino-1-naphthaldehyde	
C6	4-(Dimethylamino)benzaldehyde	
C7	1,2,4,5-Benzenetetramine tetrahydrochloride	
C8	4-{(E)-1,3-dihydro-2H-benzimidazol-2-thione-5-yl}imino]methyl}benzaldehyde	
C9	N-carbamimidoyl-3-(naphthalen-2-yl)propanamide	

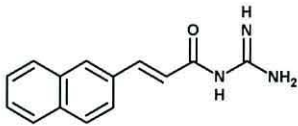
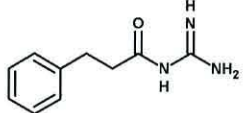
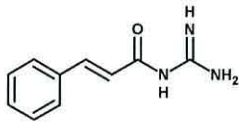
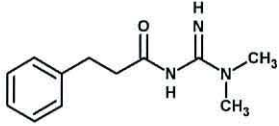
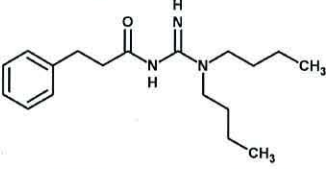
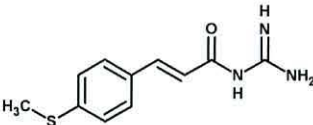
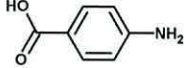
C10	(E)-N-carbamimidoyl-3-(naphthalen-2-yl)acrylamide	
C11	N-carbamimidoyl-3-phenylpropanamide	
C12	N-carbamimidoylcinnamamide	
C13	N-(N,N-dimethylcarbamimidoyl)-3-phenylpropanamide	
C14	N-(N,N-dibutylcarbamimidoyl)-3-phenylpropanamide	
C15	(E)-N-carbamimidoyl-3-(4-(methylthio)phenyl)acrylamide	
C16	4-Aminobenzoic acid	

Table 4.2: Summary of compounds used in the preparation of S1-S17.

4.5.1 SYNTHESIS OF C1

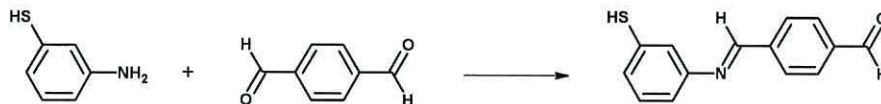


Figure 4.4: C1 formed from C2 and C4.

An excess of C4 (3.7825 g) was added to 75 ml ethanol until all material had dissolved. C2 (1 ml) was then added to the solution and stirred vigorously for *ca.* 16 hrs. The precipitate was filtered *in vacuo* and washed with copious amounts of ethanol. The precipitate, or C1, (Figure 4.4) presented as a yellow solid with a yield of 87.3%.

4.5.2 SYNTHESIS OF TITANIA NANOPARTICLES

C16-capped TiO₂ nanoparticles were synthesised using the aqueous one-step process reported by Rahal *et al.*¹⁸² Synthesis of the precursor [Ti(OiPr)₃O₂CC₆H₄NH₂]_m occurred by initially allowing Ti(OiPr)₄ (4 mL) to dissolve in toluene (25 mL), before adding it dropwise to a solution of *p*-NH₂C₆H₄CO₂H (1.85 g), also in toluene (10 mL). After *ca.* 4 h, the yellow precipitate was gravity filtered and washed with copious amounts of hexane. Hydrolysis of [Ti(OiPr)₃O₂CC₆H₄NH₂]_m was undertaken by heating a solution of N(*n*Bu)₄Br (0.16 g) to reflux in water (100 mL). To this, [Ti(OiPr)₃O₂CC₆H₄NH₂]_m (1.83 g) was added and stirred vigorously, whereby a yellow precipitate formed, denoted *n*TiO₂/PABA, or S15. The suspension was allowed to continue refluxing for a further 2 h, before being gravity filtered and washed with deionized water (2 x 25 mL) and ethanol (50 mL). The resultant cake was then dried at 70°C for *ca.* 12 h. Subsequent units were successfully coupled onto these nanoparticles by immersion in ethanolic compound-containing solutions of excess C3, C4 or C5, with catalytic traces of acetic acid. These were allowed to react for one week before filtering and washing with copious amount of solvent, and overnight drying in a dessicator.

4.6 ERRORS

MONOLAYER DEPOSITION

All final areas per molecule for monolayer deposition have been calculated using the average of all final data points whereby after several depositions the area was seen to differ only a little between depositions. These are represented on each graph with the aid of a horizontal line through the relevant points.

MULTI-LAYER DEPOSITION

For molecular growth presented as a change in frequency vs molecular mass, each point was calculated by averaging all recorded final frequency values for that particular monolayer. The error is established using the difference between the greatest final frequency change and the average.

INDIVIDUAL CURRENT JUMPS EVENTS

The individual current jump values referred to in section 5.7 have been calculated using the average of all data points occurring during that particular jump event. Errors were calculated using the standard deviation of the same points.

CURRENT JUMP HISTOGRAMS

Individual current jump events occurring between 0 and 2 nA for systems S3_a-S7_a are summarised as histograms with an implied possible error of ± 0.05 nA. This value affords the maximum expected error based on analysis of individual current jumps.

5.0 RESULTS

5.1 FORMATION OF S1

Many of the systems formed in this thesis rely on the initial deposition of 4-[(3-mercaptophenylimino)-methyl]-benzaldehyde, or C1, onto an Au surface to form S1. C1 is ideal for the initial self-assembly step as it consists of a conjugated region terminated with a thiol functional group on one end and an aldehyde on the other. The thiol group allows the molecule to covalently bond to a gold surface, whereas the aldehyde allows the subsequent addition of amine-terminated moieties with which to extend the wire. S1, which stands nearly perpendicular at full coverage, has been characterised both physically and electronically in earlier work, which allows for a comparison.²¹

Section 5.1 includes an analysis of the chemical synthesis of C1, before continuing on to analyse the physical and electronic properties of the deposited monolayer on an Au(111) quartz crystal. This was done using QCM to monitor the assembly process and XPS to confirm bonding is occurring as expected. The STM was then used to identify the *I-V* characteristics of the monolayer.

5.1.1 C1 SYNTHESIS: ANALYSIS

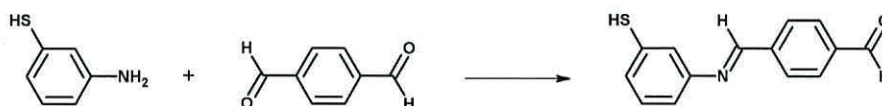


Figure 5.1: C1 formed from C2 and C4.

Mass spectrometry analysis revealed peaks at 242.17 (C1), 274.20 (C1 + methanol), 349.21 (C1 attached to one unit of C2), 449.29 (unknown) and 481.27 (dimer). A microanalysis report of C, H and N provided atomic percentages on average of 68.96%, 4.40% and 5.95% respectively. This showed close agreement with the theoretical values of 69.66%, 4.59% and 5.83%. FT-IR analysis revealed peaks at 3415 (C-H), 3158 (=C-H), 2956, 2925, 2855, 2744 (C-H), 1698 (C=O), 1638, 1607 (C=N), 1590, 1504, 1471 1402, (C=C), 1308, 1208 cm^{-1} (C-

H). This confirms the presence of an aromatic compound containing both aldehyde (C=O) and imine (C=N) environments. UV-Vis analysis indicates λ_{max} at 208 nm, 274 nm, and a shoulder at *ca.* 329 nm.

5.1.2 PHYSICAL CHARACTERISATION: QCM

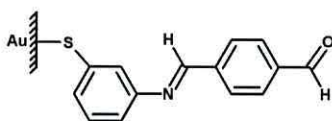


Figure 5.2: C1 self-assembled onto an Au substrate via an Au-thiol linkage to form S1.

The gold coated substrate was immersed in a C1-containing solution for 10 minutes at a time, for a maximum of 120 minutes. At this point, a plateau was reached whereby the frequency was judged to be stable for a minimum of three immersions, indicating a complete deposition of S1 (Figure 5.2). A Sauerbrey analysis concluded that the average area occupied by a single unit of C1 after 70 minutes was $0.206 \pm 0.002 \text{ nm}^2$ (Figure 5.3). This suggests that a closely packed monolayer of S1 was assembled, as the cross sectional area of benzene in an end-on arrangement is 0.25 nm^2 . It is clear from this value that a limited amount of any of the following may be present in the system; solvent, unremoved physisorbed material, or undesirable contaminants, all of which can result in a non-ideal value.

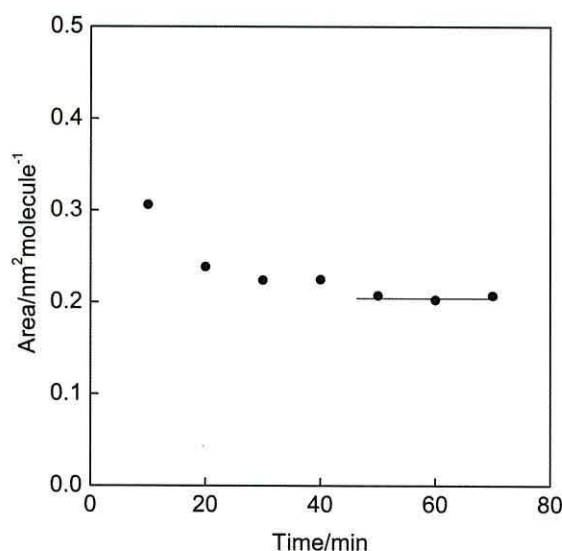


Figure 5.3: Typical QCM results for the deposition of C1 on to an Au-coated substrate to form S1.

5.1.3 PHYSICAL CHARACTERISATION: XPS

A sample of S1 was prepared on gold-coated, highly ordered pyrolytic graphite (HOPG) under duplicate conditions as for those prepared and monitored using QCM. Samples were washed with acetone and allowed to dry between each deposition. A minimum of twelve, ten minute-long depositions provided adequate surface coverage of S1. For clarity, a normalised summary of the XPS results obtained for the S, N, C and O elements has been outlined in Table 5.1

Element	BE / eV	Proportion of element / %	Normalised Intensity
S 2p	163.1	68.5	1
	164.3		
	168.0	31.5	
	169.2		
N 1s	399.4	100	1.4
C 1s	284.8	84	17.9
	286.6	10	
	288.0	6	
O 1s	531.7	100	3.8

Table 5.1: An elemental, RSF-corrected comparison of the key components in S1, normalised to the S 2p intensity.

The high resolution scan of the S 2p spectrum, shown in Figure 5.4, was resolved into two separate, prominent peaks, which can be further deconvoluted into two sets of doublets. The doublet consisting of peaks at 163.1 (S 2p_{3/2}) and 164.3 eV (S 2p_{1/2}) is characteristic of the gold-sulfur linkage, thus confirming that C1 is bonding with the gold surface via a covalent gold-sulfur bond. The higher energy set of doublets at 168.0 (S 2p_{3/2}) and 169.2 eV (S 2p_{1/2}) correspond to the presence of an oxidised sulfur species, suggesting that some material present had not reacted with the gold surface. At a ratio of 1:2.2, we can see that the majority of sulfur species belong to the Au-S bond, rather than the presence of unreacted sulfur species.

High resolution scans of the N 1s spectra, shown in Figure 5.5 (b), reveals a lone, symmetrical peak at 399.4 eV, indicative of an imine (C=N) presence.¹⁸³ This is expected, due to the

presence of the central imine component in the S1 structure. The relative intensities of sulfur to nitrogen were 1:1.4, showing a slight discrepancy from the anticipated 1:1 ratio we would have expected for S1. This may be accounted for by the difference in depth of both species, with the sulfur group being closer to the Au surface than the nitrogen group. This results in a more intense nitrogen signal, although for such a short (*ca.* 1.2 nm) wire, the effects are thought to be minimal.¹⁸⁴

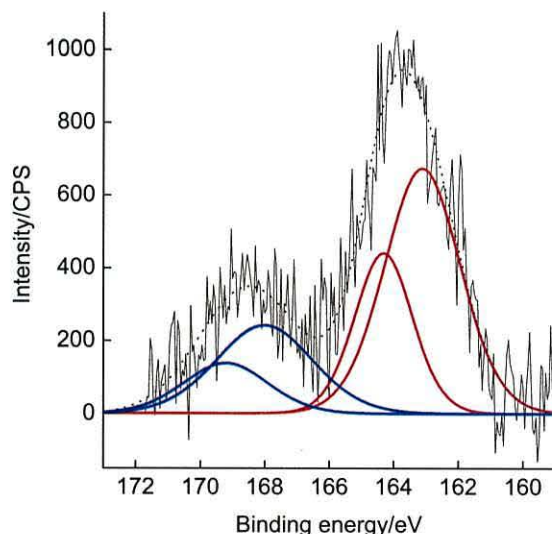


Figure 5.4: The S 2p XPS spectra of system S1 with red peaks modelling the Au-S linkage and blue peaks corresponding to the presence of an oxidised sulfur species.

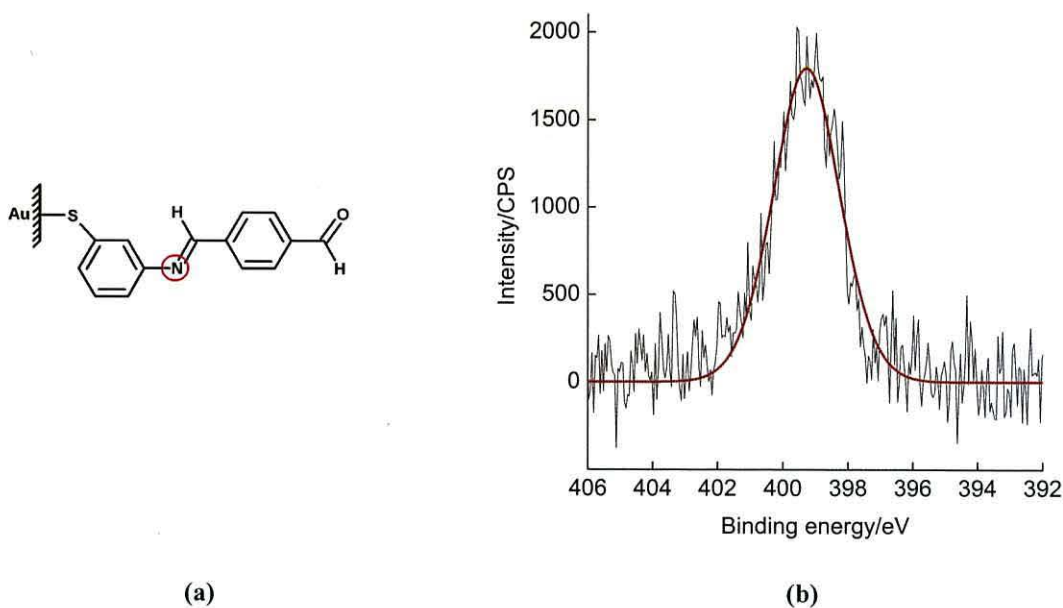


Figure 5.5: (a) The structure of S1 with red representing the imine linkage, and (b) the corresponding peak in the N 1s XPS spectrum.

The C 1s domain exhibits a well-defined peak with a high energy shoulder. Upon deconvolution, this asymmetrical region gave rise to three peaks, at 284.8 eV, 286.6 eV and 288.0 eV (Figure 5.6 (a)). These correspond to carbon atoms in the C-C/C-H, C-N and C=O environment, the ratios of which are approximately 14:2:1. As expected, the peak with the greatest concentration of carbon atoms is due to the presence of C-C and C-H bonds found in the conjugated backbone. The imine presence, however, is approximately twice as concentrated as that of the aldehyde carbon due to the presence of carbon atoms on either side of the central imine element, as opposed to the single carbon attached to the terminating aldehyde group.

The high resolution scan of the O 1s spectrum (Figure 5.6 (b)) can be resolved into a single peak centred at 531.7 eV, the expected value for oxygen in a C=O environment. The normalised intensity, however, is nearly four times greater than expected for S1, which contains only one oxygen atom. This discrepancy is thought to be caused by the presence of oxygen-containing contaminants such as residual solvent or surface oxide.

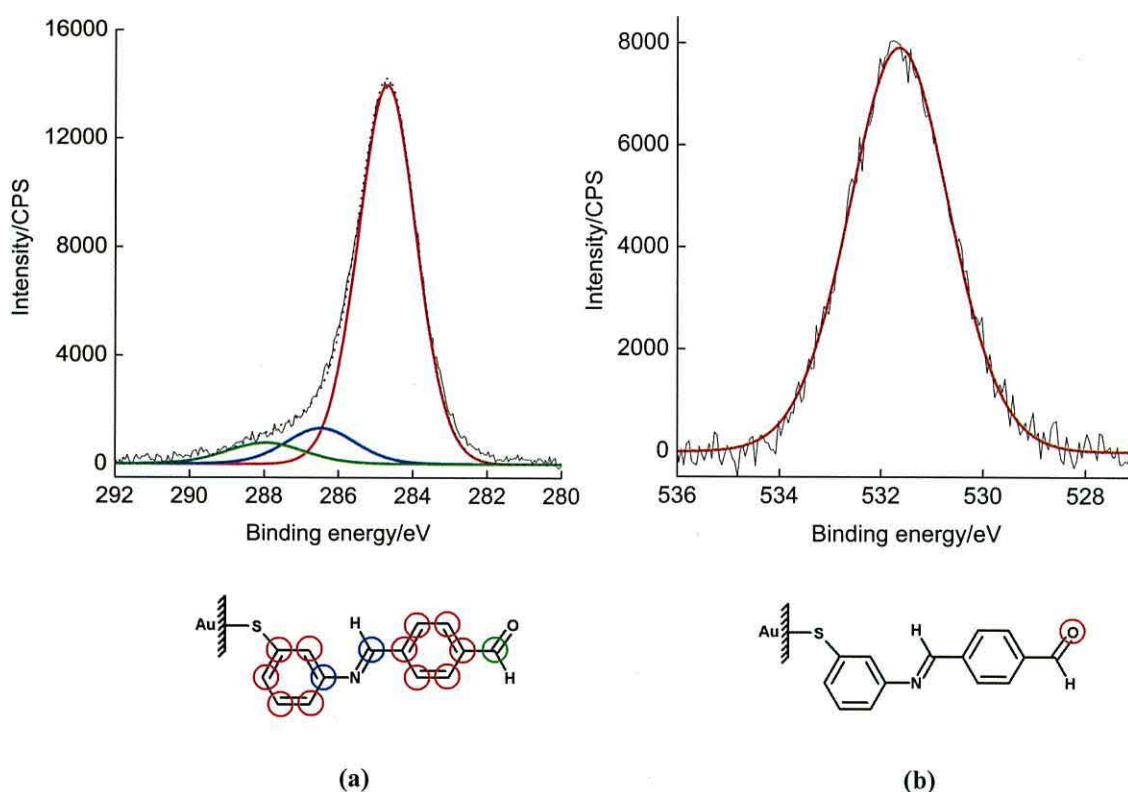


Figure 5.6: (a) High resolution spectra modelling (a) the C 1s domain with accompanying structures showing the three different carbon environments present in S1 and (b) the O 1s domain with accompanying structure showing the single oxygen environment present in S1.

5.1.4 ELECTRICAL CHARACTERISATION: I - V

The symmetrical I - V plot exhibited by S1 (Figure 5.7 (a)) demonstrates the weakly donating electrical properties of the system, with rectification ranging from 1.2 to 1.6 and an $\langle RR \rangle$ of 1.4 at ± 1 V. Such a low value suggests that the current exhibits little to no preference in conducting either in the forward or reverse direction. This can be compared to previous studies on S1 using the same (STS) technique (Figure 5.7 (b))²¹ as well as an alternative electromagnetic cantilever technique (Figure 5.7 (c)).¹⁷⁷

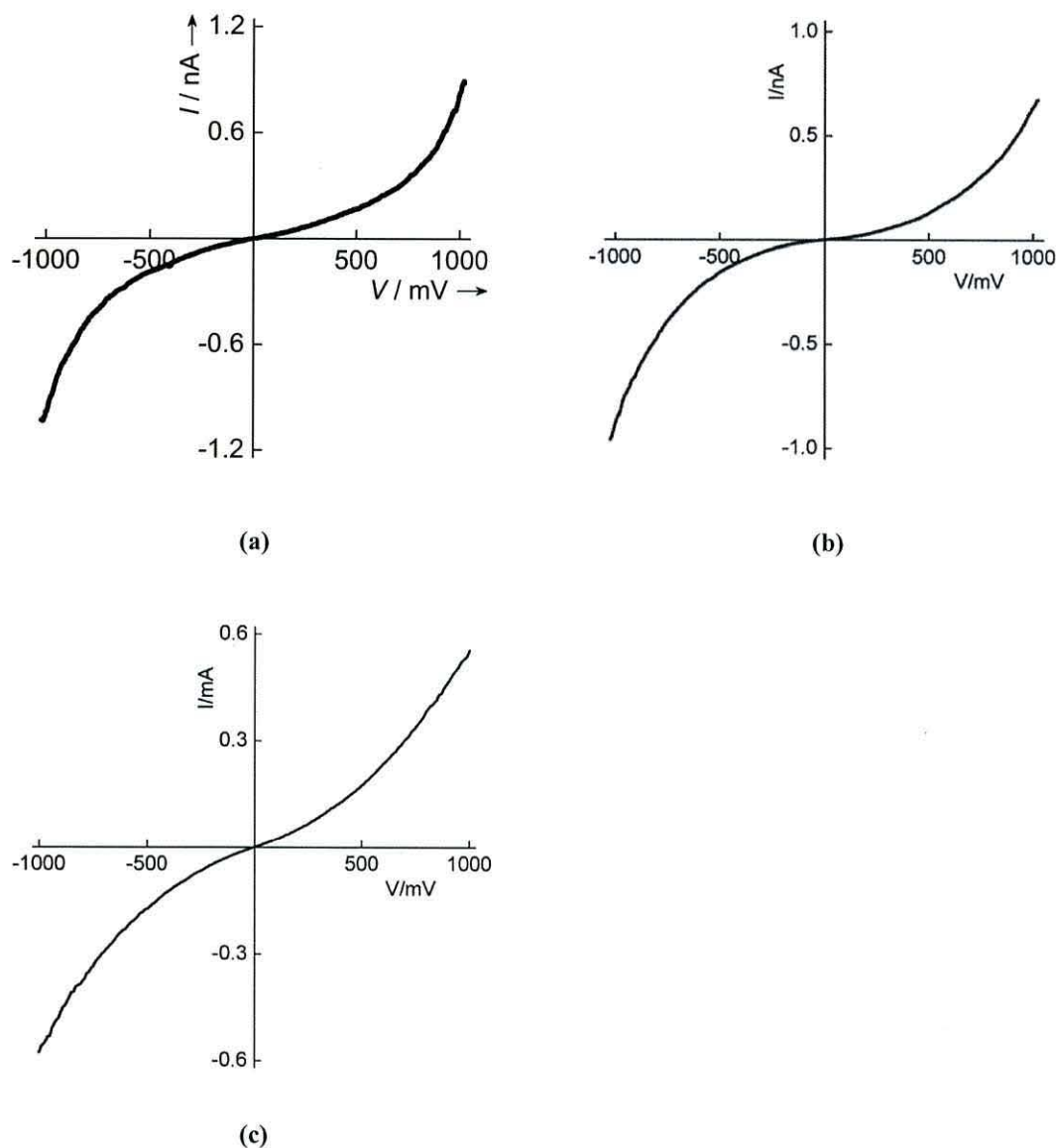


Figure 5.7: (a); Symmetrical I - V plot following the deposition of C1 onto an Au-coated substrate to form S1, (b) results obtained by Ashwell *et al.*²¹ in a previous study on the same system and (c) results obtained by Dr Laurie Phillips using the magnetic cantilever technique.¹⁷⁷

Each plot exhibits a similar shape, although the current differs from one to the next, from the nA scale (Figure 5.7 (a) and (b)), to mA (Figure 5.7 (c)). This is a reflection on the number of molecules being contacted. Therefore, the greater the measured current, the more molecules we would expect to be present between the two electrodes.

5.1.5 SUMMARY

Section 5.1 describes the successful assembly of C1 onto an Au(111) surface to form S1, as outlined in the literature. A Sauerbrey analysis of the deposition process allows us to conclude that C1 packs with the aromatic backbone near-perpendicular to the surface, with an average area per molecule of $0.206 \pm 0.002 \text{ nm}^2$. Exhibiting consistent areas throughout, C1 was found to bind to Au in the relatively short time of 70 minutes. XPS analysis of the S1 monolayer confirmed the majority of sulfur species to be involved in surface bonding. The existence of a single N 1s peak at 399.4 eV also indicates an imine presence, as expected for S1. Upon confirmation of a well-packed, homogenous monolayer, S1 was characterised electronically with regards to the system's I - V properties. Average rectification values of 1.4 at $\pm 1 \text{ V}$ indicated little to no preference in the favoured direction of current flow. Physical and electronic characterisation of this particular system has proven essential, as C1 has been utilised as the initial monolayer in many systems studied in this thesis.

5.2 FORMATION OF S2

Under certain conditions, the unstable C=N bond in C1 may be cleaved,¹⁸⁵⁻¹⁸⁷ leaving the 3-aminothiophenol, or C2 unit, to react with the gold surface. It does this by binding chemisorptively via either the thiol or amine substituents (Figure 5.8).

5.2.1 PHYSICAL CHARACTERISATION: QCM



Figure 5.8: C2 bonding to gold via either the sulfur or amine functional group to form (a) S2_a or (b) S2_b.

The self-assembly of C2 onto an Au-coated quartz crystal was monitored using a Sauerbrey analysis to monitor progress. The substrate was immersed in solution for 10 minutes at a time, until subsequent depositions resulted in only minor frequency changes of 4.61 Hz. The resultant graphical representation (Figure 5.9) indicates an initial plateau at *ca.* 0.223 nm² molecule⁻¹, before ultimately resulting in a final area per molecule of 0.153 ± 0.006 nm² molecule⁻¹. This value is significantly lower than that predicted for such a molecule and suggests the system is either forming multilayers or is congested with other, undesirable material.

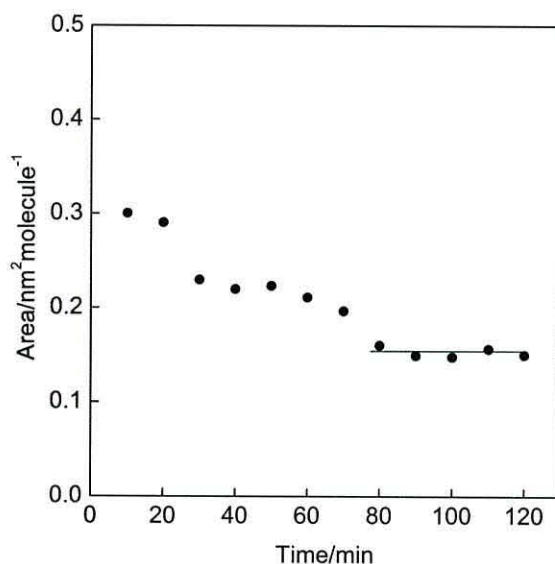


Figure 5.9: Typical QCM results for the deposition of C2 on to an Au-coated substrate to form S2_a and S2_b.

5.2.2 PHYSICAL CHARACTERISATION: XPS

A sample of S2 was prepared on gold-coated, highly ordered pyrolytic graphite (HOPG) for monolayer characterisation by XPS. A total of twelve, ten minute-long depositions were carried out in order to provide adequate surface coverage, as indicated by the Sauerbrey analysis undertaken in Section 5.2.1. A summary of the normalised data obtained for sulfur and nitrogen has been outlined in Table 5.2.

Element	BE / eV	Proportion of element / %	Normalised Intensity
S 2p	162.0	54	1
	163.2		
	163.8	46	
	165.0		
N 1s	399.0	55	1.8
	400.3	45	

Table 5.2: An elemental, RSF-corrected comparison of the key components in S2, normalised to the S 2p intensity.

Angle-resolved XPS analysis has confirmed a dominant bonding configuration involving the amine functionality, with a maximum yield of 66%. The N 1s spectra (Figure 5.10 (a)) exhibits an asymmetrical peak with a slight but distinct higher energy shoulder. Deconvolution indicated that the asymmetrical peak manifests as two differing nitrogen environments with binding energies of 399.0 eV and 400.3 eV respectively, at a ratio of 55:45 for a take-off angle of 0° relative to the substrate normal. The higher energy value corresponds to the terminal -NH₂ group,¹⁸³ whilst the lower energy value is associated with the attachment of NH₂ to a metallic surface which results in a lowering of the N 1s binding energy relative to *ca.* 400 eV. A similar shift has been observed in XPS studies involving amines on gold nanoparticles,^{188,189} alkylamines electrochemically attached or self-assembled to a gold surface,^{190,191} and the self-assembly of the related 4-mercaptoaniline compound on gold.¹⁹² Although the lower energy value has been found to correspond to that of a bound amine element, the actual bonding mechanism remains ambiguous. This confirms the majority of bonding occurs through the nitrogen species, rather than the sulfur.

Further evidence for this was provided by analysis of the S 2p spectra (Figure 5.10 (b)). Deconvolution of the broad spectrum, taken at an angle of 0° with respect to the surface normal showed doublets at 163.8 and 165.0 eV corresponding to SH and at 162.0 and 163.2 eV due to the presence of an Au-S bond. The fact that both sulfur environments were present, as well as both nitrogen environments, provides further evidence to support the presence of bonding via both the nitrogen and sulfur group, to varying degrees. However, a discrepancy occurs when comparing the separate nitrogen environments to those of sulfur. The ratio of Au-S to SH is 54:46, suggesting that the majority of sulfur is bound to the gold surface, rather than the nitrogen moiety. Thus we can assume that the technique is not entirely reliable in differentiating between the two values. Further evidence that the majority of molecules are

binding via the nitrogen can be seen in the ratio of N:S, which at 0° is 1.8:1 and 1.2:1 at 30° . As the angle changed from being perpendicular to the substrate to a grazing angle, the nitrogen intensity decreases. This is expected from a sample in which the nitrogen species is closer to the gold surface than the sulfur, so that as sampling becomes more surface sensitive, less nitrogen is detected. Similar outcomes have been reported for the self-assembly of the *para*-substituted aminothiophenol on gold,^{192,193} with bound to unbound nitrogen environments occurring in a 70:30 ratio, but are in conflict with reports of C2 assembling solely through the thiol moiety.¹⁹⁴

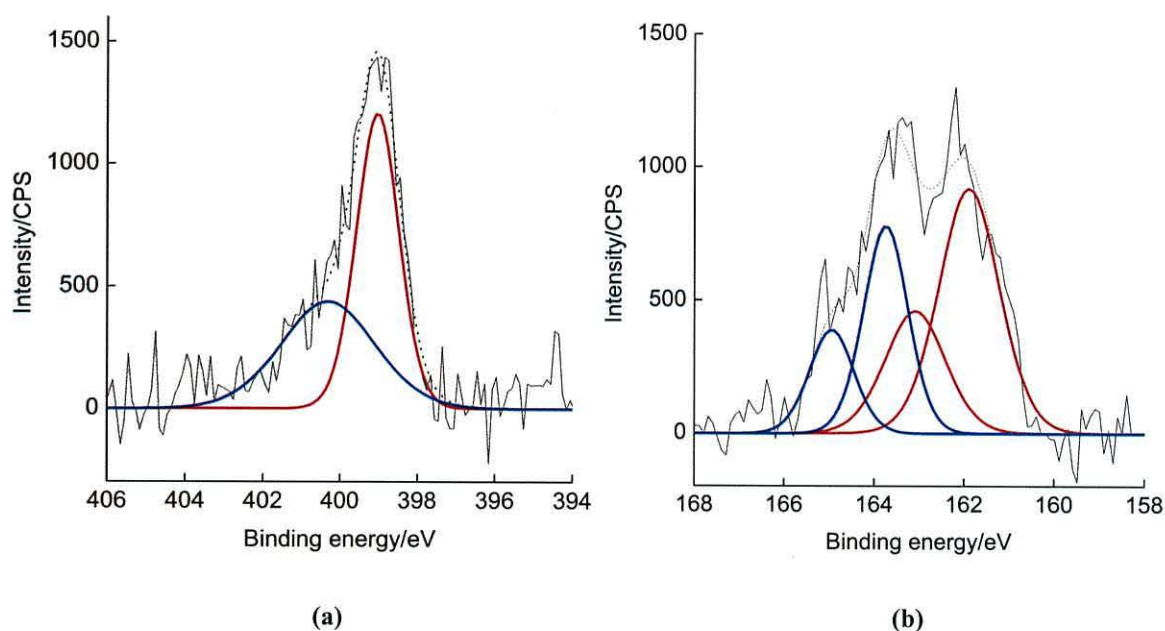


Figure 5.10: (a) N 1s core level spectra of 3-aminothiophenol at a takeoff angle of 0° relative to the surface normal and (b) corresponding S 2p spectra, clearly showing two sets of doublets.

5.2.3 SUMMARY

Section 5.2 has described the deposition of C2 on an Au(111) substrate. In this case, the Sauerbrey analysis could not provide conclusive evidence as to the final area occupied by a single molecule. This was due to a large frequency change resulting in an area of $0.153 \pm 0.006 \text{ nm}^2 \text{ molecule}^{-1}$. However, subsequent XPS analysis indicated a relatively defect-free monolayer. The presence of two peaks in the N 1s domain centred at 399.0 and 400.3 eV are representative of the Au-N and -NH₂ environments, with a ratio to suggest more than 50% of C2 molecules assembled on the metal surface via the nitrogen headgroup, rather than the sulfur. Thus C2, and by implication, its *para*-substituted counterpart, which is a frequently

used anchoring molecule,¹⁹⁵ has proved a flawed candidate for the initial anchoring self-assembled layer due to the formation of a mixed monolayer. Any further depositions would result in an incomplete layer formation with little long range order. This means any electrical characterisation could not be carried out with a high degree of confidence in the ensuing results. Therefore, anchoring groups should not include a terminating amine group, instead, it would be preferable to use an aldehyde-terminated thiol, such as C1, although as stated, C1 can be cleaved to form C2.

5.3 FORMATION OF S3_A

The deposition of the initial S1 monolayer has been previously discussed in Section 5.1.2. Here we outline the subsequent deposition of a strongly electron accepting 2,6-diaminoanthra-9,10-quinone, or C3 unit to form the S3_a wire. C3 consists of an aromatic backbone terminated at either end with an amine moiety, as well as two central C=O groups. The electron withdrawing C=O functionalities help to create an electron-poor unit whereas the amines allow C3 to react with S1 via a condensation reaction.

5.3.1 PHYSICAL CHARACTERISATION: QCM

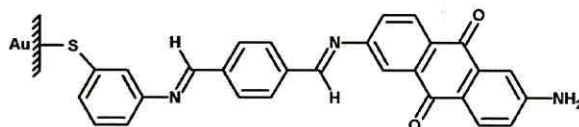


Figure 5.11: C3 has been shown to self-assemble onto S1 to form S3_a.

The second component of the multi-step wire, C3, was deposited onto S1 in two-hourly immersions for a maximum of 26 hours to form S3_a (Figure 5.11). The deposition time increased considerably for the successful self-assembly of C3 due to the bulky nature of the compound and slow imine bond formation. A Sauerbrey analysis revealed an average area occupied by a single molecule similar to that of the previous layer, at around 0.218 ± 0.013 nm² (Figure 5.12). This suggests that the wire's first two components deposit in an approximately 1:1 ratio.

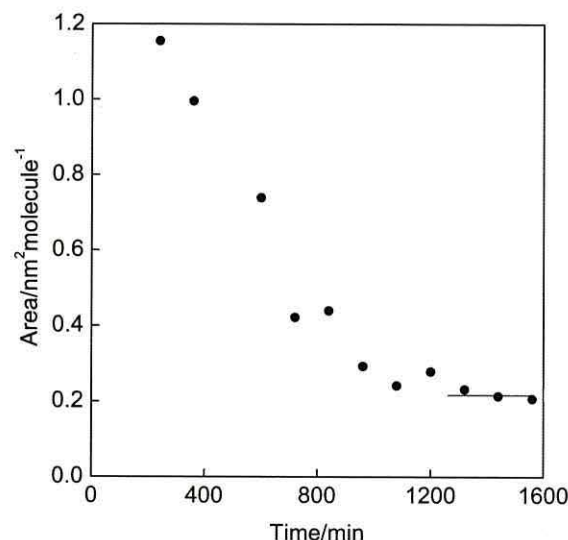


Figure 5.12: Typical QCM results for the deposition of C3 onto S1 to form S3_a.

5.3.2 PHYSICAL CHARACTERISATION: XPS

A sample of S3_a was prepared for XPS analysis on gold-coated, highly ordered pyrolytic graphite (HOPG). A total of twelve, two hour depositions were carried out in order to provide adequate surface coverage, as established by the Sauerbrey analysis undertaken in Section 5.3.1. A summary of the normalised data obtained for the main elements is provided in Table 5.3.

Element	BE / eV	Proportion of element / %	Normalised Intensity
S 2p	162.4	37	1.0
	163.6	18	
	168.4	30	
	169.6	15	
N 1s	398.9	67	1.8
	399.9	33	
C 1s	284.8	89	36.5
	286.7	5	
	288.3	6	
O 1s	531.8	100	10.2

Table 5.3: An elemental, RSF-corrected comparison of the key components in S3_a, normalised to the S 2p intensity.

Of particular interest at this stage of the multistep process was the evaluation of the N 1s spectra. We have previously seen that the successful assembly of C1 onto gold results in a single nitrogen peak at 399.3 eV, identified as the centrally positioned -N=C bond. With the addition of C3 to this system, the N 1s spectra could be seen to display not one, but two identifiable peaks at 398.9 and 399.9 eV (Figure 5.13), corresponding to the imine (C=N) and terminating amine (-NH_2) environments respectively. Comparison of the peak areas shows that the imine presence accounts for 67% of the total available nitrogen, and the amine for the remaining 33%. This 2:1 ratio suggests that C3 effectively reacted with S1 via a condensation reaction in a 1:1 ratio, as suggested by the QCM data. The resultant system contained two imine components and a terminating amine moiety which allows for continued step-by-step assembly. The ratio of nitrogen to sulfur was 1:1.8, rather than 1:3 as expected from the successful deposition of the two layers. This may be due to an incomplete C3 layer, or the presence of C2 in the initial monolayer, thus reducing the nitrogen signal intensity.

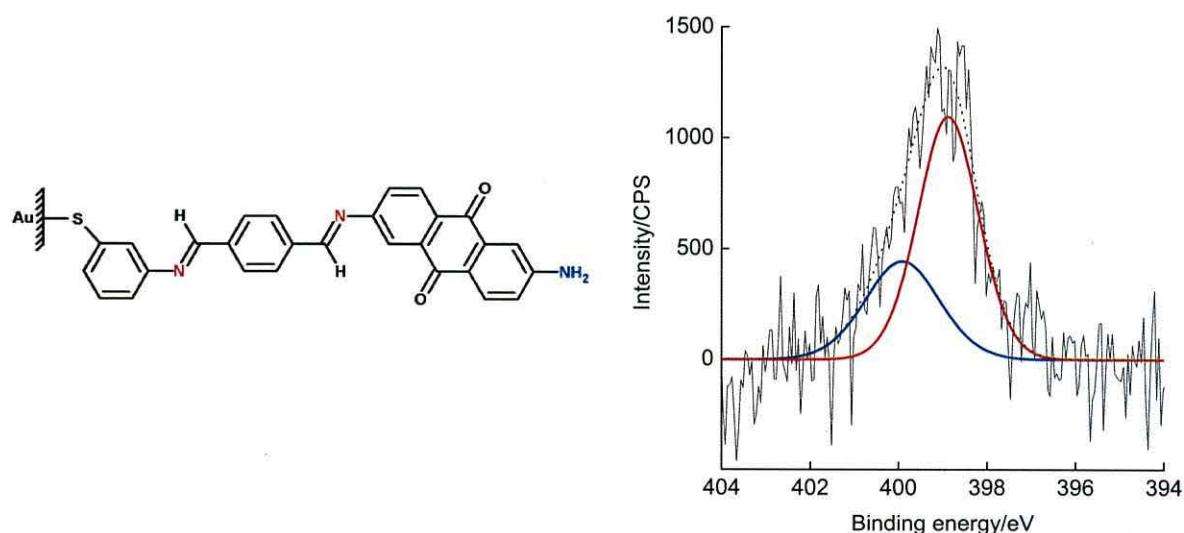


Figure 5.13: The structure of S3_a , with red representing the imine linkages and blue the terminating amine group, with corresponding red and blue peaks modelled in the N 1s spectrum of S3_a .

5.3.3 ELECTRICAL CHARACTERISATION: I - V

The addition of a strong electron acceptor to S1 resulted in a non-symmetrical structure and I - V plot. Rectification occurred in the negative quadrant with an $\langle RR \rangle$ of 3.7 at ± 1 V. This showed that preferential electron flow was from the cathode (Au tip) to the C3 acceptor on one side and from the weakly donating thiolate to the anode (Au-coated substrate) on the

other side *i.e.* cathode $|A_s\text{-}\pi\text{-bridge-D}_w|$ anode, where subscripts denote the strength of the donor or acceptor moieties (w = weak, s = strong). Further evidence to the asymmetrical properties of $S3_a$ can be seen in results obtained by Ashwell *et al.* (Figure 5.14 (b)), with an $\langle RR \rangle$ of between 4 (for the EMC method) and 6 (using the STM) at $\pm 1V$.²¹

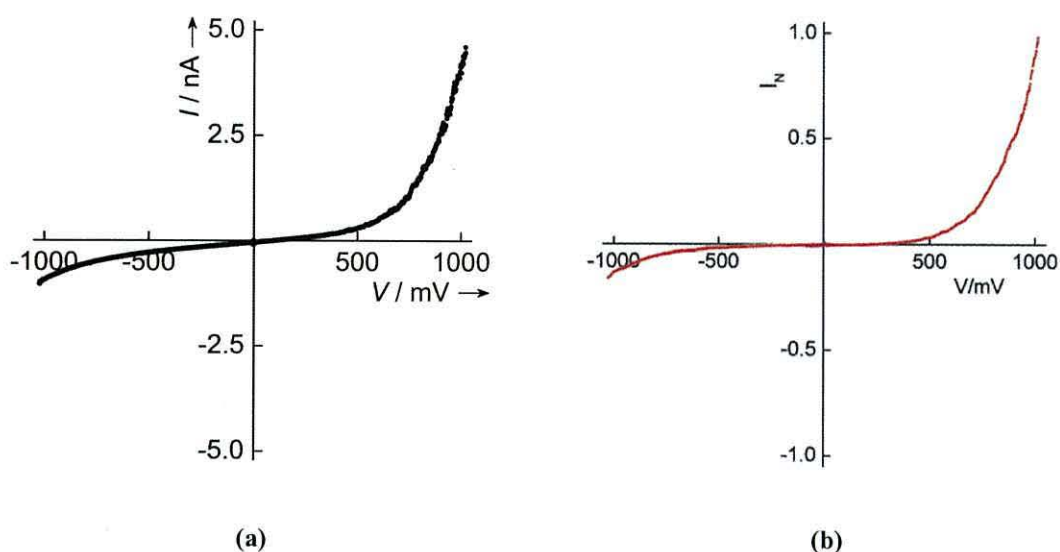


Figure 5.14: (a); Asymmetrical I - V plot following the deposition of C3 onto S1 and (b); Normalised results obtained by Ashwell *et al.* in a previous study on $S3_a$ using the STM technique.²¹

5.3.4 SUMMARY

Having successfully characterised the formation of anchoring layer S1, confirmation of the imine bond formation between S1 and subsequent amine-terminated compounds was sought. C3 in particular was an ideal candidate, with amine headgroups at either end to allow for continued assembly. The Sauerbrey analysis revealed a final area per molecule of $0.218 \pm 0.013 \text{ nm}^2$, approximately that obtained by the first layer ($0.206 \pm 0.002 \text{ nm}^2$). This suggests that an amine headgroup on C3 reacted, albeit slowly, to the terminal aldehyde on S1 in a 1:1 ratio, confirming the formation of a second, densely packed monolayer. Further confidence in this result was gained by XPS analysis, which revealed nitrogen peaks centred at 398.89 and 399.93 eV in an approximately 2:1 ratio. These were attributed to two imine and one amine environment, which corresponds well with the molecular structure of $S3_a$.

The subsequent investigation into the system's current-voltage response revealed an $\langle RR \rangle$ of 3.7 at $\pm 1V$, with rectification occurring in the negative quadrant. This accepting nature is

essential in creating a rectifying system, and is due to the presence of two central C=O functional groups. As predicted, preferential electron flow was from the Au tip to the C3 acceptor and from the weakly donating C1 to the Au substrate. This demonstrates the ability to tune molecular wires to display desired electronic properties. In conclusion, C3 has been successfully self-assembled onto the weakly donating C1 to form a short rectifying wire of *ca.* 2.2 nm in length. The presence of a terminating amine group allows the wire to be further extended, as described in Section 5.4.

5.4 FORMATION OF A 10-STEP SYSTEM: S3_A-S7_A

Thus far, a multilayer system has been successfully formed. This consists of the initial C1 monolayer and the subsequent addition of C3, proving that the method of self-assembly used can indeed create multilayer wires. Furthermore, by exploiting the ability of amine and aldehyde moieties to react with one another, S3_a can be extended to form a ten-component system, as shown in Figure 5.15, whilst being monitored using a Sauerbrey analysis.

5.4.1 PHYSICAL CHARACTERISATION: QCM

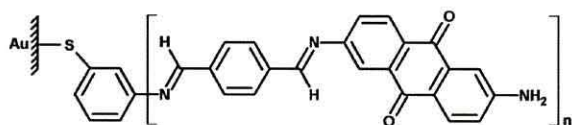


Figure 5.15: The formation of S3-7_a consisting of between 1 and 5 repeating C3 units.

As with the previous system, the weakly electron donating C1 was assembled onto a gold-coated quartz crystal, and subsequently reacted with electron accepting C3 to form the first two layers of the system. The wire was then extended using alternating bridging units consisting of a single benzene ring with *para*-substituted aldehyde groups and the electron accepting C3. Depositions of the C4 bridging unit typically occurred over periods of 10 to 20 minutes for up to 240 minutes in total to ensure complete and uniform coverage of the layer. By alternating C3 and C4 units, wires containing between 1 and 5 C3 units were constructed. Evidence of the 1:1 ratio in which these layers were deposited can be seen in a comparison between the frequency change at each stage of the assembly process and the molecular mass of each component. By comparing the total mass of the wire at each stage with the total

measured change in frequency, an assumption can be made as to the completeness of a monolayer. For example, a non-linear relationship would suggest the formation of an incomplete monolayer. A linear relationship, as observed in Figure 5.16 whereby the two values are proportional, suggests that the wire assembles with one C4 unit to every one C3, whereas a bulkier component would be expected to deposit at a ratio of 2:1 or more.

The stepwise assembly of S4_a in particular has been confirmed in the literature by infrared spectroscopy on capped gold nanoparticles.¹⁹⁶ This was done by reacting the nanoparticles with C2 and then C4 to create the initial C1-type structure. Alternating C3 and C4 units were coupled on to this to produce a wire reflecting the structure of system S4_a. Evidence of coupling between the respective aldehyde and amine-terminated units was provided by the presence of a carbonyl stretching peak at 1697 cm⁻¹ and 1690 cm⁻¹ in the aldehyde-terminated sequences only.

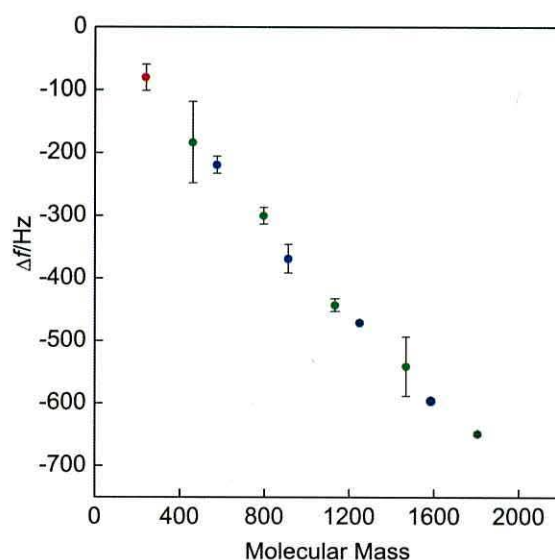


Figure 5.16: The total change in frequency from the clean (starting) value measured against the molecular mass of each constituent layer. Red corresponds to the initial anchoring layer, S1, green to that of C3 and blue to C4.

5.4.2 ELECTRICAL CHARACTERISATION: *I-V*

For clarity, a summary of the *I-V* results obtained for S3_a-S7_a have been presented in Table 5.4. For each plot, the forward and reverse sweeps have been averaged.

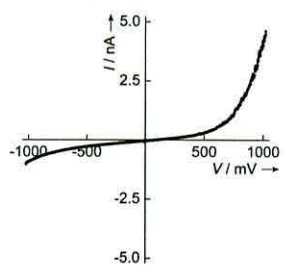
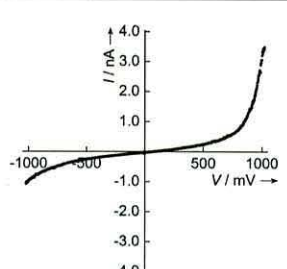
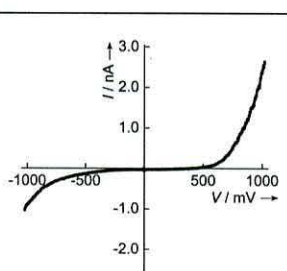
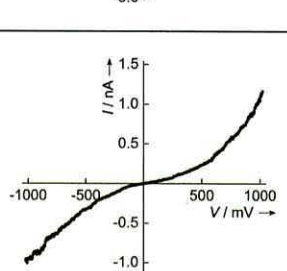
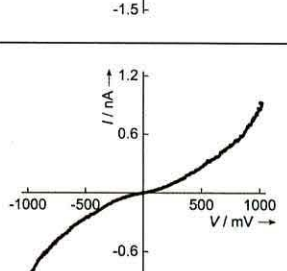
System	No. C3 units	Length/nm	Rectification $\langle RR \rangle$ at $\pm 1V$	I - V characteristics
S3 _a	1	2.5	3.7	
S4 _a	2	4.3	3.3	
S5 _a	3	6.1	2.8	
S6 _a	4	7.9	1.2	
S7 _a	5	9.7	1.2	

Table 5.4: A summary of S3_a-S7_a with respect to their electrical properties.

As seen in Section 5.3, the addition of electron accepting C3 to weakly donating S1 results in a non-symmetrical structure. Therefore S3_a exhibits a non-symmetrical I - V plot with an $\langle RR \rangle$ of 3.7 at ± 1 V. This provides evidence that preferential electron flow is from the cathode (Au tip) to the C3 acceptor on one side and from the weakly donating thiolate to the anode (Au-coated substrate) on the other side *i.e.* cathode | A_s- π -bridge-D_w | anode.

The I - V plot for S4_a also exhibited an asymmetrical curve with rectification occurring once again at negative bias. This is due to the addition of a strong electron acceptor into the sequence of donor and acceptor moieties: cathode | A_s- π -bridge-A_s-D_w | anode. An $\langle RR \rangle$ of 3.3 at ± 1 V has been recorded. Compared to the $\langle RR \rangle$ demonstrated by system S3_a (3.7 at ± 1 V), the $\langle RR \rangle$ exhibited by S4_a is unexpectedly low. With the addition of further electron accepting units in S4_a, the $\langle RR \rangle$ would be expected to increase, but the presence of the initial weak donor (C1) is thought to act as a limiting factor. Similarly, S5_a showed an $\langle RR \rangle$ of 2.8 at ± 1 V, similar to both S3_a and S4_a.

System S6_a comprises a | D_w-A_s- π -bridge-A_s- π -bridge-A_s- π -bridge-A_s | sequence which resulted in an $\langle RR \rangle$ of 1.2 at ± 1 V. Unlike systems S3_a-S5_a, system S6_a possesses very little asymmetry. This may be due to the largely electron accepting nature of the wire dominating electron flow through the system, effectively producing a symmetrical system, which from previous reports are shown to produce symmetrical I - V plots. This can also be seen after the addition of a further C3 unit to system S7_a, yielding symmetrical plots with an $\langle RR \rangle$ of 1.2 at ± 1 V, as seen in Table 5.4. Furthermore, the relationship between molecular wire length and conductance suggests a change in the dominant electron transfer process between S5_a (*ca.* 6.1 nm) and S6_a (*ca.* 7.9 nm) may have occurred. Although many reports demonstrate this change in wires shorter than S6_a, transitions have been seen to occur up to 6.8 nm, as reported by several groups following the systematic statistical examination of molecular wires of varying lengths. An investigation into this aspect of the molecular wires' electron transport properties has been carried out in Section 5.7 in an effort to identify whether this is indeed the case.

5.4.3 SUMMARY

With evidence of effective aldehyde-amine coupling in Section 5.3, the S3_a wire was extended with the addition of alternating C3 and C4 units. This resulted in a series of five related wires consisting of between one and five anthraquinone components. A Sauerbrey analysis of each step in the growth process showed that assembly progressed in an approximately 1:1 ratio, although the possibility of building a complete wire over the course of 10 steps without the presence of a certain amount of defects and unwanted material is doubtful. Each wire was analysed with respect to its *I-V* characteristics. A general trend was identified, in that rectification decreased with increasing molecular length. Average rectification ratios at ± 1 V were seen to decrease from 3.7 for S3_a to 2.8 for S5_a, before culminating in a ratio of 1.2 for S6_a and S7_a. This change has been attributed to the increasing electron accepting nature of the wire dominating electron flow through the system, as well as a possible change in charge transport mechanism between S5_a and S6_a.

5.5 RECTIFICATION INVESTIGATION OF S4_b AND S4_c

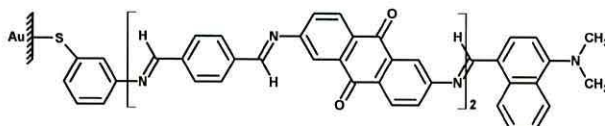


Figure 5.17: C5 self-assembled onto S4_b.

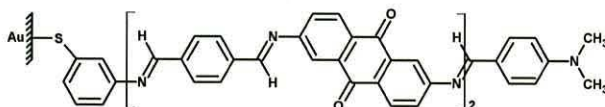


Figure 5.18: C6 self-assembled onto S4_c.

In order to examine the effect of steric hindrance on rectification, S4_a was modified by the addition of a terminating group consisting of either one (4-(dimethylamino)benzaldehyde, or C6), or two (4-dimethylamino-1-naphthaldehyde, or C5) benzene rings (Figures 5.17 and 5.18). Both compounds possess an aldehyde functional group on one end, which allows them to chemically bond with the terminating amine group on C3. The dimethylamino group acts as a cap on the wire to halt any further elongation of the system via self-assembly. C5 and C6

were chosen for this particular study as they had previously been used in a similar study by Ashwell *et al.*

5.5.1 PHYSICAL CHARACTERISATION: QCM

To form S4_b, C5 was deposited onto S4_a in 10 minute increments for up to 120 minutes. A typical example of this can be seen in Figure 5.19 (a), whereby a stable frequency was reached after 70 minutes at an area of $0.245 \pm 0.005 \text{ nm}^2 \text{ molecule}^{-1}$.

Similarly, to form S4_c, C6 was assembled onto S4_a in 15 minute increments for 150 minutes (Figure 5.19 (b)). A plateau was reached at $0.317 \pm 0.012 \text{ nm}^2 \text{ molecule}^{-1}$, as supplied by Michael Henry (Bangor University) where previous monolayers exhibited average areas of $0.30 \text{ nm}^2 \text{ molecule}^{-1}$. This value, greater than seen thus far suggests that an incomplete first layer had affected the area per molecule in all subsequent depositions.

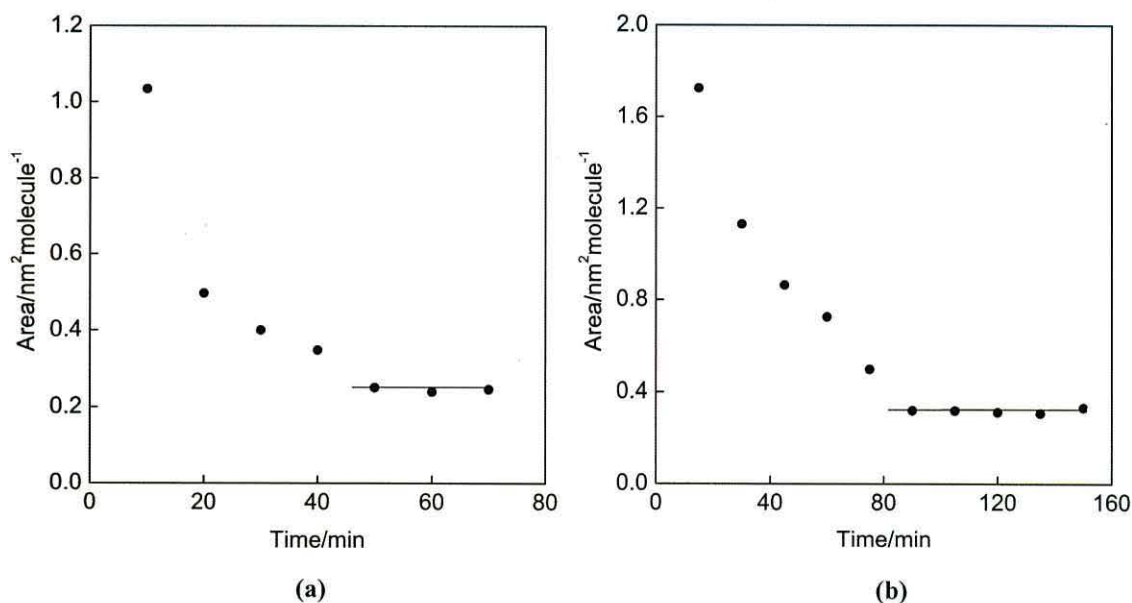


Figure 5.19: A typical deposition of (a) C5 and (b) C6 onto S4_a.

5.5.2 ELECTRICAL CHARACTERISATION: *I-V*

Both systems S4_b and S4_c are electron donors that exhibit rectification in the positive quadrant (Figure 5.20 (a) and (b)). The double-ringed structure demonstrated an $\langle RR \rangle$ of 8.3 at $\pm 1 \text{ V}$, with a maximum value of 13.3 at $\pm 1 \text{ V}$. In comparison, the single-ringed structure possessed

an $\langle RR \rangle$ of only 2.8 at ± 1 V. As the initial four layers remained identical for S4_b and S4_c, the final layer must be responsible for the difference in rectification. This suggests that the presence of a double ring molecule in S4_b increases the steric hindrance between the 5th layer and the rest of the system (Figure 5.21), causing a twist about the dihedral separating components C3 and C5, as proposed by Ashwell *et al.*³⁹ The LUMO orbitals of these components would then be out of alignment, hindering electron movement across that particular section. The rectification was less prominent in S4_c since the final component is less bulky, leading to much smaller twist than that witnessed in system S4_b. The relative planarity of S4_c did not appear to affect the flow of electrons greatly, resulting in a fairly low rectification ratio (2.8 at ± 1 V).

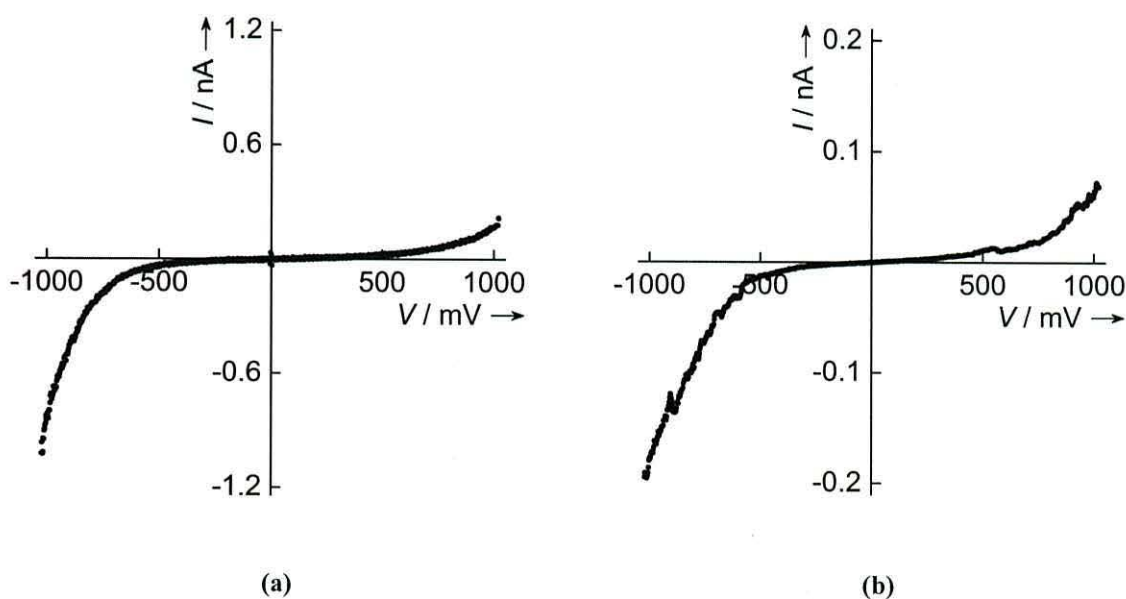


Figure 5.20: Asymmetrical I - V plots following the deposition of (a) C5 and (b) C6 to S4_a.

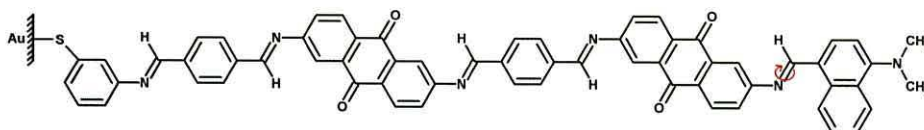


Figure 5.21: System S4_b with the dihedral twist indicated between the terminating naphthaldehyde unit and the rest of the wire.

5.5.3 SUMMARY

Section 5.5 has provided further evidence that the introduction of a bulky component into a relatively planar wire affects the ability of electrons to move through the system. This is

reflected in the measured $\langle RR \rangle$ of both systems, with the bulkier wire exhibiting the greatest value, at 8.3 at ± 1 V. This study has been extended in Section 5.6 to look at any change in I - V properties and the magnitude of such changes with the addition of C5 to wires of varying lengths.

5.6 FORMATION OF 11-STEP SYSTEM S3_B-S7_B

5.6.1 PHYSICAL CHARACTERISATION: QCM

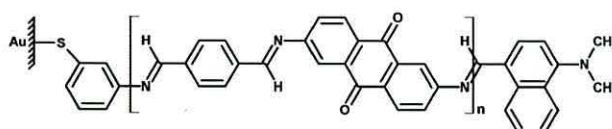


Figure 5.22: Self-assembled wires consisting of up to 12 components were constructed with $n = 1$ -5 for systems S3_b-S7_b.

In a continuation of the previous study, a variation on the 11-step wire consisting of 1-5 repeating C3 units was assembled. Each terminating C3 unit in systems S3_a-S7_a was capped with a double-ringed C5 molecule (Figure 5.22). Once again, the formation of these wires was monitored using a Sauerbrey analysis, with a linear relationship showing the 1:1 deposition throughout, as seen in Figure 5.23.

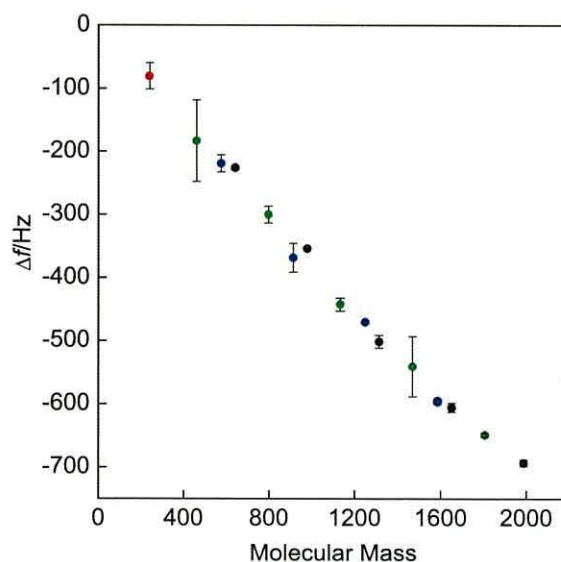


Figure 5.23: The total change in frequency from the clean (starting) value measured against the total molecular mass as each constituent layer is added. Red corresponds to the initial anchoring layer, C1, green to that of C3, blue to C4 and black to C5.

5.6.2 ELECTRICAL CHARACTERISATION: I - V

For clarity, a summary of the I - V results obtained for S3_b-S7_b has been presented in Table 5.5. For each plot, the forward and reverse sweeps have been averaged.

The first wire of this series comprised the initial C1 molecule self-assembled onto gold, with C3 and then C5 subsequently deposited. The I - V character of this system proved relatively symmetrical, with an $\langle RR \rangle$ of 1.3 at ± 1 V. This can be compared to S3_a (Figure 5.24 (a)), which produced an asymmetrical plot, showing that the addition of C5 altered the electrical response of the system. As C5 is an electron donating moiety, its addition to S3_a resulted in a symmetrical D-A-D system, hence the symmetrical I - V plot.

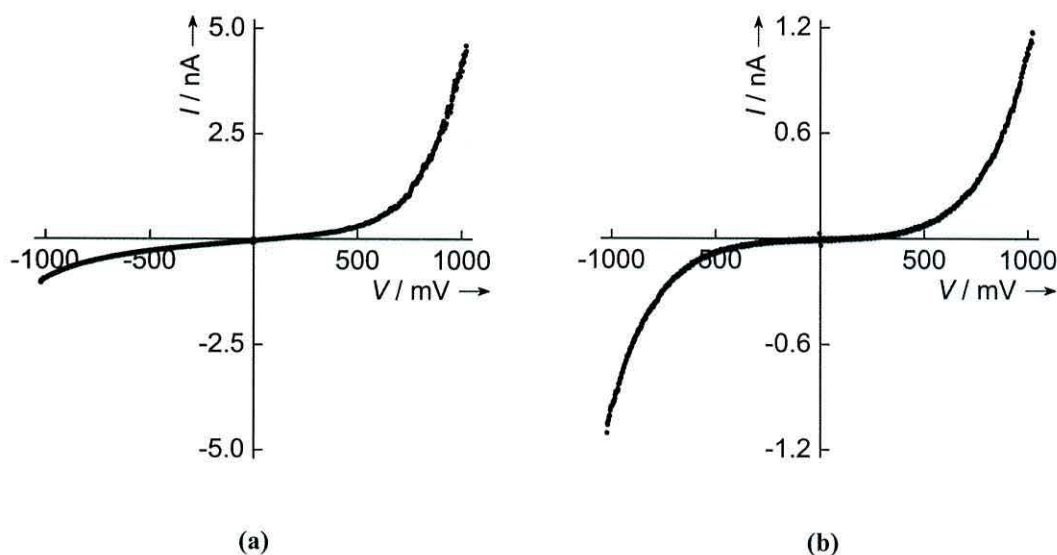


Figure 5.24: I - V characteristics of (a) S3_a and (b) S3_b.

As the number of C3 units increased to 2 and then 3, rectification could be seen to occur in the positive quadrant, with an $\langle RR \rangle$ of 8.6 and 11.5 at ± 1 V respectively. This suggests that the addition of C5 to these intermediate-length wires causes rectification to switch to the opposite quadrant to that exhibited by the preceding C3-terminating systems (Figure 5.25). This implies that the bulky C5 unit either introduces enough steric hindrance to hinder electron movement between the C5 unit and the rest of the system, or, due to the strongly electron donating properties of the final layer, electron flow reverses to flow from the bottom electrode through to the gold probe, *i.e.* cathode | D_w-A_s- π -bridge-A_s-D_s | anode.

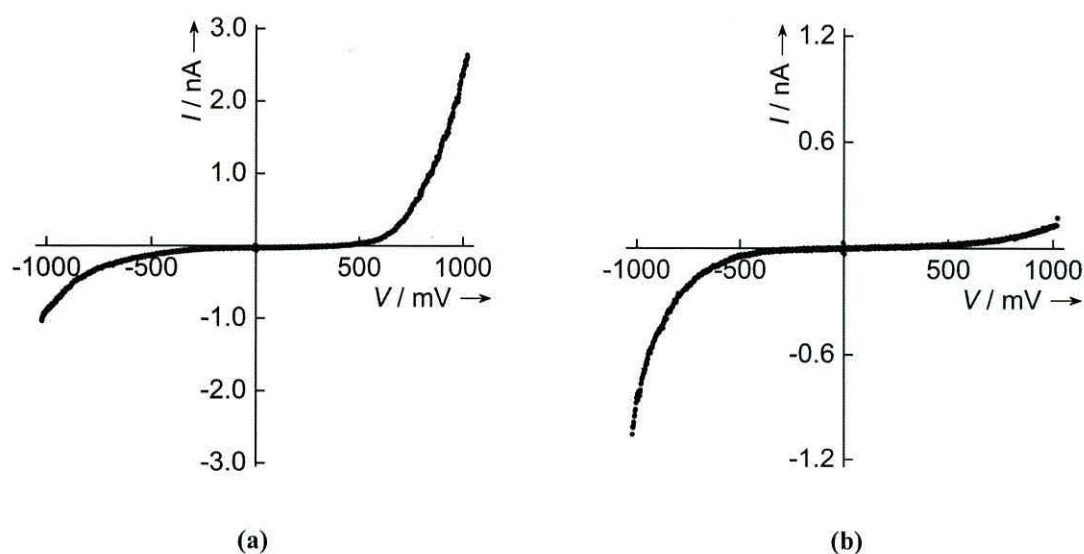


Figure 5.25: I - V characteristics of (a) S5_a and (b) S5_b.

However, as evidenced in Table 5.5, once the system was extended to include 4 and 5 C3 units capped with C5, the I - V plots showed the same return to symmetry as seen for S6_a and S7_a (Figure 5.26). Average rectification ratios exhibited by these lengthier wires were measured as 1.3 and 1.8 at ± 1 V respectively. The I - V properties of these lengthy wires can be explained in two parts. Firstly, the largely electron accepting nature of the majority of the wire dominates electron flow, with both terminating donor moieties having little effect on the overall electrical response. Secondly, it is possible that with the increased molecular length, we are witnessing a change in dominant electron transfer process, as suggested in Section 5.4.2.

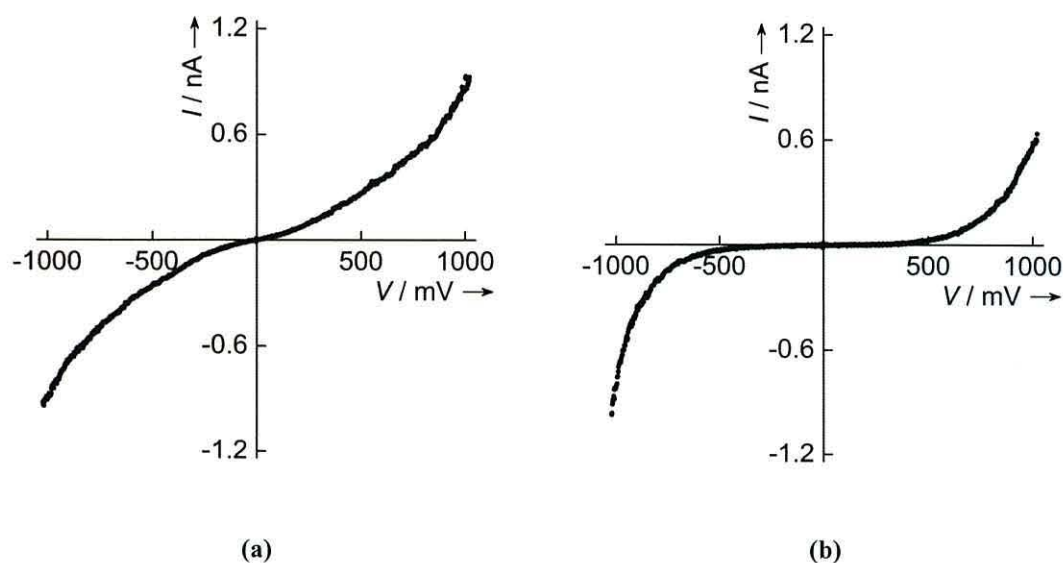


Figure 5.26: I - V characteristics of (a) S7_a and (b) S7_b.

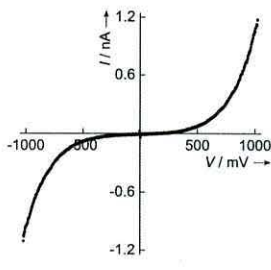
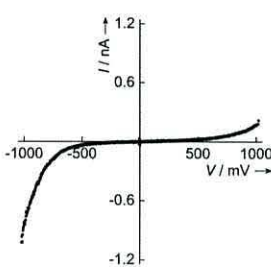
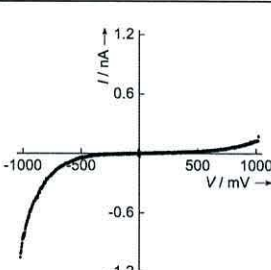
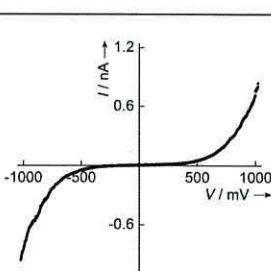
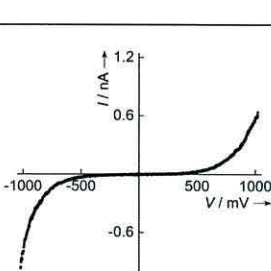
System	No. C3 units	Length/nm	Rectification $\langle RR \rangle$ at $\pm 1V$	I - V characteristics
S3 _b	1	3.2	1.3	
S4 _b	2	5.0	8.6	
S5 _b	3	6.8	11.5	
S6 _b	4	8.6	1.3	
S7 _b	5	10.4	1.8	

Table 5.5: A summary of S3_b-S7_b with respect to their electrical properties.

5.6.3 SUMMARY

The rectification study in Section 5.5 was extended to cover systems S3_b-S7_b. Once again, a linear relationship between frequency change and molecular mass was observed, confirming the coupling of C5 to each wire via an amine-aldehyde coupling reaction. A comparison of each system before and after the addition of a terminating C5 unit has demonstrated the ease with which rectification can be altered. The presence of C5 has the ability to alter *I-V* behaviour from rectifying to symmetrical (S3_a to S3_b) and from rectifying in one direction to the other (S4_a to S4_b and S5_a to S5_b). It was only the longest two wires that remained unchanged, which has been attributed to the chiefly electron accepting nature of the two wires, as well as the possibility of a change in dominant electron transfer mechanism from one dependant on length to one that is independent.

5.7 CURRENT JUMPS

Systems S3_a-S7_a are ideal candidates with which to examine charge transport properties in a series of conjugated wires. Differing only in the number of repeating C4 and C3 units, the five self-assembled wires measure between *ca.* 2.5 to 9.7 nm in length. All systems are bound to the gold substrate via a sulfur headgroup, with a terminating amine functional group at the opposite end of the wire to enable electronic coupling between the wire and probe tip during sampling. Typically, anchoring groups which are able to provide efficient molecule-metal electronic coupling include, but are not exclusive to, thiols,¹⁹⁷ carboxylates¹⁹⁸ and amines.^{61,199,200} Although single-molecule conductance studies principally involve symmetrically contacted wires, reports of wires comprised of differing functional groups have also been investigated.²⁰¹ The effect of employing asymmetrical contacts in such studies has been discussed in a comparative conductance study between HS(CH₂)₁₀COOH, HOOC(CH₂)₁₀COOH and SH(CH₂)₁₀SH, as reported by Martin *et al.*²⁰² Using the I(s) method developed by Haiss *et al.*, the asymmetric arrangement was found to produce the lowest current of the three systems. This lowered charge transport efficiency suggests that single molecule conductance measurements are influenced not only by the anchoring group, but also the contact symmetry. By selecting suitably effective surface binding groups, such as thiols and amines for systems S3_a-7_a, we can ensure that current jump events are due to coupling between the probe and terminating functional moiety.

Using the $I(t)$, method of Haiss *et al.*, single molecule conductivity experiments have been carried out on systems $S3_a-7_a$. Once a suitably flat substrate area had been located, the gold probe was lowered to a fixed distance above the surface under a constant voltage. The tip was then allowed to drift over the SAM, the current being monitored as a function of time. Events in the $I(t)$ domain consisted of abrupt increases and decreases in current, the increase persisting for typically 20 to 430 ms. These events are attributed to the terminating amine group spontaneously adsorbing to, and desorbing from the drifting tip as it passed by. As the system is expected to consist of well-packed monolayers, we would expect the resultant current jumps to occur in integer multiples of the single-molecule value, with higher values corresponding to the probe contacting two or more molecules at the same time. The current jump results presented in Figures 5.27-31 were gathered from 500 jumps on each of the five $S3_a-7_a$ systems. Due to the small number of events occurring at values above 2 nA, all histograms have been presented to a maximum ΔI of 2 nA.

System $S3_a$ is comprised of one C3 unit reacted with the initial C1 monolayer via a condensation reaction involving their respective terminating amine and aldehyde moieties. QCM studies have proven that $S3_a$ assembles in a densely packed arrangement. Figure 5.27 (a) depicts a typical current jump event, lasting 240 ms with an $I-I_0$ of *ca.* 0.35 ± 0.05 nA. 500 such current jumps were analysed to produce the histogram in Figure 5.27 (b). The most populous range, in which 49 of the total jump events occurred was centred at between 0.15 and 0.20 ± 0.05 nA, and is believed to correspond approximately to single-molecule contact between the gold probe and SAM. Tentative evidence of secondary peaks were seen to occur at 0.45-0.50 nA, 0.55-0.60 nA, 0.90-0.95 nA, 1.20-1.25 nA, and finally 1.80-1.85 nA, thought to be caused by multiple contact events, although these do not necessarily occur at integer values of the initial 0.15-0.20 nA range.

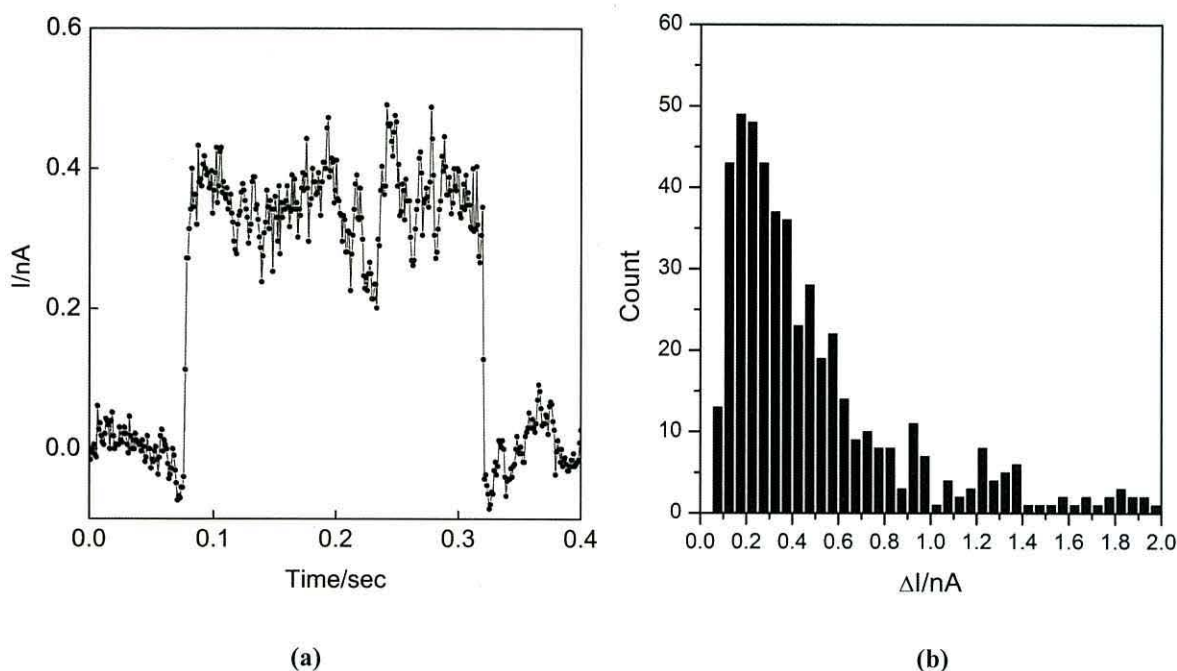


Figure 5.27: (a) A typical current jump observed during the single molecule current analysis of S3_a and (b) a graphical summary of the results taken from 500 current jump events.

System S4_a is the second of the five wires under investigation, and consists of two C3 units. With 53 current jumps falling within the range of $0.25\text{--}0.30 \pm 0.05$ nA, this proved the most populous region, and is thought to correspond to current flow through single molecule contact. Secondary peaks appeared to occur at approximately integer values of 0.45–0.50 nA, 0.65–0.70 nA and 1.40–1.45 nA, which can be attributed to two, three and five-molecule contacts events. Figure 5.28 (a) depicts a typical current jump for system S4_a, lasting 30 ms, with an $I-I_0$ value of approximately 0.44 ± 0.05 nA. 500 such events were analysed to produce the histogram in Figure 5.28 (b).

Figure 5.29 (a) portrays a typical current jump event observed in the single molecule conductance analysis of S5_a. The measured current can be seen to undergo a sharp increase to *ca.* 0.27 ± 0.03 nA for 30 ms before returning to its original ‘pre-jump’ value. A total of 500 current jumps were analysed in order to produce the histogram in Figure 5.29 (b). The greatest number of current jump events, in this case 52 out of the total 500, were seen to occur in the range $0.20\text{--}0.25 \pm 0.05$ nA. Assuming this corresponds to single molecule conductance, secondary maxima in the regions of 0.45–0.50 nA, 0.65–0.70 nA, 0.85–0.90 nA, 1.05–1.10 nA and 1.30–1.35 nA can be attributed to the tip contacting between two and six molecules, respectively.

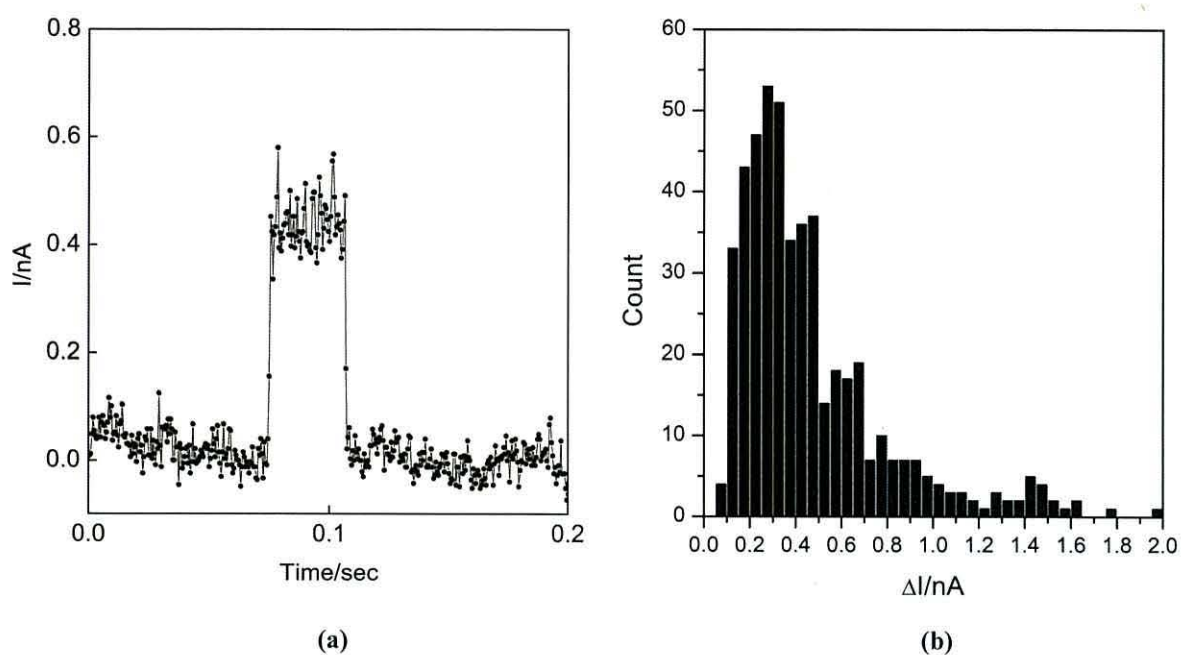


Figure 5.28: (a) A typical current jump observed during the single molecule current analysis of $S4_a$ and (b) a graphical summary of the results taken from 500 current jump events.

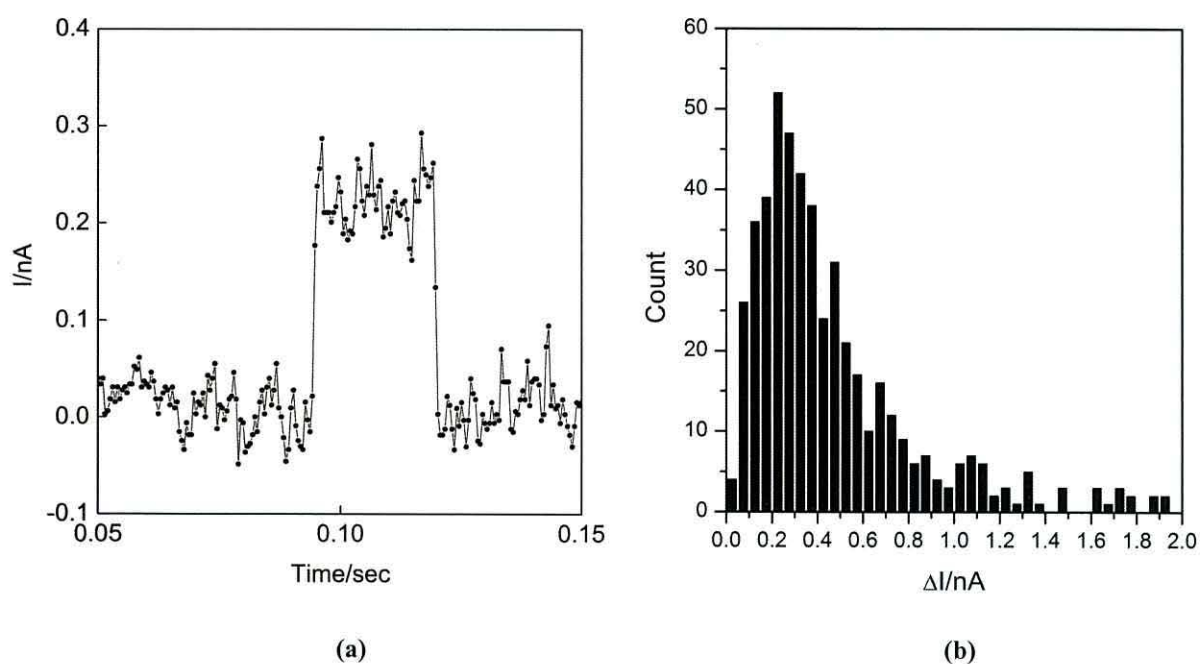


Figure 5.29: (a) A typical current jump observed during the single molecule current analysis of $S5_a$ and (b) a graphical summary of the results taken from 500 current jump events.

A typical current jump observed in the conductance study on system S6_a (Figure 5.30 (a)) can be seen to exhibit a ΔI of 0.37 ± 0.02 nA and lifetime of 30 ms. A total of 500 current jumps were recorded and collated to form the subsequent histogram (Figure 5.30 (b)). It is clear that the most frequently observed current value lies within the range $0.20\text{-}0.25 \pm 0.05$ nA, with a total of 51 recorded events. Six further peaks have been identified between $0.35\text{-}0.40$ nA, $0.50\text{-}0.55$ nA, $0.65\text{-}0.70$ nA, $1.30\text{-}1.35$ nA, $1.50\text{-}1.55$ nA and $1.90\text{-}1.95$ nA, all of which are appreciably larger than the counts observed in neighbouring current ranges.

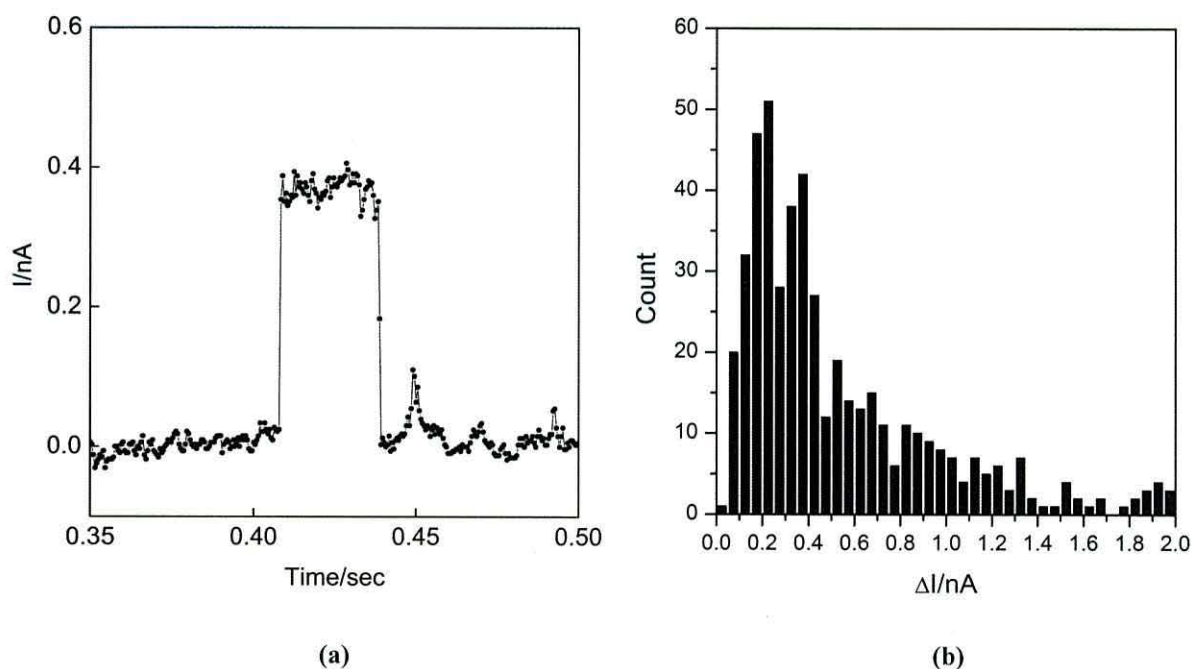


Figure 5.30: (a) A typical current jump observed during the single molecule current analysis of S6_a and (b) a graphical summary of the results taken from 500 current jump events.

System S7_a is the longest, and final molecular system upon which single molecule studies have been conducted. A typical current jump event (Figure 5.31 (a)), depicts an event lifetime of 30 ms and a ΔI of 0.41 ± 0.02 nA. Unlike the previous four systems, the peak current was found to lie at the relatively low value of $0.10\text{-}0.15 \pm 0.05$ nA, with a total of 42 counts (Figure 5.31 (b)). This too is lower than maxima recorded for the previous systems. As well as this peak, secondary peaks can be observed at $0.25\text{-}0.30$ nA, $0.50\text{-}0.60$ nA, $0.70\text{-}0.75$ nA, $0.85\text{-}0.90$ nA, $1.15\text{-}1.25$ nA and $1.45\text{-}1.50$ nA. This suggests contact is being made between the tip and a number of molecules ranging from 2 to 12.

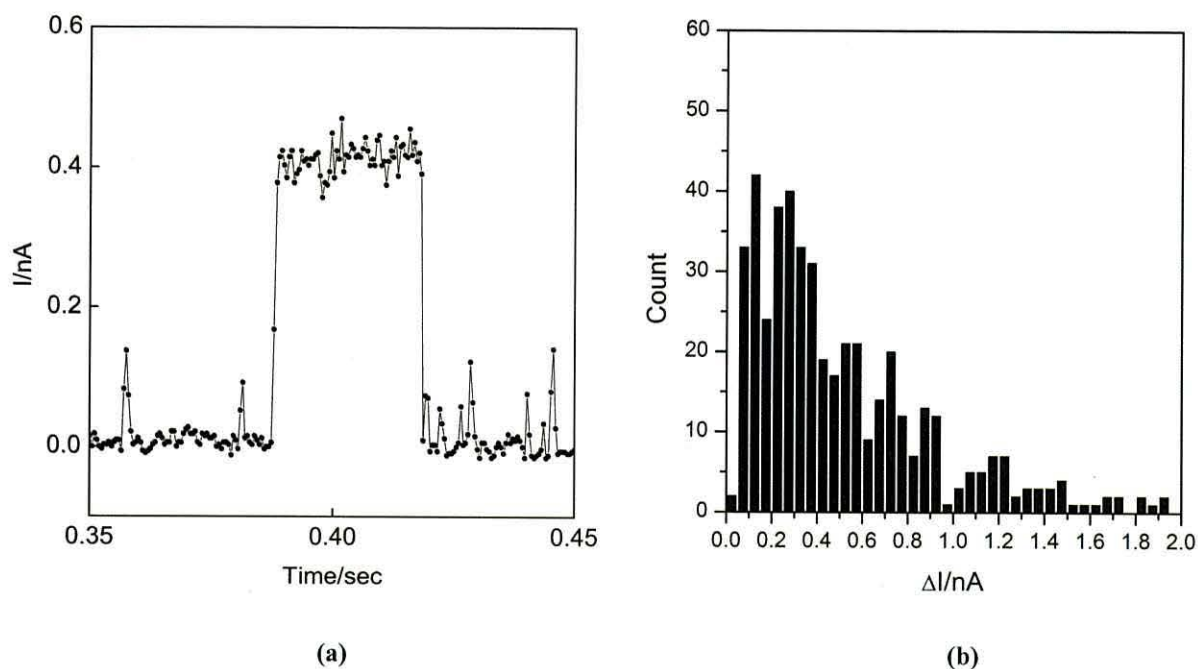


Figure 5.31: (a) A typical current jump observed during the single molecule current analysis of S7_a and (b) a graphical summary of the results taken from 500 current jump events.

5.7.1 SUMMARY

By compiling a histogram representing the entirety of the current jump results gathered from 500 jumps on S3_a-S7_a, the current response of each system can be directly compared with that of the others (Figure 5.32). A general pattern can be observed, in that the majority of current jumps occur between 0 and 1 nA (between 82% and 90%), showing little difference in the more commonly observed current jumps between systems, all of which are in the range of $0.1\text{-}0.3 \text{ nA} \pm 0.05 \text{ nA}$. Apparent peaks can be observed at positions between 0 and 2 nA, labelled as Maxima (M) 1-5. This shows that rather than a gradual decline with increasing ΔI , the jump frequency appears to undulate. We can consider these as single and multiple adsorption-desorption events occurring as the probe passes over the surface.

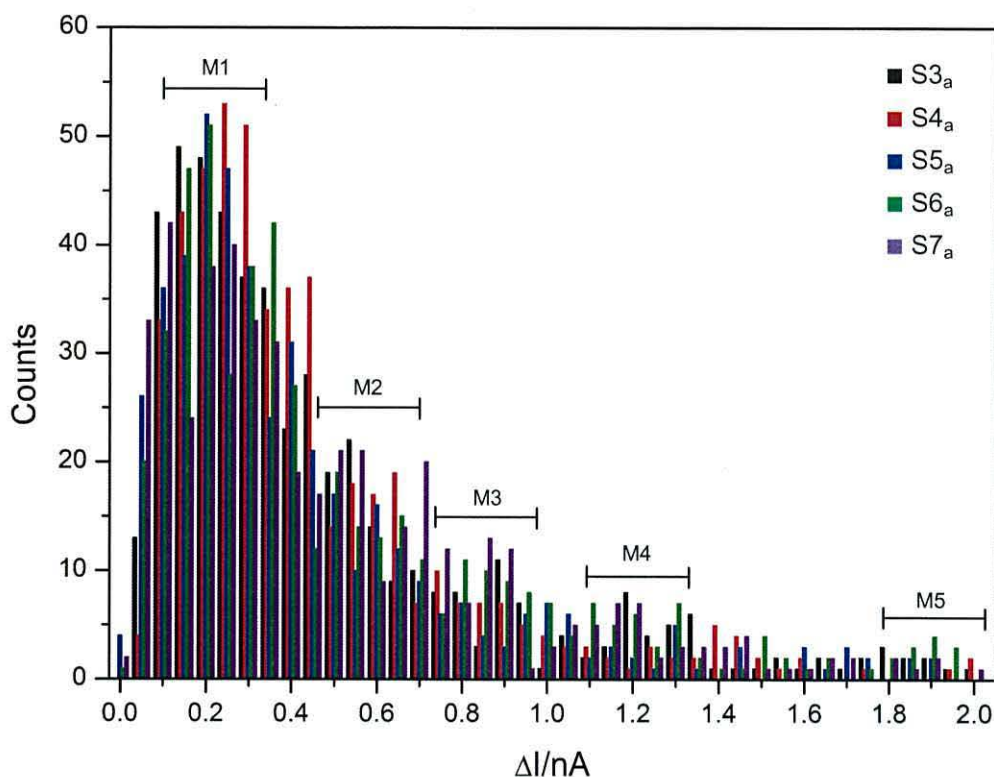


Figure 5.32: A graphical summary of the current jump surveys carried out on systems S3_a-S7_a between 0 and 2 nA at intervals of 0.05 ± 0.05 nA.

The current maxima detailed in Table 5.6 indicate very little change in current with increasing molecular length, and no obvious transition is seen to occur as the wire grows systematically longer. This suggests the presence of a principal charge transport mechanism in which little length dependence is exhibited. Thus we can speculate that the dominant charge transport mechanism in systems S3_a-7_a is that of incoherent hopping, which is independent of length. This is in agreement with reports suggesting transitions in dominant transport mechanisms from tunnelling to hopping can occur in conjugated systems as short as 2.5 nm,¹⁷¹ the approximate length of the shortest wire. This does not, however, confirm the transition between charge transport mechanisms as identified in Section 5.4.2 and 5.6.2. The apparent change in rectification between systems S5_a and S6_a as well as S5_b and S6_b was tentatively attributed to the presence of differing dominant transport processes. In order to increase confidence in either set of results, temperature-dependant current analysis should ideally be undertaken. Supposing such a transition were to occur between S5_a and S6_a, we would expect S3_a-S5_a to appear independent of temperature effects with little change in single molecule current with increasing temperature. Above this threshold we might expect the current to show a significant temperature-dependence. The second hypothesis, whereby all five systems

consistently exhibit a similar single-molecule current increase, would be confirmed if all wires could demonstrate the existence of temperature-dependant current changes. This would then confirm the presence of a principally thermally activated hopping regime.

System	Maximum no. Current Jumps (nA)
S3 _a	0.15-0.20
S4 _a	0.25-0.30
S5 _a	0.20-0.25
S6 _a	0.20-0.25
S7 _a	0.10-0.15

Table 5.6: A summary of the most commonly occurring current jumps for systems S3_a-S7_a.

As the wires increase in length with each subsequent C4 and C3 unit, the overall reliability of the current study with regards to single molecule contact decreases. We can understand this in terms of the self-assembly process utilised in the formation of each wire. With the shorter wires, QCM studies have proven that we may be reasonably confident that densely packed multilayers have been formed. Therefore, when the Au tip makes contact with a molecule resulting in a small but well-defined current jump of magnitude 0.15-0.30 nA it is highly likely that it is the terminating amine group on C3 that is being contacted. As additional C4 and C3 units are assembled to produce to lengthier wires, it is possible that the number of successfully reacted molecules decreases, thereby causing a certain amount of disorder within the system. In addition, these defects may continue throughout the assembly process, resulting in a final system containing wires of varying lengths. If this were indeed the case, we might expect a decrease in the frequency of multiple-contact events, although in reality such a decrease is not observed.

We can also consider the angle at which systems S3_a-7_a assemble on the Au surface. The initial C1 unit is known to form a well-packed monolayer with a C-S-Au angle of 120°. This results in a tilted template for all future depositions, which can lead to exposure of the conjugated backbone. It is therefore possible that as well as contacting the terminating amine group, the Au tip may be burying itself in, and directly probing, the system's π -system (Figure

5.33). We also suggest that current jumps may be due to the tip encountering surface architectures such as grain boundaries as it drifts across the substrate. Furthermore, we have shown that the $I(t)$ technique is not reliant on molecules ‘flipping’ up to contact the tip, as suggested by Haiss *et al.*

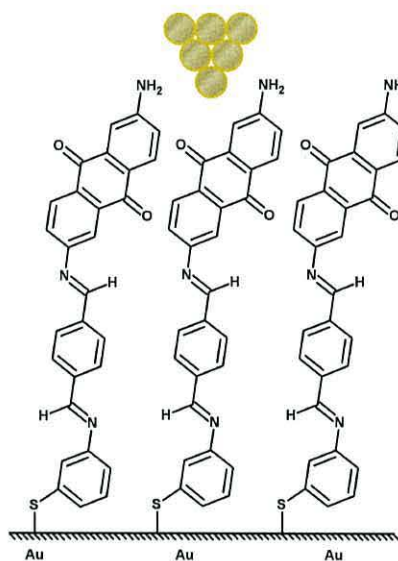


Figure 5.33: It is feasible that the Au probe is burying itself in the conjugated backbone of S3_a.

5.8 FORMATION OF S8_A-S10_A

The wires outlined in this Section are identical to those of S3_a-S5_a with the exception that each electron accepting C3 unit has been replaced with an electron donating C7 unit. C7 is composed of an aromatic benzene ring substituted with four amine moieties and four HCl counterparts. Amines are well known electron donating groups due to the presence of a lone pair that increases the electron density of the attached aromatic ring, which in turn forms an electronically dense backbone along the wire. One or more of these amine groups were expected to react favourably with an aldehyde group and hence be able to form a self-assembled wire of alternating C7 and C4 units. Once again, physical characterisation was performed using QCM to monitor the assembly process and XPS to determine the bonding structure. I - V properties were determined using STM.

5.8.1 PHYSICAL CHARACTERISATION: QCM

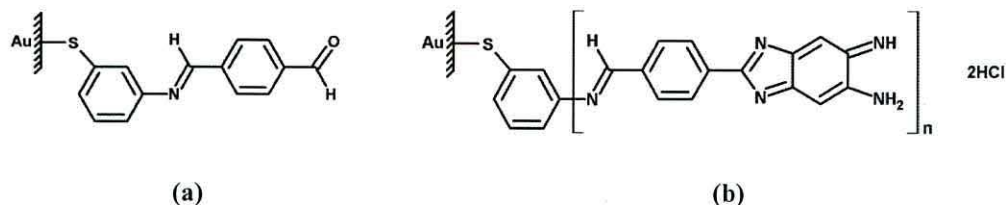


Figure 5.34: (a) C1 self-assembled onto an Au substrate via an Au-thiol linkage to form S1, and (b) the subsequent deposition of 1, 2 and 3 units to 1,2,4,5-benzenetetramine tetrahydrochloride, or C7.

The formation of S8_a (Figure 5.34 (b)) involved the initial deposition of C1 (Figure 5.34 (a)) onto a gold-coated quartz crystal, as outlined in Section 5.1.2 to yield an area per molecule of $0.204 \pm 0.003 \text{ nm}^2$ (Figure 5.35 (a)). The quartz crystal was then immersed in a solution containing C7 for 20 minutes at a time for a total of between 120 and 320 minutes. Once the frequency was judged to be stable for a number of readings, deposition was stopped. The Sauerbrey analysis concluded that the average area occupied by a single unit of C7 was $0.214 \pm 0.010 \text{ nm}^2$ (Figure 5.35 (b)). Although slightly lower than anticipated for such a bulky molecule, this is not entirely unexpected, as a similar value was obtained for the initial monolayer. A similar value for the deposition of C3 onto S1 has also been seen. This may be due to the presence of trapped solvent or HCl, as well as the presence of unwanted physisorbed material, all of which would result in a value slightly less than that of the ideal value. To extend the wire to include two and three C7 units, a bridging terephthalaldehyde (C4) component was assembled at every other step. It should be noted that owing to poor C4 assembly, due in part to its size, area calculations are reported for the entire wire, rather than for individual components. All calculations are inclusive of 2 HCl moieties. Depositions of the second and third C7 units were once again carried out in 20 minute intervals, with average total areas measuring 0.270 ± 0.007 and $0.230 \pm 0.003 \text{ nm}^2 \text{ molecule}^{-1}$ respectively (Figure 5.35 (c) and (d)). Similarly, the final assembly of C5 onto system S10_a resulted in an area of $0.198 \pm 0.009 \text{ nm}^2 \text{ molecule}^{-1}$.

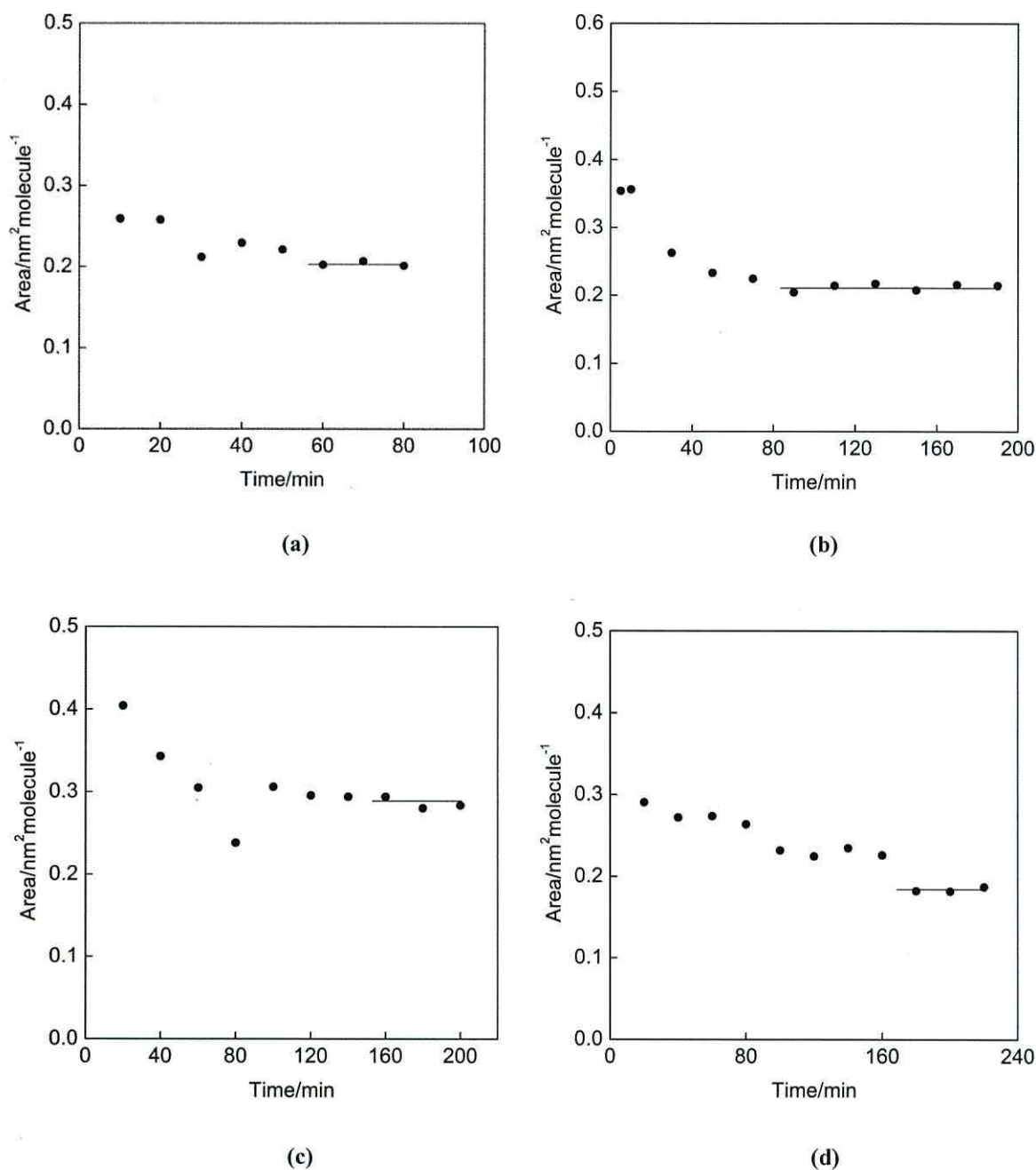


Figure 5.35: Typical QCM results for the deposition of (a) C1 on to an Au-coated substrate to form S1 and (b)-(d) the subsequent deposition of 1, 2 and 3 C7 units onto S1.

A relatively linear relationship between the total frequency change from the clean value and molecular mass is exhibited during the construction of system S10_a (Figure 5.36). The majority of points indicate a deposition ratio of 1:1, with an outlier recorded for the wire comprising three C7 units. This can be attributed to poor deposition or the presence of other adventitious material.

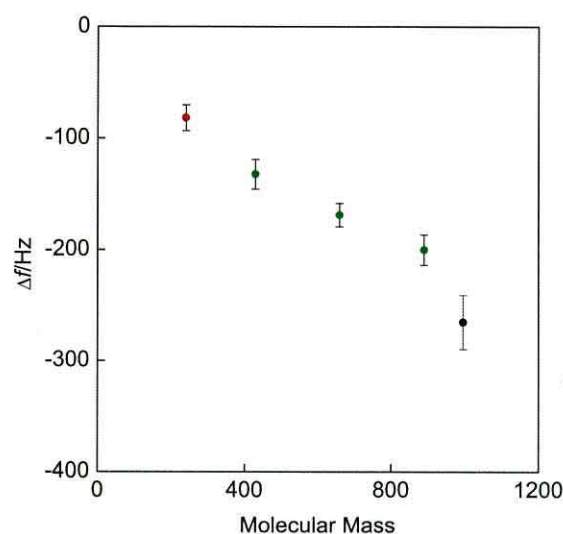


Figure 5.36: The total change in frequency from the clean (starting) value measured against the molecular mass of each constituent layer. Red corresponds to the initial anchoring layer, S1, green to that of C7 and black to C5.

5.8.2 PHYSICAL CHARACTERISATION: XPS

A sample of S8_a was prepared on Au-coated HOPG under the same conditions as for those prepared and monitored using QCM. A minimum of twelve, ten minute-long depositions were carried out for the anchoring C1 SAM, followed by twelve, twenty minute depositions of C7.

Angle resolved XPS studies were carried out at 0° (vertical) and 80°. At 0°, the high resolution scan of the S 2p spectrum was fitted by applying an S 2p_{3/2} to 2p_{1/2} area ratio of 2:1 and a peak separation of 1.2 eV to the Au-S and SH doublets (Figure 5.37). The doublet consisting of peaks at 162.1 and 163.3 corresponds to the expected Au-S bond. However, the presence of a second set of doublets at 163.6 and 164.8 eV indicated that SH was also present in the sample. At an Au-S to SH ratio of 55:45, we can suggest a number of scenarios having occurred. Firstly, we shall consider that, as outlined in Section 5.2, an amount of C1 degraded during the deposition process, breaking the unstable imine bond to form C2. This would mean that the initial monolayer consisted of a combination of C1 and C2. If this were indeed the case, C7 would only react with the molecules that had not degraded, resulting in unreacted aminothiophenol molecules. As 3-aminothiophenol, or C2, reacts with Au via both the sulfur and nitrogen, the presence of SH can be attributed to the presence of C2 bound to Au via the amine functional group. A summary of the possible binding combinations present in S8_a have been presented in Figure 5.38.

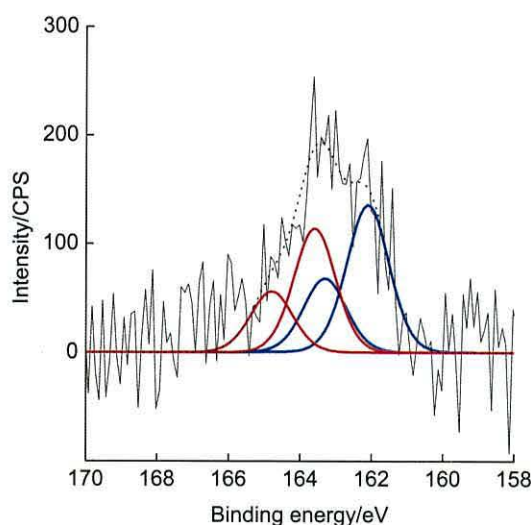


Figure 5.37: S 2p spectra of S8_a taken at 0° (vertical) with blue lines denoting the modelled peaks identifying the presence of an Au-S bond and red lines the presence of -SH.

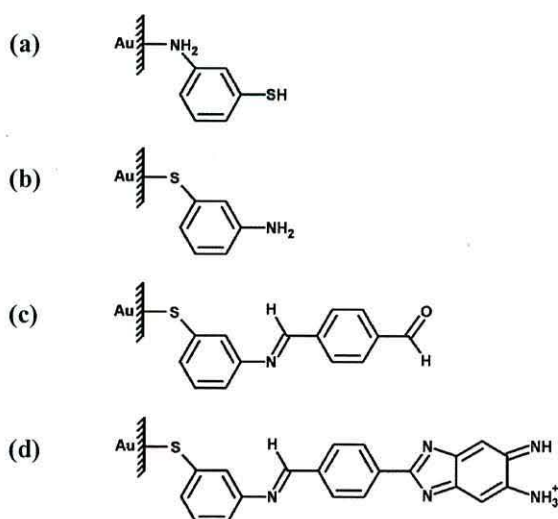


Figure 5.38: (a) C2 bound to the Au surface via the amine group, (b) C2 bound to the Au surface via the sulfur group, (c) C1 bound to the Au surface via sulfur group and (d) C1 bound to the Au surface via the sulfur group and subsequently reacted with C7.

The N 1s spectra of S8_a taken from an angle of 0° (vertical) displayed a main peak at 399.6 eV and a higher energy shoulder at 402.1 eV (Figure 5.39 (a)). The lower energy value is assigned to a C=N or Au-NH₂ environment, and the higher energy value to the protonated amine form. This value is comparable with literature assignments for protonated aminophenyl groups (402 eV),²⁰³ protonated nitrogen species in SiW₁₂O₄₀⁴⁻/4-aminophenyl films (401.9 eV)²⁰⁴ and the ammonium group in L-Tyrosine (402.2 eV).²⁰⁵ This can be compared with the

spectra obtained at 80° (Figure 5.39 (b)) whereby the peak ratio, in this case at 399.6 and 401.9 eV, changed from 86:14 to 52:48. This increase in NH_3^+ concentration is expected as the grazing angle enhances the signal from surface species relative to bulk species, and so we would expect the higher energy peak to increase in concentration from the previous spectra.

As the complete formation of S8_a was under question, further analysis was carried out to compare the ratio of nitrogen to sulfur species. The ratio can be seen to change from 74:26 to 83:17 as the angle changes from 0° to 80°. The decrease in sulfur concentration was expected, as the grazing angle became more surface sensitive. We can relate these relative intensities to the theoretical N to S ratio for each possible bonding combination, which ranges from 1:1 for C2 and C1 bound to Au, to 5:1 for the complete wire. At 0°, the ratio was 2.9:1, which supports the suggestion that S8_a is composed of a combination of molecules assembled onto the Au surface.

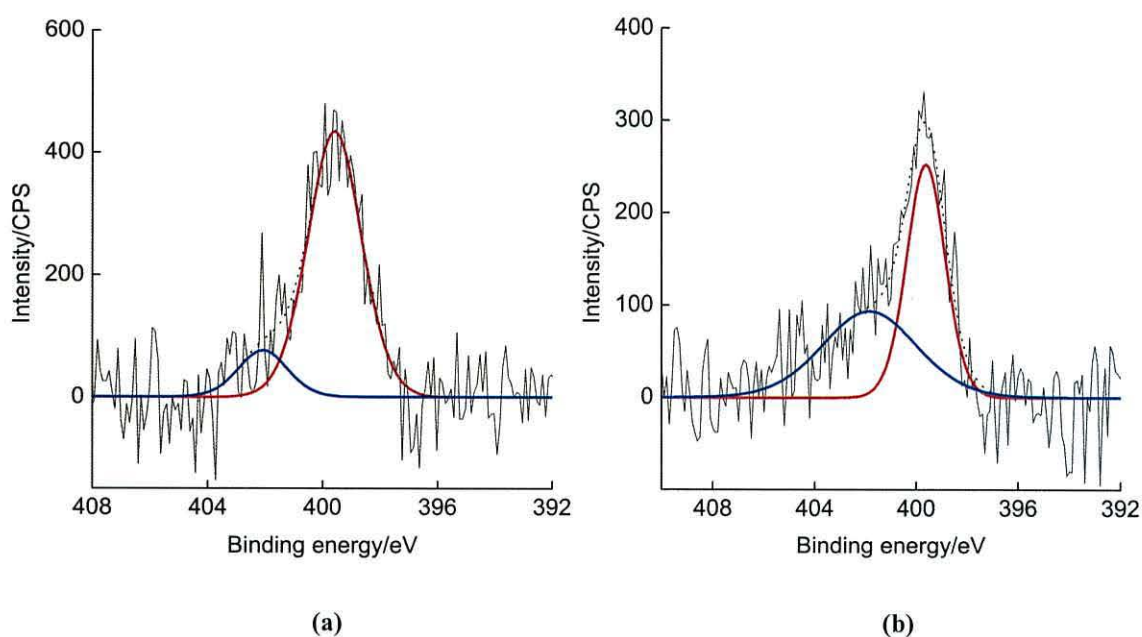


Figure 5.39: Modelled N 1s spectra taken at (a) 0° and (b) 80° show an increase in the higher energy shoulder ~ 402 eV with increased grazing angle.

5.8.3 ELECTRICAL CHARACTERISATION: I - V

For clarity, a summary of the I - V results obtained for S8_a-S10_a have been presented in Table 5.7. For each plot, the forward and reverse sweeps have been averaged.

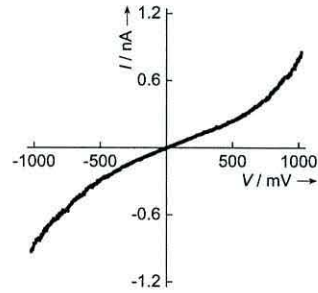
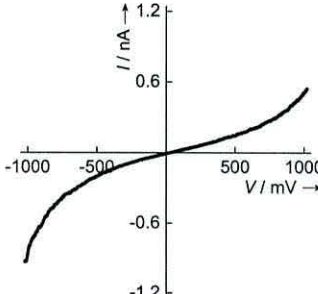
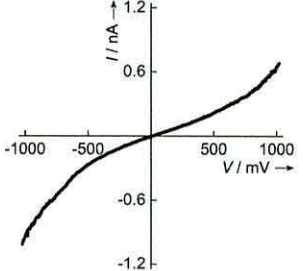
System	No. C7 units	Length/nm	Rectification $\langle RR \rangle$ at ± 1 V	I - V characteristics
S8 _a	1	1.8	1.4	
S9 _a	2	3.1	1.8	
S10 _a	3	4.4	1.5	

Table 5.7: A summary of S8_a-S10_a with respect to their electrical properties.

The addition of the first electron donating C7 unit to S1 resulted in a wire approximately 1.8 nm in length. The electron donating nature of the wire gave rise to symmetrical I - V properties with an $\langle RR \rangle$ of 1.4 at ± 1 V. This suggests that S8_a exhibits little to no preference in the direction of current flow through the wire. As the wire is comprised of two donating units *i.e.* electrode | D- π -bridge-D | electrode, this is to be expected. The I - V plots for S9_a and S10_a can

also be seen to exhibit symmetrical curves with an $\langle RR \rangle$ of 1.8 and 1.5 at ± 1 V respectively. There is very little difference in the average rectification values for each wire. This is owing to the overall electron donating nature of the wire dominating electron flow through the system, allowing current to flow equally in both directions.

5.8.4 SUMMARY

The assembly and subsequent characterisation of S8_a-S10_a has proved to be more complicated than that of S3_a-S5_a. Section 5.8 has attempted to demonstrate the predicted coupling of a single aldehyde to two amine functionalities, resulting in average areas per molecule of 0.214 ± 0.010 , 0.270 ± 0.007 and 0.230 ± 0.003 nm² for the assembly of one to three C7 units. Due to problematic C4 deposition, confidence in the Sauerbrey analysis is not as high as it could be and in such a case XPS characterisation is imperative. Such an examination revealed the presence of not only C1 as an anchoring molecule, but also C2, which, as established in Section 5.2, can bind to the gold surface via either of its two substituents, thus impairing the successful assembly of S8_a. Replacing the electron accepting C3 unit of systems S3_a-S5_a with that of electron donating C7, resulted in symmetrical *I-V* features, with the $\langle RR \rangle$ ranging from 1.4 to 1.8 at ± 1 V for the three wires. Again, these must be treated with some caution as the XPS results were not conclusive.

5.9 FORMATION OF S11

An analogue of C1, 4-{(E)-1,3-dihydro-2H-benzimidazol-2-thione-5-yl}imino]methyl} benzaldehyde, or C8, has been self-assembled onto gold in order to investigate its suitability as an initial anchoring group in the synthesis of a multi-component wire. C8 is composed of an aromatic backbone with a terminating aldehyde group at one end and a thiol group at the other. Literature reports suggest C8 may assemble on gold surfaces via either a neutral or cationic form,¹⁹² with the aldehyde providing a point for amine-terminated compounds to react in order to elongate the wire.

5.9.1 PHYSICAL CHARACTERISATION: QCM

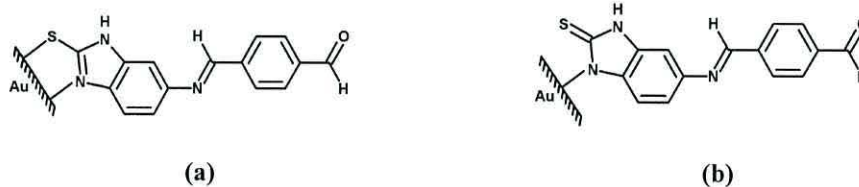


Figure 5.40: C8 self-assembled onto an Au substrate via an (a) Au-N and Au-S linkage or (b) an Au-N linkage to form S11.

A gold quartz crystal was dipped into a C8-containing solution in 10 minute increments for a total of between 70 and 170 minutes. Once the frequency was judged to be stable over several depositions a Sauerbrey analysis was carried out to reveal a typical area per molecule of $0.257 \pm 0.013 \text{ nm}^2$ (Figure 5.41). This suggests the assembly of S11 results in a closely packed monolayer, and can be compared to the cross sectional area of benzene in an end-on arrangement of *ca.* 0.25 nm^2 .

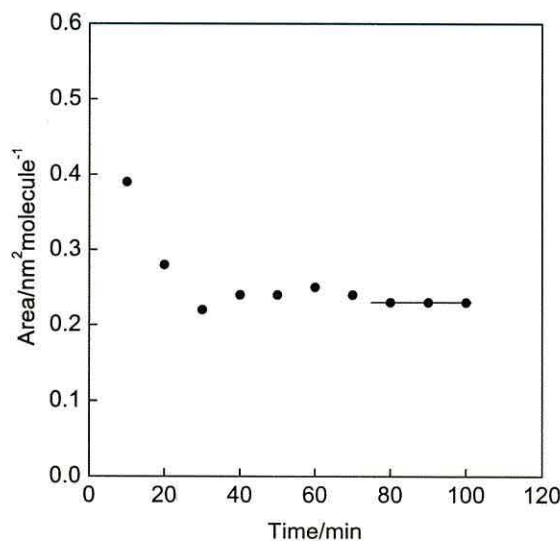


Figure 5.41: Typical QCM results for the deposition of C8 onto an Au-coated substrate to form S11.

5.10 FORMATION OF S12_A-S13_A

Following the initial deposition of C8 to form the monolayer S11, an electron accepting C3 unit was assembled via a condensation reaction to form the bilayer system, S12_a.

5.10.1 PHYSICAL CHARACTERISATION: QCM

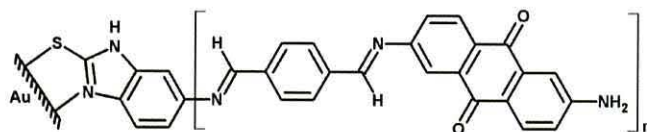


Figure 5.42: The formation of S12_a-13a consisting of between 1 and 2 repeating C3 units.

The second component, C3, was deposited on top of S11 in two-hourly immersions for a maximum of *ca.* 15 hours to form S12_a (Figure 5.42). As observed previously, the deposition time for C3 was much longer than that of the initial monolayer, owing to the bulky nature of the compound and slow imino bond formation. The subsequent Sauerbrey analysis revealed the average area occupied by a single molecule similar to that of the previous layer, at around $0.207 \pm 0.010 \text{ nm}^2$, (Figure 5.43 (a)). This suggests that the wire's components deposited in a 1:1 ratio. S12_a can also be extended using a C4 and a second C3 unit to form S13_a, a four-component system that mirrors that of S4_a. Calculated areas for the final two layers were 0.213 ± 0.006 (Figure 5.43 (b)) and $0.268 \pm 0.008 \text{ nm}^2 \text{ molecule}^{-1}$ (Figure 5.43 (c)) after a total of 760 and 1050 minutes respectively. These results can be combined (Figure 5.43 (d)) to show a linear relationship in the deposition of all four layers, providing evidence that each unit is assembling in an approximately 1:1 ratio. Confirmation of the two initial assembly steps has been provided by XPS in the literature,¹⁹² indicating the successful formation of S12_a on Au(111).

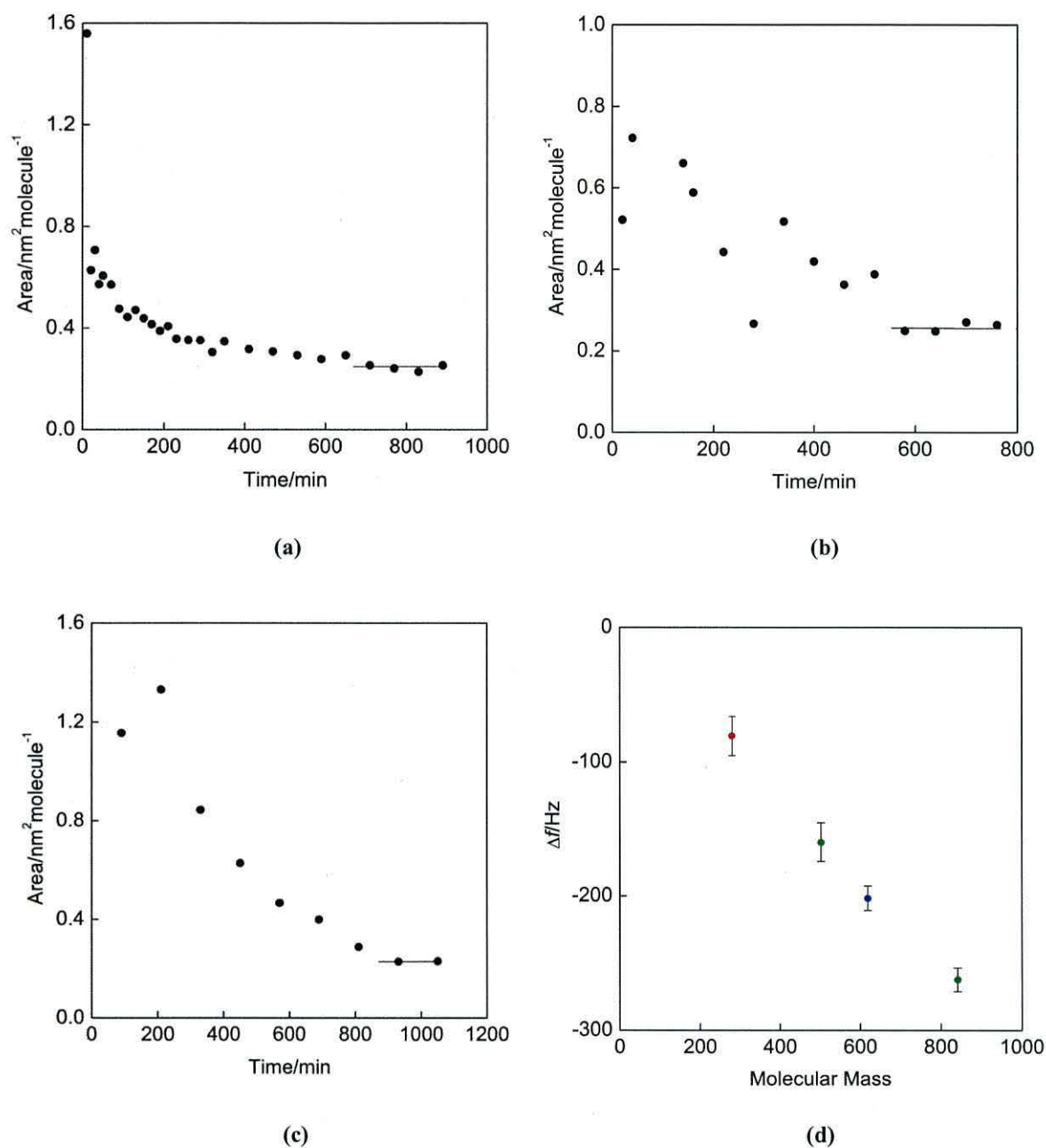


Figure 5.43: Typical QCM results for the deposition of (a) C3 onto S11 to form S12_a, (b) C4 onto S12_a and (c) a second C3 unit to form S13_a. (d) shows the total change in frequency from the clean (starting) value measured against the molecular mass of each constituent layer. Red corresponds to the initial anchoring layer, S11, green to that of C3 and blue to C4.

5.11 FORMATION OF S14

Thus far, the majority of self-assembled systems under investigation have almost exclusively involved the anchoring of an initial monolayer via a reactive thiol headgroup. Whilst the covalent Au-S bond is beneficial to the formation of SAMs, the number of possible bonding geometries have resulted in fluctuating conductance traces in a number of studies. In contrast, parallel investigations involving an anchoring amine functionality have resulted in reports of improved definition and reliability.^{206,207} This can be attributed to the contact resistance between respective headgroups and the Au electrode, which is greater for Au-S than for Au-NH₂.²⁰¹ The resistance is dependent on electronic coupling efficiency between the headgroup and electrode, of which amines rather than thiols exhibit improved alignment between the Fermi level of Au and its own molecular orbitals. It is for this reason that increasing interest is being shown in SAMs formed via an Au-NH₂ linkage, and why the assembly of C7, a molecule substituted with only -NH₂ groups is studied in this Section (Figure 5.44). The suitability of C7 as an alternative anchoring molecule is two-fold; the molecule can bind to Au with one or more -NH₂ groups, and extension of the wire is possible with the introduction of an aldehyde-terminated compound, such as C4.

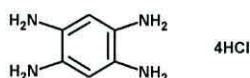


Figure 5.44: C7 acts as an anchoring layer on Au.

5.11.1 PHYSICAL CHARACTERISATION: QCM

C7 was deposited on a gold-coated quartz crystal from solution in 5 minute immersions for a total of between 70 and 140 minutes. The deposition was judged to be complete at an area per molecule of *ca.* $0.132 \pm 0.005 \text{ nm}^2$. Although this value initially appeared low, repetitions revealed similar areas of 0.117 ± 0.003 and $0.137 \pm 0.0002 \text{ nm}^2 \text{ molecule}^{-1}$ (Figure 5.45). It should also be noted that all area calculations are inclusive of 2 HCl moieties.

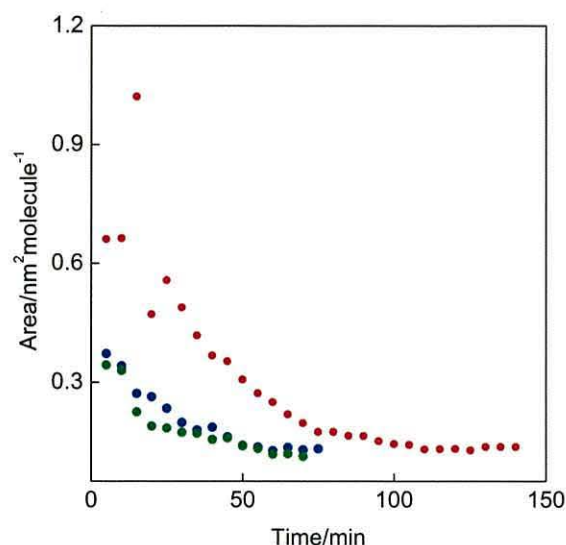


Figure 5.45: Typical QCM results for the deposition of C7 on to an Au-coated substrate to form S14. Red, blue and green circles denote separate depositions of C7.

5.11.2 PHYSICAL CHARACTERISATION: XPS

A sample of S14 was prepared by immersing an Au coated HOPG substrate in a solution of C7 every 5 minutes for a total of 125 minutes. C7 can be expected to bind to gold with either a single or pair of nitrogen atoms. This may be via the nitrogen lone pair or by the formation of a covalent bond between the deprotonated nitrogen and gold. Of particular interest is the high resolution scan of the N 1s spectrum. This gives an indication of the number of bonding nitrogen atoms per molecule. There is clearly a peak within the range of 398-401 eV. However, deconvolution of the asymmetrical curve yields a range of results (Table 5.8), each of which shall be analysed and discussed separately.

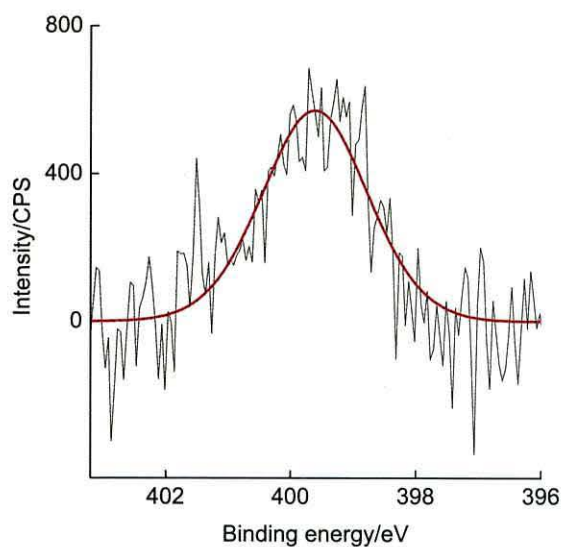
Analysis	N 1s BE / eV	Proportion of element / %	Inference
1	399.6	100	-NH ₂
2 (a)	399.2 400.0	50 50	Au-N NH ₂
2 (b)	399.3 400.4	57 43	Au-N -NH ₂
3	399.1 399.9	30 70	Au-N -NH ₂

4	399.4 401.1	44 56	Au-N -NH ₃ ⁺
---	----------------	----------	---------------------------------------

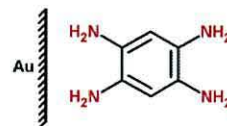
Table 5.8: Summary of the possible N 1s binding configurations of S14.

ANALYSIS 1 AND 2: PHYSISORPTION AND BONDING VIA TWO AMINE SUBSTITUENTS

The simplest analysis of the N 1s spectrum (Figure 5.46 (a)) yields a single broad, symmetrical peak centred at 399.6 eV upon deconvolution. This value lies slightly closer to the typical value of an unbound, primary -NH₂ presence (~400 eV), rather than that of a bound Au-N (~399 eV). The lower energy value has also been seen in Section 5.2, with the attachment of C2 to gold via the nitrogen. However, this does not provide any information on the actual bonding mechanism. Thus, we can speculate that C7 is not chemically bound to the Au surface, but is instead weakly physisorbed, at an unknown orientation. However, as the binding energy of the symmetrical peak falls roughly between the afore-mentioned values, it is possible that the main peak at 399.6 eV arises from twin peaks of similar intensity at ~399 and 400 eV. In order to consider this possibility, the symmetrical peak was further deconvoluted into two smaller peaks, of which the areas and peak widths were constrained to be approximately equal. This gave rise to binding energy values of 399.2 eV (Au-N) and 400.0 eV (-NH₂), at a ratio of 50:50 (Figure 5.47 (a)). At this ratio, we can deduct that C7 is weakly adsorbed to the Au surface via the lone electron pairs of two nitrogen groups (Figure 5.47 (c)). Using the constrained model as a guide, the main peak can be deconvoluted into two unconstrained peaks at 399.3 and 400.4 eV at a ratio of 57:43 (Figure 5.47 (b)). This corresponds approximately to the model whereby two nitrogen moieties are bound to the Au surface, with the residual two remaining unbound.

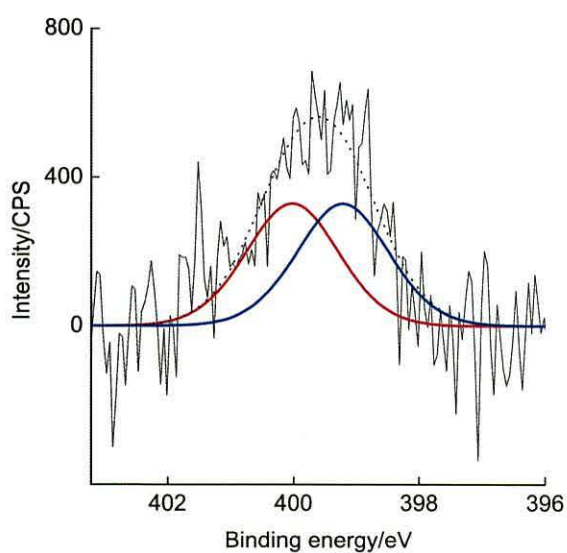


(a)

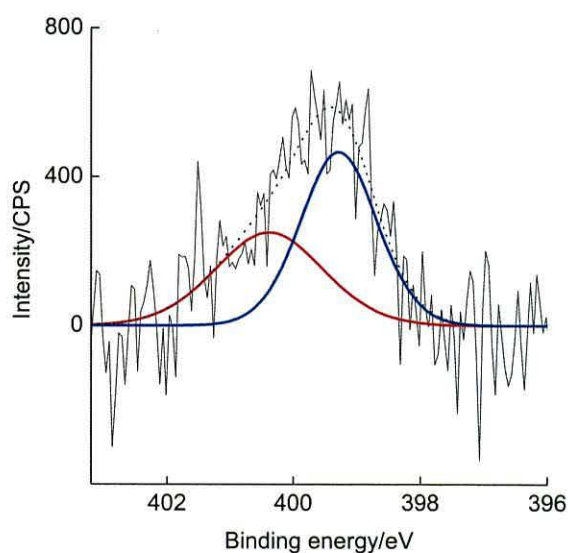


(b)

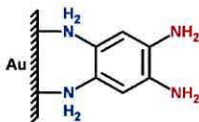
Figure 5.46: (a) The N 1s spectrum of S14 and (b) the corresponding structure with red donating the physisorbed amine form. Note counterions have not been included for clarity.



(a)



(b)



(c)

Figure 5.47: (a) The constrained N 1s spectrum of S14, (b) the unconstrained N 1s spectrum of S14 and (c) the corresponding structure with red donating the unbound amine form and blue donating the bound amine form. Note counterions have not been included for clarity.

ANALYSIS 3: BONDING VIA ONE AMINE SUBSTITUENT

The calibrated N 1s spectrum (Figure 5.48(a)) yields two component peaks upon deconvolution, the larger of which (70% concentration) occurred at 399.9 eV, and the smaller of which (30% concentration) occurred at 399.1 eV. The presence and area of the peak at 399.9 eV indicates the majority of analysed nitrogen atoms belong to an unbound NH_2 moiety, with 30% belonging to a bound nitrogen. If we are to consider this 30:70 ratio in terms of the four nitrogen moieties present in the C7 molecule, we can speculate that approximately one in every four (25:75 as opposed to 30:70) nitrogen atoms are attached to the gold surface (Figure 5.48 (b)).

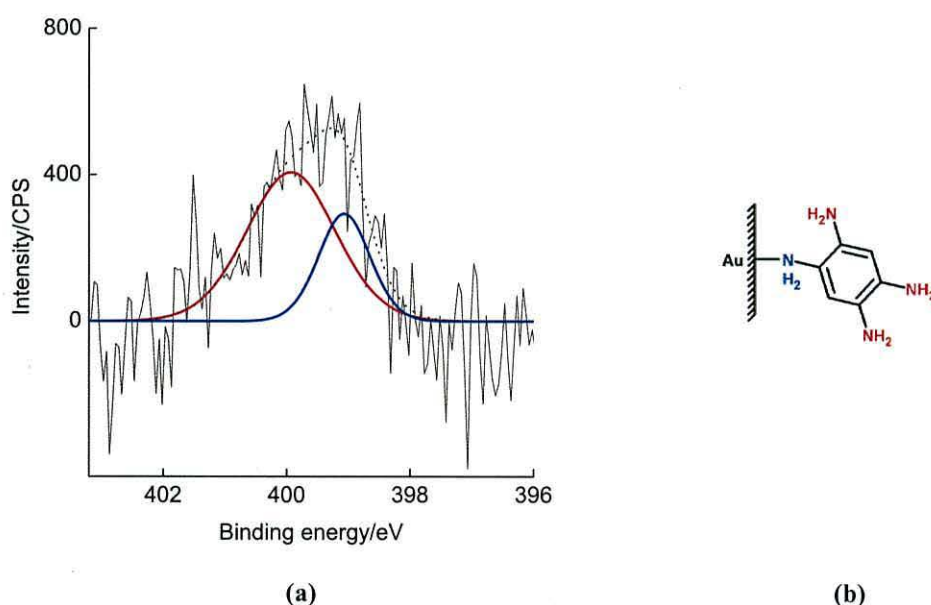


Figure 5.48: (a) The N 1s spectrum of S14 and (b) the corresponding structure with red denoting the unbound amine form and blue denoting the bound amine form. Note counterions have not been included for clarity.

ANALYSIS 4: BONDING VIA TWO AMINE SUBSTITUENTS WITH TWO ADDITIONAL PROTONATED AMINES

The final analysis of the N 1s spectrum involves a wider region of data than used previously. This creates a shift in the higher energy shoulder from ~400 eV to 401.1 eV. This is accompanied by a lower energy peak at 399.4 eV. A comparison of the peak areas shows 56% of the nitrogen occurring at a binding energy of 401.1 eV, and the remaining 44% at 399.4 eV

(Figure 5.49 (a)). The peak at 399.4 eV is indicative of a bound nitrogen (Au-N), the ratio of which advocates approximately two nitrogen atoms binding to the Au surface (Figure 5.49 (b)). Literature suggests that the broader peak at 401.1 eV is due to the presence of a protonated amine group ($-\text{NH}_3^+$),¹⁸⁸ of which there are approximately two. These protonated amines may be formed by the reaction of an amine with a dissociated hydrogen ion from either HCl or H₂O. It is possible that either of these compounds could be present to cause the protonation, as HCl is present in C7, and H₂O present in the atmosphere.

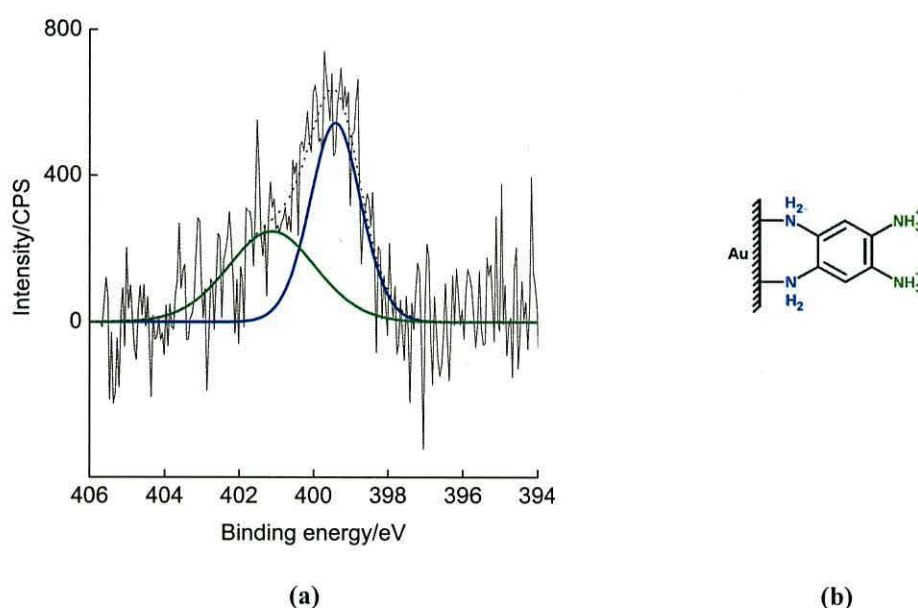


Figure 5.49: (a) The modelled N 1s spectrum of S14 and (b) the corresponding structure with green donating the protonated amine form and blue donating the bound amine form. Note counterions have not been included for clarity.

5.11.3 SUMMARY

An investigation into the assembly characteristics of C7 on Au(111) has revealed an apparently disordered state, as evidenced by the relatively low area per molecule (0.117-0.137 nm²). Although approximately half of the expected value, the reproducibility of the systems suggests that assembly is occurring in a similar way each time. Upon XPS analysis, a broad peak between 398 and 401 eV is evidenced in the N 1s domain. Deconvolution of this peak cannot be conclusively ascribed to any one binding mode. Instead, four possible bonding configurations have been investigated. The first mode involves a single, broad peak centred at 399.6 eV, indicating physisorption of C7 to the Au surface. Constraint of this region into two

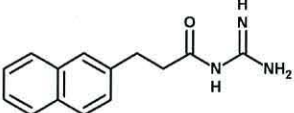
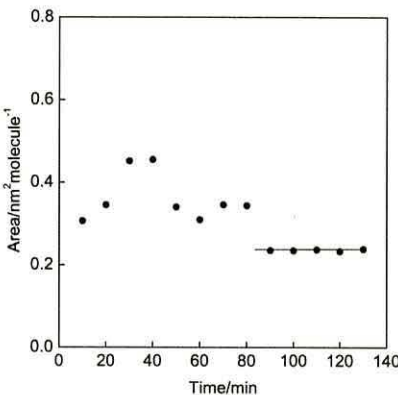
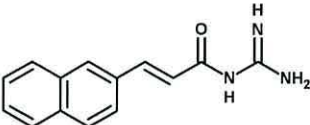
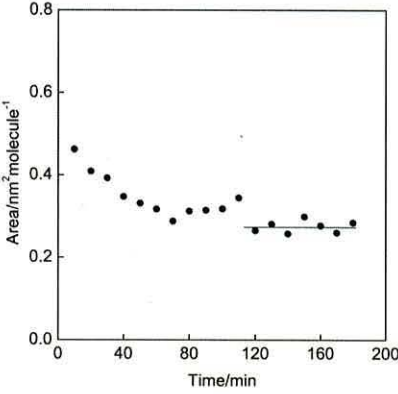
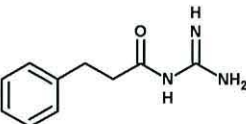
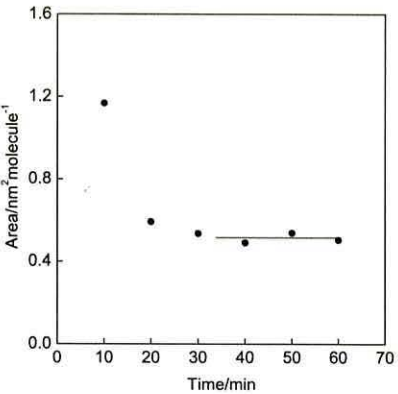
separate peaks reveals binding energies centred at 399.2 (57%) and 400.0 eV (43), indicating bonding between two of the four -NH_2 groups and the Au surface. A third analysis reveals two peaks centred at 399.9 (70%) and 399.1 eV (30%), which implies metal-molecule bonding is occurring through only one of the four available -NH_2 moieties. The fourth possibility also involves deconvolution into two peaks, with binding energies centred at 401.1 eV (56%) and 399.4 eV (44%). Again, bonding is alleged to occur through two -NH_2 groups, with the remaining two becoming protonated. XPS analysis, coupled with a Sauerbrey study points to the presence of different bonding geometries, inclusive of multilayer formation and physisorption. The resultant disordered system determines its unsuitability as an anchoring layer in SAM formation.

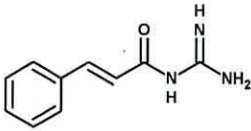
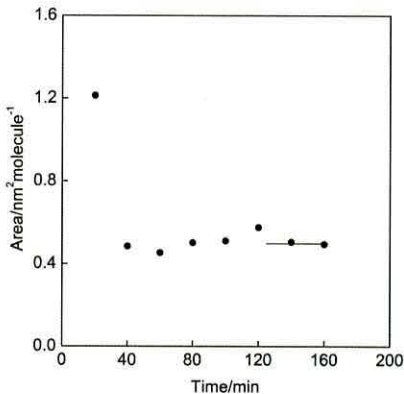
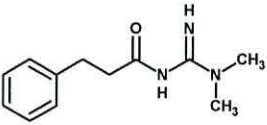
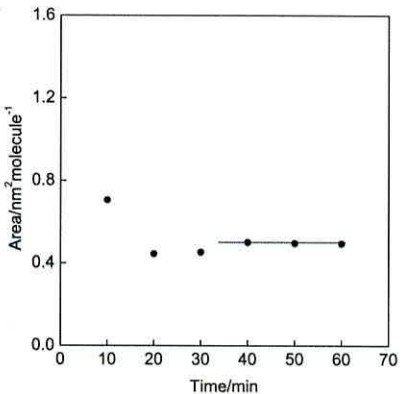
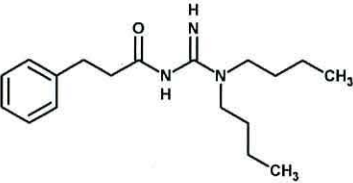
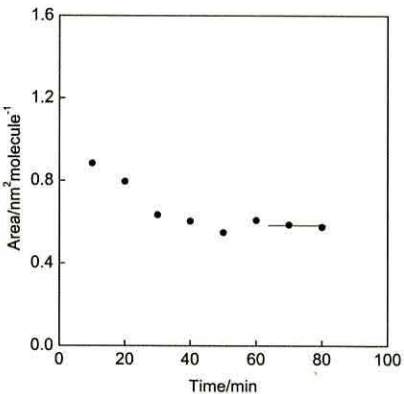
5.12 ASSEMBLY CHARACTERISTICS OF C9-C15

Guanidine-containing compounds are attracting an increasing amount of attention, resulting in numerous biological applications, including anti-HIV drugs²⁰⁸ and anti-cholinesterase inhibitors.²⁰⁹ The routine use of such compounds at biological interfaces is due to the selective ability of guanidinium cations to recognise receptors such as phosphates and carboxylates by hydrogen bonding, electrostatic and π -stacking interactions.²¹⁰ In this way, monolayers of guanidine-containing molecules have been shown to immobilise complementary molecules at the air-water interface, effectively creating a 2D repeating pattern. C9-C15 are structurally similar, with each compound containing a guanidine functional group, and varying degrees of aromaticity. These related compounds have been studied with regards to their self-assembly properties on gold.

5.12.1 PHYSICAL CHARACTERISATION: QCM

Each compound was deposited on a gold-coated quartz crystal in 10 or 20 minute increments. The crystals were then removed from solution, washed and allowed to dry before a frequency measurement was taken. The time taken for a stable frequency to be reached varied from a total of 60 to 180 minutes. For clarity, a summary of the QCM analysis results obtained for C9-C15 have been presented in Table 5.9.

COMPOUND	STRUCTURE	SAUERBREY ANALYSIS
C9		
Area: $0.236 \pm 0.002 \text{ nm}^2 \text{ molecule}^{-1}$		
C10		
Area: $0.275 \pm 0.021 \text{ nm}^2 \text{ molecule}^{-1}$		
C11		
Area: $0.511 \pm 0.024 \text{ nm}^2 \text{ molecule}^{-1}$		

C12		
Area: $0.500 \pm 0.006 \text{ nm}^2 \text{ molecule}^{-1}$		
C13		
Area: $0.498 \pm 0.003 \text{ nm}^2 \text{ molecule}^{-1}$		
C14		
Area: $0.581 \pm 0.006 \text{ nm}^2 \text{ molecule}^{-1}$		

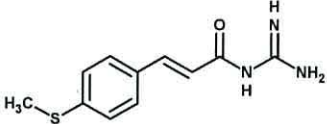
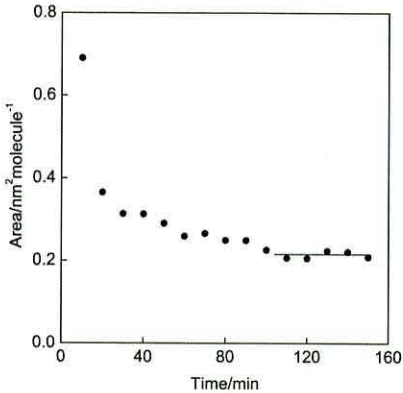
C15		
	Area: $0.213 \pm 0.009 \text{ nm}^2 \text{ molecule}^{-1}$	

Table 5.9: Sauerbrey results for the deposition of C9-C15 onto an Au(111) surface.

C9 and C10 exhibited similar areas of 0.236 ± 0.002 and $0.275 \pm 0.021 \text{ nm}^2 \text{ molecule}^{-1}$ respectively. As these compounds are almost identical, the similarity is not unexpected. C11 and C12, however, displayed areas of 0.511 and $0.500 \text{ nm}^2 \text{ molecule}^{-1}$ respectively. As expected, these structures are also closely related. From Table 5.9, we can see that C9 and C10 consist of the same structures as C11 and C12, except for the presence of a terminating naphthalene group in place of a single benzene unit. Therefore, we can consider the apparent difference in packing geometries with respect to (i) molecule-molecule, (ii) molecule-substrate and (iii) headgroup-substrate interactions within the SAM. The balance between these competing reactions greatly affects the resultant thin film structure.²¹¹⁻²¹⁴ An example outlining the importance of these competing interactions is that of alkanethiol SAM packing geometries on Au (111), as reported by Barenna *et al.*²¹⁵ They demonstrated that an increase in alkyl chain length resulted in dominant intermolecular van der Waals interactions within the system. Consequently, SAMs of these molecules formed a close-packed, upright monolayer. In contrast, shorter molecules comprising around ten carbon atoms favoured a tilted geometry (50° with respect to the Au surface) due to contributions from the molecule-substrate interaction.

Firstly, the intermolecular π -bonding between neighbouring aromatic systems shall be considered. A comparison of theoretically calculated interaction energies between face-to-face oriented benzene-benzene and naphthalene-naphthalene molecules reveals energies estimated at $1.3\text{-}3.4 \text{ kcal mol}^{-1}$ and $3.8\text{-}7.5 \text{ kcal mol}^{-1}$, respectively.^{216,217} This indicates that

for the naphthalene-containing molecules, C9 and C10, intermolecular interactions due to π - π bonding dominate over the molecule-substrate interactions. This allows the molecules to form an upright, densely-packed monolayer, and hence exhibit a lower area per molecule.

As the inter-molecule interaction is less significant in C11 and C12, it is possible that the molecule-substrate interaction has more of an effect. Indeed, Oteyza *et al.*²¹⁸ expressed the belief that as molecule-molecule interactions weaken, the molecule-substrate interactions become more prominent. This would result in a large number of molecules lying parallel to the metal surface rather than upright, with increased bonding interactions between the aromatic system and surface, which would in turn hinder the successful self-assembly of a homogenous monolayer. From this, we can conclude that the self-assembly of C11 and C12 results in a system with a large amount of disorder, in which some molecules lie parallel to the Au surface, rather than perpendicular. Thus, the area per molecule for C11 and C12 is calculated as twice that of C9 and C10.

The structure of C13 is identical to that of C11, with the exception of two methyl groups on the terminating amine moiety. The self-assembly of this compound results in a final area per molecule of $0.498 \pm 0.003 \text{ nm}^2$, similar to that of C11 and C12. This indicates an arrangement whereby the molecule is lying parallel to the Au surface. Furthermore, reports suggest that dimethylamino groups, often used in capping gold nanoparticles, are capable of bonding to gold surfaces via the nitrogen lone pair.²¹⁹ Therefore, C13 is expected to bond via both the lone pair as well as the π -orbitals of the aromatic ring.

C14 exhibits the greatest area per molecule of the series of $0.581 \pm 0.006 \text{ nm}^2$ at surface saturation. Again, this molecule consists of only one aromatic ring, which suggests a geometry whereby the molecule is lying parallel to the surface. The added presence of two branching butyl chains on the terminating amine group would also be expected to have an effect on the area, causing it to increase.

C15, unlike C9-14, contains a sulfur functional group substituted onto the aromatic ring, as well as a terminating guanidine moiety. Although C15 consists of a single benzene ring, it does not result in a similar molecular area as the corresponding C11 and C12 molecules. Instead, an area of $0.213 \text{ nm}^2 \text{ molecule}^{-1}$ was achieved after a series of fifteen depositions. Once again, this can be attributed to the molecule-substrate interactions between the reacting

headgroup and gold surface. Unlike the afore-mentioned C11 and C12 molecules, C15 is likely to bind to the surface via the sulfur rather than the nitrogen, due to the higher binding energy of the Au-S (40-45 kcal mol⁻¹) to Au-NH₂ (9-18 kcal mol⁻¹) bond. Thus, C11-14 would be expected to bind to the gold surface via one or more nitrogen lone pairs. It is well known that molecules containing a functional group with a large surface affinity often adopt upright configurations.^{214, 220, 221} This allows C15 to condense into a well packed monolayer, and hence the area of 0.213 ± 0.009 nm² molecule⁻¹, which corresponds approximately to the cross-sectional area of benzene (*ca.* 0.25 nm² molecule⁻¹) in an end-on arrangement. Although the value obtained is slightly lower than this value, it can be explained by the presence of any remaining solvent, unremoved physisorbed material, or undesirable contaminants.

5.12.2 PHYSICAL CHARACTERISATION: XPS

Samples of C10-C15 were prepared for XPS on gold-coated HOPG under duplicate conditions for those monitored using a Sauerbrey analysis. Due to an extended period of time between sample preparation and XPS analysis, all subsequent findings must be viewed with a certain amount of caution. Whilst there is no doubt that a peak is distinguishable from background noise in the N 1s domain, it is broad and poorly defined, with an approximate range of 7 eV between 398 and 405 eV. Therefore, although the results confirm the presence of nitrogen-containing compounds, we cannot conclusively infer the individual nitrogen environments. Whilst the XPS results are inconclusive, QCM studies have confirmed adsorption, and from previous studies we can proposed adsorption via a gold-amine bond for the majority of compounds as identified in other nitrogen-containing compounds.

5.13 FORMATION OF S15-S17

Section 5.13 describes the formation of system S17 on TiO₂ via a three step process. The initial step involved the addition of a suitably reactive anchoring group to the TiO₂ substrate to form S15. Secondly, a single C4 unit was assembled onto S15 from solution in order to form S16 through the chemical coupling of terminating amine and aldehyde groups. This was followed by the assembly of an electron accepting C3 molecule, via the same condensation reaction as the previous step, to form S17, which measures *ca.* 2.4 nm in length. Confirmation of each step was provided by QCM, with additional XPS analysis of S15. This study has also been repeated on TiO₂ nanoparticles, with analysis using IR Spectroscopy. As well as

constructing systems S15 to S17, the particulate-based wire was extended over a further three steps to create a structure mirroring that of S4_b on gold.

5.13.1 FORMATION OF S15

The ability of organic functional groups such as organosilanes⁸⁹ and carboxylic acids⁹¹ to chemically bond with and modify TiO₂ surfaces has been well documented. Much interest lies in particular with the acid-modified surfaces, and it is for this reason that C16 was chosen as the initial monolayer in the stepwise formation of systems S15 through to S17. Comprising a single aromatic ring with *para*-substituted amine and carboxylic acid groups, C16 is an ideal candidate. The carboxylic acid is able to self-assemble onto the TiO₂ substrate in a variety of possible bonding configurations, as outlined in Section 1, whereas the amine group allows for extension of the wire via the same aldehyde-amine coupling seen throughout.

5.13.2 PHYSICAL CHARACTERISATION: QCM

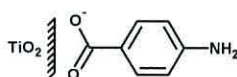


Figure 5.50: C16 self-assembled onto a TiO₂ substrate via a TiO₂-acid linkage to form S15.

S15 was formed by immersing a TiO₂-coated quartz crystal in a solution of C16. By depositing the material of interest on a quartz crystal, we were once again able to monitor the rate of deposition and calculate the total surface coverage of a monolayer. For the deposition of C16, a TiO₂-coated quartz crystal was immersed for between 5 and 20 minutes in solution, washed with ethanol and allowed to dry before having its frequency measured. A typical QCM deposition profile of C16, (Figure 5.51) results in a plateau being reached after 410 minutes at an area of $0.246 \pm 0.002 \text{ nm}^2 \text{ molecule}^{-1}$. This corresponds approximately to the cross-sectional area of a benzene ring, suggesting that C16 assembles on a TiO₂ surface as a closely packed monolayer, S15 (Figure 5.50).

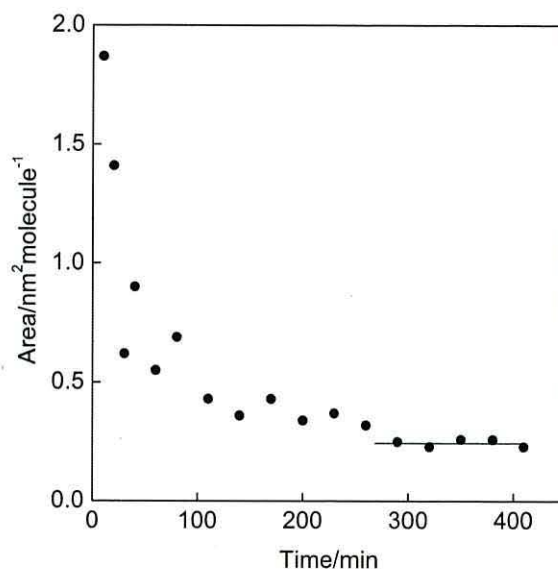


Figure 5.51: Typical QCM results for the deposition of C16 on a TiO₂-coated substrate to form S15.

5.13.3 PHYSICAL CHARACTERISATION: XPS

A sample of S15 was prepared on a TiO₂-coated quartz crystal, and its frequency monitored throughout the deposition process. Once a satisfactory number of depositions confirmed that the frequency had stabilised at a suitable area, the sample was considered ready for XPS analysis.

Analysis of the high resolution N 1s spectra (Figure 5.52) revealed a lone, symmetrical peak at 399.9 eV. This indicated the presence of a single nitrogen environment, the binding energy of which corresponds to an unbound amine (-NH₂) presence. The absence of a peak at 396 eV,²²² corresponding to a Ti-N environment confirms C16 is not bound to the TiO₂ surface via the nitrogen moiety.

The presence of C16 on the surface could be further confirmed by analysis of the C 1s and O 1s spectra. The high resolution scan of the C 1s region revealed a principal peak with a high energy shoulder, as well as a smaller peak discernible at a higher energy. Upon deconvolution, three distinct peaks were established at 284.8 eV (calibration peak), 286.2 eV and 288.4 eV. These are assigned to carbon atoms in aromatic C=C bonds, C-NH₂ and RCOO⁻ respectively, thus confirming the presence of three different carbon environments in S15.

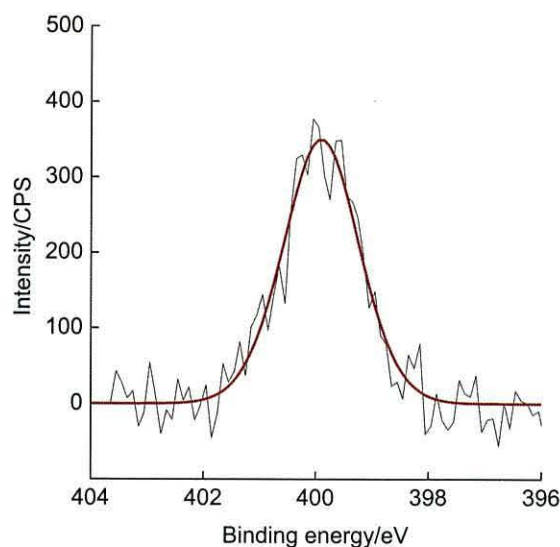


Figure 5.52: The modelled N 1s spectrum of S15.

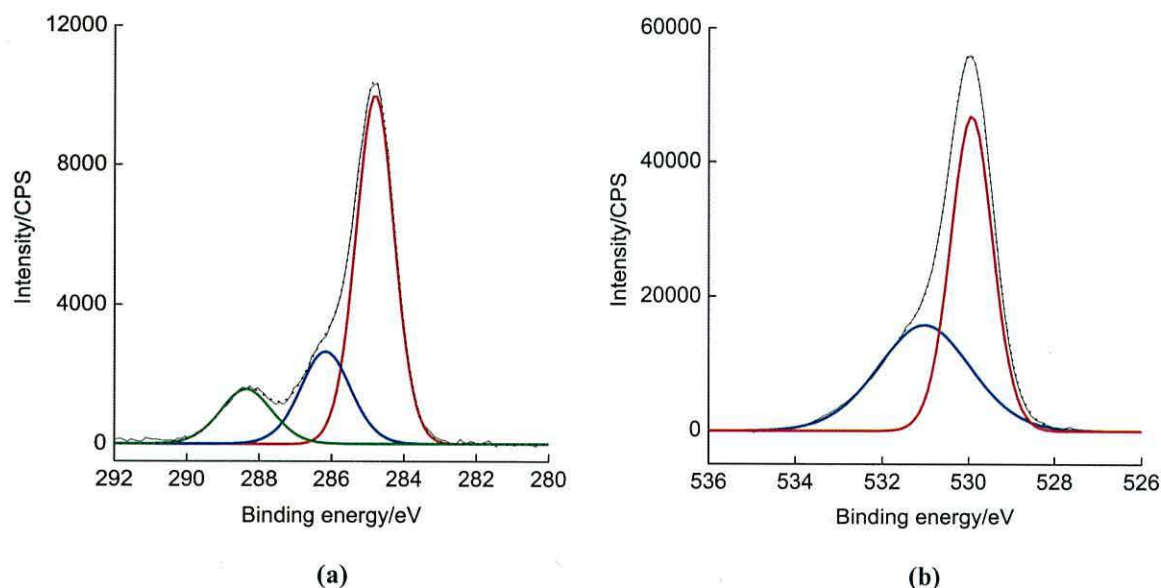


Figure 5.53: (a) High resolution spectra of the C 1s domain denoting three different environments (represented by red, blue and green lines) and (b) high resolution spectra of the O 1s domain denoting two different oxygen environments (red and blue lines).

Analysis of the O 1s domain clearly indicated the presence of a central peak with a high energy shoulder. Upon deconvolution, two peaks centred at 529.9 eV and 531.0 eV were obtained. The lower energy peak matches literature reports of lattice oxygen in the TiO₂ surface,²²³ with the higher energy peak being assigned to a carboxylate environment. The latter value is indicative of both oxygen atoms present on C16 being bound symmetrically to the TiO₂ surface. This can be compared to the C 1s spectra of free C16,¹⁸² which exhibits two peaks at 531.8 eV and 532.2 eV, each corresponding to a single oxygen in the O-C=O moiety.

The absence of a peak centred at 532.2 eV in the spectra of S15 suggests the negative charge on C16 is delocalised across both oxygen atoms, resulting in the single peak at 531.0 eV.

The high resolution scan of the Ti 2p spectrum, (Figure 5.54) was resolved into two well-defined, prominent peaks at 458.5 eV and 464.2 eV. These are typical values for the Ti^{4+} $2p_{3/2}$ and $2p_{1/2}$ states, respectively.²²⁴⁻²²⁶ The energy separation between the two states of 5.68 eV provides further evidence of the presence of Ti^{4+} ,^{227,228} which is found in the TiO_2 chemical environment. For clarity, the expected peak separation for pure Ti-Ti would be slightly higher, at *ca.* 6.15 eV.²²⁹

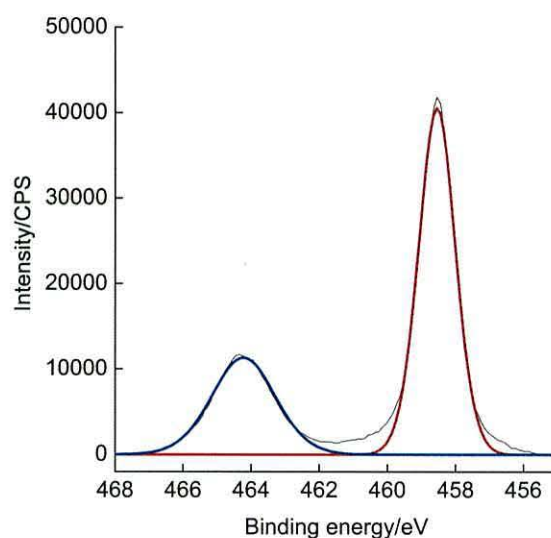


Figure 5.54: High resolution spectra of the Ti 2p domain, with red corresponding to the Ti^{4+} $2p_{3/2}$ state and blue corresponding to the Ti^{4+} $2p_{1/2}$ state.

To confirm C15 was binding to the TiO_2 surface via the acid group, rather than the amine, an angle-resolved XPS study was carried out on the system. This was done by reducing the take-off angle with regards to the surface normal, allowing depth-resolved studies on S15 to monitor the oxygen distribution in the substrate and near-substrate regions at six angles between 0° and 80° . However, the following analysis should be treated with caution as the molecule is small enough that angle resolved studies may not effectively resolve the atomic positioning of elements. In particular, we can compare the total oxygen content, as well as the separate oxygen environments with varying take-off angle. The O 1s data taken at 15° , 45° and 80° has been considered in order to provide a sufficient range of data. Table 5.10 shows a summary of the values obtained in terms of peak binding energy, percentage ratio of each

peak, as well as combined peak areas. It has been established that as the angle increases, the percentage concentration of the two peaks alters. At 15°, the peak at 529.9 eV is clearly of the greatest concentration (59%), whereas it can be observed to decrease to 54% of the total oxygen content at 45° and to 45% at 80°. Thus, as the scan becomes more surface sensitive, the lower energy signal at *ca.* 530 eV becomes less concentrated than the higher energy peak centred at *ca.* 531 eV. This suggests the assignment of chemical environments is indeed appropriate, as the TiO₂ signal would be expected to decrease with increasingly shallow angle, resulting in the greater signal intensity of the carboxylate peak. Further evidence of the decreasing TiO₂ signal with increased angle can be established by investigation of the Ti 2p spectrum, whereby both signals were also seen to decrease in intensity.

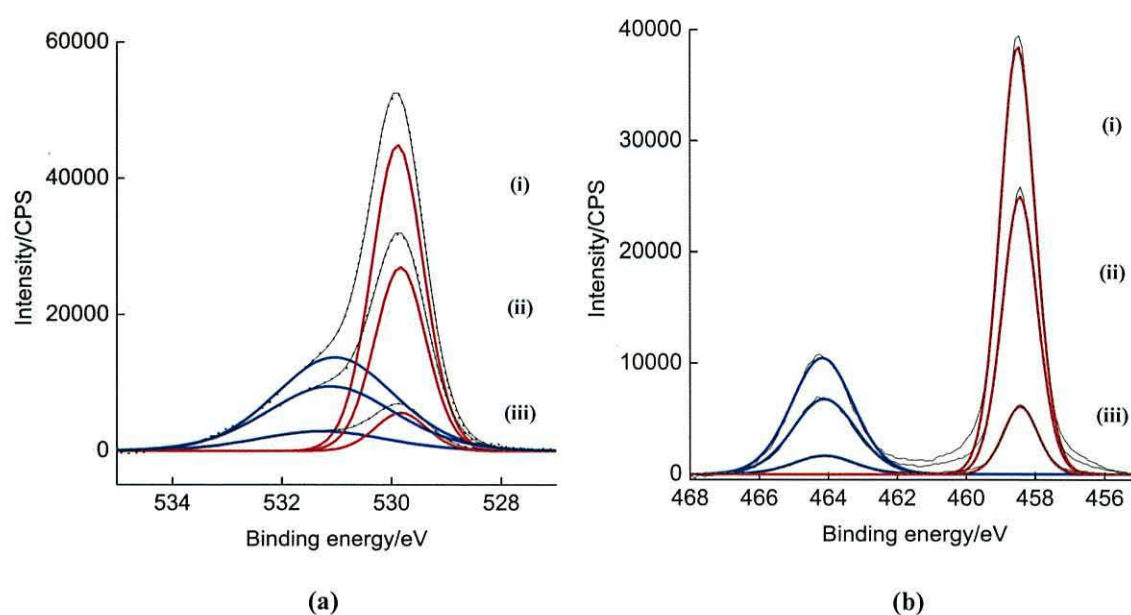


Figure 5.55: An overlay of the (a) O 1s spectra and (b) Ti 2p spectra at (i) 15°, (ii) 45° and (iii) 80°.

Angle	Binding energy/eV	Assignment	Percentage concentration/%	Total area
15°	529.9 531.0	TiO ₂ RCOO ⁻	59 41	91907.2
45°	529.8 531.1	TiO ₂ RCOO ⁻	54 46	60100.6
80°	529.8 531.3	TiO ₂ RCOO ⁻	45 55	15164.2

Table 5.10: Summary of the angle-resolved O 1s results.

However, analysis of the oxygen data by itself may result in an imperfect analysis, as excess oxygen is often present in spectra in which both the substrate surface and assembled molecule should be free of such contamination. Indeed, a comparison of the normalised $\text{NH}_2\text{:RCOO}^-$ peak areas reveals a N:O ratio of 1:44 at 0° , rather than the expected 1:2. It is therefore likely that the signal is caused not only by the carboxylate oxygen, but also that of one or more unidentified contaminants, with possible examples including H_2O , CO and CO_2 . The presence of carbon in the contaminants is a distinct possibility, as the N:C ratio is 1:60, many times higher than the expected ratio of 1:7. Therefore, a similar analysis of the N 1s spectrum was also carried out (Table 5.11).

Angle	Binding energy/eV	Assignment	Total area
15°	399.8	$-\text{NH}_2$	649.9
45°	399.9	$-\text{NH}_2$	539.9
80°	399.8	$-\text{NH}_2$	221.6

Table 5.11: Summary of the angle-resolved N 1s results.

Unexpectedly, the trend in decreasing peak intensity with increasing surface sensitivity seen in the O 1s spectrum was repeated for the N 1s spectrum (Figure 5.57), with areas decreasing from 649.9 at 15° to 543.7 at 45° and finally to 206.3 at 80° . A decreasing intensity may indicate that the layer is disordered with, for example, some molecules physisorbed on the TiO_2 surface and therefore horizontally aligned as well as vertically aligned via chemisorption.

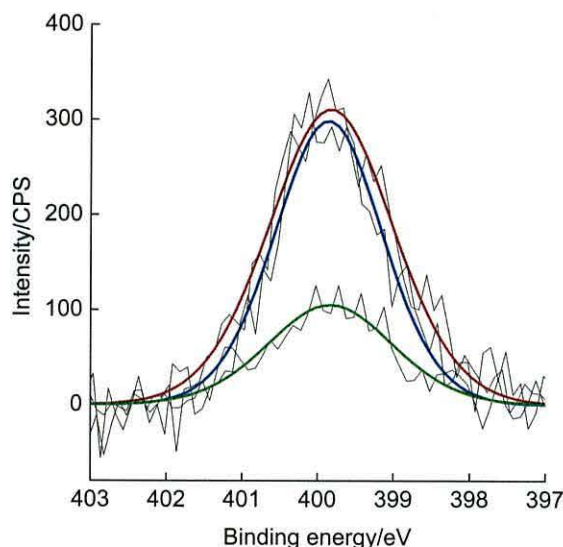


Figure 5.57: An overlay of the modelled N 1s spectra at 15° (red), 45° (blue) and 80° (green).

5.13.4 FORMATION OF S16 AND S17

Following the initial deposition of C16 to form the monolayer S15, a bridging C4 unit was subsequently assembled via the well-known reaction between terminating amine and aldehyde groups to form S16 (Figure 5.58 (a)). This was followed by a C3 molecule (Figure 5.58 (b)), mirroring the extension template seen throughout the majority of systems.

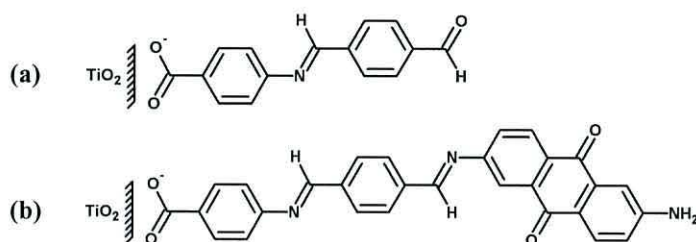


Figure 5.58: (a) S16 formed by the self-assembly of C4 onto S15 and (b) the subsequent formation of S17 by the self-assembly of C3 onto S16.

5.13.5 PHYSICAL CHARACTERISATION: QCM

In order to mimic the assembly of S1, C4 was reacted with S15 to form S16. S15 was dipped in solution in 20 minute depositions for between 140 and 260 minutes (Figure 5.59 (a)). The Sauerbrey analysis revealed a final area of $0.245 \pm 0.020 \text{ nm}^2 \text{ molecule}^{-1}$, which is in good agreement with the area calculated for the initial monolayer ($0.246 \pm 0.002 \text{ nm}^2 \text{ molecule}^{-1}$).

This suggests that the aldehyde moiety on C4 reacted with the terminating amine group on S15 to form a multilayer system in a 1:1 ratio.

S17 was subsequently formed by depositing C3 onto the as-prepared S16 in two-hourly immersions for a maximum of 12 hours to form S17 (Figure 5.59 (b)). As noted previously, the deposition time increased considerably for the successful self-assembly of C3 due to the bulky nature of the compound and slow imino bond formation. A Sauerbrey analysis revealed the average area occupied by a single molecule of C3 to be $0.189 \pm 0.018 \text{ nm}^2 \text{ molecule}^{-1}$. This value was lower than that exhibited by the previous two layers and may have been caused by trapped solvent, as well as any remaining physisorbed material, resulting in a less than ideal value.

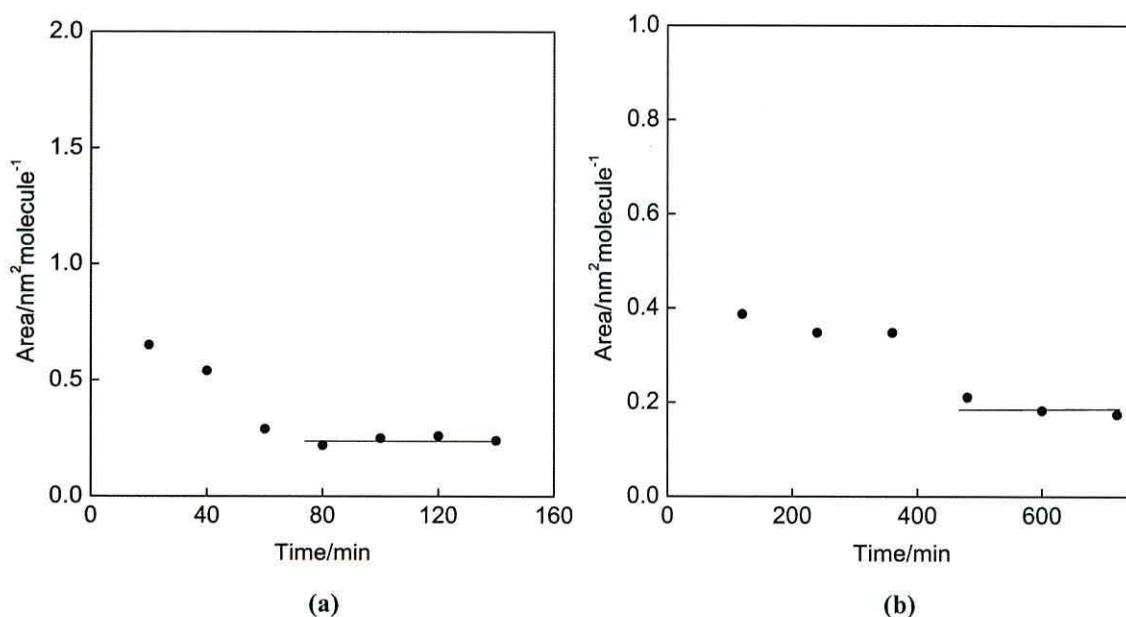


Figure 5.59: Typical QCM results for the deposition of (a) C4 onto S15 and (b) C3 onto S16.

5.13.6 INFRARED SPECTROSCOPY ANALYSIS OF TITANIA NANOPARTICLES

As a complementary technique to XPS analysis with which to confirm the step-by-step coupling predicted in the formation of systems S15-17, TiO₂ nanoparticles were prepared in parallel. Infrared analysis of these nanoparticles provides an insight into the specific resonant frequencies of each functional group present. Such investigations were carried out at each stage of construction, culminating in a system measuring *ca.* 4.9 nm in length comprised of a total of six molecular components (Figure 5.60)

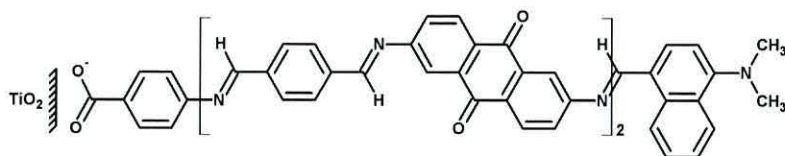


Figure 5.60: S17 was extended by a further three steps, with analysis via FT-IR spectroscopy.

FT-IR samples were prepared in KBr and the resultant spectra normalised to the peak at 3400 cm^{-1} . The FTIR analysis of S15 is in good agreement with that of work published by Rahal *et al.*,¹⁸² with peaks at 3416 (OH), 1626 (OH) 1607, 1540, 1489, 1405 ($\nu_s(\text{COO})$, $\nu_{as}(\text{COO})$, $\nu(\text{C}=\text{C})$), 1304, 1182 ($\nu(\text{C}-\text{O})$, $\nu(\text{C}-\text{N})$), 500-900 ($\nu(\text{Ti}-\text{O})$). Of particular interest are the bands at 1607, 1540, 1489 and 1405 cm^{-1} , as these can be attributed to asymmetric $\nu_{as}(\text{CO}_2^-)$ and symmetric $\nu_s(\text{CO}_2^-)$ stretches respectively. This confirms the chemisorption of C16 to TiO_2 nanoparticles as a carboxylate, with a $\Delta\nu$ range, where $\Delta\nu = [\nu_{as}(\text{CO}_2) - \nu_s(\text{CO}_2)]$, of 118-135 cm^{-1} . This suggests the molecule coupled to TiO_2 by either a bidentate bridging or chelating coordination. The wide band between 2500 and 3600 cm^{-1} is most likely due to the presence of adsorbed hydroxyl groups, water, and any remaining solvent. The $\nu(\text{Ti}-\text{O}-\text{Ti})$ structure is thought to be responsible for the broad region between 500 and 900 cm^{-1} , and can be seen in all subsequent spectra. After coupling with each aldehyde-terminating C4 unit, a $\text{C}=\text{O}$ stretching band is observed at 1683 and 1693 cm^{-1} , respectively. This peak is suppressed when reacted with the next amine-terminating C3 unit (Figure 5.61), indicating the successful assembly of each constituent molecule.

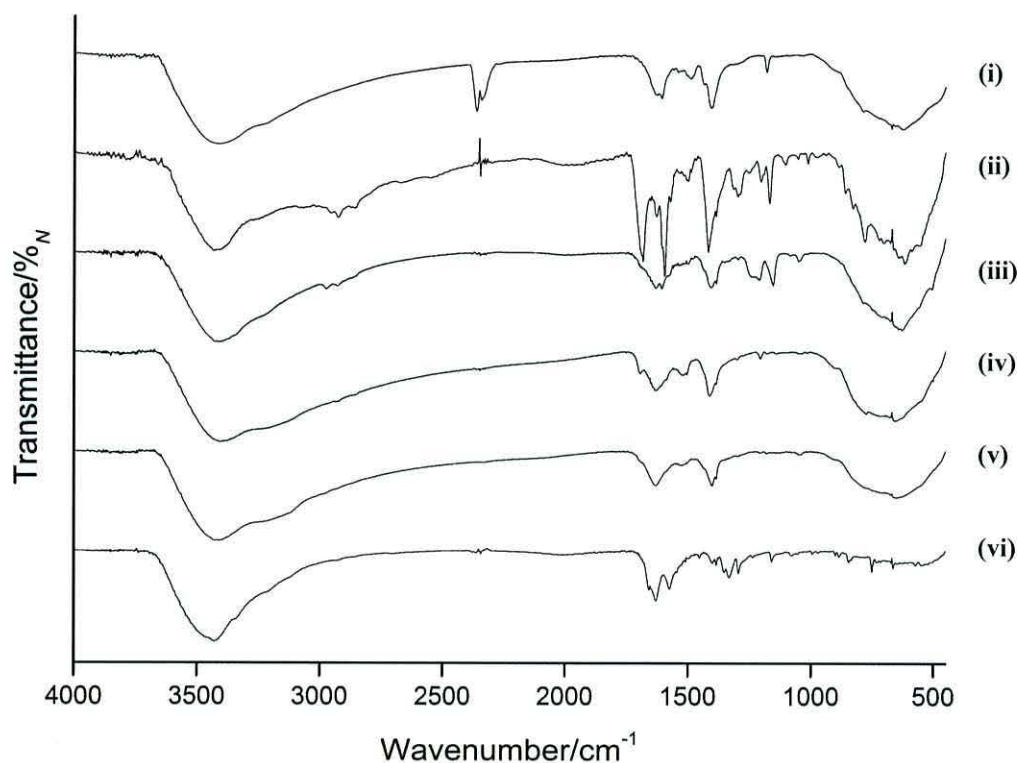


Figure 5.61: FT-IR spectra normalised to $\sim 3400\text{ cm}^{-1}$ peak showing the stepwise formation of (i) the initial S15 monolayer on TiO_2 nanoparticles, and coupling in turn with C4 ((ii) and (iv)), C3, ((iii) and (v)) and (vi) a terminating C5 unit.

5.13.7 SUMMARY

Section 5.13 has investigated the ability of C16 to self-assemble onto a TiO_2 surface from solution. With an average area per molecule of $0.246 \pm 0.002\text{ nm}^2$, this is consistent with areas demonstrated by similar molecules on gold. Assembly via the carboxylate group is proven using XPS, which identifies a N 1s peak centred at 399.9 eV corresponding to an unbound amine group. Angle-resolved studies were not entirely conclusive, although this is not unexpected for such a small molecule. The presence of a single peak between 531.0 eV and 531.3 eV in the O 1s spectrum is attributed to RCOO^- , which indicates that bonding between the carboxylate and TiO_2 surface involves equivalent oxygen environments, with delocalisation occurring across the O-C=O region. This is confirmed by infrared analysis of the corresponding nanoparticles, where the CO_2^- stretching values imply a bridging or chelating binding form. The subsequent addition of a C4 unit onto S15 to form S16 reveals a reasonable area per molecule of $0.245 \pm 0.020\text{ nm}^2$, similar to that of the first layer. This suggests the formation of an ordered, relatively defect-free multilayer construct. Infrared analysis of the corresponding system illustrates the presence of the terminating aldehyde

functional group by the emergence of a well-defined band at 1683 cm^{-1} . The suppression of this peak following the addition of an amine-terminating C3 unit indicates the successful assembly of a third molecule onto the TiO_2 nanoparticles. This is reflected in the Sauerbrey analysis, although between final depositions of layer 2 and 3, a lowering of the molecular area was observed, from 0.245 ± 0.020 to $0.189 \pm 0.018\text{ nm}^2$. This has been attributed to the presence of contaminants or trapped solvent within the system.

6.0 CONCLUSIONS

This thesis has reported the formation of novel molecular wires of varying lengths. With respect to substrate-anchoring group selection, those wires assembled on gold were reacted with thiol and amine functional groups, and those on TiO_2 with carboxylic acids. Anchoring of the initial monolayer was approached using an in-situ self-assembly process with surface coverage verified by Sauerbrey analysis of the QCM data. This gave an indication of the homogeneity of the deposited system, as well as likely packing orientation of individual molecules. Extension of this first layer to form molecular wires of up to *ca.* 10.4 nm in length occurred by chemical coupling of alternate amine and aldehyde end-groups to form a central imine bond. The successful metal-molecule and subsequent molecule-molecule bonding was confirmed using XPS to identify the presence of those elemental environments present in the assembled system. Of particular interest in this report is the N 1s environment, which has been found to exist in various systems as an amine, imine, protonated amine and gold-bound amine. This is particularly relevant to analysis of compounds containing both thiol and amine head-groups, as we have shown that such molecules can assemble onto gold via either of these substituents. With respect to their conductive properties, various molecular wires have been studied by (a) analysis of their *I-V* characteristics using Scanning Tunnelling Spectroscopy to determine the presence and scale of rectification, and (b) single molecule current using the *I(t)* method.

The process of assembling multi-component wires was monitored throughout the construction process, enabling the identification of packing characteristics of each additional layer. The longest wire formed in this manner was that of S7_b, consisting of 11 molecular units. This was shown to assemble in an approximately linear Δf vs MM relationship. Analysis of the area per molecule for each subsequent layer revealed a close-packed, relatively upright arrangement. In contrast, the Sauerbrey analysis of C11-C14 resulted in a single molecule area twice that seen previously and is believed to correspond to molecules adopting a position parallel to the surface. This has shown the dependence of molecular geometry not only on the anchoring group-metal interaction, but also molecule-metal and molecule-molecule interactions. Hence, QCM measurements have proven invaluable in determining a molecule's favoured situation, although results can be skewed by the presence of unsolicited material. Therefore XPS analyses were also carried out on the majority of anchoring layers. This proved particularly

important for system S2_a and S2_b, where it was determined that self-assembly favoured the formation of Au-N bonds rather than that of the expected Au-S bond. This was established by the presence of two N 1s peaks at 399.0 and 400.3 eV, which corresponds to nitrogen present in both the Au-N and -NH₂ environments. This allowed C2 to be ruled out as an initial anchoring layer, as it would result in less than 50% coverage of subsequent deposits. As well as confirming the presence of the initial monolayer, this method was also used to demonstrate the imine formation created by the successful addition of another layer.

As well as studying the assembly characteristics of molecules assembling onto gold, this thesis has also confirmed the ability of wires to assemble in a stepwise fashion on TiO₂ surfaces using a combination of Sauerbrey, XPS and infrared spectroscopy techniques. These systems are of particular interest due to their relevance in the construction of hybrid microelectronics systems.

Thus far the synthesis of molecular wires has been discussed in general. Some wires, such as S3_a-S7_a and S3_b-S7_b are of particular interest with respect to their rectifying behaviour. By synthesising a wire composed chiefly of electron accepting units and capping it at varying stages with the bulky C5 end-group it has been shown how electron flow can be altered in such molecular systems. This can be summarised most elegantly by comparison of S5_a and S5_b, the *I-V* characteristics of which are represented in Figure 6.1. The asymmetric curve in Figure 6.1 (a) demonstrates current flow in system S5_a with rectification of 2.8 at ± 1 V in the negative quadrant. The addition of a bulky C5 group results in Figure 6.1 (b). This too is asymmetric, but with an average rectification ratio of 11.5 ± 1 V in the positive quadrant.

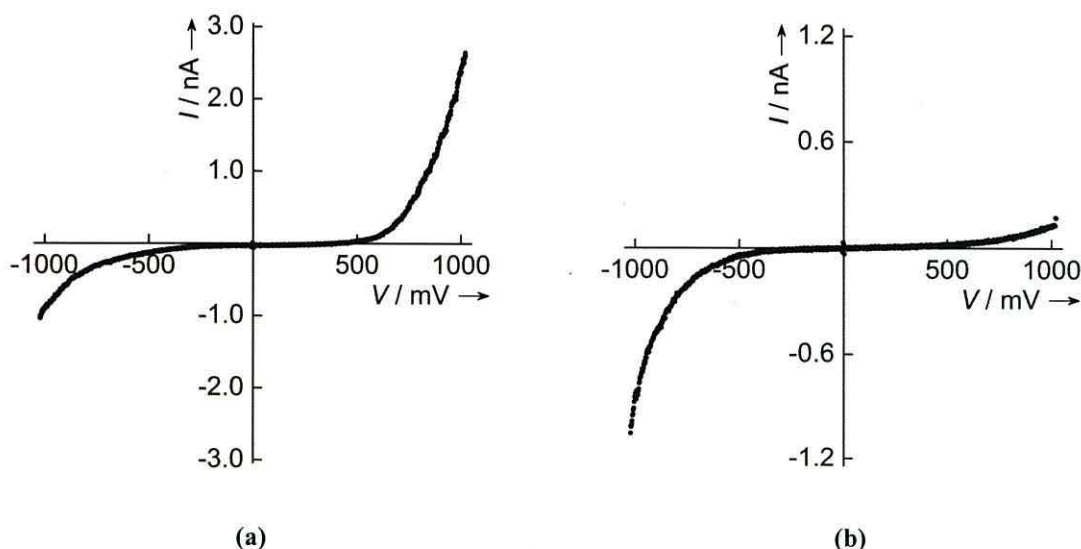


Figure 6.1: *I-V* characteristics of (a) S5_a and (b) S5_b.

We can conclude from this that an increase in steric hindrance hinders electron movement across the final section of the wire. Interestingly, rectification does not appear to be present in the final two systems, and this has been tentatively attributed to a change in the dominant charge transport mechanism with increasing molecular length. Further investigation into this hypothesis was carried out by statistical examination of single molecule current measurements on each of the five C3-terminating systems. This was implemented using the afore-mentioned $I(t)$ method of analysis, the results of which were considered dissimilar to those of the $I-V$ findings. Rather than demonstrating a length-dependant current change across the series of wires, the single molecule current remained relatively similar. The inference gained from this study, in that all five wires exhibited dominant hopping charge transport with no apparent transition from one mechanism to the other, is in contrast to that gained from analysis of the $I-V$ properties of each systems. As no conclusive interpretation can be made, future work should include an investigation into the effect of temperature on conductivity.

7.0 FURTHER WORK

The QCM technique has proven to be an invaluable tool throughout this work, allowing adsorption processes to be monitored and final surface areas per molecule to be calculated. From this, the packing characteristics of numerous systems have been inferred. However, the QCM method does not take into account tilting of the molecule relative to the surface, which is expected to occur in systems comprising the initial C1 molecule. In order to address this issue, further surface analysis, via surface plasmon resonance (SPR) for example, would be necessary. Not only can this provide an indication of the tilting angle of the SAM, it would also detect small changes in molecular thickness, and thus be used to confirm the successful addition of each consecutive monolayer. This quantitative technique has been demonstrated on a number of planar and nanoparticulate surfaces, including Au²³⁰ and TiO₂,²³¹ which is ideal for the systems in question. Furthermore, in addition to monitoring SAM formation using the traditional QCM method, it may prove beneficial to perform concurrent electrochemical QCM (EQCM) measurements. This complementary technique would allow any frequency changes upon addition or removal of mass to be directly related to the electrochemically stimulated adsorption and desorption of the organic monolayers from the gold electrode, thus providing information regarding monolayer stability, adsorption energy, formation kinetics, molecular orientation, and morphology.

Questions arising over the dominant charge transport mechanism occurring in systems S3_a-S7_a would benefit from further current-response studies performed at a range of temperatures. The existing work suggests two possible scenarios, supported by separate current-voltage and single molecule conductance studies. One indicates a possible mechanism changeover from tunnelling to hopping with increasing molecular length, and the other indicates a dominant tunnelling mechanism in all wires independent of length. Temperature-dependant single molecule studies revealing a change in current-response across the molecular length scale, with little change in wires S3_a-S5_a and a greater dependence in wires S6_a and S7_a, would imply a change in charge transport mechanism. However, if all five wires exhibited this temperature dependence, it can be surmised that the change in current-voltage characteristics between S5_a and S6_a are in fact due to the increasingly electron accepting nature of the wire, rather than a change in charge transport mechanism. Further recommended avenues for characterising electron transfer in SAMs include the use of electrochemical impedance

spectroscopy, which has proven an effective means of studying electron transfer reactions in a series of alkanethiols of varying chain lengths.²³² By measuring the impedance of a system over a range of frequencies, the effects of increasing thin film thickness can be systematically measured, providing information regarding electron transfer, adsorption kinetics, and the degree of defects present in the assembled system.

8.0 REFERENCES

1. <http://newsroom.intel.com/docs/DOC-2032>, accessed on 16/05/12
2. G. E. Moore, *Electronics*, 1965, **38**, 8
3. J. M. Tour, *Acc. Chem. Res.*, 2000, **33**, 791-804
4. B. A. Mantooth and P. S. Weiss, *Proc. IEEE*, 2003, **91**, 1785-1802
5. A. Coskun, M. Banaszak, R. D. Astumian, J. F. Stoddart and B. A. Grzybowski, *Chem. Soc. Rev.*, 2012, **41**, 19-30
6. J. R. Heath, *Ann. Rev. Mater. Res.*, 2009, **39**, 1-23
7. J. Del Nero, F. M. de Souza and R. B. Capaz, *J. Comput. Theor. Nanosci.*, 2010, **7**, 1-14
8. C. Joachim, J. K. Gimzewski and A. Aviram, *Nature*, 2000, **408**, 541-548
9. A. Aviram and M. A. Ratner, *Chem. Phys. Lett*, 1974, **29**, 277-283
10. J. A. Jones, L. A. Qin, H. Meyerson, I. K. Kwon, T. Matsuda and J. M. Anderson, *J. Biomed. Mater. Res. A*, 2008, **86A**, 261
11. N. T. Flynn, T. N. T. Tran, M. J. Cima and R. Langer, *Langmuir*, 2003, **19**, 10909-10915
12. J. Tang, Y. Wang, J. E. Klare, G. S. Tulevski, S. J. Wind and C. Nuckolls, *Angew. Chem. Int. Ed.*, 2007, **46**, 3892-3895
13. L. Grill, K. Rieder, F. Moresco, S. Stojkovic, A. Gourdon and C. Joachim, *Nano Lett.*, 2005, **5**, 859-863
14. G. J. Ashwell, B. Urasinska and W. D. Tyrrell, *Phys. Chem. Chem. Phys.*, 2006, **8**, 3314
15. G. J. Ashwell, A. Mohib and J. R. Miller, *J. Mater. Chem.*, 2005, **15**, 1160-1166

16. N. Robertson and C. A. McGowan, *Chem. Soc. Rev.*, 2003, **32**, 96-103
17. R. Mas-Ballesté, O. Castillo, P. J. S. Miguel, D. Olea, J. Gómez-Herrero and F. Zamora, *Eur. J. Inorg. Chem.*, 2009, **2009**, 2885-2896
18. J. H. Burroughes, D. D. C. Bradley, A. R. Brown, R. N. Marks, K. Mackay, R. H. Friend, P. L. Burns and A. B. Holmes, *Nature*, 1990, **347**, 539-541
19. D. L. Pearson and J. M. Tour, *J. Org. Chem.*, 1997, **62**, 1376-1387
20. C. Wang, A. S. Batsanov and M. R. Bryce, *Faraday Discuss.*, 2006, **131**, 221
21. G. J. Ashwell, P. Wierchowicz, L. J. Phillips, C. J. Collins, J. Gigon, B. J. Robinson, C. M. Finch, I. R. Grace, C. J. Lambert, P. D. Buckle, K. Ford, B. J. Wood and I. R. Gentle, *Phys. Chem. Chem. Phys.*, 2008, **10**, 1859-1866
22. J. D. Slinker, N. B. Muren, S. E. Renfrew and J. K. Barton, *Nat. Chem.*, 2011, **3**, 228-233
23. D. Porath, G. Cuniberti and R. Di Felice, *Top. Curr. Chem.*, 2004, **237**, 183
24. E. Braun, Y. Eichen, U. Sivan and G. Ben-Yoseph, *Nature*, 1998, **391**, 775-778
25. D. Porath, A. Bezryadin, S. de Vries and C. Dekker, *Nature*, 2000, **403**, 635-638
26. H. Cohen, C. Nogues, R. Naaman and D. Porath, *PNAS*, 2005, **102**, 11589-11593
27. S. Iijima, *Nature*, 1991, **354**, 56-58
28. R. Saito, M. Fujita, G. Dresselhaus and M. S. Dresselhaus, *Appl. Phys. Lett.*, 1992, **60**, 2204-2206
29. C. Dekker, *Phys Today*, 1999, **52**, 22-28
30. P. Jarosz, C. Schauerman, J. Alvarenga, B. Moses, T. Mastrangelo, R. Raffaele, R. Ridgley and B. Landi, *Nanoscale*, 2011, **3**, 4542-4553

31. K. H. An, W. S. Kim, Y. S. Park, Y. C. Choi, S. M. Lee, D. C. Chung, D. J. Bae, S. C. Lim and Y. H. Lee, *Adv. Mater.*, 2001, **13**, 497-500
32. C. Hu and S. Hu, *Journal of Sensors*, 2009, **2009**, 187615
33. S. J. Tans, A. R. M. Verschueren and C. Dekker, *Nature*, 1998, **393**, 49-52
34. A. C. Brady, B. Hodder, A. S. Martin, J. R. Sambles, C. P. Ewels, R. Jones, P. R. Briddon, A. M. Musa, C. A. Panetta and D. L. Mattern, *J. Mater. Chem.*, 1999, **9**, 2271
35. G. Ho, J. R. Heath, M. Kondratenko, D. F. Perepichka, K. Arseneault, M. Pézolet and M. R. Bryce, *Chem. Eur. J.*, 2005, **11**, 2914-2922
36. G. J. Ashwell, J. R. Sambles, A. S. Martin, W. G. Parker and M. Szablewski, *J. Chem. Soc., Chem. Commun.*, 1990, **19**, 1374
37. R. M. Metzger, *Adv. Mater. Opt. Electron.*, 1998, **8**, 229-245
38. R. M. Metzger, T. Xu and I. R. Peterson, *J. Phys. Chem. B*, 2001, **105**, 7280-7290
39. G. J. Ashwell and A. Mohib, *J. Am. Chem. Soc.*, 2005, **127**, 16238-16244
40. G. J. Ashwell, W. D. Tyrrell and A. J. Whittam, *J. Mater. Chem.*, 2003, **13**, 2855-2857
41. C. F. Brinker, Y. Lu, A. Sellinger and H. Fan, *Adv. Mater.*, 1999, **11**, 579
42. G. M. Whitesides and B. Grzybowski, *Science*, 2002, **295**, 2418
43. P. Monnard and D. W. Deamer, *The Anatomical Record*, 2002, **268**, 196-207
44. N. Krasnogor, S. Gustafson, D. A. Pelta and J. L. Verdegay, *Systems Self-Assembly: Multidisciplinary Snapshots*, 2008, Elsevier Science
45. K. Ariga, J. P. Hill, M. V. Lee, A. Vinu, R. Charvet and S. Acharya, *Sci. Technol. Adv. Mater.*, 2008, **9**, 014109
46. F. Schreiber, *J. Phys. Condens. Matter*, 2004, **16**, R881-R900

47. F. Schreiber, *Prog. Surf. Sci.*, 2000, **65**, 151-257
48. J. C. Huie, *Smart Mater. Struct.*, 2003, **12**, 264
49. J. C. Love, L. A. Estroff, J. K. Kriebel, R. G. Nuzzo and G. M. Whitesides, *Chem. Rev.*, 2005, **105**, 1103-1170
50. W. C. Bigelow, D. L. Pickett and W. A. Zisman, *J. Colloid Sci.*, 1946, **1**, 513-538
51. P. E. Laibinis and G. M. Whitesides, *J. Am. Chem. Soc.*, 1992, **114**, 9022-9028
52. R. M. Crooks and A. J. Ricco, *Acc. Chem. Res.*, 1998, **31**, 219-227
53. Y. Liu, C. Lin, H. Li and H. Yan, *Angew. Chem.*, 2005, **117**, 4407-4412
54. http://www.prochimia.com/pdf/ProChimia_Catalog_2006.pdf, accessed on 05/05/08
55. S. H. Gyepi-Garbrah and R. Šilerová, *Phys. Chem. Chem. Phys.*, 2002, **4**, 3436-3442
56. C. Lee, H. E. Canavan, L. J. Gamble and D. G. Castner, *Langmuir*, 2005, **21**, 5134-5141
57. R. G. Nuzzo and D. L. Allara, *J. Am. Chem. Soc.*, 1983, **105**, 4481-4483
58. S. D. Evans and A. Ulman, *Chem. Phys. Lett.*, 1990, **170**, 462-466
59. D. V. Leff, L. Brandt and J. R. Heath, *Langmuir*, 1996, **12**, 4723-4730
60. R. C. Hoft, M. J. Ford, A. M. McDonagh and M. B. Cortie, *J. Phys. Chem. C*, 2007, **111**, 13886-13891
61. M. S. Hybertsen, L. Venkataraman, J. E. Klare, A. C. Whalley, M. L. Steigerwald and C. Nuckolls, *J. Phys.: Condens. Matter*, 2008, **20**, 374115
62. W. Paik, S. Han, W. Shin and Y. Kim, *Langmuir*, 2003, **19**, 4211-4216
63. O. M. Magnussen, B. M. Ocko, M. Deutsch, M. J. Regan, P. S. Pershan, D. Abernathy, G. Grubel and J. Legrand, *Nature*, 1996, **384**, 250-252

64. K. Shimazu, Y. Sato, I. Yagi and K. Uosaki, *Bull. Chem. Soc. Jpn.*, 1994, **67**, 863-865
65. J. C. Love, D. B. Wolfe, R. Haasch, M. L. Chabinyc, K. E. Paul, G. M. Whitesides and R. G. Nuzzo, *J. Am. Chem. Soc.*, 2003, **125**, 2597-2609
66. H. Sellers, A. Ulman, Y. Shnidman and J. E. Eilers, *J. Am. Chem. Soc.*, 1993, **115**, 9389-9401
67. M. Bourg, A. Badia and R. B. Lennox, *J. Phys. Chem. B*, 2000, **104**, 6562-6567
68. H. Basch and M. A. Ratner, *J. Chem. Phys.*, 2003, **119**, 11926-11942
69. H. Basch and M. A. Ratner, *J. Chem. Phys.*, 2003, **119**, 11943-11950
70. C. D. Bain, E. B. Troughton, T. Tao, J. Evall, G. M. Whitesides and R. G. Nuzzo, *J. Am. Chem. Soc.*, 1989, **111**, 321-335
71. W. Mar and M. L. Klein, *Langmuir*, 1994, **10**, 188-196
72. K. M. Beardmore, J. D. Kress, N. Grønbech-Jensen and A. R. Bishop, *Chem. Phys. Lett.*, 1998, **286**, 40-45
73. L. H. Dubois and R. G. Nuzzo, *Annu. Rev. Phys. Chem.*, 1992, **43**, 437-463
74. P. Fenter, A. Eberhardt and P. Eisenberger, *Science*, 1994, **266**, 1216-1218
75. P. Fenter, F. Schreiber, L. Berman, G. Scoles, P. Eisenberger and M. J. Bedzyk, *Surf. Sci.*, 1998, **412/413**, 213-235
76. P. Maksymovych, D. C. Sorescu and J. T. Yates, *J. Phys. Chem. B*, 2006, **110**, 21161-21167
77. M. G. Roper, M. P. Skegg, C. J. Fisher, J. J. Lee, V. R. Dhanak, D. P. Woodruff and R. G. Jones, *Chem. Phys. Lett.*, 2004, **389**, 87-91
78. P. Maksymovych, O. Voznyy, D. B. Dougherty, D. C. Sorescu and J. T. Yates Jr., *Prog. Surf. Sci.*, 2010, **85**, 206-240

79. S. J. Stranick, A. N. Parikh, D. L. Allara and P. S. Weiss, *J. Phys. Chem.*, 1994, **98**, 11136-11142
80. L. Venkataraman, J. E. Klare, I. W. Tam, C. Nuckolls, M. S. Hybertsen and M. L. Steigerwald, *Nano. Lett.*, 2006, **6**, 458
81. S. Y. Quek, L. Venkataraman, H. J. Choi, S. G. Louie, M. S. Hybertsen and J. B. Neaton, *Nano Lett.*, 2007, **7**, 3477-3482
82. G. Fagas and J. C. Greer, *Nanotechnology*, 2007, **18**, 424010
83. E. J. Fernández, E. García-Luzuriaga, A. Laguna, J. M. López-de-Luzuriaga and M. E. Olmos, *Gold Bulletin*, 2010, **43**, 80
84. C. Xu, L. Sun, L. J. Kepley and R. M. Crooks, *Anal. Chem.*, 1993, **65**, 2102
85. A. Fujishima, T. N. Rao and D. A. Tryk, *J. Photochem. Photobiol., C*, 2000, **1**, 1-21
86. G. P. Burns, *J. Appl. Phys.*, 1989, **65**, 2095-2097
87. S. Meth, N. Savchenko, M. Koltypin, D. Starosvetsky, F. A. Viva, A. Groysman and C. N. Sukenik, *Corros. Sci.*, 2010, **52**, 125-129
88. Y. Yang, Y. Lai, Q. Zhang, K. Wu, L. Zhang, C. Lin and P. Tang, *Colloids Surf. B*, 2010, **79**, 309-313
89. Q. Chen and N. L. Yakovlev, *Appl. Surf. Sci.*, 2010, **257**, 1395-1400
90. R. Luschtinetz, J. Frenzel, T. Milek and G. Seifert, *J. Phys. Chem. C*, 2009, **113**, 5730-5740
91. Q. Qu, H. Geng, R. Peng, Q. Cui, X. Gu, F. Li and M. Wang, *Langmuir*, 2010, **26**, 9539-9546
92. H. Shin, M. R. De Guire and A. H. Heuer, *J. Appl. Phys.*, 1998, **83**, 3311-3317
93. Y. Gao, Y. Masuda and K. Koumoto, *Chem. Mater.*, 2004, **16**, 1062-1067

94. Y. Weng, L. Li, Y. Liu, L. Wang and G. Yang, *J. Phys. Chem. B*, 2003, **107**, 4356-4363
95. E. H. Cordes and W. P. Jencks, *J. Am. Chem. Soc.*, 1962, **84**, 832
96. J. E. Klare, G. S. Tulevski and C. Nuckolls, *Langmuir*, 2004, **20**, 10068-10072
97. J. M. La Nauze, J. R. Coggins and H. B. F. Dixon, *Biochem. J.*, 1977, **165**, 409-411
98. M. E. Belowich and J. F. Stoddart, *Chem. Soc. Rev.*, 2012, **41**, 2003-2024
99. M. Yang and M. C. Biewer, *Tetrahedron Lett.*, 2005, **46**, 349-351
100. R. C. Horton Jr., T. M. Herne and D. C. Myles, *J. Am. Chem. Soc.*, 1997, **119**, 12980-12981
101. S. M. Landge, E. Tkatchouk, D. Benítez, D. A. Lanfranchi, M. Elhabiri, W. A. Goddard III and I. Aprahamian, *J. Am. Chem. Soc.*, 2011, **133**, 9812-9823
102. D. Xu and R. Warmuth, *J. Am. Chem. Soc.*, 2008, **130**, 7520-7521
103. F. J. Uribe-Romo, J. R. Hunt, H. Furukawa, C. Klöck, M. O'Keeffe and O. M. Yaghi, *J. Am. Chem. Soc.*, 2009, **131**, 4570-4571
104. F. Huguenin, M. Ferreira, V. Zucolotto, F. C. Nart, R. M. Torresi and O. N. Oliveira, *Chem. Mater.*, 2004, **16**, 2293-2299
105. S. Srivastava and N. A. Kotov, *Acc. Chem. Res.*, 2008, **41**, 1831-1841
106. T. G. Shutava, D. S. Kommireddy and Y. M. Lvov, *J. Am. Chem. Soc.*, 2006, **128**, 9926-9934
107. T. Tang, J. Qu, K. Müllen and S. E. Webber, *Langmuir*, 2006, **22**, 26-28
108. R. K. Iler, *J. Colloid Interface Sci.*, 1966, **21**, 569-594
109. G. Decher and J. D. Hong, *Ber. Bunsen Ges. Phys. Chem.*, 1991, **95**, 1430-1434
110. Z. Liang, C. Wang, Z. Tong, W. Ye and S. Ye, *React. Funct. Polym.*, 2005, **63**, 85-94

111. B. Bush, G. Xu, C. Carraro and R. Maboudian, *Sensors and Actuators A*, 2006, **126**, 194-200
112. X. B. Yan, X. J. Chen, B. K. Tay and K. A. Khor, *Electrochem. Commun.*, 2007, **9**, 1269-1275
113. M. M. de Villiers, D. P. Otto, S. J. Strydom and Y. M. Lvov, *Adv. Drug Deliv. Rev.*, 2011, **63**, 701-715
114. M. Macdonald, N. M. Rodriguez, R. Smith and P. T. Hammond, *J. Controlled Release*, 2008, **131**, 228-234
115. L. Richert, P. Lavallo, E. Payan, X. Z. Shu, G. D. Prestwich, J. Stoltz, P. Schaaf, J. Voegel and C. Picart, *Langmuir*, 2004, **20**, 448-458
116. W. Chen and T. J. McCarthy, *Macromolecules*, 1997, **30**, 78-86
117. A. Pockels, *Nature*, 1981, **43**, 437
118. Rayleigh, *Philos. Mag.*, 1899, **48**, 321
119. I. Langmuir, *J. Am. Chem. Soc.*, 1917, **39**, 1848-1906
120. K. B. Blodgett, *J. Am. Chem. Soc.*, 1934, **56**, 495-495
121. J. Curie and P. Curie, *Rendu*, 1880, **91**, 294
122. G. J. Ashwell and A. Chwialkowska, *Chem. Commun.*, 2006, **13**, 1404-1406
123. G. Sauerbrey, *Z. Phys. A: Hadrons Nucl.*, 1959, **155**, 206-222
124. W. H. King Jr., *Anal. Chem.*, 1964, **36**, 1735-1739
125. T. Nomura and M. Okuhara, *Anal. Chim. Acta*, 1982, **142**, 281-284
126. K. K. Kanazawa and J. G. Gordon, *Anal. Chem.*, 1985, **57**, 1770-1771
127. H. Bakowsky, T. Richter, C. Kneuer, D. Hoekstra, U. Rothe, G. Bendas, C. Ehrhardt and U. Bakowsky, *BBA*, 2008, **1778**, 242-249

128. J. Rickert, T. Weiss, W. Kraas, G. Jung and W. Göpel, *Biosensors and Bioelectronics*, 1996, **11**, 591-598
129. R. Bunkar, R. Asrey, K. D. Vyas, V. K. Rao, S. Kumar, A. R. Srivastava and M. P. Kaushik, *Indian J. Sci. Technol.*, **3**, 139
130. S. K. Vashist and P. Vashist, *Journal of Sensors*, 2011, **571405**
131. M. M. Rahman, K. J. Oh and I. C. Jeon, *J. Sci. Res.*, 2009, **1**, 292-299
132. D. Qu and M. Morin, *J. Electroanal. Chem.*, 2001, **517**, 45-53
133. D. W. Hatchett, R. H. Uibel, K. J. Stevenson, J. M. Harris and H. S. White, *J. Am. Chem. Soc.*, 1998, **120**, 1062-1069
134. S. Chen, B. Wu and C. Cha, *J. Electroanal. Chem.*, 1997, **420**, 111-118
135. P. T. Varineau and C. A. Buttry, *J. Phys. Chem.*, 1987, **91**, 1292-1295
136. H. Hertz, *Ann. Phys.*, 1887, **267**, 983-1000
137. S. Hagström, C. Nordling and K. Siegbahn, *Phys. Lett.*, 1964, **9**, 235-236
138. N. V. Alov, *J. Anal. Chem.*, 2005, **60**, 297-300
139. F. Maier, T. Cremer, C. Kolbeck, K. R. J. Lovelock, N. Paape, P. S. Schulz, P. Wasserscheid and H. Steinruck, *Phys. Chem. Chem. Phys.*, 2010, **12**, 1905-1915
140. O. Seitz, T. Böcking, A. Salomon, J. J. Gooding and D. Cahen, *Langmuir*, 2006, **22**, 6915-6922
141. M. Vijayaraj and C. S. Gopinath, *J. Catal.*, 2006, **241**, 83-95
142. G. Witte and C. Wöll, *J. Mater. Res.*, 2004, **19**, 1889
143. M. G. S. Ferreira, R. G. Duarte, M. F. Montemor and A. M. P. Simões, *Electrochim. Acta*, 2004, **49**, 2927-2935
144. P. Pfluger and G. B. Street, *J. Chem. Phys.*, 1984, **80**, 544-553

145. F. J. Low, *Science*, 1969, **164**, 501
146. R. Newman, *JAIC*, 1979, **19**, 42
147. Y. M. Rabkin, *ISIS*, 1987, **78**, 31-54
148. D. K. James and J. M. Tour, *Chem. Mater.*, 2004, **16**, 4423-4435
149. M. D. Porter, T. B. Bright, D. L. Allara and C. E. D. Chidsey, *J. Am. Chem. Soc.*, 1987, **109**, 3559-3568
150. M. R. Ghadiri, J. R. Granja, R. A. Milligan, D. E. McRee and N. Khazanovich, *Nature*, 1993, **366**, 324-327
151. L. H. Kidder, V. F. Kalasinsky, J. L. Luke, I. W. Levin and E. N. Lewis, *Nat. Med.*, 1997, **3**, 235-237
152. B. J. Holland and J. N. Hay, *Polymer*, 2001, **42**, 4825-4835
153. T. Tjomsland, J. Hilland, A. A. Christy, J. Sjöblom, M. Riis, T. Frissø and K. Folgerø, *Fuel*, 1996, **75**, 322-332
154. G. Binnig, H. Rohrer, C. Gerber and E. Weibel, *Phys. Rev. Lett.*, 1982, **49**, 57-61
155. G. Binnig and H. Rohrer, *IBM J. Res. Develop.*, 2000, **44**, 279
156. http://www.iap.tuwien.ac.at/www/surface/STM_Gallery/stm_schematic.html,
accessed on 30/07/09
157. K. Slowinski, R. V. Chamberlain, C. J. Miller and M. Majda, *J. Am. Chem. Soc.*, 1997, **119**, 11910-11919
158. E. Whittle, D. A. Dows and G. C. Pimentel, *J. Chem. Phys.*, 1954, **22**, 1943-1943
159. C. E. D. Chidsey, C. R. Bertozzi, T. M. Putvinski and A. M. Majsce, *J. Am. Chem. Soc.*, 1990, **112**, 4301-4306

160. D. M. Adams, L. Brus, C. E. D. Chidsey, S. Creager, C. Creutz, C. R. Kagan, P. V. Kamat, M. Lieberman, S. Lindsay, R. A. Marcus, R. M. Metzger, M. E. Michel-Beyerle, J. R. Miller, M. D. Newton, D. R. Rolison, O. Sankey, K. S. Schanze, J. Yardley and X. Zhu, *J. Phys. Chem. B*, 2003, **107**, 6668-6697
161. A. A. Kocherzhenko, F. C. Grozema and L. D. A. Siebbeles, *Phys. Chem. Chem. Phys.*, 2011, **13**, 2096-2110
162. M. A. Rampi and G. M. Whitesides, *Chem. Phys.*, 2002, **281**, 373-391
163. F. F. Fan, J. Yang, L. Cai, D. W. Price Jr., S. M. Dirk, D. V. Kosynkin, Y. Yao, A. M. Rawlett, J. M. Tour and A. J. Bard, *J. Am. Chem. Soc.*, 2002, **124**, 5550-5560
164. L. Luo, S. H. Choi and C. D. Frisbie, *Chem. Mater.*, 2011, **23**, 631-645
165. Y. Lo, S. Sun and Y. Kao, *Phys. Rev. B*, 2011, **84**, 075106
166. B. Mann and H. Kuhn, *J. Appl. Phys.*, 1971, **42**, 4398-4405
167. S. Ho Choi, B. Kim and C. D. Frisbie, *Science*, 2008, **320**, 1482-1486
168. L. Luo and C. D. Frisbie, *J. Am. Chem. Soc.*, 2010, **132**, 8854-8855
169. S. H. Choi, C. Risko, M. C. Delgado, B. Kim, J. Brédas and C. D. Frisbie, *J. Am. Chem. Soc.*, 2010, **132**, 4358-4368
170. T. Hines, I. Diez-Perez, J. Hihath, H. Liu, Z. Wang, J. Zhao, G. Zhou, K. Müllen and N. Tao, *J. Am. Chem. Soc.*, 2010, **132**, 11658-11664
171. W. B. Davis, W. A. Svec, M. A. Ratner and M. R. Wasielewski, *Nature*, 1998, **396**, 60-63
172. R. Yamada, H. Kumazawa, S. Tanaka and H. Tada, *Appl. Phys. Express.*, 2009, **2**, 025002
173. B. Xu and N. J. Tao, *Science*, 2003, **301**, 1221-1223

174. W. Haiss, R. J. Nichols, H. van Zalinge, S. J. Higgins, D. Bethell and D. J. Schiffrin, *Phys. Chem. Chem. Phys.*, 2004, **6**, 4330-4337
175. R. J. Nichols, W. Haiss, S. J. Higgins, E. Leary, S. Martin and D. Bethell, *Phys. Chem. Chem. Phys.*, 2010, **12**, 2801-2815
176. D. Kockmann, B. Poelsema and H. J. W. Zandvliet, *Nano Lett.*, 2009, **9**, 1147-1151
177. L. Phillips, Molecule-inserted Silicon Nanogaps, PhD Thesis, 2011, Bangor University
178. K. A. Marx, *Biomacromolecules*, 2003, **4**, 1099-1120
179. P. Wierzchowiec., Functional Molecular Wires and Devices, PhD Thesis, 2008, Bangor University
180. D. I. Rozkiewicz, B. J. Ravoo and D. N. Reinhoudy, *Langmuir*, 2005, **21**, 6337-6343
181. Y. Luo, M. Piantek, M. Bernien, W. Kuch and R. Haag, *Appl. Phys. A*, 2008, **93**, 293-301
182. R. Rahal, S. Daniele, L. G. Hubert-Pfalzgraf, V. Guyot-Ferréol and J. Tranchant, *Eur. J. Inorg. Chem.*, 2008, **2008**, 980-987
183. M. Ahmed, J. A. Byrne and J. A. D. McLaughlin, *e-J. Surf. Sci. Nanotech.*, 2009, **7**, 217-224
184. C. D. Bain and G. M. Whitesides, *J. Phys. Chem.*, 1989, **93**, 1670-1673
185. V. Saggiomo and U. Lüning, *Tetrahedron Lett.*, 2009, **50**, 4663-4665
186. C. D. Meyer, C. S. Joiner and J. F. Stoddart, *Chem. Soc. Rev.*, 2007, **36**, 1705-1723
187. S. C. Cantrill, S. J. Rowan and J. F. Stoddart, *Org. Lett.*, 1999, **1**, 1363-1366
188. A. Kumar, S. Mandal, P. R. Selvakannan, R. Pasricha, A. B. Mandale and M. Sastry, *Langmuir*, 2003, **19**, 6277-6282

189. M. Aslam, L. Fu, M. Su, K. Vijayamohanan and V. P. Dravid, *J. Mater. Chem.*, 2004, **14**, 1795-1797
190. A. Adenier, M. M. Chehimi, I. Gallardo, J. Pinson and N. Vilà, *Langmuir*, 2004, **20**, 8243-8253
191. S. Weigelt, J. Schnadt, A. K. Tuxen, F. Masini, C. Bombis, C. Busse, C. Isvoranu, E. Ataman, E. Lægsgaard, F. Besenbacher and T. R. Linderoth, *J. Am. Chem. Soc.*, 2008, **130**, 5388-5389
192. G. J. Ashwell, A. T. Williams, S. A. Barnes, S. L. Chappell, L. J. Phillips, B. J. Robinson, B. Urasinska-Wojcik, P. Wierzchowiec, I. R. Gentle and B. J. Wood, *J. Phys. Chem. C*, 2011, **115**, 4200-4208
193. J. Sharma, S. Mahima, B. A. Kakade, R. Pasricha, A. B. Mandale and K. Vijayamohanan, *J. Phys. Chem. B*, 2004, **108**, 13280-13286
194. L. Niu, C. Kvarnström and A. Ivaska, *J. Electroanal. Chem.*, 2007, **600**, 95-102
195. J. J. W. M. Rosink, M. A. Blauw, L. J. Geerligs, E. van der Drift, B. A. C. Rousseeuw, S. Radelaar, W. G. Sloof and E. J. M. Fakkeldij, *Langmuir*, 2000, **16**, 4547-4553
196. G. J. Ashwell, L. J. Phillips, B. J. Robinson, S. A. Barnes, A. T. Williams, B. Urasinska-Wojcik, C. J. Lambert, I. M. Grace, T. I. Cox and I. C. Sage, *Angew. Chem. Int. Ed.*, 2011, **50**, 8722-8726
197. W. Haiss, C. Wang, R. Jitchati, I. Grace, S. Martín, A. S. Batsanov, S. J. Higgins, M. R. Bryce, C. J. Lambert, P. S. Jensen and R. J. Nichols, *J. Phys.: Condens. Matter*, 2008, **20**, 374119
198. S. Martín, W. Haiss, S. Higgins, P. Cea, M. C. López and R. J. Nichols, *J. Phys. Chem. C*, 2008, **112**, 3941-3948
199. J. R. Widawsky, M. Kamenetska, J. Klare, C. Nuckolls, M. L. Steigerwald, M. S. Hybertsen and L. Venkataraman, *Nanotechnology*, 2009, **20**, 434009

200. Q. Lu, K. Liu, H. Zhang, Z. Du, X. Wang and F. Wang, *ACS Nano*, 2009, **3**, 3861-3868
201. F. Chen, X. Li, J. Hihath, Z. Huang and N. Tao, *J. Am. Chem. Soc.*, 2006, **128**, 15874-15881
202. S. Martín, D. Z. Manrique, V. M. García-Suárez, W. Haiss, S. J. Higgins, C. J. Lambert and R. J. Nichols, *Nanotechnology*, 2009, **20**, 125203
203. S. S. C. Yu, E. S. Q. Tan, R. T. Jane and A. J. Downard, *Langmuir*, 2007, **23**, 11074-11082
204. S. Liu, Z. Tang, Z. Shi, L. Niu, E. Wang and S. Dong, *Langmuir*, 1999, **15**, 7268-7275
205. J. Reichert, A. Schiffrin, W. Auwärter, A. Weber-Bargioni, M. Marschall, M. Dell'Angela, D. Cvetko, G. Bavdek, A. Cossaro, A. Morgante and J. V. Barth, *ACS Nano*, 2010, **4**, 1218-1226
206. I. S. Kristensen, D. J. Mowbray, K. S. Thygesen and K. W. Jacobsen, *J. Phys. : Condens. Matter*, 2008, **20**, 374101
207. A. Nishikawa, J. Tobita, Y. Kato, S. Fujii, M. Suzuki and M. Fujihira, *Nanotechnology*, 2007, **18**, 424005
208. K. Nagasawa and Y. Hashimoto, *The Chemical Record*, 2003, **3**, 201-211
209. E. V. Rozengart, N. E. Basova, B. S. Zhorov, S. N. Moralev, V. S. Saakov, A. A. Suvorov and A. E. Khovanskikh, *J. Evol. Biochem. Physiol.*, 2003, **39**, 393-404
210. P. S. Dieng and C. Sirlin, *Int. J. Mol. Sci.*, 2010, **11**, 3334-3348
211. S. M. Barlow and R. Raval, *Surf. Sci. Rep.*, 2003, **50**, 201-341
212. J. V. Johannes, G. Costantini and K. Kern, *Nature*, 2005, **437**, 671
213. N. Oncel and S. L. Bernasek, *Appl. Phys. Lett.*, 2008, **92**, 133305
214. G. E. Poirier and E. D. Pylantt, *Science*, 1996, **272**, 1145

215. E. Barenna, E. Palacios-Lidón, C. Munuera, X. Torrelles, S. Ferrer, U. Jonas, M. Salmeron and C. Ocal, *J. Am. Chem. Soc.*, 2004, **126**, 385
216. T. Sato, T. Tsuneda and K. Hirao, *J. Chem. Phys.*, 2005, **123**, 104307
217. M. Rubeš, O. Bludský and P. Nachtigall, *ChemPhysChem*, 2008, **9**, 1702-1708
218. D. G. de Oteyza, I. Silanes, M. Ruiz-Osés, E. Barrena, B. P. Doyle, A. Arnau, H. Dosch, Y. Wakayama and J. E. Ortega, *Adv. Funct. Mater.*, 2009, **19**, 259-264
219. V. J. Gandubert and R. B. Lennox, *Langmuir*, 2005, **21**, 6532
220. D. B. Dougherty, J. Lee and J. T. Yates Jr, *J. Phys. Chem. B*, 2006, **110**, 11991-11996
221. A. Dmitriev, N. Lin, J. Weckesser, J. V. Barth and K. Kern, *J. Phys. Chem. B*, 2002, **106**, 6907-6912
222. Y. Nosaka, M. Matsushita, J. Nishino and A. Y. Nosaka, *Sci. Technol. Adv. Mater.*, 2005, **6**, 143-148
223. J. Liqiang, S. Xiaojun, C. Weimin, X. Zili, D. Yaoguo and F. Honggang, *J. Phys. Chem. Solids*, 2003, **64**, 615-623
224. M. A. Kanjwal, N. A. M. Barakat, F. A. Sheikh and H. Y. Kim, *J. Mater. Sci.*, 2010, **45**, 1272-1279
225. A. B. Boffa, H. C. Galloway, P. W. Jacobs, J. J. Benítez, J. D. Batteas, M. Salmeron, A. T. Bell and G. A. Somorjai, *Surf. Sci.*, 1995, **326**, 80-92
226. V. Georgieva, H. Donkov, D. Spassov, I. Jordanova and A. Grechnikov, *J. Phys. Conf. Ser.*, 2010, **223**, 012025
227. G. Liu, W. Jaegermann, J. He, V. Sundström and L. Sun, *J. Phys. Chem. B*, 2002, **106**, 5814-5819
228. F. Zhang, S. Jin, Y. Mao, Z. Zheng, Y. Chen and X. Liu, *Thin Solid Films*, 1997, **310**, 29-33

229. S. Karakalos, A. Siokou, F. Sutara, T. Skala, F. Vitaliy, S. Ladas, K. Prince, V. Matolin and V. Chab, *J. Chem. Phys.*, 2010, **133**, 074701-11
230. L. E. Bailey, D. Kambhampati, K. K. Kanazawa, W. Knoll and C. W. Frank, *Langmuir*, 2002, **18**, 479-489
231. M. G. Manera, P. D. Cozzoli, M. L. Curri, G. Leo, R. Rella, A. Agostiano and L. Vasanelli, *Synth. Met.*, 2005, **148**, 25-29
232. L. V. Protsailo and W. R. Fawcett, *Electrochim. Acta*, 2000, **45**, 3497-3505

9.0 PUBLICATIONS AND CONFERENCES

1. G. J. Ashwell, A. T. Williams, **S. A. Barnes**, S. L. Chappell, L. J. Phillips, B. J. Robinson, B. Urasinska-Wojcik, P. Wierchowicz, I. R. Gentle, B. J. Wood, *J. Phys. Chem. C*, 2011, **115**, 4200–4208
 2. G. J. Ashwell, L. J. Phillips, B. J. Robinson, **S. A. Barnes**, A. T. Williams, B. Urasinska-Wojcik, C. J. Lambert, I. M. Grace, T. I. Cox, I. C. Sage, *Angew. Chem. Int. Ed.*, 2011, **50**, 8722–8726
-

1. International Conference on Materials for Advanced Technologies 2009, Singapore, *Growth of Functional Molecular Wires on Solid Supports*
2. British Council International Network of Young Scientists Initiative 2009, Singapore, *Growth of Functional Molecular Wires on Solid Supports*
3. Royal Society of Chemistry Young Scientist Symposium 2011, Wrexham, *Growth of Functional Molecular Wires on Solid Supports*

Self-Assembly of Amino–Thiols via Gold–Nitrogen Links and Consequence for in situ Elongation of Molecular Wires on Surface-Modified Electrodes

Geoffrey J. Ashwell,^{*,†,‡} Aled T. Williams,[‡] Susan A. Barnes,[‡] Sarah L. Chappell,[‡] Laurie J. Phillips,[‡] Benjamin J. Robinson,^{†,‡} Barbara Urasinska-Wojcik,[‡] Piotr Wierzchowicz,[‡] Ian R. Gentle,[§] and Barry J. Wood[§]

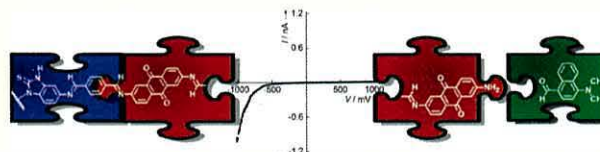
[†]Physics Department, Lancaster University, Lancaster LA1 4YB, U.K.

[‡]College of Physical and Applied Sciences, Bangor University, Gwynedd LL57 2UW, U.K.

[§]School of Chemistry and Molecular Biosciences, University of Queensland, Brisbane, Queensland 4072, Australia

Supporting Information

ABSTRACT: The stepwise synthesis of molecular wires on goldnanoparticles and gold electrodes has been performed using amino-terminated and aldehyde-terminated thiols as anchoring groups to provide surface-active sites for imino coupling. X-ray photoelectron spectroscopy provides evidence that 4-mercaptoaniline (**1**) binds via either substituent, Au–S–C₆H₄–NH₂ (N 1s, 400.1 eV) or Au–N(H₂)–C₆H₄–SH (N 1s, 399.1 eV), therefore depleting the number of reactive amine sites at the surface. In contrast, 4-[(4-mercaptophenylimino)methyl]benzaldehyde (**2**) binds exclusively via a thiolate link (Au–S–wire–CHO) and, in relation to the former, highlights the significance of the second substituent. Amines compete with thiols for self-assembly on gold and may even bond via deprotonated nitrogen. For instance, 4-[(*E*)-1,3-dihydro-2*H*-benzimidazol-2-thione-5-yl]imino[methyl]benzaldehyde (**3**) binds via a nitrogen of the imidazole ring and the self-assembled monolayer (SAM) exhibits a 2.2 eV shift of the N 1s binding energy (SAM, 398.3 eV; solid sample, 400.5 eV) compared with a 1.0 eV shift for **1**. Its in situ formed molecular wires with one to five bridged anthraquinone units exhibit symmetrical current–voltage characteristics, but the behavior alters to rectifying when the electron-accepting sequence is terminated by a 4-(dimethylamino)-1-naphthalene donor. Forward bias corresponds to electron flow from cathode to acceptor and from donor to anode, but the electrical asymmetry is dependent upon the number of bridging units. Molecules with two anthraquinones exhibit an optimum rectification ratio of 55 at ± 1 V.



INTRODUCTION

There is currently much interest in the stepwise synthesis of molecular wires on solid supports^{1–6} and its application to molecular electronic devices,^{7–12} as it affords subnanometer control of the length of the molecule which may be synthesized and elongated within the electrode gap. Hence, horizontally aligned metallic nanogaps on insulating substrates^{7–9} and vertically separated electrode structures, Au–SiO₂/Si₃N₄–Au^{10,11} and Si–SiO₂–Si,¹² have been bridged by activating the electrodes with anchoring groups that permit growth perpendicular to each (e.g., Si–CH=CH–C₆H₄–CHO on Si(111))¹² and, thereafter, by coupling chemical building blocks, for example, H₂N–wire–NH₂, in one step or alternating with OHC–wire–CHO in multistep processes. This modular approach contrasts with conventional techniques whereby molecular bridging is dependent upon the availability of self-assembling wire-like molecules that match the width of the preformed electrode gap. Moreover, it combines ease of synthesis with the means of modifying the current–voltage (*I*–*V*) characteristics by sequencing electron donors, bridges, and acceptors along the molecular backbone.^{5,11}

The chemistry of self-assembled monolayers (SAMs) is dependent upon the availability of reactive groups at the surface¹³ and the

subsequent stepwise coupling on solid supports is important for the multistep synthesis of complex molecules that may be unattainable by conventional means. It has been applied to conjugated materials and recent reports, albeit few in number, concern the electrical characterization of wire-like molecules synthesized via metal ion coordination of terpyridyl units,^{6,8} alkyne–azide click chemistry^{9,14} and, relevant to this study, use of Schiff base chemistry to form imine links between component units.^{1–5,10–12} Imino coupling at the solid–liquid interface was demonstrated by Horten et al.¹⁵ by exposure of an aldehyde-terminated SAM [Au–S–(CH₂)₄–CHO] to an ethanolic solution of an alkylamine at ambient temperature and has since been applied to the synthesis of π -conjugated molecular wires. However, among the frequently used anchoring molecules that provide a reactive surface is 4-mercaptoaniline (**1**),^{1,3,4,14} but as shown here, it binds to gold via either of its substituents. For the greater part, chemisorption is via the nitrogen which results in a

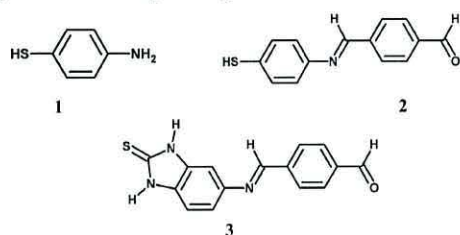
Received: January 1, 2011

Revised: January 11, 2011

Published: February 22, 2011

disordered arrangement and depletion of the surface-active amine sites for stepwise extension of these embryonic wires.

In what follows, we report the *in situ* synthesis of wire-like structures on gold nanoparticles and gold-coated substrates and note that it is prudent to use aldehyde-terminated thiols as the initial building block. In addition to **1**, we report stepwise elongation using the following anchoring molecules: 4-[(4-mercaptophenylimino)methyl]benzaldehyde (**2**) which adsorbs via a gold–thiolate link and 4-[(*E*)-1,3-dihydro-2*H*-benzimidazol-2-thione-5-yl]imino]methyl]benzaldehyde (**3**), which adsorbs via a nitrogen of its imidazole ring. SAMs of **3** exhibit symmetrical *I*–*V* characteristics when linked *in situ* to electron acceptors but show rectifying behavior when the sequence is terminated by an electron donor. The optimum rectification ratio of 55 at ± 1 V is significantly higher than values of ca. 2–6 often reported for molecular diodes^{16–20} and compares favorably with the highest ratio to date of 160 at ± 1 V, which was obtained for a σ -bridged donor–acceptor sequence.⁵



EXPERIMENTAL METHODS

Self-Assembling Precursor 2. 4-Mercaptoaniline (0.75 g, 6 mmol) and excess terephthalaldehyde (1.6 g, 12 mmol) were reacted in ethanol (50 cm³) for 3 h at ambient temperature with stirring. The solvent was removed *in vacuo* and the pale yellow product was recrystallized and washed with ethanol: yield, 90%; mp 215 °C. UV (C₂H₅OH): λ_{max} = 356 nm. IR (KBr): ν = 1691 cm^{−1} (C=O), 2550 cm^{−1} (S–H). XPS: S 2p_{3/2} 163.9 eV, S 2p_{1/2} 165.1 eV (SH), N 1s 399.0 eV (CH=N). Anal. Found: C, 69.3; H, 4.7; N, 5.4. Calcd for C₁₄H₁₁NOS: C, 69.69; H, 4.60; N, 5.81. MS: *m/z* (%), 241 (100) [M]⁺. Limited solubility did not permit NMR analysis.

Self-Assembling Precursor 3. 5-Aminobenzimidazole-2-thione (0.5 g, 3 mmol) and excess terephthalaldehyde (1.2 g, 9 mmol) were reacted in ethanol (70 cm³) for 3 h at ambient temperature with stirring. The solvent was reduced *in vacuo* to 50% of its original volume yielding 4-[(5-((benzimidazole-2-thione)imino)methyl]benzaldehyde as pale yellow microcrystals. The product was washed with ethanol and then recrystallized from acetone: yield, 75%; mp 241 °C; UV (C₂H₅OH): λ_{max} = 384 nm. IR (KBr): ν = 1610 cm^{−1} (C=N), 1697 cm^{−1} (C=O). XPS: S 2p_{3/2} 162.3 eV (C=S), S 2p_{1/2} 163.5 eV (C=S), N 1s 398.9 eV (CH=N), 400.5 (N–H). Anal. Found: C, 64.0; H, 3.8; N, 14.6. Calcd for C₁₅H₁₁N₃OS: C, 64.04; H, 3.94; N, 14.95. MS *m/z* (%): 280 (100) [M – H][−]. Limited solubility did not permit NMR analysis.

Capped Nanoparticles. Functionalized gold nanoparticles were prepared by adapting the method of Brust et al.²¹ Tetraoctylammonium bromide (2.2 g, 4 mmol) in toluene (100 cm³) was added to an aqueous solution (100 cm³) of gold(III) chloride trihydrate (0.32 g, 0.8 mmol, 50 cm³). The mixture was stirred to transfer auric chloride to the organic phase, to which 4-mercaptoaniline (0.25 g, 2 mmol) and then an aqueous

solution of sodium borohydride (0.76 g, 20 mmol, 50 cm³) were added with stirring. The organic phase was separated after 16 h, evaporated *in vacuo*, and the capped nanoparticles washed with water (2 × 30 cm³) and ethanol (2 × 30 cm³). They were treated alternately with chloroform solutions of terephthalaldehyde (0.40 g, 3 mmol, 50 cm³) and 2,6-diaminoanthra-9,10-quinone (0.72 g, 3 mmol, 50 cm³) for 48 h each at ambient temperature and the process repeated to yield molecular wires via Schiff base chemistry. Reaction with the dialdehyde yielded a CO stretch at 1690 cm^{−1} each time whereas subsequent reaction with the diamine resulted in its loss, consistent with efficient imine coupling at each stage of the reaction process.

RESULTS AND DISCUSSION

Amino–Thiol Anchoring Molecule (1). SAMs formed from 4-mercaptoaniline (HS–C₆H₄–NH₂)^{1,3,4,14} and its derivatives (e.g., HS–C₆H₄–C₆H₄–NH₂)² have been used as templates for the *in situ* synthesis of molecular wires on gold substrates by coupling the surface-based amine with aldehyde-terminated units and next amino-terminated units. They are not ideal candidates for use as initial building blocks and, from studies reported herein, we demonstrate that amino–thiols assemble on gold via either of the two substituents and that binding via the nitrogen atom may be as high as 70%. Thus, to avoid an inherently disordered arrangement and a depleted amine surface, it is preferable to use aldehyde-terminated thiols as initial building blocks for stepwise growth on gold supports.^{5,8,10,11}

The spontaneous attachment of amines to metallic surfaces^{22–25} is manifested by a lowering of the N 1s binding energy relative to ca. 400.0 eV obtained for bulk samples,²⁶ for example, to 399.3 eV for alkylamines on gold nanoparticles²² and 398.1 eV when electrochemically grafted to gold surfaces.²⁷ These shifts correspond to chemically distinctive N 1s binding modes, but the nature of the bonding is ambiguous. Theoretical studies have explored anchoring via a nitrogen lone pair, R–N(H₂)–Au,^{28,29} as well as via a deprotonated form, R–N(H)–Au, in which the molecule covalently bonds to the surface with a significant shortening of the N–Au bond length.²³ The latter was reported as energetically unfavorable, but unequivocal evidence of the different bonding types is provided by X-ray crystal structures of the cationic and neutral forms of gold(III) complexes of 2-(diphenylthiophosphino)aniline.³⁰ Their respective Au–N(H₂)–C and Au–N(H)–C motifs display a shortening of the dimensions of the deprotonated form (from 2.157 to 2.055 Å for Au–N and 1.448 to 1.358 Å for N–C) and broadening of the angle from 121.4 to 129.9°. Thus, the different types of bonding and potential coexistence should not be overlooked in the self-assembly of amines from solution.

X-ray photoelectron spectroscopy (XPS) studies on SAMs formed from amino–thiols confirm that both substituent groups compete for bonding with gold and exhibit analogous N 1s shifts, albeit attenuated by the presence of the unbound amine of thiolate bonded molecules. SAMs were formed by immersion of plasma cleaned gold-coated highly oriented pyrolytic graphite (HOPG) in acetone solutions of 4-mercaptoaniline (1 mg cm^{−3}) for 1 h whereafter physisorbed material was removed by washing with copious volumes of solvent. Spectra were recorded using a Kratos Axis Ultra spectrometer with an Al K α X-ray source ($h\nu$ = 1486.6 eV) operated at 15 kV and 150 W. Angle-resolved measurements were acquired at takeoff angles of 0, 30, and 80° relative to the substrate normal and axis of the analyzer lens with

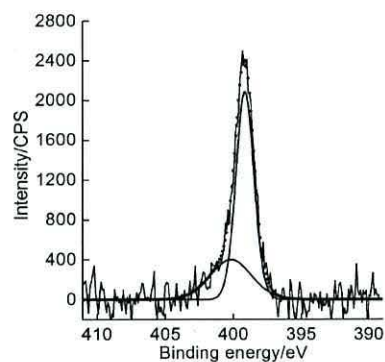


Figure 1. N 1s core level spectrum at a takeoff angle of 0° of a SAM formed from **1** on gold-coated HOPG. Peaks were located with all parameters unconstrained, and their combined spectra are represented by the dotted line.

pass energies of 160 eV at steps of 1 eV for survey scans and 40 eV at steps of 0.05 eV for high-resolution scans. Binding energies were referenced against the Au $4f_{7/2}$ peak at 84.0 eV and the spectra analyzed using CasaXPS MFC Application version 1.0.0.1 software. Peaks were located by using Gaussian–Lorentzian functions and, except where noted, the binding energies, areas under the curves, and full widths at half-maximum (fwhm) were unconstrained except for the customary 1.2 eV peak separation and 2:1 area ratio imposed on the S $2p_{3/2}$ and S $2p_{1/2}$ components of the sulfur doublet.

The N 1s spectrum of self-assembled 4-mercaptoaniline is asymmetric and exhibits a slight, albeit significant, shoulder on the high-energy side. Deconvolution indicates contributions from different nitrogen environments and, for each of the depth-sensitive takeoff angles of 0 and 30° , reveals peaks centered about 399.1 eV (Au–N) and 400.1 eV (NH_2) with area ratios of ca. 70:30 (Figure 1). The latter is characteristic of the binding energies of amines,²⁶ as expected for the parent molecule, and the 1 eV shift is consistent with results from previous studies on alkylamines bound to gold.^{22–25} The N 1s spectra suggest that ca. 70% of molecules bind to the substrate via the amine substituent, and this correlates with the S 2p spectra which show ca. 30% bind via gold thiolate links (Figure 2). This interpretation is supported by angle-resolved XPS studies at takeoff angles of 0, 30, and 80° relative to the substrate normal where the depth from which data are obtained diminishes as the photoelectron takeoff angle is increased. Deconvolution of the S 2p spectra provides evidence that the bound and unbound species locate on opposite sides of the film (Table 1). For example, data obtained for the two depth-sensitive angles, 0 and 30° , are almost indistinguishable, but when compared to those from grazing angle studies, 80° , the relative peak areas of the substrate-bound thiolate (S $2p_{3/2}$, 161.9 eV) decrease with increasing takeoff angle whereas those of the free thiol (S $2p_{3/2}$, 163.6 eV) and oxidized sulfur (S $2p_{3/2}$, 168 eV) increase. It suggests that both groups locate at the upper surface which is consistent with these self-assembling molecules being bound via the nitrogen. The high concentration of the oxidized form is a common occurrence and probably arises as a consequence of XPS studies being performed 2 weeks after film preparation and from the sulfur being located at the surface where it is vulnerable to oxidation.

In previous reports of XPS studies on SAMs formed from **1**, Sharma et al.³¹ alluded to bonding via the amine functionality in

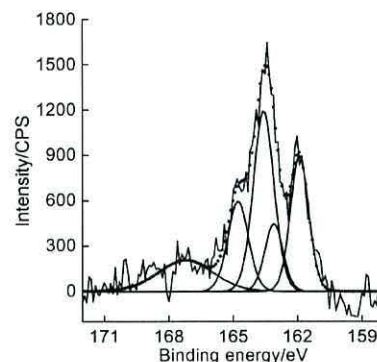


Figure 2. S 2p core level spectrum at a takeoff angle of 0° of a SAM formed from **1** on gold-coated HOPG. Doublets resulting from the substrate-bound and unbound species were located by applying a characteristic S $2p_{3/2}$ to S $2p_{1/2}$ peak area ratio of 2:1 and separation of 1.2 eV whereas the broad spectrum of the oxidized sulfur was fitted using a single peak with a fwhm of 3 eV. Their combined spectra are represented by the dotted line.

Table 1. Binding Energies (S $2p_{3/2}$ and S $2p_{1/2}$), Full Widths at Half-Maxima, and Relative Peak Areas for Different Sulfur Environments in SAMs of **1** and Dependence on Takeoff Angle

environment	angle/deg	binding energy/eV	fwhm/eV	% ^a
S 2p (Au–S)	0	161.9, 163.1	1.0	33
	30	161.9, 163.1	1.1	31
	80	161.8, 163.0	1.1	21
S 2p (SH)	0	163.6, 164.8	1.1	51
	30	163.5, 164.7	1.3	51
	80	163.6, 164.8	1.6	57
S 2p (SO_x)	0	167.2	3.0 ^b	16
	30	167.2	3.0 ^b	18
	80	168.5	3.0 ^b	22

^a Relative peak areas expressed as a percentage. ^b The $2p_{3/2}$ and $2p_{1/2}$ sublevels cannot be differentiated and a single peak was used to fit the SO_x spectrum.

capped nanoparticles whereas Rosink et al.¹ attributed the unbound thiol to molecules sandwiched between chemisorbed molecules without comment on the 1 eV shift of the N 1s peak relative to the binding energy normally associated with free amine. SAM **1** has been used as the initial building block for in situ growth of molecular wires on solid supports,^{13,4,14} but it is not an ideal candidate. Its growth axis is tilted ca. 60° from the substrate normal, and its films are inherently disordered as a result of the alternative types of attachment. Nonetheless, the depleted amine surface is reactive and, as part of this investigation, wire-like molecules were synthesized on gold nanoparticles capped by **1** by reacting first terephthalaldehyde (OHC–wire–CHO) and then 2,6-diaminoanthra-9,10-quinone (H_2N –wire– NH_2) from THF solutions to which catalytic traces of glacial acetic acid were added. Stepwise coupling via imine links is indicated by infrared spectra of the capped nanoparticles which show emergence and subsequent loss of a CO stretch at 1690 cm^{-1} following reaction with aldehyde and amino-terminated units, respectively (Figure 3).

Aldehyde–Thiol Anchoring Molecule (2). To avoid inherently disordered arrangements, as above, the aldehyde-terminated

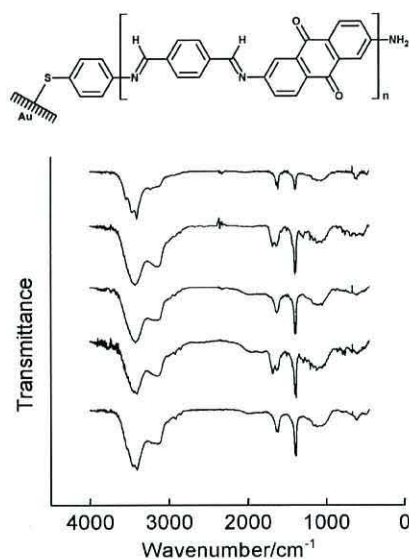


Figure 3. Structure of the molecular wire and normalized transmittance (arbitrary units) vs wavenumber at each stage of its stepwise growth. The spectra are offset and, in decreasing order, correspond to gold nanoparticles capped by **1** (step 1) and coupled in turn with terephthalaldehyde (steps 2 and 4) and 2,6-diaminoanthra-9,10-quinone (steps 3 and 5). FTIR spectra were recorded for nanoparticles dispersed in KBr.

thiol that corresponds to the molecule formed from the first stage of in situ coupling, 4-[(4-mercaptophenylimino)methyl]benzaldehyde, was synthesized ex situ and adsorbed from acetone (1 mg cm^{-3}) on gold-coated HOPG and Au(111) on mica. Plasma cleaned substrates were immersed for 1 h and then washed with copious volumes of solvent to remove physisorbed material. Chemisorption is confirmed by XPS, which yields a symmetrical nitrogen peak at 399.0 eV (N 1s, $\text{CH}=\text{N}$) and a characteristic sulfur doublet at 162.1 and 163.3 eV (S 2p, $\text{Au}-\text{S}$). It is also demonstrated by scanning tunneling microscopy which shows the thiolate-linked molecule to be tilted toward the substrate, probably by ca. 60° for an $\text{Au}-\text{S}-\text{C}$ angle of 120° , and packed in rows with a mean intermolecular spacing of 0.56 nm and an area of $0.59 \text{ nm}^2 \text{ molecule}^{-1}$ (Supporting Information). The reactive aldehyde surface of the film acts as a template for in situ growth and wires, analogous to those shown in Figure 3, were synthesized by coupling first 2,6-diaminoanthra-9,10-quinone and then terephthalaldehyde and, thereafter, by repeating these steps. Substrates were immersed in THF solutions of each and washed with pure solvent, and reaction was monitored at each stage from the frequency change for growth on the electrodes of 10 MHz crystals.

The electrical properties were investigated by scanning tunneling spectroscopy using contacting gold probes. Data were obtained at different locations across each of the films and averaged each time from multiple scans on the same spot. The $I-V$ profile was found to be almost independent of the experimental range of set point conditions (600 pA at 80–300 mV), which affect the magnitude of the current by altering the distance between the probe and surface but appear to have minimal effect on the shape of the curve. The anthraquinone-terminated wire (see Figure 3) exhibits slight electrical asymmetry as a consequence of the electron-accepting tail on one side and weakly electron-donating thiolate link on the other and the bias for higher current corresponds to electron flow from the cathode to acceptor and donor to anode (Figure 4). However, when the

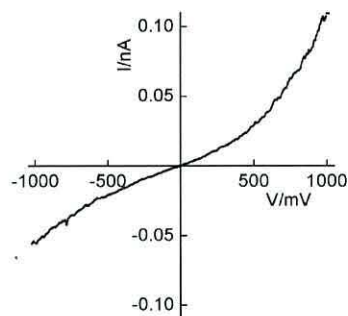


Figure 4. $I-V$ characteristics of the molecular wire shown in Figure 3 where $n = 2$. It was synthesized by self-assembly of **2** on gold-coated HOPG (step 1) and coupling sequentially with 2,6-diaminoanthra-9,10-quinone (steps 2 and 4) and terephthalaldehyde (step 3). The slight electrical asymmetry is reproducible and the higher current at positive bias corresponds to electron flow from the gold STM probe to gold substrate.

electron-accepting sequence is terminated by a donor, for example, by coupling with 4-(dimethylamino)-1-naphthaldehyde, electrical asymmetry is maintained but at opposite bias.

Benzimidazol-2-thione Anchoring Molecule (3). The anchoring molecule was adsorbed on gold by immersing plasma cleaned substrates for ca. 1 h in an acetone solution of 4-[(*E*)-1,3-dihydro-2*H*-benzimidazol-2-thione-5-yl]imino]methyl]benzaldehyde (0.1 mg cm^{-3}) and then rinsing with copious volumes of solvent to remove physisorbed material. Chemisorption was confirmed by XPS but, unlike most other sulfur-containing molecules, its S 2p spectra cannot be used to verify binding to gold as the precursor occurs not as a thiol but as a thione.^{32,33} Its powdered samples exhibit peaks at 162.3 eV (S $2p_{3/2}$) and 163.5 eV (S $2p_{1/2}$), consistent with the binding energies of sulfur in thiourea,³⁴ and the data are indistinguishable from those of gold thiolate links. For the chemisorbed film, we refer instead to the N 1s spectrum which provides an indication of the potential binding. Deconvolution using a two-peak fitting routine revealed binding energies of 398.3 and 399.8 eV with a peak area ratio of 2:1 and fwhm of 1.4 and 1.9 eV, respectively. We attribute the former to an $\text{Au}-\text{N}$ link (cf. 398.1 eV for *n*-butylamine electrochemically grafted to gold)²⁷ and note that the latter, which corresponds to two nitrogens, falls midway between the NH and $\text{C}=\text{N}$ peaks of the powdered forms of **3**. Deconvolution using a three-peak fitting routine was achieved by applying equal areas, consistent with the three different nitrogen environments within the molecule, as well as equal peak widths to each (Figure 5). It gave binding energies of 398.3 eV ($\text{Au}-\text{N}$), 399.3 eV ($\text{CH}=\text{N}$), and 400.2 eV (NH) and the N 1s core level spectra conform to the anchored structures shown in Figure 6.

Assembly via a thiolate link with rotation about the $\text{S}-\text{C}$ single bond would bring the benzimidazole nitrogen within bonding distance of the substrate and, based on the low-energy N 1s peak at 398.3 eV, it is assumed that **3** binds to the substrate via either an $\text{Au}-\text{N}$ link alone or with an $\text{Au}-\text{S}$ link as shown in Figure 6. It has been reported that benzimidazole-2-thione and benzthiazole-2-thione adopt bidentate geometries when chemisorbed on gold^{35,36} and the X-ray crystal structure of a cationic Au(I) complex of the former shows bonding identical to the arrangement in Figure 6 with $\text{Au}-\text{N}$ and $\text{Au}-\text{S}$ bond lengths of 2.050 and 2.316 Å, respectively.³⁷ Moreover, in this work, covalent bonding via a nitrogen link is also evident from XPS studies of an

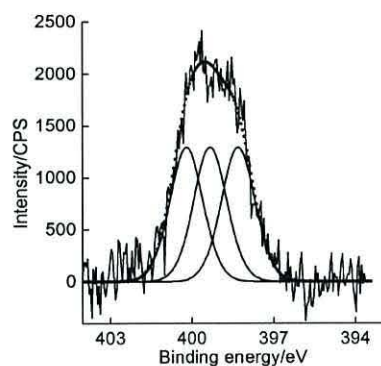


Figure 5. N 1s core level spectrum of **3** anchored on gold-coated HOPG. Peak location was achieved by applying equal areas and widths to each, but significantly, the binding energy (398.3 eV) and fwhm (1.4 eV) of the low-energy peak are consistent with those obtained using an unconstrained two-peak fitting routine.

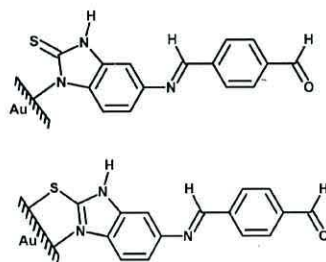


Figure 6. Potential structures of neutral and cationic forms of the chemisorbed molecule consistent with the N 1s (NH, C=N and Au—N link) and S 2p (C=S or Au—S) core level spectra, but the latter also shows 30–50% SO_x , which suggests that the gold thiolate link is broken in many instances.

embryonic molecular wire, formed in situ by reaction with 2,6-diaminoanthra-9,10-quinone and whose N 1s spectra exhibit a well-defined low-energy shoulder (Figure 7). Deconvolution using a three-peak fitting routine with the areas constrained by the ratio of the three different nitrogen environments within the molecule yields peaks at 397.7 eV (Au—N), 398.8 eV ($\text{CH}=\text{N} \times 2$) and 400.0 eV (NH and NH_2). The low-energy Au—N peak is shifted by 0.6 eV relative to the binding energy of the initially formed SAM, which may be attributed to electron transfer between the imidazole ring and electron-accepting anthraquinone tail as the shift is reversed when the film is reacted subsequently with electron-donating 4-(dimethylamino)-1-naphthaldehyde. The N 1s data for SAM **3** including its stepwise-formed wires (cf. 399.1 eV for SAM **1**) may be compared with the limiting value of 397.0 eV for gold nitride,³⁸ and we draw a parallel with the relation between binding energy and bonding distance which has been demonstrated for metal amido, imido, and nitrido complexes.³⁹ The low-energy shift provides evidence of covalent bonding via an imidazole nitrogen, but we are less confident of binding via a thiolate link. Ambiguity arises from the almost identical S 2p binding energies of the SAM (S $2p_{3/2}$ 162.1 eV) and thione group of the solid sample of **3** (S $2p_{3/2}$ 162.3 eV, C=S) as well as from XPS studies performed 3 weeks after initial assembly which exhibit unusually high concentrations of oxidized sulfur (Figure 7). Typical values are 30–50% of the total, which indicates that many molecules are not bound via Au—S

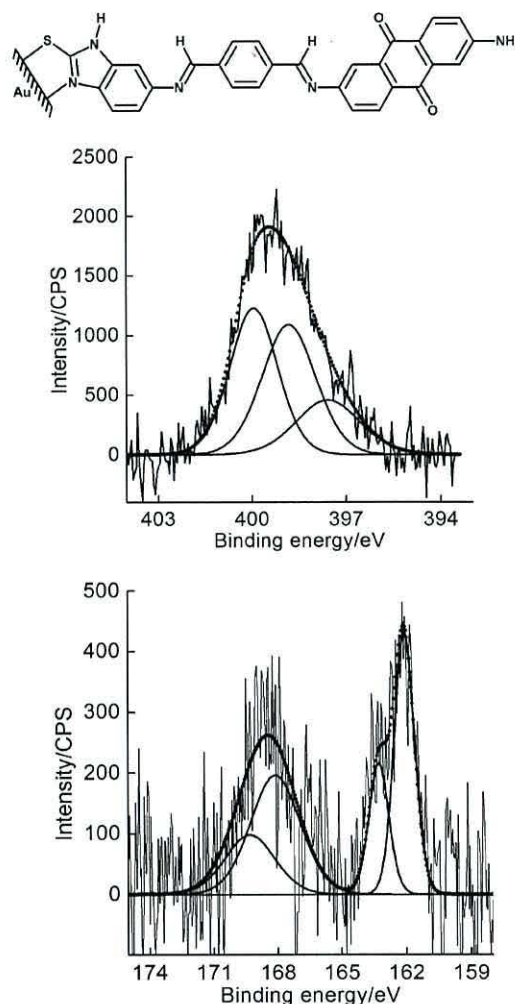


Figure 7. Molecular structure of an embryonic molecular wire (top) formed in situ from the reaction of SAM **3** and 2,6-diaminoanthra-9,10-quinone and its N 1s (middle) and S 2p (bottom) core level spectra. N 1s peaks were located by applying a 1:2:2 area ratio to the three different nitrogen environments and the S 2p doublets by applying a characteristic S $2p_{3/2}$ to S $2p_{1/2}$ peak area ratio of 2:1 and separation of 1.2 eV.

links and it is feasible that the oxidized group acts as a counterion for cationic forms of the molecule.

Following the self-assembly of **3** on gold-coated HOPG to provide a reactive aldehyde surface, stepwise elongation of this embryonic molecular wire was performed by sequential immersion of the coated substrate in solutions of 2,6-diaminoanthra-9,10-quinone (0.1 mg cm^{-3} , THF) and terephthalaldehyde (0.1 mg cm^{-3} , ethanol) to which catalytic traces of acetic acid were added. Electron-accepting wires with one to five anthraquinone units were synthesized, and the sequence terminated by immersion in a solution of 4-(dimethylamino)-1-naphthaldehyde (0.1 mg cm^{-3} , THF) to provide acceptor–donor structures. Reaction times were optimized from studies of in situ synthesis on the gold electrodes of 10 MHz quartz crystals, and prior to measurement, substrates were washed with copious volumes of solvent to remove physisorbed material and air-dried. Stoichiometric coupling is indicated by the frequency change which varies linearly with the molecular weight of the stepwise formed wire. It is

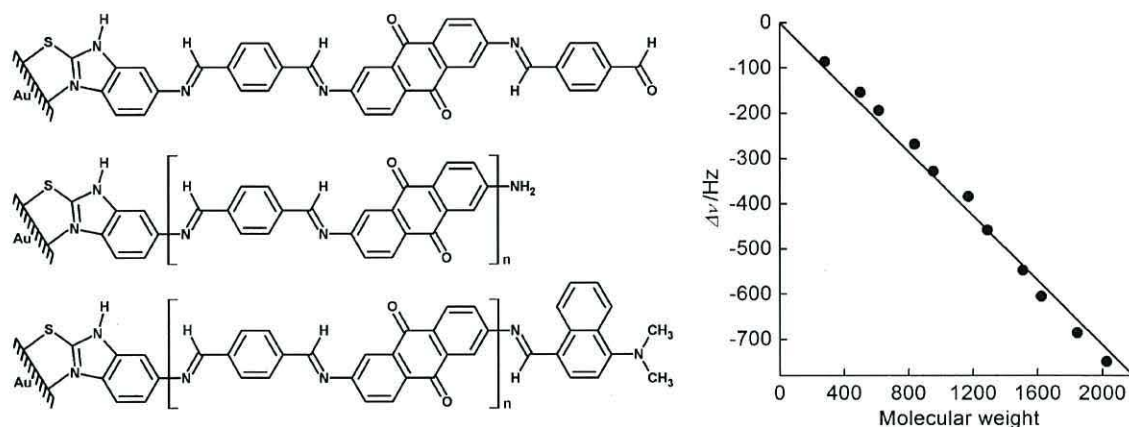


Figure 8. Molecular structures of wire-like oligomers (left) and variation of the frequency change with molecular weight at each stage of the formation of an acceptor–donor wire with five bridged anthraquinone units when synthesized on the gold electrodes of a 10 MHz quartz crystal (right). Following self-assembly of 3 (step 1), elongation was performed by immersing the coated substrates in solutions of the following molecular building blocks: 2,6-diaminoanthra-9,10-quinone (steps 2, 4, 6, 8, 10), terephthalaldehyde (steps 3, 5, 7, 9), and 4-dimethylamino-1-naphthaldehyde (step 11). Immersion was prolonged until there was no further change in frequency following rinsing with copious volumes of solvent and drying in air.

illustrated in Figure 8 which displays the frequency data for each of the 11 reaction steps of a 10.5 nm long wire with five bridged anthraquinone units and terminated by 4-(dimethylamino)-naphthalene. The frequency is affected by the mass of the coating as well as solvent trapped in the film, and we note that the linear dependence, as shown, is not evident from all studies on stepwise-formed wires.

Electrical properties at different stages of the growth of stepwise-formed molecular wires shown in Figure 8 were investigated by scanning tunneling spectroscopy using contacting gold probes and a set point current and voltage of 600 pA at 80 mV. They were obtained at different locations across each of the films with the data averaged for multiple scans on the same spot. I – V characteristics of each of the electron-accepting wires with one to five bridged anthraquinones appear symmetrical but exhibit imperceptibly higher currents at negative substrate bias (Figure 9). This contrasts with the more pronounced electrical asymmetry from analogous wire-like sequences formed from SAM 2 where the higher current, which occurs at positive substrate bias, arises from a weakly electron-donating anchoring group (Figure 4). However, this time, the bridged benzimidazole/anthraquinone combination is well-matched and, when coupled to an extended anthraquinone tail and terminated by a 4-(dimethylamino)naphthalene donor, the in situ formed wires exhibit rectifying behavior as expected for Au/acceptor–donor/Au sequences. The direction of electron flow at forward bias is from the gold substrate (cathode) to electron-accepting end of the wire and from the electron-donating end to gold probe (anode) and the electrical asymmetry arises from a mismatch between the Fermi energies of the electrodes and adjacent molecular energy levels at opposite bias. Rectification ratios of ca. 55 at ± 1 V were obtained for molecules with two anthraquinones (Figure 10), which is high compared with many of those reported for molecular diodes.^{40–43} Ratios of 2–6 at ± 1 V are customary,^{16–20} and we note that the observed value compares favorably with the highest to date: 160 at ± 1 V for a σ -bridged donor–acceptor wire⁵ and 50–150 at ± 1 V for a donor–(π -bridge)–acceptor molecule in which a sterically hindered nonplanar arrangement plays a pivotal role in improving rectification by maintaining the integrity of the electron-donating and electron-accepting

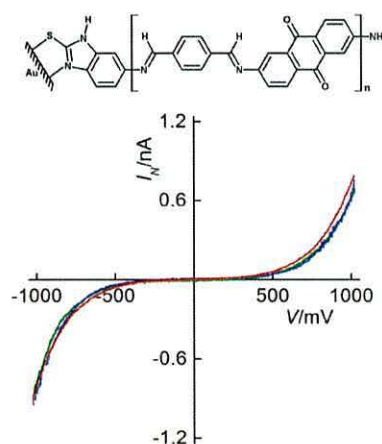


Figure 9. Molecular structure of a stepwise-formed oligomer and normalized I – V plots of films at different stages of formation: $n = 1$ (red), $n = 2$ (blue), and $n = 3$ (green). The sign corresponds to the substrate electrode, and the current is normalized to that of the first oligomer at -1 V. The almost identical I – V profiles are unexpected.

ends.⁴⁴ Higher values still have been obtained for organic bilayer arrangements,⁴⁵ but they may be classified as rectifying junctions rather than molecular diodes.

Molecular rectification requires an aligned acceptor–donor sequence: the anchoring group and anthraquinone combination are electron-accepting and the integrity of the electron-donating side is retained by sterically induced out-of-plane rotations of the bulky double-ring (dimethylamino)naphthalene moiety. Steric hindrance has been used to enhance the rectification from cationic donor–(π -bridge)–acceptor dyes,⁴⁴ and its efficacy is implied by the electrical asymmetry shown in Figure 10. However, the behavior is dependent upon the number of bridged anthraquinones: the first member of the series ($n = 1$) exhibits a rectification ratio of ca. 3 at ± 1 V, which is anomalous, and ratios for the longer analogues, ca. 55 at ± 1 V ($n = 2$), ca. 7 at ± 1 V ($n = 3$), and ca. 2 at ± 1 V ($4 \leq n \leq 5$), diminish with increasing molecular length. These differences cannot be explained simply from the energy mismatch at reverse bias but are attributed

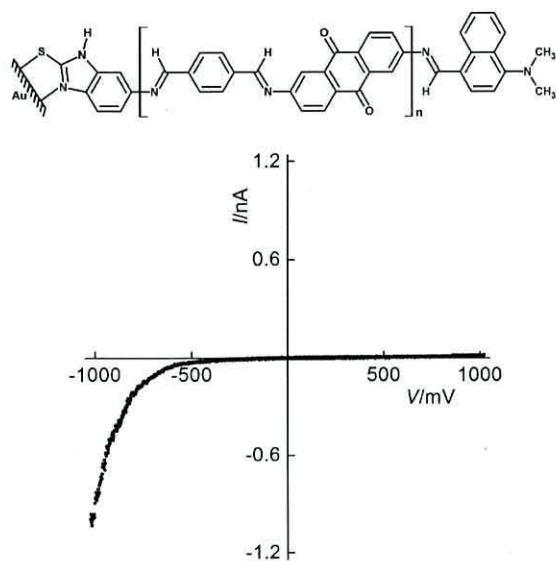


Figure 10. Molecular structure of a donor–acceptor wire and I – V characteristics of the oligomer with two bridged anthraquinones ($n = 2$). Analogues where $n = 1, 3, 4$, and 5 exhibit diminished rectification ratios, but the direction of electron flow at forward bias is consistent in each case. The sign corresponds to the substrate electrode.

instead to the electron-accepting anthraquinone sequence and its effect on the end group interfacing with the substrate electrode and, in part, to an electric field dependence to compensate for length. There have been reports of a crossover from tunneling to hopping as the lengths of oligo(*p*-phenylene ethynylene)⁴⁶ and oligophenylene-imine^{3,4} exceed 2.8 and 4.0 nm, respectively, with their currents displaying an exponential dependence, $I \propto e^{-\beta l}$ where β is a decay constant, below the threshold and a reciprocal length dependence, $I \propto l^{-1}$, in the hopping regime. Our rectifying wires range from 3.4 to 10.5 nm and thus, assuming an $I \propto l^{-1}$ dependence, it may be appropriate for the rectification ratio to be evaluated against field rather than voltage. Consistent with this, the ratio decreases from 55 at ± 1 V for the second shortest ($l = 5.2$ nm) to 7 at ± 1 V for the third ($l = 7.0$ nm), but the 8-fold discrepancy is reduced by a factor of 4 when compared at ± 143 MV m⁻¹ (Figure 11), which is equivalent to a voltage drop of 1 V across the length of the longer wire. I – E profiles for analogues where $2 \leq n \leq 5$ are alike at forward bias (negative quadrant) but exhibit slight disparity at reverse bias (positive quadrant) resulting in rectification ratios of 2 to 3 at ± 96 MV m⁻¹, which corresponds to the experimental limit of electric field for the longest wire. Although evaluation against field reduces the discrepancy, this does not apply to the first member of the series (red curve, Figure 11) where the data suggest that the anchoring group coupled to a single anthraquinone is a weak acceptor and reduces rectification from the acceptor–donor arrangement.

Summary of N 1s Shifts. The influence of a gold surface on the XPS spectra of **3** is manifested by a lowering of the N 1s binding energy to 398.3 eV (cf. 400.5 eV for NH in the parent compound) and corresponds to the molecule being covalently bonded to the surface. Likewise, the N 1s binding energy of **1** is shifted to 399.1 eV (bound, 70%) with a less intense peak at 400.0 eV (unbound, 30%), and we draw a parallel with the angle-resolved

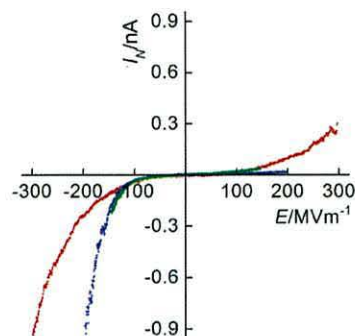


Figure 11. Normalized current vs electric field of rectifying acceptor–donor oligomers whose molecular structure is shown in Figure 10 and has one (red, $n = 1$), two (blue, $n = 2$), and three (green, $n = 3$) bridged anthraquinones. The current is normalized to that of the second oligomer at $E = -50$ MV m⁻¹ where the lengths used to calculate electric field correspond to the distances between the anchored nitrogen and the hydrogens of the dimethylamino group including the van der Waals radii of each. Data for analogues where $4 \leq n \leq 5$ overlap the blue curve but, for clarity, are excluded from the plot.

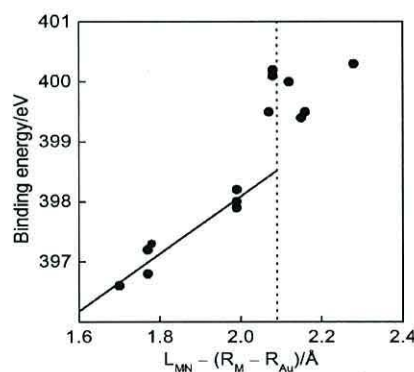


Figure 12. N 1s binding energies vs normalized metal–nitrogen distances where L_{MN} is the bond length from X-ray crystal structures of the metal complexes, R_M and R_{Au} are the covalent radii of the metal atom and gold, respectively, and the dotted line corresponds to the sum of the bonding radii of Au (1.34 Å) and N (0.75 Å). Nitrogen environments: Cr≡N (396.6 eV);³⁹ W=N–C (397.3 eV);³⁹ Ta=N–C (396.8–397.2 eV);³⁹ Ta–N (397.9–398.2 eV);³⁹ Cu(phen)₂ (399.4–399.5 eV);⁴⁷ Ag–N (400.0 eV);^{48–50} Pd–N (399.5 eV);⁵¹ Pd–NH₃ (400.1–400.2 eV);^{51,52} Pt–NH₃ (400.3 eV).^{53,54} From the data in this figure, the binding energy of 398.3 eV for SAM **3**, which shifts to 397.7 eV when the molecules are coupled in situ with an electron-accepting tail, approximates to an Au–N bond length of 2.0 Å.

S 2p spectra which confirm a preponderance of unbound thiol and oxidized sulfur at the upper surface. Binding energies of 399.1 eV for **1** and 398.3 eV for **3** are each assigned to adsorption, the former via the nitrogen lone pair of the amine functionality and the latter via an Au–N link. The disparity in binding interaction probably arises from altered bonding distances and, consistent with this, Wu et al.³⁹ have reported a linear dependence between the N 1s binding energies of metal nitride (Cr≡N), imido (Ta=N, W=N), and amido (Ta–N) complexes and the metal–nitrogen bond lengths normalized for the covalent bonding radii of each. This relation is demonstrated in Figure 12 which includes data from ref³⁹ as well as N 1s binding energies of Pd, Pt, Cu, and Ag coordination complexes for which X-ray

crystallographic data are available.^{47–54} We find that the reported linear dependence is limited to metal–nitrogen bond lengths shorter than the sum of the covalent radii whereas, for weaker interaction, the N 1s binding energies (e.g., Pt(NH₃)₄X₂, 400.3 eV)⁵⁴ resemble those of uncoordinated ligands.²⁶ As a ballpark approximation, the Au–N bonding distances within the SAMs may be estimated from the N 1s spectra by comparison with the data in Figure 12. For example, the peak at 398.3 eV for SAM 3 corresponds to a bonding distance of ca. 2.0 Å, which is consistent with the lower end of the bond length range from X-ray crystallographic studies of gold complexes (1.94 Å ≤ L_{Au–N} ≤ 2.25 Å).^{30,37,55–62} In contrast, the peak at 399.1 eV for SAM 1, which is customary for amines on gold,^{22–24} corresponds to a longer bonding distance of ca. 2.1 Å and is in reasonable agreement with 2.157 Å obtained for the Au–NH₂ motif in the X-ray crystal structure of the Au(III) complex of 2-(diphenyl-thiophosphino)aniline.³⁰

CONCLUSIONS

The XPS data confirm the assembly of aminothiols via either of the two substituents and samples reported herein indicate ca. 30% via a thiolate link and 70% via an amine link for 1 and, for example, a 60:40 ratio in SAMs formed from the meta-substituted isomer, 3-mercaptoaniline (see Supporting Information).⁶³ Despite the depleted amine surface and inherent disorder, the SAMs^{3,4,14} may be used as a template for in situ synthesis of molecular wires but, as the number of surface-active sites is variable, this may be problematic when comparing subtle differences in their solid state properties. It is preferable to use an aldehyde-terminated thiol (2) as the initial building block and, in particular, the meta-substituted^{5,10,11} rather than para-substituted isomer to achieve wire-like growth perpendicular to the substrate. Oligomers have been formed in situ on gold-coated substrates functionalized by 4-[(4-mercaptophenylimino)methyl]benzaldehyde (2) and 4-[(E)-1,3-dihydro-2H-benzimidazol-2-thione-5-yl]imino[methyl]benzaldehyde (3). Those formed from the latter act as molecular diodes and exhibit an optimum rectification ratio of 55 at ±1 V when linked to an anthraquinone tail terminated by a (dimethylamino)naphthalene donor. Rectification arises from an energy mismatch between the Fermi levels and molecular levels at reverse bias, and the current ratio compares favorably with the highest to date of 160 at ±1 V for a donor–acceptor sequence separated by a σ-electron bridge.⁵

ASSOCIATED CONTENT

S Supporting Information. N 1s and S 2p core level spectra, alternative peak fitting of the XPS data, and I–V characteristics of in situ formed wires. This material is available free of charge via the Internet at <http://pubs.acs.org>.

AUTHOR INFORMATION

Corresponding Author

*E-mail: g.j.ashwell@lancaster.ac.uk.

ACKNOWLEDGMENT

We thank the EPSRC and EC FP7 ITN “FUNMOLS” Project No. 212942 for financial support and the EPSRC-funded XPS Access Facility at Cardiff University for analytical data.

REFERENCES

- (1) Rosink, J. J. W. M.; Blauw, M. A.; Geerligs, L. J.; van der Drift, E.; Rousseeuw, B. A. C.; Radelaar, S. *Langmuir* **2000**, *16*, 4547–4553.
- (2) Luo, Y.; Piantek, M.; Miguel, J.; Bernien, M.; Kuch, W.; Haag, R. *Appl. Phys. A: Mater. Sci. Process.* **2008**, *93*, 293–301.
- (3) Choi, S. H.; Kim, B. S.; Frisbie, C. D. *Science* **2008**, *320*, 1482–1486.
- (4) Choi, S. H.; Risko, C.; Ruiz Delgado, M. C.; Kim, B.; Bredas, J.-L.; Frisbie, C. D. *J. Am. Chem. Soc.* **2010**, *132*, 4358–4368.
- (5) Ashwell, G. J.; Urasinska-Wojcik, B.; Phillips, L. J. *Angew. Chem., Int. Ed.* **2010**, *49*, 3508–3512.
- (6) Tuccitto, N.; Ferri, V.; Cavazzini, M.; Quici, S.; Zhavnerko, G.; Licciardello, A.; Rampi, M. A. *Nat. Mater.* **2009**, *8*, 41–46.
- (7) Taniguchi, M.; Nojima, Y.; Yokota, K.; Terao, J.; Sato, K.; Kambe, N.; Kawai, T. *J. Am. Chem. Soc.* **2006**, *128*, 15062–15063.
- (8) Tang, J.; Wang, Y.; Klare, J. E.; Tulevski, G. S.; Wind, S. J.; Nuckolls, C. *Angew. Chem., Int. Ed.* **2007**, *46*, 3892–3895.
- (9) Chen, X.; Braunschweig, A. B.; Wiester, M. J.; Yeganeh, S.; Ratner, M. A.; Mirkin, C. A. *Angew. Chem., Int. Ed.* **2009**, *48*, 5178–5181.
- (10) Ashwell, G. J.; Wierzchowiec, P.; Bartlett, C. J.; Buckle, P. D. *Chem. Commun.* **2007**, 1254–1256.
- (11) Ashwell, G. J.; Wierzchowiec, P.; Phillips, L. J.; Collins, C.; Gigon, J.; Robinson, B. J.; Finch, C. M.; Grace, I. M.; Lambert, C. J.; Buckle, P. D.; Ford, K.; Wood, B. J.; Gentle, I. R. *Phys. Chem. Chem. Phys.* **2008**, *10*, 1859–1866.
- (12) Ashwell, G. J.; Phillips, L. J.; Robinson, B. J.; Urasinska-Wojcik, B.; Lambert, C. J.; Grace, I. M.; Bryce, M. R.; Jitchati, R.; Tavasli, M.; Cox, T. I.; Sage, I. C.; Tuffin, R. P.; Ray, S. *ACS Nano* **2010**, *4*, 7401–7406.
- (13) Sullivan, T. P.; Huck, W. T. S. *Eur. J. Org. Chem.* **2003**, 17–29.
- (14) Luo, L.; Frisbie, C. D. *J. Am. Chem. Soc.* **2010**, *132*, 8854–8855.
- (15) Horton, R. C.; Herne, T. M.; Myles, M. C. *J. Am. Chem. Soc.* **1997**, *119*, 12980–12981.
- (16) Díez-Pérez, I.; Hihath, J.; Lee, Y.; Yu, L.; Adamska, L.; Kozhushner, M. A.; Oleynik, I. I.; Tao, N. J. *Nat. Chem.* **2009**, *1*, 635–641.
- (17) Elbing, M.; Ochs, R.; Koentopp, M.; Fischer, M.; von Hanisch, C.; Weigend, F.; Evers, F.; Weber, H. B.; Mayor, M. *Proc. Natl. Acad. Sci. U.S.A.* **2005**, *102*, 8815–8820.
- (18) Jiang, P.; Morales, G. M.; You, W.; Yu, L. P. *Angew. Chem., Int. Ed.* **2004**, *43*, 4471–4475.
- (19) Ng, M.-K.; Yu, L. *Angew. Chem., Int. Ed.* **2002**, *41*, 3598–3601.
- (20) Ng, M.-K.; Lee, D.-C.; Yu, L. P. *J. Am. Chem. Soc.* **2002**, *124*, 11862–11863.
- (21) Brust, M.; Walker, M.; Bethell, D.; Schiffrin, D. J.; Whyman, R. *Chem. Commun.* **1994**, 80–802.
- (22) Kumar, A.; Mandal, S.; Selvakannan, P. R.; Pasricha, R.; Mandale, A. B.; Sastry, M. *Langmuir* **2003**, *19*, 6277–6282.
- (23) Aslam, M.; Fu, L.; Su, M.; Vijayamohan, K.; Dravid, V. P. *J. Mater. Chem.* **2004**, *14*, 1795–1797.
- (24) Weigelt, S.; Schnadt, J.; Tuxen, A. K.; Masini, F.; Bombis, C.; Busse, C.; Isvoranu, C.; Ataman, E.; Lægsgaard, E.; Besenbacher, F.; Linderoth, T. R. *J. Am. Chem. Soc.* **2008**, *130*, 5388–5389.
- (25) Gallardo, I.; Pinson, J.; Vilà, N. *J. Phys. Chem. B* **2006**, *110*, 19521–19529.
- (26) National Institute of Standards and Technology (NIST) X-ray photoelectron spectroscopy database (<http://srdata.nist.gov/xps/default.aspx>).
- (27) Adenier, A.; Chehimi, M. M.; Gallardo, I.; Pinson, J.; Vilà, N. *Langmuir* **2004**, *20*, 8243–8253.
- (28) Fagas, G.; Greer, J. C. *Nanotechnology* **2007**, *18*, No. 424010.
- (29) Quek, S. Y.; Venkataraman, L.; Choi, H. J.; Louie, S. G.; Hybertsen, M. S.; Neaton, J. B. *Nano Lett.* **2007**, *7*, 3477–3482.
- (30) Fernández, E. J.; García-Luzuriaga, E.; Laguna, A.; López-de-Luzuriaga, J. M.; Olmos, M. E. *Gold Bull.* **2010**, *43*, 80–87.
- (31) Sharma, J.; Mahima, S.; Kakade, B. A.; Pasricha, R.; Mandale, A. B. *J. Phys. Chem. B* **2004**, *108*, 13280–13286.

- (32) Form, G. R.; Raper, E. S.; Downie, T. C. *Acta Crystallogr.* **1976**, B32, 345–348.
- (33) Kitano, Y.; Ishitani, A.; Sato, H.; Imamura, S.; Ashida, T. *Acta Crystallogr.* **1991**, C47, 1269–1271.
- (34) Luck, S.; Foerch, R.; Sales, K. D.; Urch, D. S. *J. Chem. Soc., Faraday Trans. 1* **1989**, 85, 4129–4137.
- (35) Ansar, S. M.; Haputhanthri, R.; Edmonds, B.; Liu, D.; Yu, L.; Sygula, A.; Zhang, D. *J. Phys. Chem. C* **2011**, 115, 653–660.
- (36) Beattie, D. A.; Kempson, I. M.; Fan, L. J.; Skinner, W. M. *Int. J. Miner. Process* **2009**, 92, 162–168.
- (37) Schneider, J.; Lee, Y.-A.; Pérez, J.; Brennessel, W. W.; Flaschenriem, C.; Eisenberg, R. *Inorg. Chem.* **2008**, 47, 957–968.
- (38) Butenko, Y. V.; Alves, L.; Brieva, A. C.; Yang, J.; Krishnamurthy, S.; Siller, L. *Chem. Phys. Lett.* **2006**, 430, 89–92.
- (39) Wu, J.-B.; Lin, Y. F.; Wang, J.; Chang, P. J.; Tasi, C. P.; Lu, C. C.; Chiu, H. T.; Yang, Y. W. *Inorg. Chem.* **2003**, 42, 4516–4518.
- (40) Honciuc, A.; Jaiswal, A.; Gong, A.; Ashworth, H.; Spangler, C. W.; Peterson, I. R.; Dalton, L. R.; Metzger, R. M. *J. Phys. Chem. B* **2005**, 109, 857–871.
- (41) Metzger, R. M.; Xu, T.; Peterson, I. R. *J. Phys. Chem. B* **2001**, 105, 7280–7290.
- (42) Ashwell, G. J.; Tyrrell, W. D.; Whittam, A. J. *J. Am. Chem. Soc.* **2004**, 126, 7102–7110.
- (43) Ashwell, G. J.; Gandolfo, D. S.; Hamilton, R. J. *Mater. Chem.* **2002**, 12, 416–420.
- (44) Ashwell, G. J.; Mohib, A. J. *Am. Chem. Soc.* **2005**, 127, 16238–16244.
- (45) Ashwell, G. J.; Urasinska, B.; Tyrrell, W. D. *Phys. Chem. Chem. Phys.* **2006**, 8, 3314–3319.
- (46) Lu, Q.; Liu, K.; Zhang, H.; Du, Z.; Wang, X.; Wang, F. *Nano* **2009**, 3, 3161–3168.
- (47) Clarke, R.; Latham, K.; Rix, C.; Hobday, M.; White, J. *Crys. Eng. Comm.* **2004**, 6, 42–50.
- (48) Xu, A.-W.; Su, C.-Y.; Zhang, Z.-F.; Cai, Y.-P.; Chen, C.-L. *New J. Chem.* **2001**, 25, 479–482.
- (49) Eastland, G. W.; Mazid, M. A.; Russell, D. R.; Symons, M. C. R. *J. Chem. Soc., Dalton Trans.* **1980**, 1682–1687.
- (50) Xue, G.; Dai, Q.; Jiang, S. J. *Am. Chem. Soc.* **1988**, 110, 2393–2395.
- (51) Wenkin, M.; Devillers, M.; Tinant, B.; Declercq, J.-P. *Inorg. Chim. Acta* **1997**, 258, 113–118.
- (52) Dickinson, B. N. Z. *Kristallogr.* **1934**, 88, 281–297.
- (53) Lee, G.-Y.; Jun, M.-S. *Bull. Korean Chem. Soc.* **2001**, 22, 11–12.
- (54) Maier, F.; Gottfried, J. M.; Rossa, J.; Gerhard, D.; Schulz, P. S.; Schwieger, W.; Wasserscheid, P.; Steinrück, H.-P. *Angew. Chem., Int. Ed.* **2006**, 45, 7778–7780.
- (55) Teets, T. S.; Partyka, D. V.; Esswein, A. J.; Updegraff, J. B.; Zeller, M.; Hunter, A. D.; Gray, T. G. *Inorg. Chem.* **2007**, 46, 6218–6220.
- (56) Fan, D.; Yang, C.-T.; Ranford, J. D.; Vittal, J. J. *Dalton Trans.* **2003**, 4749–4753.
- (57) Birte Ahrens, B.; Friedrichs, S.; Herbst-Irmer, R.; Jones, P. G. *Eur. J. Inorg. Chem.* **2000**, 2000, 2017–2029.
- (58) Vicente, J.; Chicote, M. T.; Guerrero, R.; Ramírez de Arellano, M. C. *Chem. Commun.* **1999**, 1541–1542.
- (59) Kim, S. J.; Kang, S. H.; Park, K.-M.; Kim, H.; Zin, W.-C.; Choi, M. G.; Kim, K. *Chem. Mater.* **1998**, 10, 1889–1893.
- (60) Best, S. L.; Chattopadhyay, T. K.; Djuran, M. I.; Palmer, R. A.; Sadler, P. J.; Sóvágó, I.; Varnagy, K. J. *Chem. Soc., Dalton Trans.* **1997**, 2587–2596.
- (61) Rossignoli, M.; Bernhardt, P. V.; Lawrance, G. A.; Maeder, M. J. *Chem. Soc., Dalton Trans.* **1997**, 323–327.
- (62) Suh, M. P.; Kim, I. S.; Shim, B. Y.; Hong, D.; Yoon, T.-S. *Inorg. Chem.* **1996**, 35, 3595–3598.
- (63) The meta-substituted isomer, 3-mercaptoaniline, also assembles on gold via its amino group and exhibits XPS peaks at 399.1 eV (N 1s) and 163.8 and 165.0 eV (Au-S, S 2p_{3/2} and S 2p_{1/2}) characteristic of Au-NH₂-C₆H₄-SH.

Synthesis of Covalently Linked Molecular Bridges between Silicon Electrodes in CMOS-Based Arrays of Vertical Si/SiO₂/Si Nanogaps**

Geoffrey J. Ashwell,* Laurie J. Phillips, Benjamin J. Robinson, Susan A. Barnes, Aled T. Williams, Barbara Urasinska-Wojcik, Colin J. Lambert, Iain M. Grace, Timothy I. Cox, and Ian C. Sage

The fabrication of nanometer-sized electrode gaps and the availability of self-assembling molecules of corresponding length^[1–4] are significant challenges in the miniaturization of molecular electronic devices. To overcome the intricacy of matching these dimensions, molecular connection is facilitated by stepwise synthesis of the bridging unit within the gap itself. It affords sub-nanometer control of molecular length by self-assembly of electrode coatings that are surface reactive and next by linking smaller chemical subunits.^[5–8] There are five examples of conjugated bridges formed in this way: four bridge metallic electrodes,^[9–12] whereas the fifth and most recent concerns a fluorene oligomer that connects silicon electrodes.^[13] In addition to bridging electrode gaps, scalability is fundamental to molecular electronic devices finding practical applications and is addressed by applying complementary metal-oxide semiconductor (CMOS) processing methods to nanogap device architectures.^[13–15] Herein, we focus upon silicon electrodes; studies, albeit few to date, have resulted in contacting by C₆₀ deposits within the gap^[16] as well as bridging by covalently linked nanoparticles^[15] and a 5.8 nm long fluorene oligomer.^[13] The latter example was the first to be grafted on both sides to silicon; herein, we present the device characteristics of a second example but with a shorter 2.8 nm span. The electrode gap was bridged by grafting 4-ethynylbenzaldehyde, Si–CH=CH–C₆H₄–CHO, to activate the surfaces and, thereafter, by coupling 2,6-diaminoanthra-9,10-quinone to connect the electrode coatings on opposite sides of the gap by imine links (Figure 1). Following the initial grafting stage, the silicon nanogaps exhibit leakage currents of

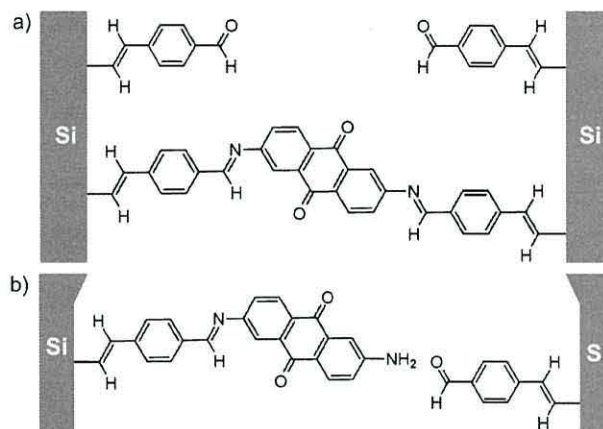


Figure 1. Reaction at the silicon surface: a) Molecular structures of the chemisorbed species and a 2.8 nm long molecular bridge formed by grafting the diethylacetal derivative of 4-ethynylbenzaldehyde and reacting the grafted molecules with 2,6-diaminoanthra-9,10-quinone at ambient temperature; b) an asymmetric nonbridging molecule coupled by an imine link to one side of the anthraquinone unit when the nanogap is too wide to accommodate the molecular bridge. The connection relies on surface roughness to match the length of the molecule to the width of the nanogap and limits the number of suitable bridging sites.

less than 2 pA at 1 V, but the current increases to 11–14 nA at 1 V upon molecular bridging. The process may be reversed by soaking in acidified solution, which detaches the linker unit and causes the current to diminish.

CMOS-based arrays of Si/SiO₂/Si sandwich structures with a surface density of about 700 devices cm^{–2} were fabricated as described in a previous report.^[13] The electrodes are arsenic-doped Si(111) and polysilicon, and the nanosized gap, which is shown as a V-shaped opening in Figure 2, is formed by selectively etching the edge of the interfacing oxide layer. Its thickness governs the minimum width of the electrode gap, and although influenced by surface roughness, approaches 2.8 nm, which is the dimension of the bridging molecule. The length of the undercut is 10–90 μm. The undercut length was varied by altering the size and shape of the exposed region of the top silicon electrode as well as the number of undercut edges. The nanogap was created by wet etching with NH₄F solution, which hydrogenates the surface and provides electrodes that are moderately resilient to oxidation. X-ray photoelectron spectra (XPS) of samples exposed to air for 50 h exhibit Si 2p peaks at 99.0 eV (Si–Si)

[*] Prof. G. J. Ashwell, Dr. B. J. Robinson

The Nanomaterials Group, Physics Department
Lancaster University, Lancaster LA1 4YB (UK)
E-mail: g.j.ashwell@lancaster.ac.uk

Dr. L. J. Phillips, S. A. Barnes, A. T. Williams, Dr. B. Urasinska-Wojcik
Nanomaterials Group, College of Physical and Applied Sciences
Bangor University (UK)

Prof. C. J. Lambert, Dr. I. M. Grace
Condensed Matter Theory Group, Physics Department
Lancaster University (UK)

Dr. T. I. Cox, Dr. I. C. Sage
QinetiQ plc, Malvern (UK)

[**] This work was supported by the Engineering and Physical Sciences Research Council, Technology Strategy Board and EC FP7 ITN “FUNMOLS” project no. 212942. CMOS = complementary metal-oxide semiconductor.

Supporting information for this article is available on the WWW under <http://dx.doi.org/10.1002/anie.201102791>.

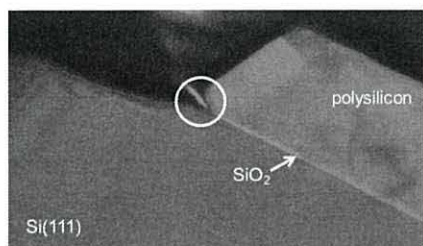


Figure 2. Scanning electron microscopy image of an Si/SiO₂/Si cross-section in which the top and bottom electrodes, arsenic-doped Si(111) and polysilicon, respectively, are separated by an ultrathin SiO₂ layer. The oxide layer is etched along its outer edge to provide a nanosized electrode gap, which is illustrated within the circle by the apex of the V-shaped undercut. Although not shown by this image, the electrodes are contacted by 2 μ m diameter aluminum plugs, which connect to 150 μ m x 150 μ m aluminum pads for contact with a probe station. For details, see the Supporting Information.

and 99.6 eV (Si–H) with only a minor peak arising from oxygen-bonded silicon. Nonetheless, the etched devices were protected immediately by chemical grafting in an inert argon atmosphere to suppress residual oxidation. The electrode surfaces were treated with the diethylacetal derivative of 4-ethynylbenzaldehyde in hexadecane (0.1 mg cm^{−1}) for 2 h at 190 °C and rinsed with copious volumes of chloroform to remove physisorbed material. Chemisorption was verified by the Si 2p core-level spectrum, which has a peak at 101.9 eV that conforms to the Si–C link, and by the Fourier-transform infrared attenuated total reflection (FTIR-ATR) spectrum which, for example, exhibits a characteristic CO stretching mode at 1703 cm^{−1} that corresponds to the aldehyde group. Analytical studies were performed on surface-treated silicon wafers, but there is no reason to assume that the etched device should not react accordingly.

Si–CH=CH–C₆H₄–CHO coatings on opposite sides of the gap permit molecular bridging of amino-terminated wires by imine links, Si–CH=CH–C₆H₄–CH=N–wire–N=CH–C₆H₄–CH=CH–Si, but the dimensions must be complementary. To achieve this, arrays of the coated devices were immersed for periods of 5 min to 2 h in THF solutions of 2,6-diaminoanthra-9,10-quinone (0.03 mg cm^{−1}) to which catalytic traces of either formic acid or acetic acid were added, then rinsed and air-dried. Direct chemical analysis of the bridged nanogap is not possible, and a proof of concept was provided instead by performing the reaction on conventional substrates, for example, large-area Si, Au, Pt, and TiO₂ surfaces as well as Au, Pt, and TiO₂ nanoparticles. Stepwise synthesis was achieved by chemisorbing molecules with surface-based aldehyde groups and next by reacting amino-terminated units and vice versa. This modular approach permits sequencing of units in a predefined manner and combines ease of synthesis with sub-nanometer control of molecular length. XPS and FTIR studies confirm that imine coupling on solid supports is independent of the underlying inorganic substrate. It is verified by a lowering of the N 1s binding energy to 398.9–399.3 eV compared with 399.9–400.3 eV for NH₂ and the loss and emergence of the CO stretching frequency of the surface aldehyde at successive reaction steps. Analytical data are

included in the Supporting Information, and the binding energy shift is consistent with data reported in the National Institute of Standards and Technology XPS database.^[17]

Current-voltage (*I*–*V*) characteristics of the molecule-inserted Si/SiO₂/Si structures were obtained by using a Keithley Instruments model 6430 sub-femtoamp source meter and a Wentworth manual probe station to contact individual devices. Data were collected following the initial grafting step, and once again following attempts to bridge the silicon electrodes by coupling 2,6-diaminoanthra-9,10-quinone linker units. The former yielded leakage currents of less than 2 pA at 1 V, as expected for an open nanogap. It is independent of the size and shape of the exposed region of the silicon electrode in different devices, which is expected, as the area of overlap of the top and bottom electrodes is similar when the exposed and unexposed regions are taken into account. In this study, 98 nanogap devices were studied, of which eight shorted, and most of the remainder showed no change in their electrical behavior following immersion in solutions of the amino-terminated linker. One device exhibited a current of 0.1 nA at 1 V, which was attributed to a nonbridging arrangement, as the current is significantly lower than theoretically derived values for covalently bridged silicon devices. In contrast, reproducible *I*–*V* characteristics and currents of 11–14 nA at 1 V were obtained on seven occasions following immersion. These data are assigned to bridged structures, but we note that the range is narrow compared with currents of 10–10,000 nA at 1 V obtained for 5.8 nm wide molecule-inserted silicon nanogaps.^[13] In both cases, we relied upon disparity between the width of the nanogap and length of the connecting molecule to minimize the number of compatible bridging sites whilst using inherent surface roughness to match the dimensions. Based on this, we suggest that the restricted current range and low yield of working devices arise from limitations imposed by this method and greater incompatibility when attempting to bridge the electrode gap with a shorter 2.8 nm long molecular wire.

We focus on a device whose *I*–*V* characteristics were unchanged when the immersion period in a solution of 2,6-diaminoanthra-9,10-quinone was increased from 5 min and 2 h. It exhibited a current of 12 nA at 1 V (Figure 3), showed indistinguishable behavior when studied in air and dry nitrogen, and its *I*–*V* characteristics were stable when cycled between ± 1 V. To confirm molecular bridging, control studies were performed to decouple the unit, and thereafter, by bridging the gap to restore the current. The imine link is broken by acidified solution, as demonstrated by XPS studies, which show a 1 eV shift of the N 1s binding energy from ca. 399.0 eV (C=N) to 400.0 eV (NH₂). The anthraquinone linker in this case became detached when the silicon nanogap was soaked for 16 h in acetic acid solution (10^{−3} M). The treated device following rinsing with chloroform and drying in air exhibited a diminished current and, although not apparent from data shown in Figure 3, the horizontal line exhibits slight asymmetry with currents of 0.08 nA at −1 V and 0.03 nA at +1 V. These values are higher than the leakage current following grafting with 4-ethynylbenzaldehyde (compared with less than 2 pA at 1 V), and the slight asymmetry is assigned to

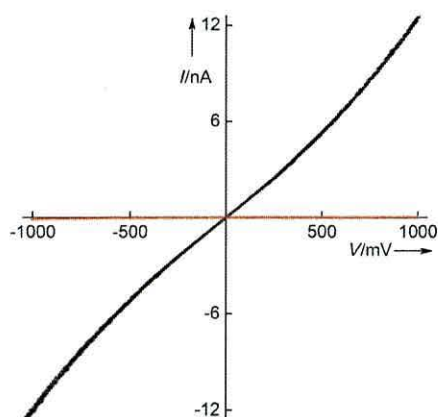


Figure 3. Symmetrical I - V characteristics of a bridged Si/SiO₂/Si nanogap device (black) and altered behavior following immersion in an acidified solution to disconnect the anthraquinone linker unit (red). The sign is assigned to the bottom Si(111) electrode of the device and, although not discernible from the scale of the plot, the currents at 1 V differ by a factor of 150 in the negative quadrant and a factor of 400 in the positive quadrant (see the Supporting Information).

incomplete exclusion of the electron-accepting linker. The current is higher when the bottom Si(111) electrode is negatively charged (cathode), and based on the behavior of molecular diodes^[18] and organic rectifying junctions,^[19] it may be assumed that an electron-accepting anthraquinone moiety is located on this side of the device (as shown for example in Figure 1 b). However, regardless of explanation, the control study shows profound changes in electrical behavior for conditions that reverse the bridging process. It supports our premise that the current of 12 nA at 1 V is not an experimental artifact but inherent to the bridged Si-molecule-Si nanogap (Figure 1 a). Besides, we reject the prospect of the behavior arising from trapped molecular deposits because rinsing repeatedly with copious volumes of solvent has no effect on the magnitude of the current or I - V characteristics.

We now turn to a molecule-inserted nanogap whose current is at the lower limit of those measured. The current of 0.1 nA at 1 V is seven times smaller than the theoretically derived value for a single molecular bridge, and unlike the smooth curve shown in Figure 3, the I - V characteristics exhibit deformations as the voltage is swept between ± 1 V (Figure 4). The magnitude makes it necessary to consider a nonbridging structure with either an interdigitating arrangement of molecules or a suitably narrow gap between the electrode coatings. The anomalous behavior probably results from single points of attachment. If the molecules anchor at one end, irregularities in the I - V profile may be explained by rotation of the subunits about their exocyclic single bonds and subtle changes in intermolecular contacting distances across the nanogap. Bridging is reliant on an exact match between the width of the gap and length of the stepwise-formed molecular bridge. Therefore, attempts were made to connect the electrodes of this device by longer molecules, for example, by coupling amino-terminated units, H₂N-wire-NH₂, followed by terephthalaldehyde, OHC-C₆H₄-CHO, and thereafter by repeating these steps. However, the process had no

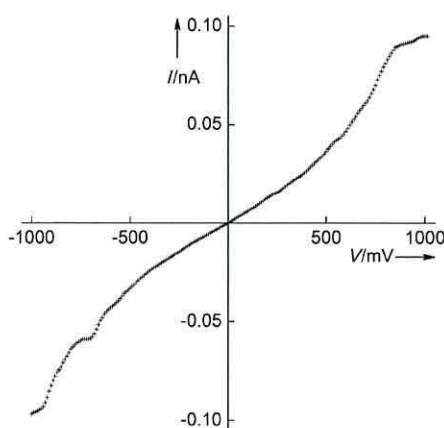


Figure 4. I - V curve of an Si/SiO₂/Si nanogap device, the current of which is at the lower limit of those observed when the 4-ethynylbenzaldehyde grafted electrodes are treated with 2,6-diaminoanthra-9,10-quinone. Anomalous distortions in the electrical characteristics are attributed to a nonbridging arrangement, with altered contacting distances induced by rotation about the exocyclic single bonds of the molecule as the voltage is swept.

discernable effect on the current or shape of the I - V curves of both the bridged (Figure 3) and unbridged devices (Figure 4). It may be assumed that the width of the electrode gap, which is dependent upon the thickness of the preformed oxide spacer layer, is reasonably similar throughout the array of silicon nanogaps, and serendipity plays a role in matching its dimensions to those of the molecule.

Ab initio transport code SMEAGOL^[20] and density functional (DFT) code SIESTA^[21] were used to predict the electrical transport properties of the silicon-contacted molecule. The relaxed geometry of the isolated molecule and optimum binding geometry to the silicon surface were calculated using DFT. It was extended to include 6 layers of Si(111), each containing 25 atoms, which were attached to infinite periodic leads. Periodic boundary conditions were imposed in the x and y directions (the transport axis is along z), and a silicon lead structure was chosen to mimic the doped behavior, that is, with a finite density of states at the Fermi energy. The zero bias electron transmission coefficient, $T(E)$, was calculated using SMEAGOL (Figure 5), and the I - V relation (Figure 6) was obtained from $T(E)$ using Equation (1):

$$I = \frac{2e}{h} \int_{-eV}^{eV} T(E) dE \quad (1)$$

Profiles of the I - V curves from theory and experiment are alike, but their currents, 0.7 nA at 1 V (Figure 6) and 12 nA at 1 V (Figure 3), differ by a factor of seventeen. This may be explained in part by a few molecular bridges rather than a single molecule bridging the gap. For so few molecules, as indicated by the modest difference, the likelihood of clustering is remote when these silicon nanogaps may be bridged along 10–90 μ m lengths. We also note that discrepancies probably arise from problems associated with the use of DFT

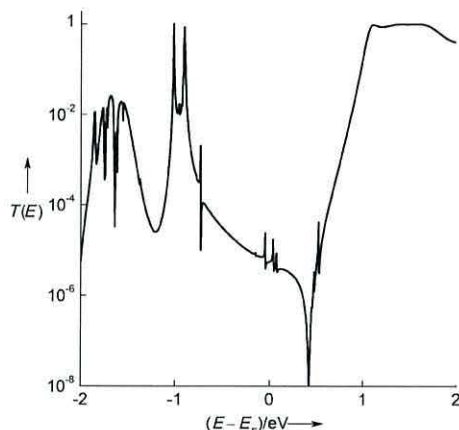


Figure 5. Theoretical transport properties: zero bias transmission coefficient of the 2.8 nm long molecular wire contacted by silicon leads as a function of $E - E_F$, where E_F is the Fermi energy and E is the energy of the transmitted electrons.

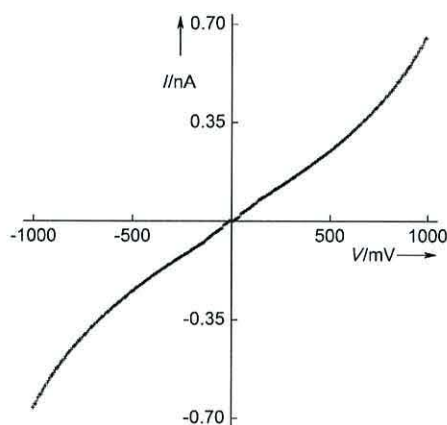


Figure 6. Theoretical I - V characteristics: the gentle reverse-S profile of the I - V curve of the silicon-contacted 2.8 nm long molecular wire mimics the experimental curve shown in Figure 3.

to estimate the HOMO–LUMO gap and the position of the Fermi energy as well as to difficulties in simulating the Si-molecule-Si device characteristics when the electrodes are highly doped and asymmetric in their morphology. The top and bottom electrodes are arsenic-doped polycrystalline silicon and Si(111), respectively. Difficulties arise from a theoretical viewpoint as there are unknown parameters at an atomic scale that probably contribute to the discrepancy between the estimated and experimentally determined currents. Details of the theoretical method is included in the Supporting Information.

In summary, there is one previous report of the electrical characterization of a molecule grafted at each end to silicon electrodes.^[13] In this work, we describe a second, albeit much shorter example, in which the bridging of silicon nanogaps is achieved by a 2.8 nm-long molecular wire. Reproducible currents and I - V characteristics following multiple rinsing cycles in chloroform confirms that the behavior does not arise from molecular deposits. In the same way, suppression of the

current following immersion in acidified solution is symptomatic of the molecular bridging unit becoming detached as imine links break under these conditions. It suggests that the current of about 12 nA at 1 V (compared with less than 2 pA at 1 V following the initial grafting step) is inherent to the Si-molecule-Si bridge. In this case, the stepwise synthesis of molecular wires within the silicon nanogap itself with covalent bonding to the electrodes on opposite sides is fundamental to matching the respective dimensions. The process has been applied herein to CMOS-based arrays, and the scalability of the technique, that is, the mass production of silicon nanogaps combined with an in situ modular approach for bridging the electrodes, points the way to molecule-inserted test-bed structures for silicon-based electronics. There is reasonable agreement between the experimental and theoretical I - V characteristics for the bridged device, and our studies have shown it to be robust when cycled between ± 1 V.

Received: April 21, 2011

Revised: May 24, 2011

Published online: July 26, 2011

Keywords: molecular electronics · nanogaps · nanotechnology · self-assembly · semiconductors

- [1] X. Chen, Z. Guo, G.-M. Yang, J. Li, M.-Q. Li, J.-H. Liu, X.-J. Huang, *Materials Today* **2010**, *13*, 28–41.
- [2] T. Li, W. Hu, D. Zhu, *Adv. Mater.* **2010**, *22*, 286–300.
- [3] A. K. Feldman, M. L. Steigerwald, X. Guo, C. Nuckolls, *Acc. Chem. Res.* **2008**, *41*, 1731–1741.
- [4] a) S. Strobel, R. M. Hernández, A. G. Hansen, M. Tornow, *J. Phys.: Condens. Matter* **2008**, *20*, 374126; b) R. Søndergaard, S. Strobel, E. Bondgaard, K. Norman, A. G. Hansen, E. Albert, G. Csaba, P. Lugli, M. Tornow, F. C. Krebs, *J. Mater. Chem.* **2009**, *19*, 3899–3908.
- [5] T. P. Sullivan, W. T. S. Huck, *Eur. J. Org. Chem.* **2003**, 17–29.
- [6] N. Tuccitto, V. Ferri, M. Cavazzini, S. Quici, G. Zhavnerko, A. Licciardello, M. A. Rampi, *Nat. Mater.* **2009**, *8*, 41–46.
- [7] a) S. H. Choi, C. Risko, M. C. Ruiz Delgado, B. Kim, J.-L. Bredas, C. D. Frisbie, *J. Am. Chem. Soc.* **2010**, *132*, 4358–4368; b) L. Luo, C. D. Frisbie, *J. Am. Chem. Soc.* **2010**, *132*, 8854–8855.
- [8] a) G. J. Ashwell, B. Urasinska-Wojcik, L. J. Phillips, *Angew. Chem.* **2010**, *122*, 3586–3590; *Angew. Chem. Int. Ed.* **2010**, *49*, 3508–3512; b) G. J. Ashwell, A. T. Williams, S. A. Barnes, S. L. Chappell, L. J. Phillips, B. J. Robinson, B. Urasinska-Wojcik, P. Wierchowicz, I. R. Gentle, B. J. Wood, *J. Phys. Chem. C* **2011**, *115*, 4200–4208.
- [9] M. Taniguchi, Y. Nojima, K. Yokota, J. Terao, K. Sato, N. Kambe, T. Kawai, *J. Am. Chem. Soc.* **2006**, *128*, 15062–15063.
- [10] a) G. J. Ashwell, P. Wierchowicz, C. J. Bartlett, P. D. Buckle, *Chem. Commun.* **2007**, 1254–1256; b) G. J. Ashwell, P. Wierchowicz, L. J. Phillips, C. Collins, J. Gigon, B. J. Robinson, C. M. Finch, I. R. Grace, C. J. Lambert, P. D. Buckle, K. Ford, B. J. Wood, I. R. Gentle, *Phys. Chem. Chem. Phys.* **2008**, *10*, 1859–1866.
- [11] J. Tang, Y. Wang, J. E. Klare, G. S. Tulevski, S. J. Wind, C. Nuckolls, *Angew. Chem.* **2007**, *119*, 3966–3969; *Angew. Chem. Int. Ed.* **2007**, *46*, 3892–3895.
- [12] X. Chen, A. B. Braunschweig, M. J. Wiester, S. Yeganeh, M. A. Ratner, C. A. Mirkin, *Angew. Chem.* **2009**, *121*, 5280–5283; *Angew. Chem. Int. Ed.* **2009**, *48*, 5178–5181.
- [13] G. J. Ashwell, L. J. Phillips, B. J. Robinson, B. Urasinska-Wojcik, C. J. Lambert, I. M. Grace, M. R. Bryce, R. Jitchati, M. Tavasli,

- T. I. Cox, I. C. Sage, R. P. Tuffin, S. Ray, *ACS Nano* **2010**, *4*, 7401–7406.
- [14] S. M. Dirk, S. W. Howell, S. Zmuda, K. Childs, M. Blain, R. J. Simonson, D. R. Wheeler, *Nanotechnology* **2005**, *16*, 1983–1985.
- [15] S. W. Howell, S. M. Dirk, K. Childs, H. Pang, M. Blain, R. J. Simonson, J. M. Tour, D. R. Wheeler, *Nanotechnology*, **2005**, *16*, 754–758.
- [16] D. A. Corley, T. He, J. M. Tour, *ACS Nano* **2010**, *4*, 1879–1888.
- [17] National Institute of Standards and Technology X-ray photoelectron spectroscopy database (<http://srdata.nist.gov/xps/default.aspx>).
- [18] G. J. Ashwell, A. Mohib, *J. Am. Chem. Soc.* **2005**, *127*, 16238–16244.
- [19] G. J. Ashwell, B. Urasinska, W. D. Tyrrell, *Phys. Chem. Chem. Phys.* **2006**, *8*, 3314–3319.
- [20] A. R. Rocha, V. M. Garcia-Suarez, S. Bailey, C. Lambert, S. Sanvito, J. Ferrer, *Phys. Rev. B* **2006**, *73*, 085414.
- [21] J. M. Soler, E. Artacho, J. D. Gale, A. Garcia, I. Junquera, P. Ordejon, D. Sanchez-Portal, *J. Phys.: Condens. Matter* **2002**, *14*, 2745–2779.
-